Physical properties of doped multiferroic $GaFeO_3$

Vom Fachbereich Material und Geowissenschaften

der Technischen Universität Darmstadt

zur Erlangung des akademischen Grades eines

Doktors der Naturwissenschaften (Dr. rer. nat.)

genehmigte Dissertation

vorgelegt von

M. Sc. Mohamed Bakr Mahmoud Mohamed

aus Kairo, Ägypten

Referent: Prof. Dr. Ing. Dr. h. c. Hartmut Fuess
Korreferent: Prof. Dr. rer. nat. Lambert Alff
Tag der Einreichung: 17.02.2011
Tag der mündlichen Prüfung: 05.04.2011

Darmstadt 2011
D17

Dedicated to My Family

Physical properties of doped multiferroic $GaFeO_3$

Abstract

Gallium iron oxide ($GaFeO_3$) is a member of a multiferroic family which exhibits ferrimagnetic and piezoelectric properties below room temperature. The physical properties of $GaFeO_3$ are strongly dependent on the distribution of cations within the structure. $GaFe_{1-x}Mn_xO_3$ polycrystalline materials have been prepared by a solid state reaction (SR) and by a sol-gel (SG) methods. Also, $GaFe_{1-x}Cr_xO_3$ was prepared by solid state reaction. The maximum Mn content amounts to 10 and 40 % for SR and SG preparation, respectively, while the maximum Cr amount is 15%. All compounds in these composition ranges crystallize in space group $P\ c\ 2_1\ n$ derived from Rietveld refinement of X-ray powder patterns. The gradual incorporation of manganese and chromium are accompanied by a decrease in the cell volume. The Curie temperature (T_C) for $GaFeO_3$ (SR) is about 225 K and increases up to above room temperature when the temperature of preparation is decreased from 1300°C to 700°C. With increasing Mn or Cr contents the transition temperatures as well as the coercive field decrease. Dielectric investigations revealed a temperature independent anomaly at around 250 K with frequency dispersion of dielectric constant for Mn doped samples prepared by both methods accompanied by lattice parameters anomaly at the same temperature without change in crystal structure. A combined neutron and Mössbauer data analysis has led to the determination of site assignment and the occupancies. The ordering of Ga and Fe cations depends on the Mn substitution. Below the magnetic transition temperature a ferrimagnetic order with a propagation vector $\mathbf{K} = \mathbf{0}$ was derived from neutron powder diffraction data. The Fe^{3+} magnetic moments are ordered along the c-axis with small components along a and b. The magnetic structure does not alter for Mn doped $GaFeO_3$ but the magnetic moment decreases as the amount of Mn increases.

Physikalische Eigenschaften von dotiertem multiferroischem $GaFeO_3$

Abstract

Gallium Eisenoxid ($GaFeO_3$) gehört zu einer Klasse multiferroischer Materialien, die ferrimagnetische und piezoelektrische Eigenschaften unterhalb von Raumtemperatur aufweisen. Die physikalischen Eigenschaften hängen wesentlich von der Verteilung der Kationen auf den kristallographischen Gitterplätzen ab. Polykristalline Proben von $GaFe_{1-x}Mn_xO_3$ wurden durch Festkörperreaktion (SR) und durch Sol-Gel (SG) Methoden dargestellt. Der maximale Gehalt an Mn beträgt 10% für SR - und 40% für SG - Präparation, während als maximale Menge an Cr 15% erreicht wird. Alle Verbindungen mit den genannten Zusammensetzungen kristallisieren in der Raumgruppe $P\ c\ 2_1\ n$, wie durch Rietveld-Verfeinerung von Pulverproben bestätigt wurde. Die wachsende Substitution von Mangan und Chrom führt zu einer Abnahme des Zellvolumens. Die Curie Temperatur T_c für $GaFeO_3$ (SR) beträgt etwa 225K, die bei 1300^o präpariert wurden. Die Curie Temperatur steigt bis Raumtemperatur an, wenn die Sintertemperatur auf 700^o gesenkt wird. Mit zunehmender Substitution durch Mn und Cr sinkt die Übergangstemperatur und die Koerzitivfeldstärke nimmt ab. Dielektrische Messungen ergaben eine Anomalie bei etwa 250 K für Mn dotierte Proben, die unabhängig von der Temperatur ist, aber abhängig von der Frequenz ist. Dies wurde bei Präparationsmethoden beobachtet. Mit hochauflösender Synchrotronstrahlung ließ sich eine Anomalie der Gitterkonstanten feststellen, ohne allerdings einen kristallographischen Phasenübergang. Durch Kombination von Neutronenbeugungs- und Mössbauerspektroskopie konnte die Besetzung der Kationenplätze bestimmt werden. Die Besetzung der Ga- und Fe-Lagen hängt von der Mn Substitution ab. Unterhalb der magnetischen Übergangsstruktur konnte eine ferrimagnetische Ordnung mit einem Propagationsvektor K=0 aus Neutronendaten abgeleitet werden. Die magnetischen Fe^{3+} Momente sind parallel zur c-Achse geordnet und haben kleine Komponenten entlang a und b. Die magnetische Struktur wird durch Mn Dotierung nicht geändert, aber das magnetische Moment nimmt mit der Substitution durch Mn ab.

Contents

4 Effect of cation distribution on dielectric and magnetic properties of $GaFeO_3$

5 Structural, magnetic and electric properties of Mn and Cr doped $GaFeO_3$

Appendices

Chapter 1

Thesis outline

Multiferroic materials with ferroelectric (FE) and ferromagnetic (FM) properties offer potential applications for functional devices. The prerequisite is a simultaneous presence of FM and FE well above room temperature in a single phase material [1]. Aside from its fundamental importance, the mutual control of electric and magnetic properties is of significant interest for applications in magnetic storage media and 'spintronics' [2, 3]. Although a certain number of materials with ferroelectricity and ferromagnetism exists, the coupling between those two properties is not always large enough [4]. The nontrivial spin lattice coupling in these multiferroics has been manifested through various forms such as linear and bilinear magnetoelectric effects [5], polarization change through field-induced phase transition [6], magnetodielectric effect [7] and dielectric anomalies at magnetic transition temperatures [8]. For bulk ceramics, combining antiferromagnetism (ferromagnetic) and electric polarization phases is a tricky problem as such properties are exclusive in most materials [9, 10]. In that respect, the discovery of ferroelectricity induced by complex lattice distortion such as in hexagonal manganite systems beside its magnetic properties has opened new possibilities [11].

Gallium iron oxide ($GaFeO_3$) has magnetic and piezoelectric properties and has been intensively studied recently for its potential application as a magnetoelectric ferrimagnet [12-14].

This material has orthorhombic crystal structure with space group $P\,c\,2_1\,n$ with four different cation sites labelled Ga_1, Ga_2 (mainly occupied by gallium) and Fe_1, Fe_2 (mainly occupied by iron) [15-17]. Physical properties, especially magnetism in $GaFeO_3$, depend strongly on the method of preparation [15, 17-20] and are highly correlated with the cation distribution among the four crystallographic sites. Several models of the magnetic structure of $GaFeO_3$ have been suggested: ferromagnetic [18], ferrimagnetic [21] or canted-antiferrimagnetic [22] structure. The interpretation of the magnetic structure and other properties require prior determination of cation occupancies.

In this thesis, a systematic study on the structural, magnetic, and electric properties of $GaFeO_3$ sample, which wse doped with transition metal ions (TM = Mn, Cr), has been carried out. The main scope of the thesis was to prepare and investigate samples that could exhibit room temperature ferrimagnetism and have dielectric properties, which would make them good candidates for practical applications. In order to understand the influence of the sample preparation conditions in relation to the sample properties, our samples were prepared by different methods and under various conditions. Detailed structural studies were performed to achieve some insight on where magnetic ions might be situated. In addition, electric properties were measured.

This thesis consists of three main experiments:

1. Preparation of unsubstituted and substituted $GaFeO_3$ polycrystalline materials under various conditions.
2. Systematic characterizations of crystal structures, including Rietveld refinements. Investigation of magnetic properties and a systematic study of dielectric properties.
3. Determine the Fe distribution among different crystallographic sites to the understanding of magnetic properties.

All obtained data and analyses were summarized, and the features of the materials prepared were studied. The thesis consists of three main parts: the literature review, experimental procedures, and discussions on the obtained results.

Because magnetoelectric multiferroicity is based on magnetic and ferroelectric properties of materials, an understanding of the fundamental properties of such materials is of high importance. The first part of the thesis deals with the introduction of fundamental concepts of magnetism, ferroelectricity, and how to couple them in multiferroic materials. A literature review on $GaFeO_3$ material is also presented. All this information is summarized in Chapter 2.

The second part of the thesis describes experimental work, which includes synthesis of polycrystalline samples $GaFeO_3$ and $GaFe_{1-x}M_xO_3$, M = Mn or Cr applying conventional and sol gel methods, setting up and operation of the equipment, as well as how measurements were performed. Experimental procedures are listed in Chapter 3. This contains the overall synthesis scheme for the various compounds, as well as the experimental principles.

In the third part, the experimental data is summarized and analyzed. A discussion on the observed and obtained results is given.

In Chapter 4, the effect of the preparation methods on the properties of $GaFeO_3$ was studied. This study covers the following aspects: structural analysis by X-ray diffraction, neutron powder diffraction, Mössbauer spectroscopy, Rietveld refinements and magnetic and dielectric measurements were carried out.

In Chapter 5, investigations on magnetic and structural properties of Mn and Cr doped $GaFeO_3$ are summarized and discussed. Characterization of crystal structures, magnetic properties and electric properties including impedance spectroscopy in case of Cr doped samples is presented and ferroelectric hysteresis in case of Mn doped samples in addition to dielectric characterization.

The final chapter of the thesis (Chapter 6) contains the summary of the current work. This section is followed by a list of the references used in this thesis.

Chapter 2

Fundamental

2.1 Magnetism: Order, structure and exchange

2.1.1 Magnetic materials

There are several classes of magnetic materials such as paramagnetic, ferromagnetic, ferrimagnetic, antiferromagnetic, superparamagnetic and spin glass. Paramagnetic behavior describes a situation where all spins are random and dynamic.

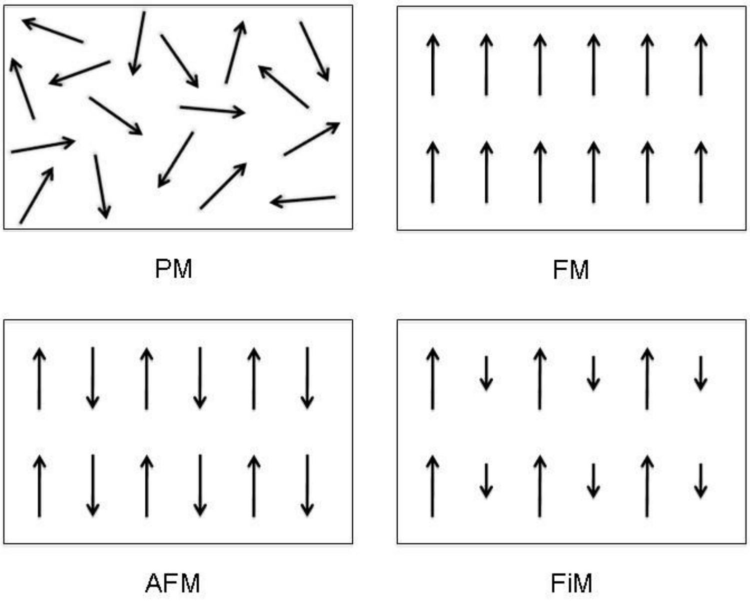

Figure 2.1: Paramagnet, ferromagnet, antiferromagnet and ferrimagnet.

On the another hand magnetic ordering occurs when the spins of one atom are coupled to spins of neighboring atoms. With magnetic order there is a transition from a paramagnetic state to one where the electron spins order at a particular temperature denoted T_C (Curie temperature) for ferro- and ferrimagnets, and T_N (Néel temperature) for antiferromagnets. Ferromagnetism results when all spins align parallel to one another, and antiferromagnetism for spins aligned antiparallel, as shown in Fig. 2.1. Ferrimagnetism occurs when electron spins are aligned antiparallel but do not cancel each other out completely, thus there is a net magnetization.

2.1.2 Exchange mechanisms

Long range magnetic order occurs at lower temperatures as a result of interactions between magnetic moments in the crystal lattice. The interactions between Heisenberg (isotropic) magnetic spins, S_i and S_j, can be expressed by the Hamiltonian:

$$H=- \Sigma_{ij}\ J_{ij}\ S_i x S_j \qquad (2.1)$$

where J_{ij} is the exchange constant. For ferromagnetic interactions, this parameter is positive and for antiferromagnetic interactions it is negative. The alignment of magnetic moments occurs spontaneously in the ferro- and antiferromagnetic states and there must therefore be some positive energy of interaction between neighbouring spins. For transition metal compounds the magnetic order is formed via a superexchange mechanism [23, 24] and the interaction depende on the covalent bonding of the metal ions with their bridging anion ligands. It tends to promote antiferromagnetic ordering. If the cation-anion-cation pathway has a linear bond angle of 180°, as in Fig. 2.2a, then strongest interactions are predicted to be antiferromagnetic. An excited state is formed in which a double charge transfer occurs between the ligand and the metal sites with the net effect being that neighboring metal ions are coupled antiparallel. However, the ferromagnetic ground state can be stabilized by superexchange when the cation-anion-cation pathway is at 90°, illustrated in Fig. 2.2b, as a result of mutually orthogonal anion orbitals in the exchange pathway. After the double ligand to metal charge transfer, the ferromagnetic excited state on the orthogonal ligand orbitals is lower in energy than the antiferromagnetic excited state due to Hund’s rule. Hence, the strength of the exchange coupling via a bridging ligand is highly dependant on the M-O-M bond angle; M = Mn^{3+}, Fe^{3+} or Cr^{3+}, …. The crossover from antiferromagnetic to ferromagnetic superexchange occurs at ~96°.

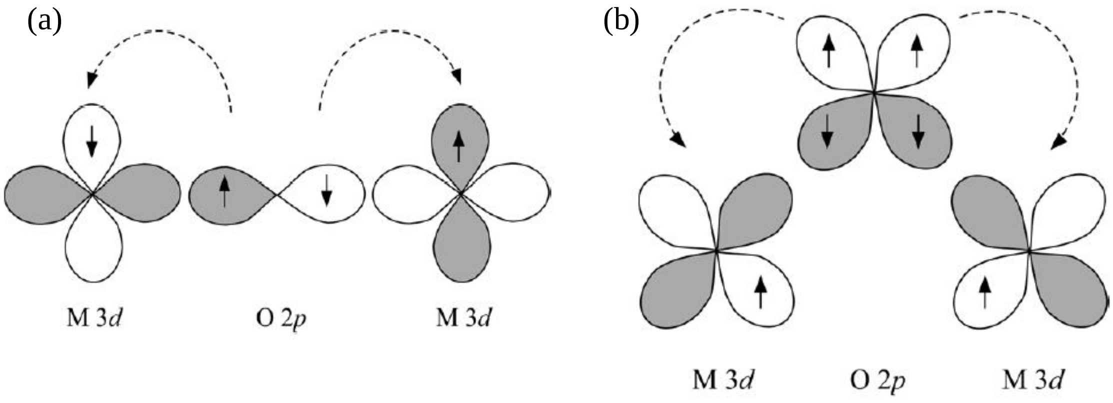

Figure 2.2: (a) A simple view of superexchange in a linear M-O-M system giving antiferromagnetic alignment of ions with a bridging oxygen ligand. (b) The superexchange pathway stabilising ferromagnetic coupling in a 90° M-O-M array [24].

Other exchange pathways are possible when the adjacent cations have different oxidation states

2.1.3 Types of magnetic order

Although an indication of the type of magnetic ordering in a material can be obtained by magnetic susceptibility measurements, it does not provide any details about the arrangement of spins. This information is best obtained through neutron diffraction techniques as neutrons are scattered by unpaired electrons. For antiferromagnets, there are numerous ways in which the equal number of up and down spins can be arranged on the lattice [25]. What arrangements are possible depends also on the type of crystal lattice in which the spins are located. Some examples are given in Fig. 2.3. The G-type ordering is very common in cubic perovskites, which have the magnetic atoms arranged on a simple cubic lattice, because all nearest neighbour atoms are forced into an antiferromagnetic alignment by the superexchange interactions that occur via the oxygen atoms. This type of ordering is found in $LaFeO_3$ [26] and $LaCrO_3$ [27]. Other cubic perovskites, such as $LaMnO_3$ [25], have alternately aligned ferromagnetic planes or the A-type ordering. In the latter case, this order is a result of the Jahn-Teller distortion of the Mn^{3+} ions. Ferrimagnets do not follow the Curie Weiss law as the magnetic structure is made up of sublattices with different molecular fields and hence different temperature dependence of the magnetization. Ferrites are a group of compounds with the chemical formula MFe_2O_4, where M is a divalent cation such as Zn^{2+}, Co^{2+} or Cu^{2+}

that show ferrimagnetic ordering [28]. They have two non-equivalent sublattices due to their spinel crystal structure which contains two types of crystallographic lattice site, octahedral and tetrahedral, with two different ions. There are also other more complex forms of magnetic order such as helical order and spin glasses [29] but that will not be discussed here as it is not applicable to the work in this thesis.

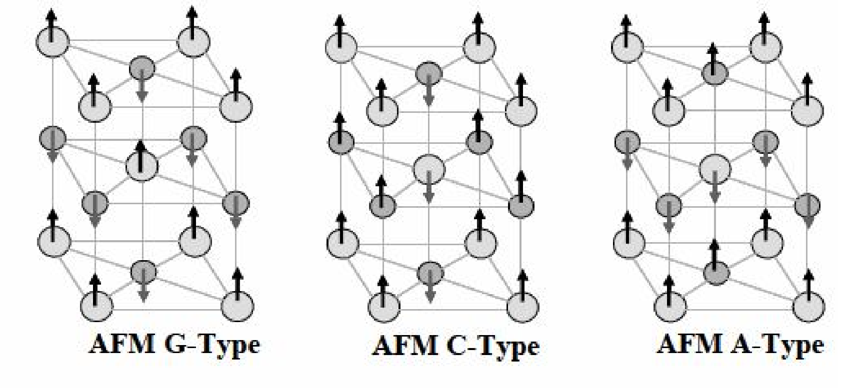

Figure 2.3: Three types of antiferromagnetic order for simple cubic lattices

2.1.4 Jahn-Teller (JT) effect

The Kramer's degeneracy theorem [30] states that the energy levels of systems with an odd number of spins, no matter what the crystal field is like, retain at least a residual degeneracy in the presence of pure electric fields (only magnetic field can lift it). Ions with an even number of electrons in the unfilled 3d-, 4d-, 5d- or 4f- shell are called the Kramer's ions. The JT effect happens only for Kramer's ions. For manganites, if the symmetry of the crystal field is so high that the ground state of Mn^{3+} ions (Kramer's ions) is predicted to be orbitally degenerate, then it will be energetically favorable for the crystal to distort to lift the orbital degeneracy. This so-called JT effect is due to an electron-lattice interaction. The JT effect in manganites arises from an electronic instability inherent to the Mn^{3+} ions in asymmetric MnO_6 octahedra. Since neighboring octahedra share one oxygen ion, the JT distortion can be cooperative. The cooperative rotation of MnO_6 octahedra leads to a change in lattice symmetry. This is usually accompanied by the shortening and stretching of six Mn-O bonds. Consequently, the resulting JT distortion leads to different electronic structures for the e_g states of Mn^{3+} ions as exemplified in Fig. 2.4. A quantitative measure of the magnitude of cooperative JT distortion is given by the octahedral distortion parameter Δ defined as:

$$\Delta=\frac{1}{6}\sum_{n=1,6}\left[\frac{\left(d_n\text{-}\langle d\rangle\right)}{\langle d\rangle}\right]^2, \qquad (2.2)$$

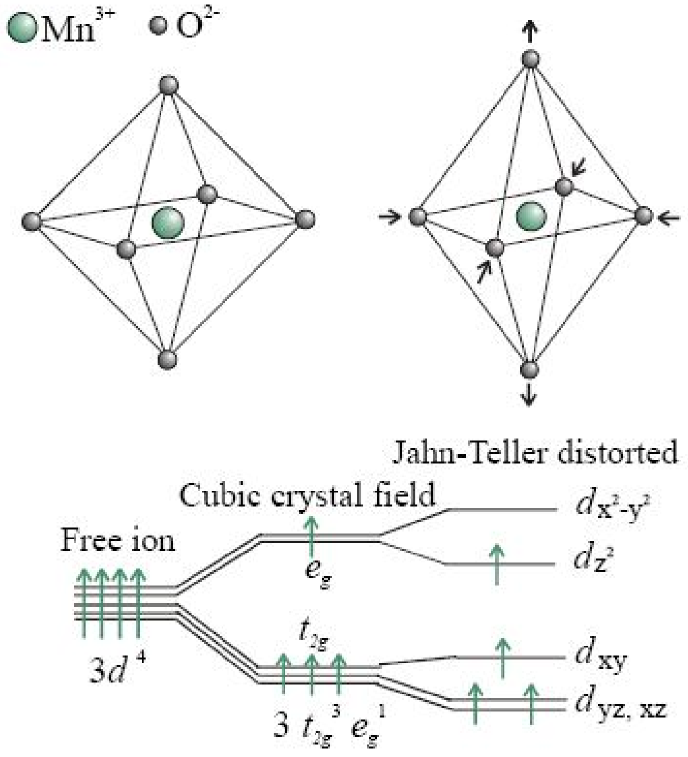

Figure 2.4: The energy levels of the 3d electrons of an Mn^{3+} ion. In a cubic crystal field, the five-fold degeneracy is lifted to two e_g and three t_{2g}–orbitals. The Jahn Teller distortion leads to a further splitting of both the t_{2g} and e_g states. Knowledge about the occupancy of the e_g states is a crucial point for understanding the fascinating properties of transition metal compounds.

where <d> and d_n are the mean Mn-O bond lengths and the six Mn-O bond lengths along six different directions, respectively. The detailed bond lengths of a certain manganite can be obtained via a Rietveld structure determination by refining the high-resolution neutron and/or x-ray powder diffraction data. Note that the Mn^{4+} ($3d^3$) ion (non-Kramer's ion) does not show the JT effect, since a net lowering of the electronic energy cannot be achieved with a preservation of the gravity center for all filled t_{2g} states in octahedral geometry. Therefore, a high concentration of Mn^{3+} ions tends to promote the distortions of MnO_6 octahedra, while the high concentration of Mn^{4+} will discourage such distortions.

2.2 Ferroelectric and dielectric properties

2.2.1 Dielectric properties of matter

Dielectric materials are electrically insulating, but still susceptible to polarization. Polarization is the alignment of dipole moments in the presence of an externally applied electric field.

2.2.1.1 Creation of a polarization

Due to the nature of atoms and their arrangement in the crystal lattice (chemical bonds, atomic coordination number), the electrons in a dielectric medium can not move over large distances. Their short hopping distance under the effect of an electric field gives rise to different types of polarization [31], Fig. 2.5:

- **electronic polarization**

All dielectric materials induce electronic polarization, which results from an oscillation of the electronic charge relative to the nucleus under the influence of the electric field. Because of the low mass of electrons, these oscillations occur at very high frequencies, above 10^{14}-10^{16} Hz. This contribution is dominating only in the optical domain area since the Maxwell relation, $n = \sqrt{\varepsilon_r}$, is verified.

- **ionic polarization**

Only materials with ionic bonds may have ionic polarization, caused by the relative displacement of cations in one direction and anions in the opposite direction. As a result, net dipole moments are induced on this new structure. The corresponding frequencies occur below the optical frequencies in the infrared range, about 10^{13} Hz. This type of polarization is characterized by vibrational spectroscopy.

- **orientation (dipolar) polarization**

Only substances with permanent dipole moments may possess an orientational polarization, which is described as the rotation of the permanent dipole moments into an applied electric field direction. This type of polarization is observed in the range of radio waves.

- **interfacial (space charge) polarization**

This polarization is due to accumulation of free charges at interfaces between different environments. This will be important in systems with high density of interfaces.

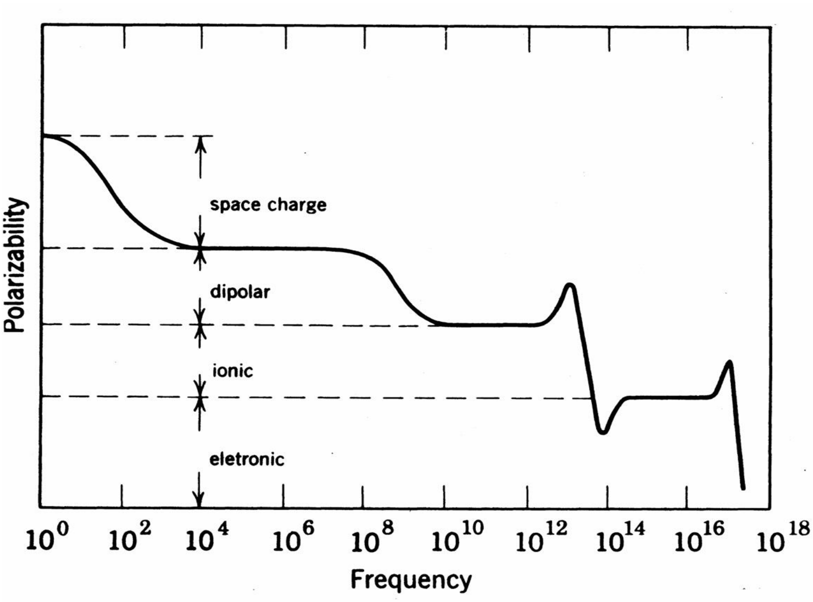

Figure 2.5: Polarizability as a function of frequency [31].

2.2.1.2 Expression of polarization

Each type of polarization appears in its own frequency range. When a field of variable frequency $f = \omega/2\pi$ is applied, the polarization of the material varies with it. When the frequency increases, the number of mechanisms involved in the polarization dynamics of the material decreases, the different polarizations of lower frequency can not be established.
Linear polarization P is proportional to the applied field E

$$P = \varepsilon_0 \times \chi_{ij} \times E + \varepsilon_0 E \qquad (2.3)$$

where χ_{ij} is the susceptibility tensor and ε_0 electric permittivity of vacuum ($\varepsilon_0 \approx 8.85410^{-12}$ F.m^{-1}). This tensor is reduced to a scalar χ for isotropic and homogeneous non-oriented ceramics and the equation becomes:

$$P = \varepsilon_r \times E \qquad (2.4)$$

The dielectric permittivity $\varepsilon = (1 + \chi)\,\varepsilon_0 = \varepsilon_r\,\varepsilon_0$ describes the response of a given material to the applied electric field. It is linked to mechanisms of chemical entities that polarizability constitutes the dielectric medium. Equation (2.4) shows that the only way to induce electric polarization in isotropic dielectric media is application of an electric field. If a sinusoidal electric field $\vec{E} = \vec{E}_0 e^{i\omega t}$ is applied on dielectric material, the polarization mechanisms will induce phase shifts δ between the applied field and polarization depending on their relaxation time:

$$\vec{P} = \vec{P}_0 e^{i(\omega t - \delta)} = \varepsilon(t)\vec{E} \qquad (2.5)$$

The dielectric permittivity in the frequency space is the Fourier transform of the dielectric response ε_r (t):

$$\varepsilon_r(\omega) = \int_0^{\infty} \varepsilon_r(t) \times e^{i\omega t} dt \qquad (2.6)$$

έ(ω) and ε"(ω) expresses the dielectric coefficient, tanδ = dielectric loss, expressed in % which is the ratio of energy dissipation and power supplied.

Each polar or polarization particle in the material exhibits characteristic response to the applied electric field. The field disturb the system. After the excitation has ceased, the system relax to a new equilibrium. Relaxation in time domain can be described by a relaxation time τ. This parameter depends on the polarization mechanism in a material. A material excited by a step voltage at time t = 0 possesses only one relaxation process with a single characteristic time constant. The Debye relaxation model describes this simple case [32]; the polarization of a sample will relax towards the steady state as a first order process characterized by a single time constant, τ, as in Fig. 2. 6.

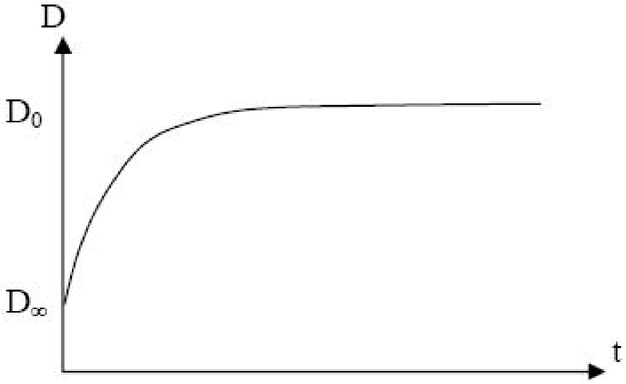

Figure 2.6: Polarization response of polar dielectric.

This can be described as

$$D = D_\infty + (D_0 + D_\infty)(1 - e^{-t/\tau}) \qquad (2.7)$$

where D = electric displacement.

D_∞ = final value of D

D_0 = initial value of D

since

$D = \varepsilon_r\varepsilon_0 E$; ε_r = complex relative permittivity.

$D_\infty = \varepsilon_\infty\varepsilon_0 E$; ε_∞ = relative permittivity at infinite frequency.

$D_0 = \varepsilon_s\varepsilon_0 E$; ε_s = static relative permittivity.

equation (2.7) can be rewritten as

$$\varepsilon_r\varepsilon_0 E = \varepsilon_\infty\varepsilon_0 E + (\varepsilon_s\varepsilon_0 E - \varepsilon_\infty\varepsilon_0 E)(1-e^{-t/\tau})$$

$$\varepsilon_r = \varepsilon_\infty + (\varepsilon_s - \varepsilon_\infty)(1-e^{-t/\tau})$$

The response of this system in a frequency domain can be obtained by a Leplace transform

$$\varepsilon_r = \varepsilon_\infty + \frac{(\varepsilon_s - \varepsilon_\infty)}{1+i\,\omega\tau} \qquad (2.8)$$

which is a single relaxation Debye equation.

ε_∞ represents the permittivity measured at a high frequency where the polarization particles are not able to respond to the applied electric field. The static permittivity, ε_s, is the limiting low frequency permittivity where the polarization is full manifested. The single relaxation Debye equation exhibits a relaxation frequency centered on $f_c = \dfrac{1}{2\pi\tau}$.

Equation (2.8) omits the currents flowing at infinite time such as would arise due to a movement of ions in a constant field. The model is expanded to include a static conductivity term σ_s, where $\sigma_s = j\omega\varepsilon_0\varepsilon_s$, an imaginary nature of σ_s is a consequence of the solution to the wave equation.

$$\varepsilon_s = \frac{\sigma_s}{i\,\omega\varepsilon_0} = -i\,\frac{\sigma_s}{\omega\varepsilon_0}$$

Include this in equation (2.8)

$$\varepsilon_r = \varepsilon_\infty + \frac{(\varepsilon_s - \varepsilon_\infty)}{1+i\,\omega\tau} - i\,\frac{\sigma_s}{\omega\varepsilon_0} \qquad (2.9)$$

$$\varepsilon_r = \varepsilon_\infty + \frac{(\varepsilon_s - \varepsilon_\infty)(1-i\,\omega\tau)}{1+(\omega\tau)^2} - i\,\frac{\sigma_s}{\omega\varepsilon_0}$$

$$\mathrm{Re}(\varepsilon_r) = \varepsilon_r' = \varepsilon_\infty + \frac{\varepsilon_s - \varepsilon_\infty}{1 + (\omega\tau)^2} \qquad (2.10a)$$

$$\mathrm{Im}(\varepsilon_r) = \varepsilon_r'' = \frac{\sigma_s}{\omega\varepsilon_0} + \frac{\omega\tau(\varepsilon_s - \varepsilon_\infty)}{1 + (\omega\tau)^2} \qquad (2.10b)$$

The first term on the right side of equation (2.10b) arises due to the static conductivity.

At $f = f_c \rightarrow \omega\tau = 1$

equations (2.10a) and (2.10b) become

$$\varepsilon_r' = \frac{\varepsilon_s + \varepsilon_\infty}{2}$$

$$\varepsilon_r'' = \frac{\sigma_s}{\omega\varepsilon_0} + \frac{\varepsilon_s - \varepsilon_\infty}{2}$$

The Debye function is plotted in Fig. 2.7, the real part shows a step down, and the half height of this step is found at $\omega = \tau^{-1}$. For the imaginary part, the top of the peak corresponds to this frequency.

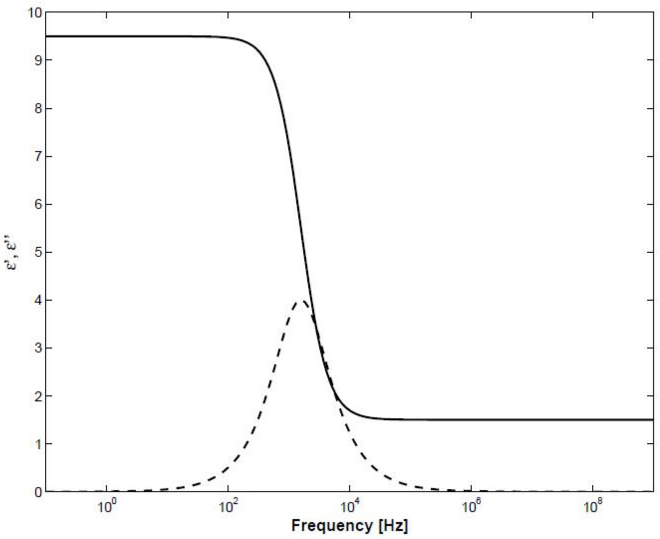

Figure 2.7: The Debye relaxation function. The full line is the real part ε′ and the dashed line is the imaginary part ε′′.

2.2.2 Ferroelectric versus relaxor ferroelectrics

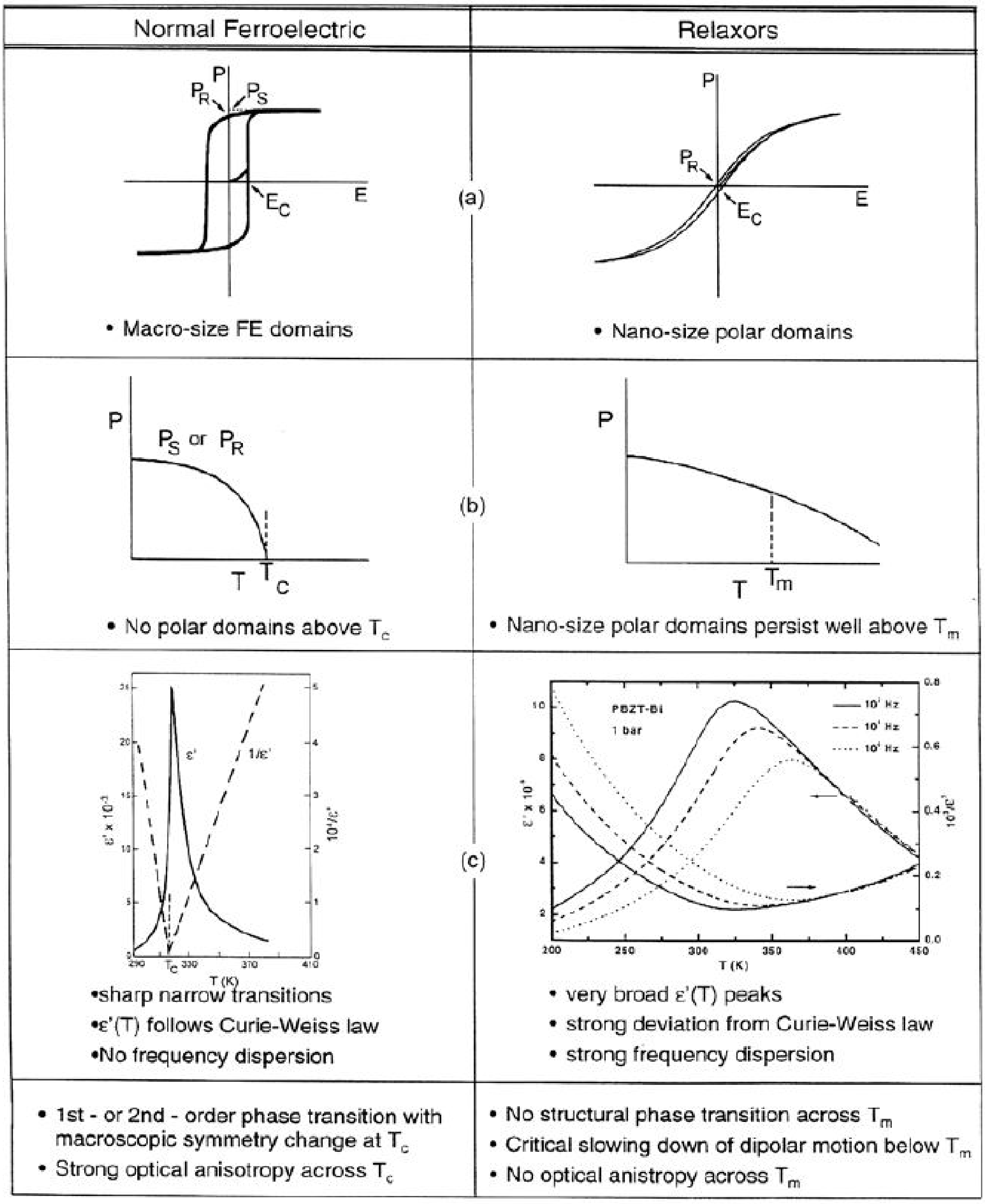

Normal Ferroelectric		Relaxors
• Macro-size FE domains	(a)	• Nano-size polar domains
• No polar domains above T_c	(b)	• Nano-size polar domains persist well above T_m
•sharp narrow transitions •ε'(T) follows Curie-Weiss law •No frequency dispersion	(c)	• very broad ε'(T) peaks • strong deviation from Curie-Weiss law • strong frequency dispersion
• 1st - or 2nd - order phase transition with macroscopic symmetry change at T_c • Strong optical anisotropy across T_c		• No structural phase transition across T_m • Critical slowing down of dipolar motion below T_m • No optical anistropy across T_m

Figure 2.8: Contrast between normal ferroelectrics and relaxor ferroelectrics [33].

The difference between ferroelectrics (FE) and relaxor ferroelectrics (RFE) can be described by three qualitatively different features in the temperature dependence of the dielectric susceptibility, as shown in Fig. 2.8. Firstly, in normal ferroelectrics the real part dielectric susceptibility, έ (T) shows a Curie-Weiss law [35] above T_c as shown by the linear $1/\varepsilon'$ versus T response.

$$\varepsilon' = \frac{C}{T - T_0}$$

By contrast ε′(T) of a relaxor exhibits strong deviation from this law for temperatures of many tens to a few hundred degrees above T_m. Secondly, there is a strong frequency dependence in the peak position, T_m of έ (T). Lastly, the polarization in FE goes to zero at T_c and in the relaxors the polarization extends well beyond T_m [34]. The fact that there is zero polarization at T_c shows that polar nanodomains vanish whereas in the relaxor the nanodomains persist well beyond the glassy transition temperature [33]. While the normal ferroelectric has a hysteresis loop that at zero field retains large polarization, in the relaxor this zero field polarization is significantly smaller owing to the fact that the nanodomains are randomly distributed. It is possible to create a large polarization when there is a sufficiently large external electric field, but once the field is removed polarization returns to being small owing to the randomness of the domains [33].

Due to these qualitatively different features one should not expect the transitions in FEs to follow the same mechanism in RFEs.

Generally ferroelectricity is harder to demonstrate in polycrystalline materials composed of crystalites, such as ceramics, than in a single crystal because of the random orientation of crystallites. This is why in some single crystals the polarization reverses quite abruptly to form a square loop, as shown in Fig. 2.9a, while in most ceramics the loop is rounded, as shown in Fig. 2.9b.

In insulating ferroelectric material, the switched charge Q due to applied electric field E depends only on the remanent polarization P_r through the relation $Q = 2P_r A$ where A is the surface area of the capacitor, whereas for a lossy dielectric material, extra contribution comes from the conductivity σ through the relation $Q = 2P_rA+\sigma EAt$, where t is the time for hysteresis measurement [37], Fig. 2.9c.

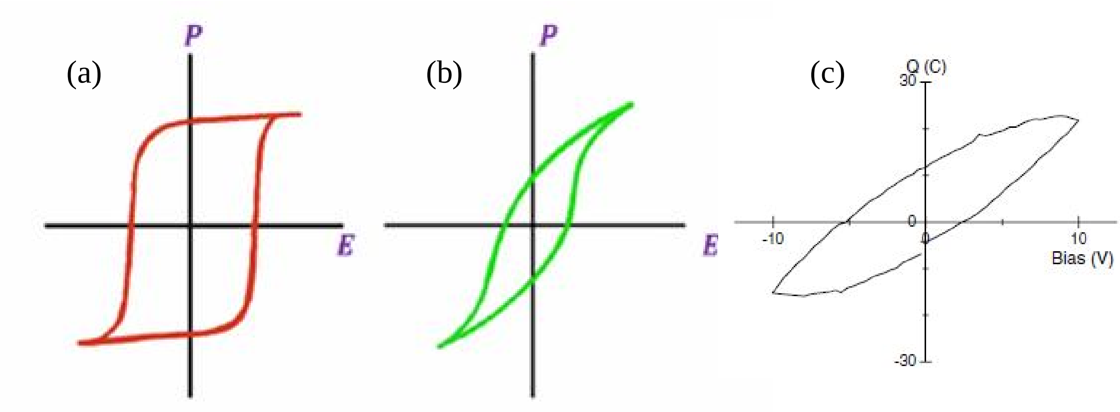

Figure 2.9: Schematic diagrams of (a) single crystal, (b) polycrystalline [35] and (c) charge versus voltage loop typical for a lossy dielectric [36].

2.3 Multiferroic and magnetoelectric materials [10, 37]

The term "multiferroic" describes materials simultaneously exhibiting at least two kinds of ferroic order [40]. A ferroic order is described as a spontaneous order that can exhibit domains (where the order parameter has different sign or direction), and whose order parameter couples to a suitable external field. For example, in ferromagnetics the magnetization (order parameter) can form domains, and it can be switched by a magnetic field, represented by a hysteresis loop as sketched in Fig. 2.10a.

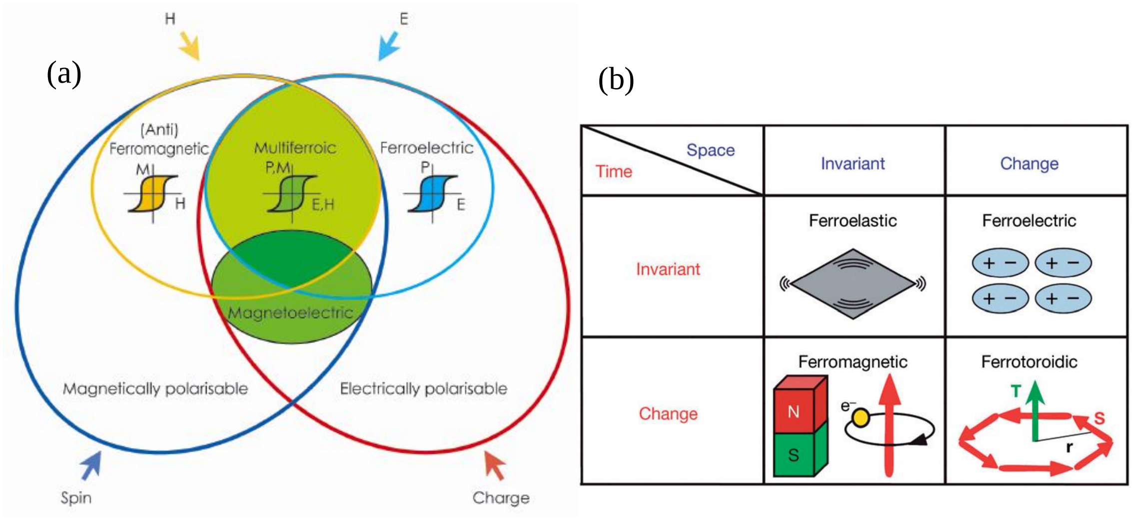

Space / Time	Invariant	Change
Invariant	Ferroelastic	Ferroelectric
Change	Ferromagnetic	Ferrotoroidic

Figure 2.10: (a) Multiferroic materials combine magnetic and ferroelectric properties [41], (b) Classification of "ferroic" orders according to symmetry [39].

Ferroic orders can be classified according to the transformation properties of the order parameter upon time reversal (change of sign of magnetic moment under symmetry operation

M (-t) = -M, whereas the polarization remains invariant P(-t) = P(t)) and space inversion (P (-x))= -P, whereas ferromagnetism remains invariant) (Fig. 2.10b). For example, ferroelastic order is invariant under both operations, whereas the order parameter of ferrotorodicity the alignment of toroidal moment arising from a ring like arrangement of spins [42] changes sign upon either operation. A ferroelectric that is also a ferromagnetic (magnetoelectric multiferroic) breaks both time reversal and spatial inversion symmetries, similar as a ferrotoroidic. The latter are also interesting for magnetoelectric applications as they intrinsically exhibit a magnetoelectric effect. The combination of ferromagnetism and ferroelectricity into a multiferroic is sketched in Fig. 2.10a. By definition then, such a material has a spontaneous magnetization that is switchable by a magnetic field and a spontaneous electric polarization that is switchable by an electric field. With a sufficient electromagnetic coupling, it is possible that the spontaneous magnetization can also be switched by an electric field or the polarization by a magnetic field. However, multiferroicity does not imply that there is a magnetoelectric effect, and conversely magnetoelectric effects can occur in the much wider class of materials that are simultaneously magnetically and electrically polarizable.

2.3.1 Magnetoelectric effect

It is well known that electricity and magnetism are intrinsically linked, their coupling given by the Maxwell equations. However, the coupling provided in these equations, while linear, involves spatial and time derivatives. In static situations electric and magnetic fields are not intrinsically coupled, though a coupling might appear as a property of certain materials. The magnetoelectric effect in a crystal is traditionally described in Landau theory by writing the free energy F of the system in terms of an applied magnetic field $\vec{H}$ and an applied electric field $\vec{E}$ [2]:

$$F(E,H) = F_0 - P_i^s E_i - M_i^s H_i - \frac{1}{2}\varepsilon_0\varepsilon_{ij}E_i E_j - \frac{1}{2}\mu_0\mu_{ij}H_i H_j - \alpha_{ij}E_i H_j -$$
$$\frac{\beta_{ijk}}{2}E_i H_j H_k - \frac{\gamma_{ijk}}{2}H_i E_j E_k - \ldots, (2.11)$$

Where i, j denote spatial indices, and summation over indices appearing twice in a term is assumed. The first term is the part of free energy and the next four terms describe spontaneous polarization and magnetization, as well as the usual polarization and magnetization by electric and magnetic fields, respectively, where ε_{ij} and μ_{ij} are relative permittivity and permeability, respectively. The 6th term gives the lowest order magnetoelectric coupling described by a linear magnetoelectric coupling via α_{ij} tensor, other terms represent higher-order magnetoelectric coupling coefficients.

For given electric and magnetic fields, polarization and magnetization are then obtained by minimizing the free energy, F, giving

$$P_i(E,H) = -\frac{\partial F}{\partial E_i} = P_i^s + \varepsilon_0 \varepsilon_{ij} \mathrm{E}_j + \alpha_{ij} \mathrm{H}_j + \ldots, (2.12)$$

$$M_i(E,H) = -\frac{\partial F}{\partial \mathrm{M}_i} = M_i^s + \mu_0 \mu_{ij} \mathrm{H}_j + \alpha_{ij} E_j + \ldots, (2.13)$$

The α_{ij} term is designated as the linear magnetoelectric effect and corresponds to the induction of polarization by a magnetic field or a magnetization by an electric field. Materials exhibiting ME effect are Cr_2O_3, $BiMnO_3$, $BiFeO_3$. Unfortunately, the magnetoelectric effect is usually much too weak to be practically applicable as the term α_{ij} is limited by the relation [43], $\alpha_{ij}^2 \leq \varepsilon_0 \mu_0 \varepsilon_{ii} \mu_{jj}$, and since ferroelectric and ferromagnetic materials have particularly large ε and μ, large magnetoelectric coupling might be expected for ferroelectric ferromagnetic, one type of "multiferroic".

2.3.2 Incompatibility between ferroelectricity and magnetism

There are a lot of ferromagnetic materials as well as a lot of ferroelectric ones. However, there are surprisingly few that are both, and understanding why was the first issue to be addressed [9]. One reason for the scarcity of multiferroics is simply symmetry: due to the need of breaking time reversal and spatial inversion symmetries.

A simple ferromagnet tends to be a metal whereas sustaining an electric polarization requires a material to be insulating. A crystal can be classified into 32 point groups. In addition, with the consideration of the magnetic symmetry, 90 magnetic point groups can be distinguished. Therefore, there are 122 point groups (also known as Shubnikov magnetic point groups) as a whole including non-magnetic point groups [44]. Only 13 point groups allow both spontaneous magnetization and electric polarization to occur [40, 45]. Yet, many materials occur in one of these 13 point groups without being multiferroic.

2.3.3 The classification of multiferroic compounds

The microscopic origin of magnetism is basically the same in all magnets: it is the presence of localized electrons, mostly in the partially filled d or f shells of transition-metal or rare-earth ions, which have a corresponding localized spin, or magnetic moment. Exchange interactions between the localized moments lead to magnetic order. The situation with ferroelectrics is quite different. There are several different microscopic sources of ferroelectricity, and accordingly one can have different types of multiferroics. Generally speaking, there are two groups of multiferroics. The materials in which ferroelectricity and magnetism have different sources and appear largely independent of one another, though there is some coupling between them. In these materials, ferroelectricity typically appears at higher temperatures than magnetism, and the spontaneous polarization P is often rather large (of order 10 - 100 $\mu C/cm^2$). Examples are $BiFeO_3$ (T_{FE} ~ 1100 K, T_N = 643 K, P ~ 90 $\mu C/cm^2$) and $YMnO_3$ (T_{FE} ~ 800 K, T_N = 76 K, P ~ 6 $\mu C/cm^2$) but the coupling between magnetism and ferroelectricity is usually rather weak. The materials challenge is to keep all their positive features and try to enhance the coupling. The second group, which we can call type-II multiferroics, are the relatively recently discovered materials [46, 47], in which a particular type of magnetic spiral or even for collinear magnetic structures causes ferroelectricity, implying a strong coupling between the two. However, the polarization in these materials is usually much smaller (10^{-2} $\mu C/cm^2$). Also depending on the origin of ferroelectricity, Cheong and Mostovoy [48] have classified ferroelectrics within two categories, ‘proper’ and ‘improper’. In ‘proper’ ferroelectrics, ferroelectricity occurs due to electronic pairing between the transition metal ion (e.g. Ti in $BaTiO_3$) and oxygen. On the other hand, in ‘improper’ ferroelectrics, ferroelectricity arises due to complex lattice distortions or by other types of ordering such as charge ordering and magnetic ordering.

2.3.3.1 Type I multiferroics

The straight forward way to achieve both magnetism and ferroelectricity in a single compound is for the former to originate from one subunit or ion, and the latter from another. For pervoskites, one can for example on the B site partially substitute ferroelectricity active (d^0) ion with a magnetic ion, Fig. 2.11.

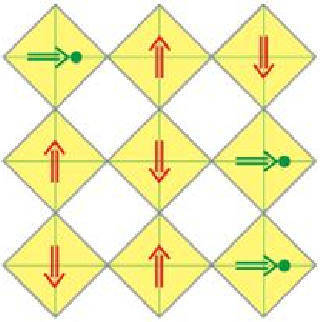

Figure 2.11: Mixed perovskites with ferroelectrically active d^0 ions (green circles) and magnetic d^n ions (red), shifts of d^0 ions from the centers of O_6 octahedra (yellow plaquettes) lead to polarization (green arrows), coexisting with magnetic order (red arrows) [41].

The general main problem with such an approach is that due to the different ion (or subunits) involved in magnetism and ferroelectricity, the magnetoelectric coupling tends to be very low in most cases [49]. As a concrete example of the "independent subsystems" approach we consider ferroelectricity due to the lone pair at the A site in perovskites with magnetic B ions [50]. Lone pairs are electrons not used in chemical bonds, occurring for example in water molecules.

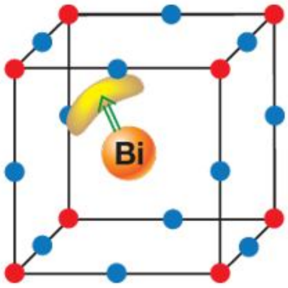

Figure 2.12: Bismuth lone pair in $BiCrO_3$ [41]. The lone pair, if localized, breaks inversion symmetry and can lead to ferroelectricity.

Lone pairs are highly polarizable contributing e.g. to the polarizability of water. In perovskites, A site Bi^{3+} or Pb^{2+} have $6s^2$ electrons not participating in bonds and thus yielding lone pairs, Fig. 2.12. If these lone pairs are localized and ordered in one direction, inversion symmetry is broken and an electric polarization results. In $PbTiO_3$ this lone pair mechanism supports the traditional mechanism stabilizing the ferroelectricity.

In $BiMnO_3$, the B site occupied by Mn^{3+} ions leads to ferromagnetism below 100 K (see Fig. 2.13a). The Bi lone pairs alone are also sufficient to stabilize ferroelectricity (below 800 K), as indicated by polarization hysteresis loops (Fig. 2.13c). The occurrence of both ferroelectricity and ferromagnetism make this an exceptional example of a real multiferroic in the strictest definition [55].

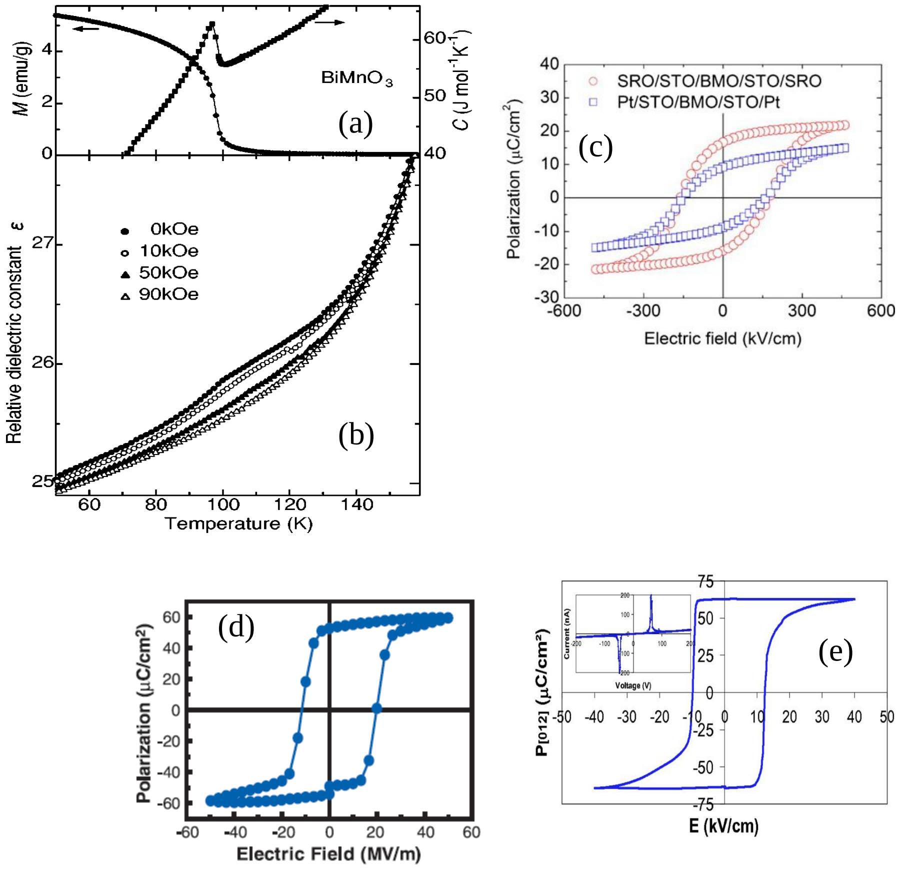

Figure 2.13: (a) $BiMnO_3$ specific heat and low field magnetization [51]. (b) $BiMnO_3$ dielectric constants in different magnetic fields [51]. (c) $BiMnO_3$ polarization [52]. (d/e) $BiFeO_3$ thin film [53] / single crystal [54] polarization.

Despite of this, however, the magnetoelectric coupling is very weak, as indicated by a very small (and almost magnetic field independent) feature in the dielectric constant at the magnetic ordering temperature (Fig. 2.13b) [51].

The small dielectric feature at the magnetic transition is consistent with the expectation for an "independent subsystem" multiferroic. In $BiFeO_3$ [56], the Fe spins order antiferromagnetically below 643 K, in a complex spin structure based on G-type antiferromagnetism (i.e. with each Fe ion surrounded by six antiparallel nearest neighbors) [57] Bi lone pairs again lead to ferroelectricity, below 1100 K, with a polarization hysteresis loop both on thin film and more recently on high quality single crystals (Fig. 2.13d and e) showing the intrinsic nature of a high (> 60 $\mu C/cm^2$, comparable with $BaTiO_3$) polarization at room temperature [53, 54]. Room temperature multiferroicity would make $BiFeO_3$ a very good prospect for applications if significant magnetoelectric coupling were present as well. In analogy with $BiMnO_3$, we would expect only very small coupling. However, sizeable coupling and control of magnetism by electric field has been demonstrated experimentally. The origin of this is connected with a spiral part of the magnetic structure and corresponding coupling in the class of "spiral multiferroics".

Another example is "Geometric ferroelectricity" multiferrocity in hexagonal manganites, like $RMnO_3$ (R = rare earth) compounds with smaller ionic radius of heavy rare earth (Ho-Lu and Y, Sc) [58]. The ferroelectricity in $YMnO_3$ (~ 800 K [59]) is caused by the tilting of the practically rigid MnO_5 block. This tilting occurs just to provide closer packing and as a result the oxygen ions move closer to the rather small Y ions (Fig. 2.14).

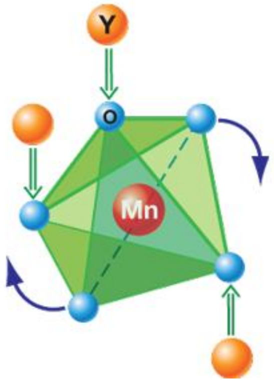

Figure 2.14: The “geometric” mechanism of generation of polarization in $YMnO_3$ [59] describes the tilting of a rigid MnO_5 block with a magnetic Mn remaining at the center. Because of the tilting, the Y-O bonds form dipoles (green arrows), and there appears two ”up” dipoles per one “down” dipole so that the system becomes ferroelectric (and multiferroic when Mn spins order at lower temperatures).

Finally, ferroelectricity due to charge ordering: in such a system the ferroelectricity is mainly due to the coexistence of inequivalent sites with different charges and inequivalent bonds such as in $LuFe_2O_4$. $LuFe_2O_4$ has a ferromagnetic structure at 250 K [62], it shows that below 350 K spontaneous polarization increases below 250 K (Fig. 2.15a). Such increase in polarization suggests a significant coupling between ferroelectricity and magnetic ordering. At 350 K, an equal number of Fe^{2+} and Fe^{3+} ions coexist randomly in a triangular lattice (Fig. 2.15b), thus, iron has an average valence of 2.5. Below 350 K a charge redistribution between layers occurs. Thus the upper layer has a ratio between Fe^{2+} and Fe^{3+} and the lower layer has opposite 1: 2 ratio [63]. So the upper layer has net +ve charge and the layer below has a net –ve charge, these two layers together (bilayer) form a dipole moment and induce ferroelectricity.

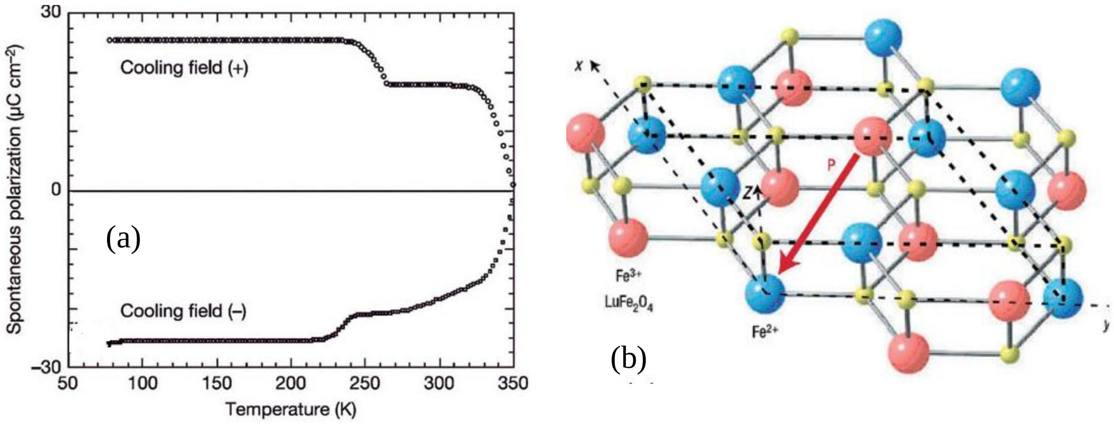

Figure 2.15: (a) Pyroelectric current measurement [63] indicated a net polarization. i.e. ferroelectricity for $LuFe_2O_4$. (b) The red arrow indicates the direction of polarization [63].

2.3.3.2 Type II multiferroics

(a) Spiral type-II multiferroics

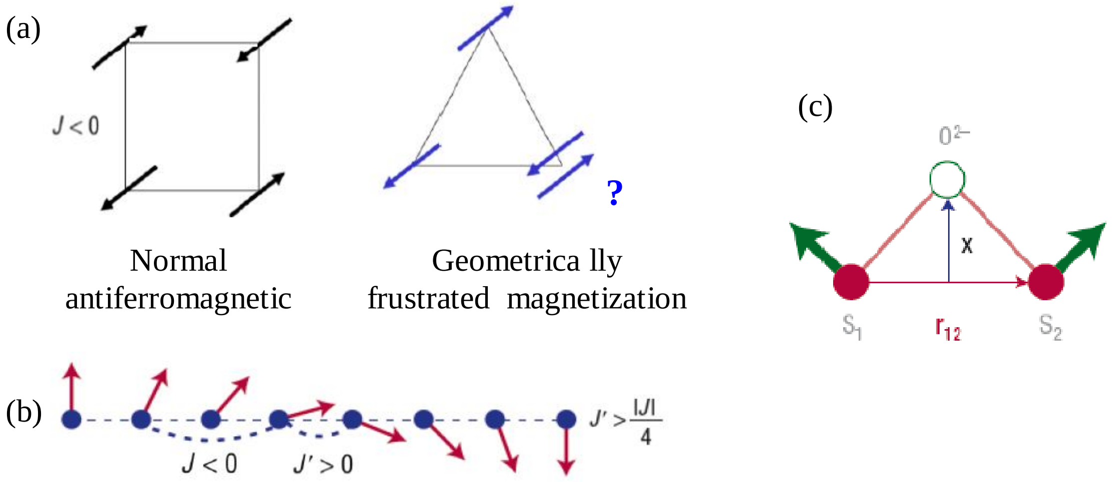

Figure 2.16: (a) Antiferromagnetic and frustration spins system. (b) Frustrated spin chains with the nearest neighbor FM and next nearest neighbor AFM interactions J and J´ [46]. (c) Ferroelectricity induced by the exchange striction in a magnetic spiral state [46].

Most of the type-II multiferroics belong to this subgroup and it is usually found in frustrated systems, where ferroelectricity and antiferromagnetism coexist with gigantic coupling. This is the case in $TbMnO_3$, $Ni_3V_2O_8$, and $MnWO_4$. The key questions are how is it possible that magnetic ordering can induce ferroelectricity and what is the role of frustration. The importance of the frustration is illustrated in Fig. 2.16. On the square lattice it is possible to satisfy the requirement of antiparallel ordering. However, on a triangular lattice things are not so straightforward. If two neighboring spins are placed antiparallel, the third spin is faced with a dilemma. In any case one of two neighbors will not have its energy minimized. As a result the system is frustrated and tends to release this frustration by forming unusual magnetic order where magnetization is inhomogeneous. The coupling between electric polarization and magnetization is governed by the symmetry of these two order parameters. As we already mentioned, the polarization $\vec{P}$ and electric field $\vec{E}$ change sign on the inversion of all coordinates, $\vec{r} \rightarrow -\vec{r}$, but remain invariant on time reversal, t → −t. The magnetization $\vec{M}$ and magnetic field $\vec{H}$ transform precisely the opposite way. Because of this difference in transformation properties, the linear coupling between $(\vec{P},\vec{E})$ and $(\vec{H},\vec{M})$ described by Maxwell’s equations is only possible when these vectors vary both in space and time; spatial derivatives of $\vec{E}$ are proportional to the time derivative of $\vec{H}$ and vice versa. This is where frustration comes into play. Its role is to induce spatial variation of magnetization. The period of magnetic states in frustrated systems depends on strengths of competing interactions and is often incommensurate (out of proportion) with the period of crystal lattice. For example, a spin chain with a ferromagnetic interaction $J' > 0$ between neighboring spins has uniform ground state with all spins parallel. An antiferromagnetic next-nearest-neighbor interaction $J < 0$ frustrates this simple ordering, and when sufficiently strong stabilizes a spiral magnetic state. Like any other magnetic ordering, the magnetic spiral (Fig. 2.16b) spontaneously breaks time-reversal symmetry. In addition it breaks inversion symmetry, because the change of the sign of all coordinates inverts the direction of the rotation of spins in the spiral. Thus, the symmetry of the spiral state allows for a simultaneous presence of electric polarization.

Ferroelectricity is induced by lattice relaxation in a magnetically ordered state. The exchange between spins of transition metal ions is usually mediated by ligands, for example oxygen ions, forming bonds between pairs of transition metals. The effect is shown in Fig. 2.16c. Interaction between spins $\vec{S}_n$ and $\vec{S}_{n+1}$ pushes negative oxygen ions in one direction perpendicular to the spin chain formed by positive magnetic ions, thus inducing electric polarization perpendicular to the chain.

The perovskite manganite TbMnO$_3$ is an example of the described mechanism. The spin structure is a sinusoidal antiferromagnetic ordering of the Mn^{3+} moments that takes place below ≈ 40 K. With further decrease of temperature below ≈ 26 K the ferroelectric phase with spontaneous polarization emerges.

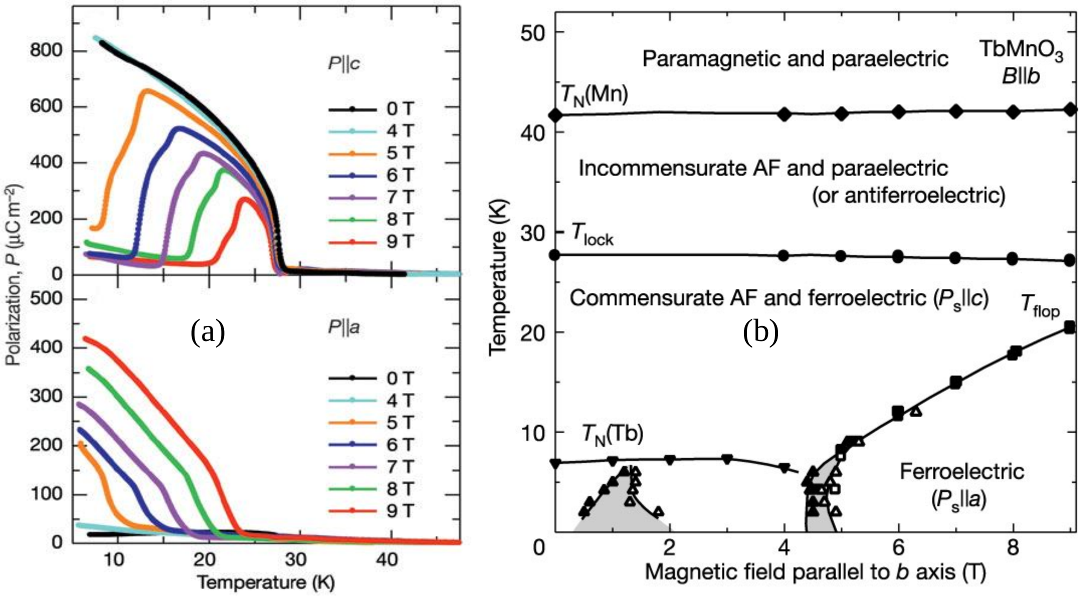

Figure 2.17: (a) Electric polarization along c and a axes at various magnetic fields in a single crystal of TbMnO$_3$. Magnetic fields are applied along the b axis. (b) Temperature versus magnetic field phase diagram for TbMnO$_3$ for magnetic field applied along the b axis. The shaded areas show magnetic field hysteresis regions [46].

The polarization along the c axis at ~10 K is about $8 * 10^{-4}$ Cm^{-2} which is still rather small compared with that of conventional ferroelectrics (~$2.6 * 10^{-2}$ Cm^{-2} at 296 K in BaTiO$_3$). Dependence of polarization upon temperature in magnetic field is revealed in Fig. 2.17a. As the magnetic field is applied along the b-axis the magnetic vector changes and the individual magnetic moments change their direction. As a result, the direction of polarization changes and becomes zero in c-direction, while it increases in a-direction. Temperature versus magnetic field phase diagram for TbMnO$_3$ is shown in Fig. 2.17b.

(b) Type-II multiferroics with collinear magnetic structures

In this case all magnetic moments are aligned along a particular axis without the necessary involvement of the spin-orbit interaction. Polarization can appear in these materials as a consequence of exchange striction because the magnetic coupling varies with the atomic positions. The simplest example is in Ca_3CoMnO_6 [2]. Ca_3CoMnO_6 consists of one-dimensional chains of alternating Co^{2+} and Mn^{4+} ions. At high temperature the distances between the ions along the chain are identical, the chain has inversion symmetry, and polarization is absent.

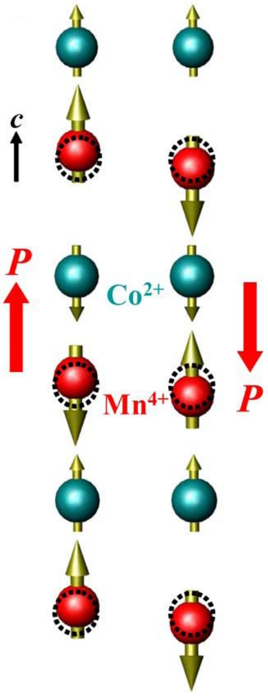

Figure 2.18: Co/Mn Ising chains with two states of ↑↑↓↓ spin ordering in Ca_3CoMnO_6. Ions are displaced from ideal positions (broken circles) by magnetostriction, leading to an electric polarization.

Magnetic ordering, however, breaks inversion symmetry: the spins form a ↑↓↓↓ type magnetic structure. Due to an exchange striction the distortion of ferro and antiferro bonds (↑↑and ↑↓) is different, and we end up in the situation of Fig. 2.18: the material becomes ferroelectric.

2. 3 Crystal structure, magnetic, electric and magnetoelectric properties of $GaFeO_3$

$GaFeO_3$ (GFO), has orthorhombic symmetry with space group P c 2_1 n. The corresponding lattice parameters at 300 K are a = 8.7193(2) Å, b = 9.3683(8) Å and c = 5.0672(3) Å [64] (Fig. 2.19) The crystallographic unit cell contains four different cation sites labeled Ga_1, Ga_2 (mainly occupied by gallium) and Fe_1, Fe_2 (mainly occupied by iron) [15, 17, 65] and 6 oxygen atoms all in general position 4a. The oxygen atoms form a distorted octahedron around Ga_2, Fe_1 and Fe_2, with cation-oxygen distances that vary from 1.94 to 2.07 Å for Ga_2, and from 1.85 to 2.36 Å for Fe_1 and Fe_2. By contrast, the environment of Ga_1 is almost a regular tetrahedron, with a mean Ga_1-O distance of 1.85 Å.

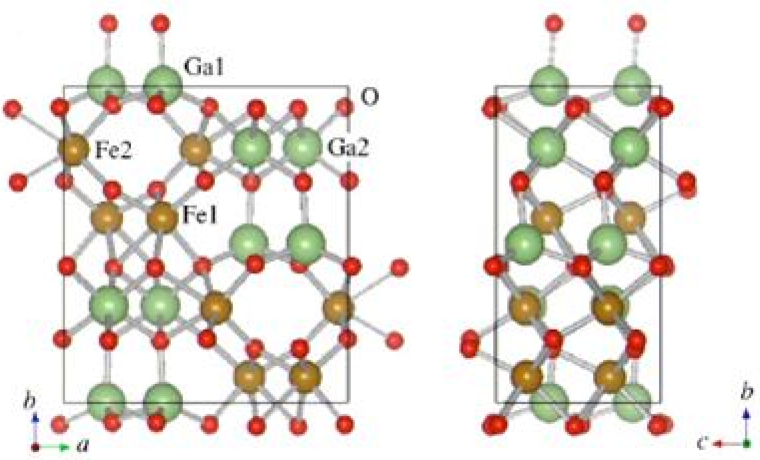

Figure 2.19: Crystal structure of GFO. Projection views along the (left) *c* and (right) *a* axes [17].

Physical properties, especially magnetism in GFO, depend strongly on the method of preparation [15, 17, 18, 20] and are highly correlated with the cation distribution among the four crystallographic sites. Single crystals prepared by the flux method, and thus at lower temperature [20], show a transition temperature of about 300 K while single crystals grown by the float zone method [17] or solid state reaction [18] show a magnetic transition temperature of about 200 K (Fig. 2.20). The temperature of the magnetic transition was reported to be 260 K for a slowly cooled sample and 210 K for a quenched sample [15] prepared by the solid state reaction (SR). Moreover, its Curie temperature may be increased to values above room temperature by increasing the Fe content x of the $Ga_{2-x}Fe_xO_3$ system ($T_c = 370$ K for $x = 1.4$) [17] (Fig. 2.20b).

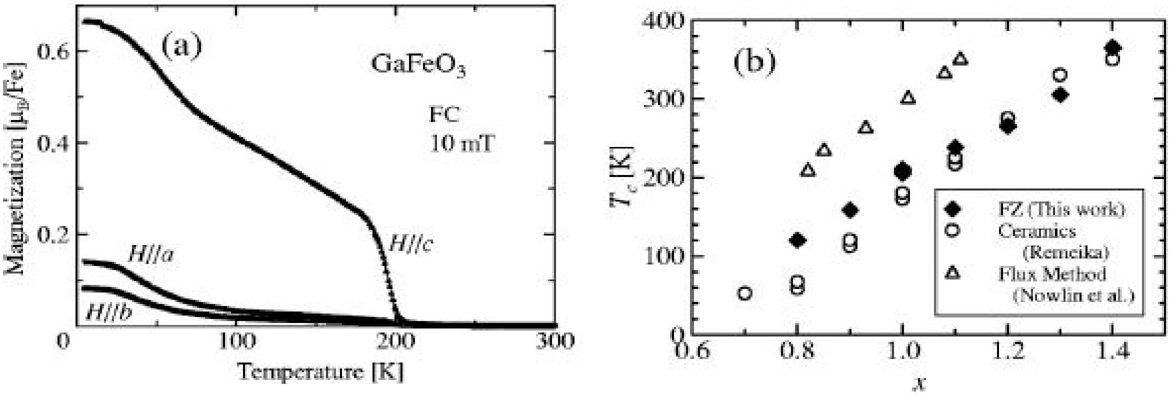

Figure 2.20: (a) Temperature dependence of magnetization of $Ga_{2-x}Fe_xO_3$ with x=1.0 in field-cooling (FC) mode for three different directions of an applied magnetic field 10 mT. (b) Magnetic transition temperature T_C in $Ga_{2-x}Fe_xO_3$ as a function of x [17].

Theoretical studies show that ideal GFO without any site disorder has an antiferromagnetic spin configuration in its ground state [66]. Several models of the magnetic structure of GFO have been suggested: ferromagnetic [18], ferrimagnetic [21] or canted-antiferrimagnetic [22] structure.

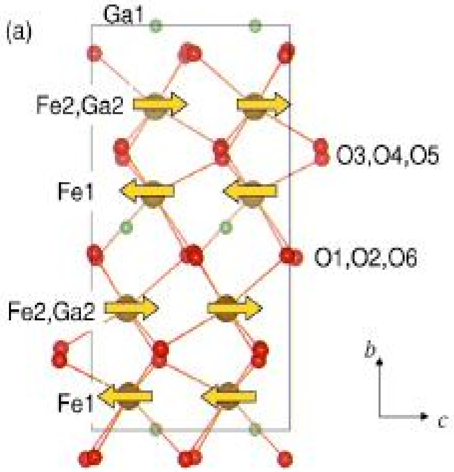

Figure 2.21: Magnetic structure of GFO. Arrows indicate Fe moments [17].

Arima et al. [17] supported a ferrimagnetic model with Fe occupancies 0.18, 0.35, 0.77 and 0.70 in Ga_1, Ga_2, Fe_1 and Fe_2 sites, respectively. Fe^{3+} magnetic moment oriented along the c-axis (Fig. 2.21) with Fe^{3+} magnetic moments at 4 K on Fe_1, Fe_2, and Ga_2 sites equal to −3.9, +4.5, and +4.7 μ_B/Fe, respectively. They suggested that the lower T_C value should be ascribed to the higher Fe occupation at the Ga_1 site, which would be specific to the high temperature synthesis.

In GFO the spontaneous magnetization and polarization should be present [67]. In terms of the group theory, two components of linear magnetoelectric effect tensor **α**, α_{bc} and α_{cb} are nonzero. The origin of the polarization along the b axis is still discussed and there are two assumptions. Abrahams et al. [64] proposed that the piezoelectric effect in gallium iron oxide primarily originates in the Ga_l tetrahedron. Ga_1-O_4 bonds of the tetrahedron Ga_1 is almost parallel to the axis b. Pressure along this direction may cause compression of this bond, and induce a dipole and therefore explain piezoelectricity observed by Remeika et al. [18]. Abrahams et al. [64] observed a decrease in the piezoelectric effect when the iron content increases in $Ga_{2-x}Fe_xO_3$. As the x value increases, the amount of Fe in Ga_2 sites increases, which leads to a distortion in the octahedron around Ga_2: the angle made by the Ga_l-O_4 bond with the polar axis would consequently become larger.

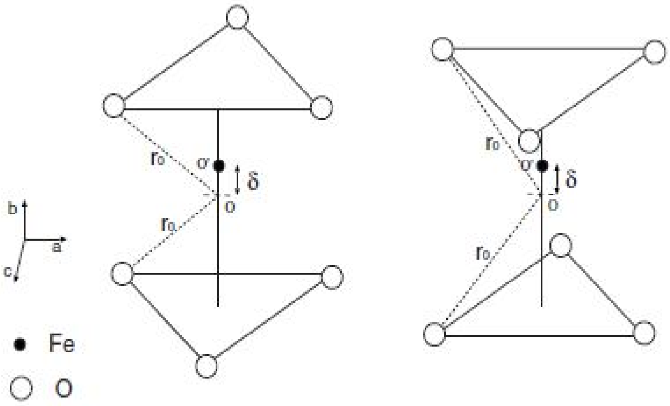

Fe_1 Fe_2

Figure 2.22: Two kinds of octahedra of oxygen atoms (white circles). Fe atoms (black circles) are displaced from the center of the octahedron O to the off-center O' along the b axis by an amount of δ; δ = 0.26 Å at Fe_1 sites and δ = −0.11 Å at Fe_2 sites [68].

Pressure along the polar direction would thus tend to rotate the Ga_l-O_4 bond rather than compress it, hence producing a smaller polarization and the piezoelectric effect. On the other hand, Arima et al. [17] assumed that each Fe atom is octahedrally surrounded by O atoms and slightly displaced from the center of the octahedron; the shift is 0.26 Å at Fe_1 sites and −0.11 Å at Fe_2 sites along the b axis (Fig. 2.22). Thereby the spontaneous electric polarization is generated along the b axis. The simple point charge calculation indicates that the electrical polarization of GFO along the b axis is as large as 2.5 µC/cm², this value has never been verified experimentally.

Rado [22] highlights the magnetoelectric coupling in GFO as an induced polarization ($P_{//b}$) by a magnetic field along the c axis ($H_{//c}$) and an induced magnetization ($\delta M_{//c}$) by an electric field along the b axis ($E_{//b}$) and draw these quantities as function of temperature and both sets tend towards zero as the magnetic ordering disappears at the Curie temperature.

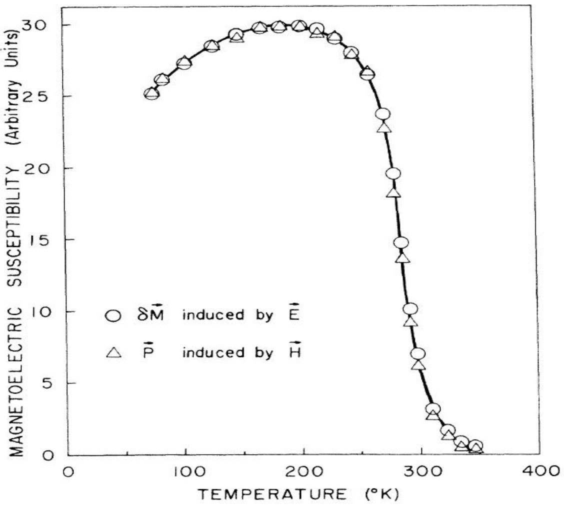

Figure 2.23: Temperature dependence of the magnetoelectric susceptibility [22].

This method allows the qualitative approach magnetoelectric coupling term α by measuring both linear magnetoelectric effect by applying a field E or H, respectively, noted $(ME)_E$ and $(ME)_H$. The dimensions of the crystals used were too small to allow a reliable quantitative measure. However the order of magnitude of the coupling coefficient α is higher than that measured for the magnetoelectric compound Cr_2O_3 (α_{zz} = 4.13 $*10^{-12}$ s /m) [43, 64]. Rado explained the magnetoelectric coupling in GFO as a combination of piezoelectricity and magnetostriction effects. In 1998, Popov et al. [69] demonstrated no direct link between magnetostriction and magnetoelectric coupling in this compound. More recently, Arima et al. [17] have observed an induced polarization along the b axis by a magnetic field applied along the c axis for $Ga_{2-x}Fe_xO_3$ crystals (0.8 < x < 1.1) as shown in Fig. 2.24. The observed butterfly curves are due to a magnetization reversal process. No electric polarization along the c axis is induced as a magnetic field applied along the b axis as shown by a broken line in Fig. 2.24. This study estimated $\alpha_{bc} = 2.1*10^{-11}$ s/m for GFO, the appearance of polarization along the c axis, induced by the application of a magnetic field along the b axis, has not been observed and the α_{cb} coefficient is estimated at a value less than 10^{-12} s/m. The different values obtained for α_{bc} and α_{cb} disagree with the results previously obtained by Rado [22].

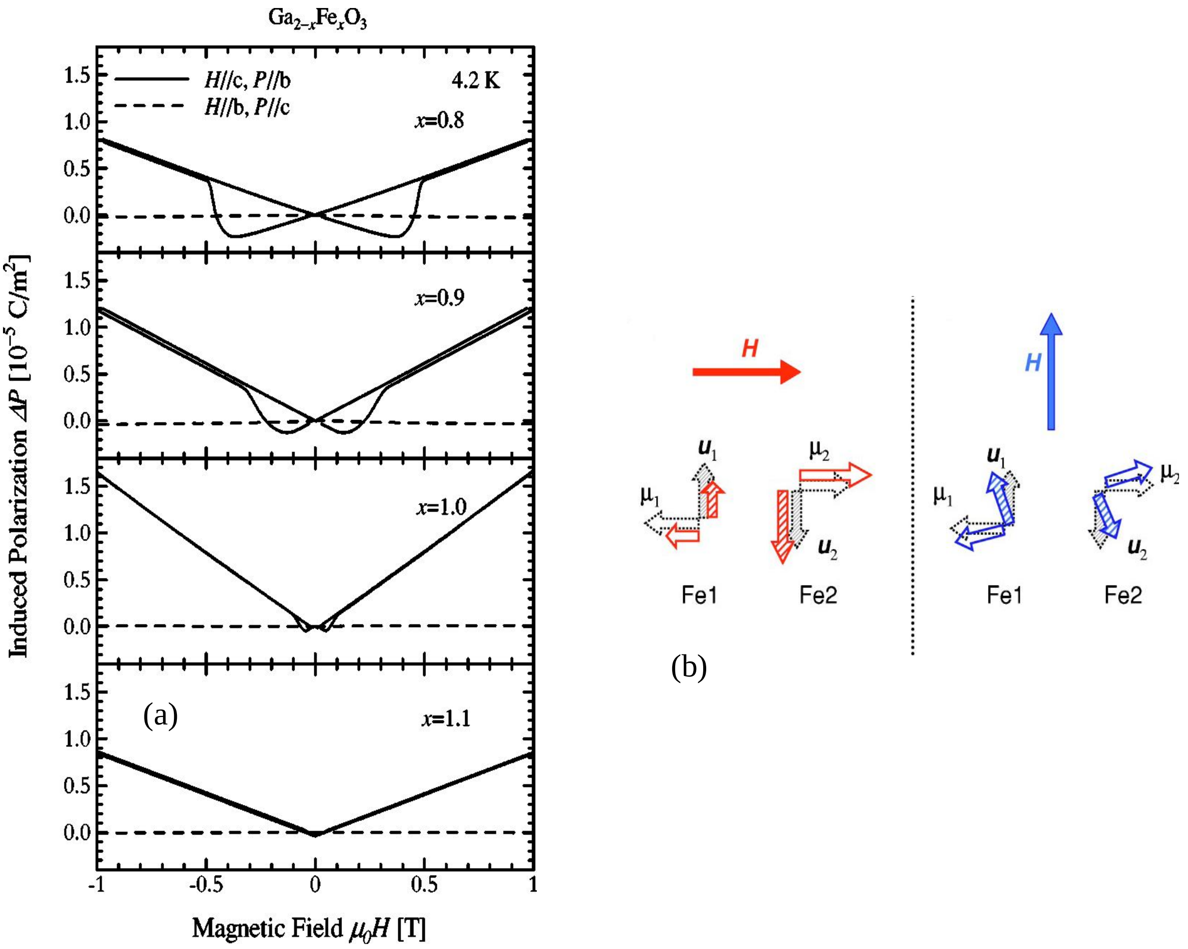

Figure 2.24: (a) Measuring of magnetoelectric effect in $Ga_{2-x}Fe_xO_3$ single crystals, (b) Qualitative explanation of a large difference between the α_{bc} and α_{cb}, where u_i is a local displacement from the center of the octahedron [17].

Arima et al. [17] explain quantitively the difference between α_{bc} and α_{cb} coefficients as follows. In the $H_{//}c$ case where a magnetic field is parallel to the Fe spin moments, the Fe_2 moment increases while the Fe_1 moment decreases. If the displacement along the b axis of Fe_2 is enlarged by the modulation of the magnetic moment, that of Fe_1 is reduced, conversely. Since the displacements of Fe_1 and Fe_2 are opposite in direction with each other, the magnetic field induced modulation of the displacement cooperatively affects the bulk polarization P_b as a result. In the $H_{//b}$ case, a magnetic field makes the Fe_2 moment canted toward the +b direction, when the Fe_1 moment is canted toward the −b direction.

There are several reports on the Mössbauer spectroscopy of this material [21, 70, 71], but the measurements were conducted by using powdered specimens and the analysis by two subspectra approximation. Bertaut et al. proposed a three sublattice ferrimagnetic model that Fe^{3+} ions occupy Fe_1, Fe_2, and Ga_2 sites with the occupancy of 0.87, 0.90, and 0.54, respectively [72].

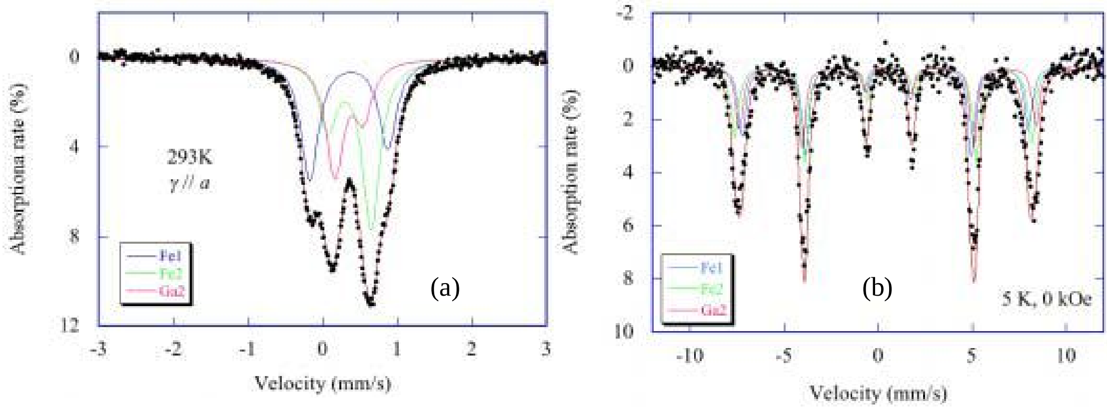

Figure 2. 25: Mössbauer spectrum for GFO at 293 K (a) and 5 K (b) [74].

At low temperature GFO shows magnetoelectric (ME) effect. In general, when the magnetic field or the electric field is applied to the material, the ME effect is caused by the change in (1) magnetic interaction due to the displacement of ions, (2) magnetic anisotropy, and (3) g-value. Especially in the case (1), Mössbauer quadrupole effect is expected to change because it is very sensitive to the local structure. More recently, Nakamura et al. [73] investigated the origin of magnetoelectric (ME) in GFO single crystal prepared by float zone method using Mössbauer spectroscopy. So, they decomposed Mössbauer spectra into three subspectra as shown in Fig. 2.25, corresponding to Fe^{3+} ions on Fe_1, Fe_2 and Ga_2 sites. The quadrupole splitting (QS) of the Fe_1 subspectrum, 1.05 mm/s, is too large to be explained by the electric field gradients (EFG) due to the lattice contribution. At 5 K, there is no difference in the quadrupole parameters between the spectra with and without applied magnetic field, suggesting that the ME effect is not caused by a displacement of ions.

An anomaly in the dielectric constant has been observed in GFO prepared by the solid state reaction method [74] near the transition temperature, $T_c = 225$ K as shown in Fig. 2.26a. A similar weak anomaly in dielectric measurement as a function of temperature has been found in other systems such as hexagonal $YMnO_3$ [75] at $T_N = 70$ K and CuO at the onset of paramagnetic to spiral antiferromagnetic transition = 270 K [76]. In a ferroelectromagnet, the difference in the dielectric constant $[\Delta\varepsilon = \varepsilon(H) - \varepsilon(0)]$ below T_C is proportional to the square of the magnetization, i.e. $\Delta\varepsilon \approx \gamma M^2$, where γ is the magnetoelectric (ME) coupling constant [7]. Sun et al. [74] observed a linear relationship between $\Delta\varepsilon$ and M^2 as indication of ME coupling and reported the magnetocapacitance of -0.5% close to T_C in GFO based on the extrapolation of the zero field anomaly, Fig. 2.26b.

Naik et al. [77] also observed dielectric anomaly in bulk GFO (prepared by solid state reaction method) around the magnetic transition temperature, but the dielectric loss does not show any clear anomaly close to T_C in zero magnetic field and this anomaly suppression in a small magnetic field of $\mu_0 H = 60$ mT (Fig. 2.26c) suggests an active ME coupling in GFO sample. The magnetodielectric (MD) coefficient calculated in this case from the equation $MD = \frac{\varepsilon(\mathrm{H}) - \varepsilon(0)}{\varepsilon(0)}$ is shown as a function of temperature in the inset of the Fig. 2.26d (right scale) and it is found to be -1.8% close to T_C in GFO, which is lower than the huge value of -60% MD and -8% MD observed in the ferromagnetic $BiMnO_3$ [51] (at T $T_C \approx 100$ K and applied magnetic field = 9 T) and E type antiferromagnetic $HoMnO_3$ [78] (at $T = 4.5$ K and $\mu_0 H = 7$ T), respectively.

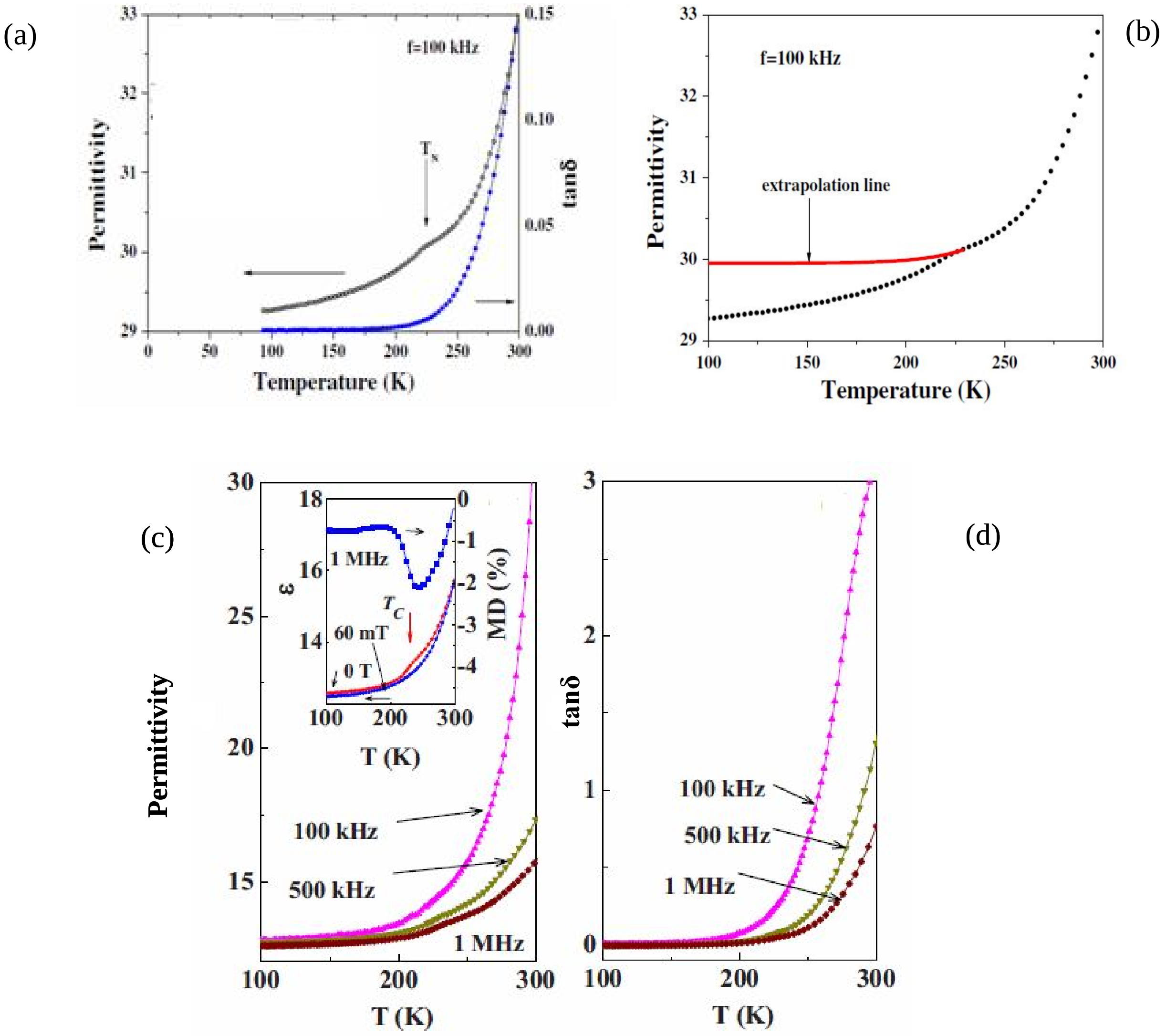

Figure 2.26: (a) Permittivity (ε') and dielectric loss (tanδ) as a function of temperature at 100 kHz for GFO. (b) Permittivity for GFO at 100 kHz and its extrapolation from the paramagnetic range [74]. Temperature dependences of (c) ε' and (d) tanδ at f =100 kHz, 500 kHz and 1 MHz; inset shows the temperature dependences of ε' in $\mu_0H = 0$ and 60 mT at f = 1 MHz and also MD coefficient (right scale) as a function of temperature at f = 1 MHz [77].

The P-E loops measured at frequency(f) =1 kHz and temperature (T) = 150, 200, and 225 K [77] (Fig. 2.27a) show unsaturated hysteresis loops rounded at the highest applied electric field, which reveals the leakage current contribution that overshadows the true polarization due to the orientation of the electric dipoles. Also, the highly frequency dependent P-E loops at T = 150 K (Fig. 2.27b) measured in different frequencies ranges (f = 1 kHz – 50 Hz) suggest that GFO sample does not appear to be ferroelectric because the P-E loops open up as the measurement frequency decreases, which is an artifact due to the leakage current contribution [79].

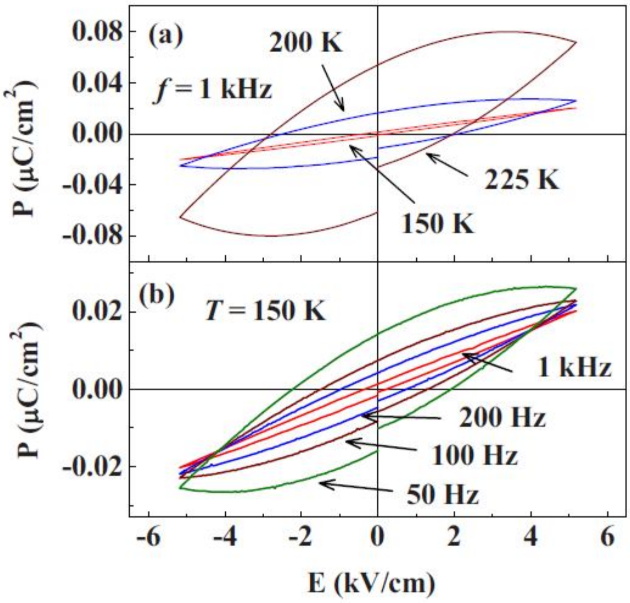

Figure 2.27: (a) P-E loops at selected temperatures (frequency of the hysteresis cycle f = 1 kHz) and (b) P-E loops at T = 150 K with different frequencies of the hysteresis cycle (f = 1 kHz–50 Hz) [77].

Very recently Shireen et al. [80] studied the effect of Al substitution on the properties of GFO. $Ga_{0.5}Al_{0.5}FeO_3$ shows a ferromagnetic behavior similar to $AlFeO_3$ and GFO with T_c of 220 K. The dielectric below T_c and it increases significantly above T_c, which unlike that of relaxor ferroelectrics, Figs. 2.28a and b. Also, $Ga_{0.5}Al_{0.5}FeO_3$ shows a ferroelectric hysteresis at relatively low temperatures (< 300 K) with saturation polarization (P_m) and remnant polarization (P_R) very much higher than in $GaFeO_3$, Figs. 2.28c and d.

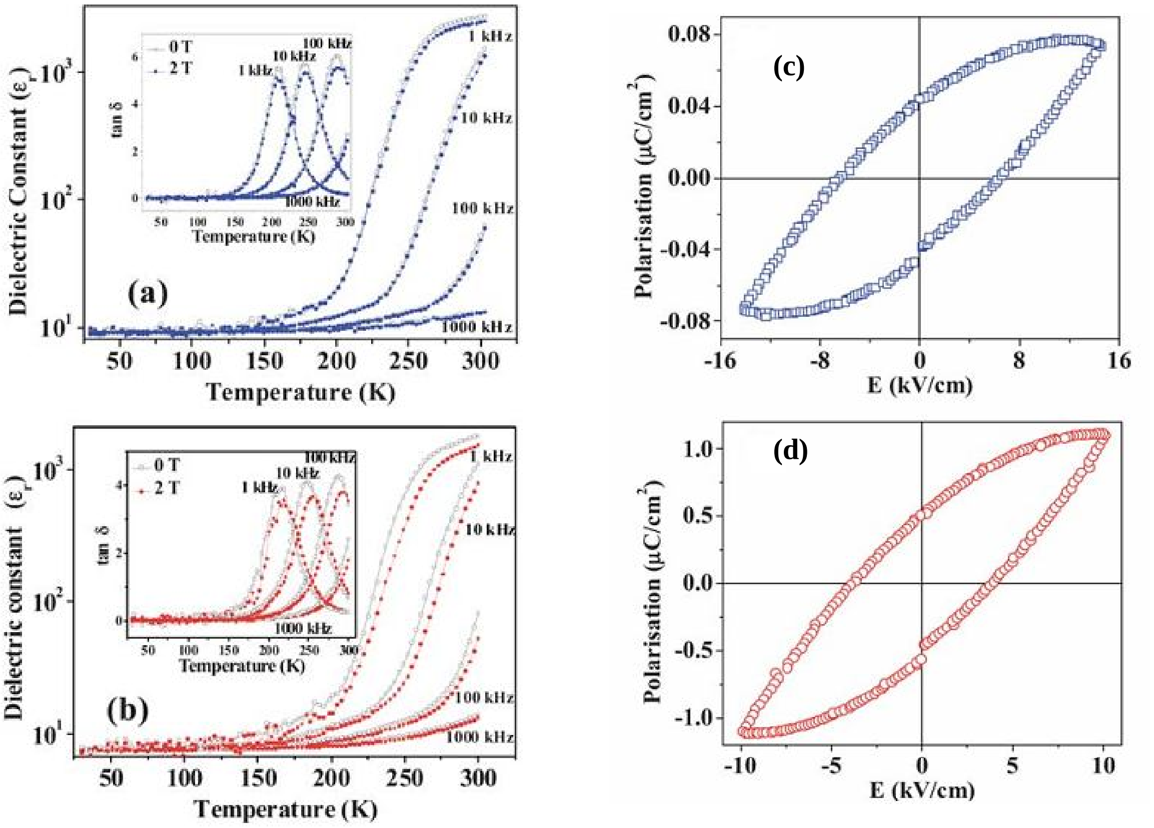

Figure 2.28: The temperature variation of dielectric properties of (a) GFO and (b) $Ga_{0.5}$ $Al_{0.5}FeO_3$. The effect of 2T is also shown for both samples. The ferroelectric hysteresis loops for (c) GFO and (d) $Ga_{0.5}$ $Al_{0.5}FeO_3$ at 200 K (1 kHz) showing leaky behavior [80].

The application of a magnetic field has a marked effect on the dielectric properties of GFO and $Ga_{0.5}$ $Al_{0.5}FeO_3$, Figs. 2.28a and b. Both these oxides show large magnetocapacitance and a significant variation of the magnetocapacitance with frequency, as shown in Fig. 2.29a. Maximum magnetocapacitance is observed in these two oxides around 40 kHz and at this frequency, $Ga_{0.5}Al_{0.5}FeO_3$ shows 60% magnetocapacitance at 2 T and 35% at 1 T. The variation of % magnetocapacitance with magnetic field for all three oxides is shown in Fig. 2.29b. The marked variation of magnetocapacitance in $GaFeO_3$ and $Al_{0.5}Ga_{0.5}FeO_3$, is note worthy and it increases with the magnetic field.

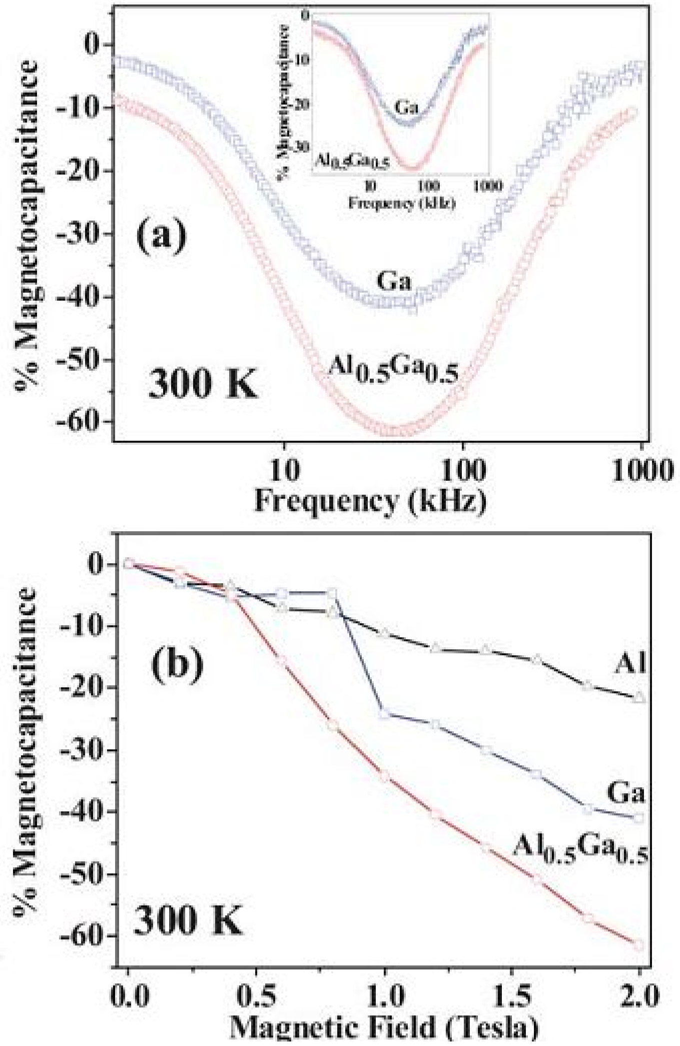

Figure 2.29: (a) The variation of % magnetocapacitance with frequency for GFO and $Ga_{0.5}Al_{0.5}FeO_3$ at a magnetic field of 2T. In the inset, the variation of % magnetocapacitance with frequency at 1 T is shown, (b) the variation of % magnetocapacitance with magnetic field for $AlFeO_3$ (0.5 kHz, 300 K), GFO (40 kHz, 300 K) and $Ga_{0.5}Al_{0.5}FeO_3$ (40 kHz, 300 K) [80].

Chapter 3

Experimental and characterization: Principles and techniques

3 Introduction

In this chapter, a brief description is given of the preparation, experimental methods and instruments used in the characterization of the samples in this thesis.

3.1 Synthesis

3.1.1 Synthesis of bulk materials by solid state reaction

Bulk $GaFeO_3$ powder was prepared by solid state reaction between Ga_2O_3 (ChemPur, 99.99%) and Fe_2O_3 (Aldrich, 99.9%). Precursor powders were calcined for ~ 20h at 900°C and then at 1050°C (20h). These powders were reground thoroughly, pelletized and sintered at 1200°C (20h) and again at 1300°C (10h) to obtain stoichiometric compounds.

$GaFeO_3$ substituted with Mn were prepared by solid state reaction with Mn_2O_3 (Aldrich, 99.99%), Fe_2O_3 and Ga_2O_3. Mn-substituted samples were fired at different temperatures. Cr-substituted $GaFeO_3$ samples were obtained from Ga_2O_3, Fe_2O_3 and Cr_2O_3 (ChemPur, 99%). The samples were annealed at 900°C (20h) and then at 1050°C (50h). These powders were reground thoroughly, pelletized and sintered at 1300°C (10h).

3.1.2 Sol gel synthesis of $GaFe_{1-x}Mn_xO_3$ solid solution

Stoichiometric amounts of $FeCl_3.6H_2O$ (Merck KgaA, 99.9%) , $Ga(NO_3)_3.6H_2O$ (Aldrich, 99.9%), $Mn(NO_3)_2.xH_2O$ (Alfa Aesar, 99.98%), a suitable amount of citric acid (Alfa Aesar, 99.999%) and ethylene glycol (EG) are mixed in distilled water. Subsequently, solutions were heated under stirring. The resultant gel precursors were decomposed at about 400°C and black powders were obtained. These precursors were heated at 500°C for 1h and then separated into different parts and annealed at 1000°C, 900°C, 800°C, 700°C and 500°C in a flow of oxygen in case of Mn doped samples.

3.2 Characterization techniques

3.2.1 Structural and physical characterization of samples

The phase purity and crystal structure of all prepared samples were characterized by X-ray diffraction (XRD). A STOE STADI/ P powder diffractometer equipped with a position sensitive counter (MoKα_1-radiation, λ = 0.709703 Å) was used. All conventional X-ray diffraction measurements were performed in ω-2θ geometry (transmission mode). The lattice constants, structural parameters and quantitative phase analyses of the samples were refined by the FULLPROF program package [81]. Existing phases in the samples were identified by matching with the ICCD database. A pseudo-Voigt function was used for simulation of the profile of the Bragg peaks and the background was interpolated between some fixed background points of the patterns.

Thermal analyses were carried out on a TA Instrument Netzsch STA 429 Simultaneous TGA-DTA. Thermogravimetric-differential thermal analysis (TG-DTA) is a thermoanalytical technique that combines measurements of mass loss and energy changes over a defined temperature range. The data plot obtained from this type of experiment is known as a TG curve where percent mass is plotted as a function of temperature (Fig. 3.1).

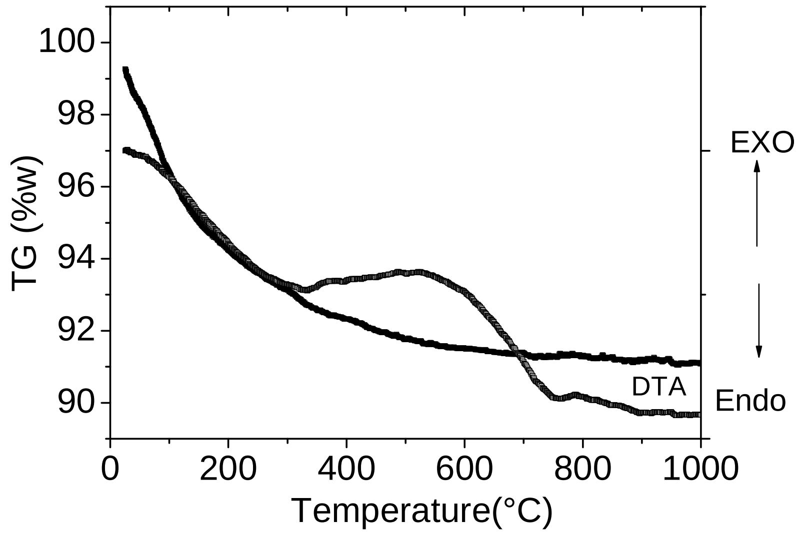

Figure 3.1: Schematic TG (solid) and DTA (dotted) curves showing a weight loss accompanied by an exothermic event for $GaFeO_3$ prepared by sol gel method.

Mass losses observed in the TG curve often represent decomposition, or evaporation of a portion of the sample. Discontinuities in the DTA curve represent energy consumption or release from phase transitions. These events include crystalline to crystalline phase transitions, as well as crystallization of amorphous materials. By determining where changes occur in the TG-DTA curves, temperatures for heat treatments can be chosen. About 10 mg of gel powder is loaded into a standard platinum crucible at room temperature. The crucible is then heated up to 1000 °C at a constant rate of 10 °C/min in air and in flow of oxygen in case of Mn doped samples. In this study, the most important consideration is the loss of all residual organics, which is indicated by flattening of the TG curve.

Surface morphologies were investigated on High Resolution Scanning Electron Microscopy (HRSEM (XL30 FEG, PHILIPS) with the acceleration voltage of 10 to 25 kV). Samples in pellet form were analyzed. In order to improve measurement precision and also improve the electrical conductivities of the samples, before the measurement some of the samples were covered by a thin Au coating. TEM experiments were performed on a PHILIPS CM20 transmission electron microscope equipped with an EDX-detector (HPGe, Voyager, Noran Instruments).

3.2.2 Magnetization measurement

A SQUID (Superconducting Quantum Interference Device) consists of a closed superconducting loop. If a sample is moved through the superconducting coils, it induces an electric current in the detection coils that is proportional to a change in the magnetic flux. Hence, the SQUID functions as a highly linear current to voltage convertor, so the variations in the voltage output are proportional to the magnetic moment of the sample. This instrument allows the detection of very low signals, with a resolution of 10^{-8} emu, and for this reason it is suited to characterize samples containing low quantities of magnetic material. The magnetization measurements were carried out in zero field-cooled (ZFC) and field-cooled (FC) conditions in the temperature interval from 5 K to 300 K under a magnetic field of 100 Oe. In the ZFC mode, the sample was cooled in zero field from 300 K to 5 K and after stabilization of the temperature, a measuring field of 100 Oe was applied. The data were then recorded whilst warming the sample. In the FC mode, the sample was cooled down from 300 to 5 K in the presence of a field of 100 Oe and then measurements were carried out whilst warming in the same field. Also M vs H hysteresis curves were measured at 10 K in applied magnetic fields H ranging up to 60 kOe.

3.2.3 Impedance spectroscopy

Impedance spectroscopy (IS) is a flexible tool for simultaneous electrical and dielectric characterization of materials. This powerful technique has been widely used to characterize the dielectric behaviour of single crystal, polycrystalline and amorphous ceramic materials. The experimental data contains three variables, real and imaginary component of the electrical response and frequencies together with four inter related electrical response formalisms: impedance (Z^*), admittance (Y^*), relative permittivity (ε^*), and electric modulus (M^*). Consequently, data can be presented in many formats; in practice, it is often found that different formats may highlight different electrical characteristics of a sample. It is the most commonly used experimental technique to analyze the dynamics of the ionic movement in solids. The general approach is to apply a monochromatic (single frequency) voltage to the sample and measure the corresponding response current as the frequency is scanned.

Equations below represent the monochromatic input voltage and the complex response current, where θ is the phase difference between voltage and current, ω is the angular frequency (ω ≡ 2 πf), t is time, and the subscript m stands for measured.

$$v(t) = V_m \sin(\omega t)$$

$$i(t) = I_m \sin(\omega t + \theta)$$

Any inductive or capacitive effects of a sample cause a corresponding phase shift of the response current with respect to the voltage. This phase shift is incorporated into the response as the phase angle θ. It is then understood that the impedance of a sample with no inductive or capacitive effects is zero and the response is purely resistive. The conventional impedance is therefore defined as $Z(\omega) = \frac{v(t)}{i(t)}$, and the magnitude of the impedance is as $|Z(\omega)| = \frac{V_m}{\mathrm{I_m}}$. The phase angle θ and the magnitude of the impedance can be determined from the real and imaginary components of impedance as shown below in Fig. 3.2,

$$Z(\omega) = Z' + jZ''$$

$$Z' = \text{real} = Z\cos(\theta)$$

$$Z'' = \text{imaginary} = Z\sin(\theta)$$

$$\theta = \tan^{-1}\left(\frac{Z''}{Z'}\right)$$

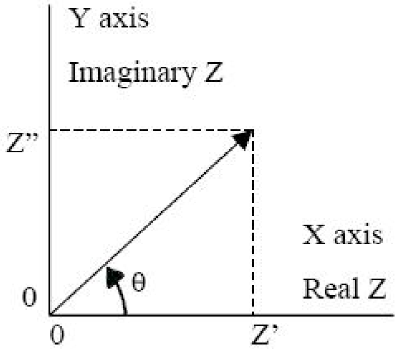

Figure 3.2: Impedance response showing real and imaginary components.

- **Impedance of ceramics**

The impedance response of a polycrystalline ceramic can have separate arcs when plotted as Z' real impedance Z vs. Z" imaginary impedance Z (Fig. 3.3). The different arcs represent different electrical aspects of the sample. The low frequency arc represents grain boundary response, and the high frequency arc represents bulk grain response. In most cases, a small arc is visible in the low frequency domain, which is typically attributed to the electrodes. Also in many cases the grain and grain boundary response are not visible as separate arcs. The arcs in the impedance response plot can also be modelled with equivalent circuits. This can yield numerical values for the different electrical aspects of a material. An example of a possible impedance response of a ceramic and the corresponding equivalent circuit is presented in Fig. 3.3. The resistance values of a given sample can be obtained from the response plots as is evident in Fig. 3.3. When the phase angle θ goes to zero the impedance response represents only "real" impedance, and the values R_1 and R_2 in Fig. 3.3 can be used to calculate the grain and grain boundary resistances. For the grain resistance this is simply the value Z_1 and for the grain boundary resistance this is the value (Z_2 - Z_1). Many times the high-frequency (or left-most) arc does not intersect with the origin of the plot. In such a case, the length of arc on the real axis is taken as the resistance R_1, similar to obtaining the resistance for the grain boundary arc (R_2). The corresponding capacitance values can be similarly calculated from the resistance values (see below). The C_1 and C_2 correspond to grain resistance (R_1) and grain boundary resistance (R_2), respectively.

$$C_1 = \frac{1}{2\pi f_1 (R_1)}$$

$$C_2 = \frac{1}{2\pi f_2 (R_2 - R_1)}$$

Where f_1 and f_2 are the frequency values for the peak of the corresponding semicircle.

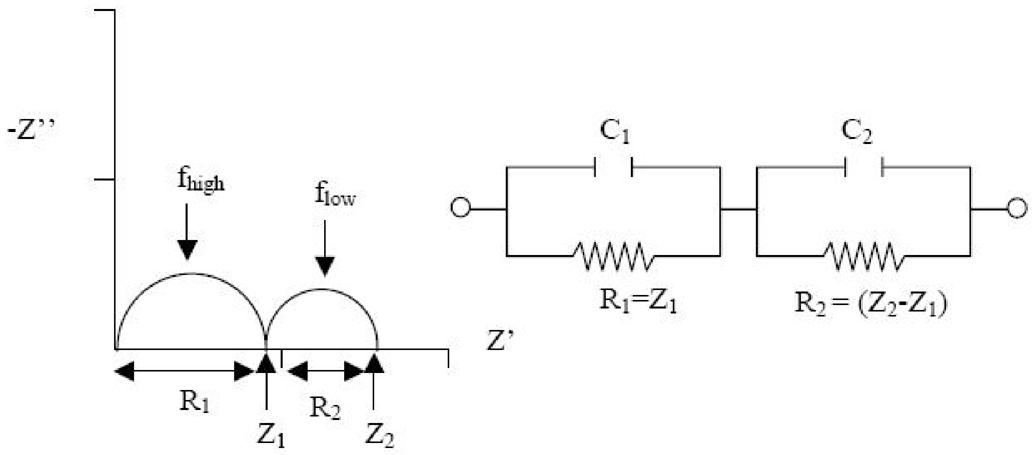

Figure 3.3: Possible impedance response plot of a polycrystalline ceramic and the corresponding RC equivalent circuit.

- **Dielectric and polarization studies**

For $GaFe_{1-x}Mn_xO_3$ prepared by solid state reaction and sol gel methods, uniaxially pressed powders heated at 1200°C, and 800°C in case of SR and SG@900°C samples, respectively were used. Then they were cold pressed using a "wet-bag" pressing technique in weber presser KIP100E isostatic press to achieve uniform distribution throughout pellets. These pellets were then sintered at 1300°C (10h) and 900°C (10h) for SR and SG@900°C samples, respectively. Silver electrodes were prepared for the samples and the dielectric measurement was controlled by a programmable electrometer (KEITHLEY 617). The complex dielectric permittivity was investigated for selected samples at 10 kHz, 50 kHz and 100 kHz in the temperature range 160K to 340 K with a step of 2 K/min, using a liquid nitrogen cryo-furnace (SMC Air liquid) and a HP4192A impedance analyzer.

For the Cr doped $GaFeO_3$ system, the uniaxially pressed powder (heated at 1050°C) was then cold pressed using a "wet-bag" pressing technique in weber presser KIP100E isostatic press to achieve uniform distribution throughout the pellet and then sintered at 1300°C (10h). Silver electrodes were prepared for the samples and the dielectric measurement was controlled by a programmable electrometer (KEITHLEY 617). The complex dielectric permittivity was investigated using a Novocontrol Alpha-A analyzer ($f = 100 - 10^7$ Hz), in the temperature range from 133 K- 350 K with a ZGS active sample cell.

The polarization hysteresis loop measurement was performed with a frequency of 4 Hz at room temperature and 255 K using a standardized ferroelectric test system (RT - 66A, Radiant Technologies). The samples were prepared as described before for dielectric measurements.

3.2.4 Neutron diffraction

Neutrons can be used as a complementary method to XRD for studying the structure of crystalline materials. Neutrons interact with the nuclei of the atoms and the unpaired electron spins while X-rays interact with the electron cloud which provides several advantages. Firstly, there is no fall off in the intensity with Bragg angle θ as the distance at which the interaction between the neutron and the nucleus occurs is much shorter than the wavelength of the neutron. Secondly, in contrast to the Z^2 dependence for X-rays, the scattering power of an atom is not strongly related to its atomic number. This means that neutron diffraction makes it possible to detect lighter elements in the presence of heavier ones, which is very useful when determining oxygen positions and distinguish between neighbouring elements such as transition metals Mn, Fe and Ni. Finally, the interaction between the neutron’s magnetic moment and those of the atoms/ions with unpaired electron spin provides information about magnetic order.

3.2.4.1 Neutron diffraction of magnetic compounds

Neutron diffraction can be used to study magnetic structures as neutrons, with spin quantum number of ½, possess a magnetic moment which can interact with unpaired electrons on cations in a crystal structure. The magnetic structure can be determined by collecting data below and above the magnetic ordering temperature, which makes it possible to identify the peaks that are a result of coherent diffraction from magnetic spins. Paramagnetic materials scatter neutrons incoherently, as the magnetic spins are randomly oriented in all directions, and provide no contribution to the Bragg peaks, only to the background. Magnetic scattering will occur for an ordered array of magnetic atoms. Ferromagnets generate magnetic peaks that are superimposed on the nuclear peaks since the atoms and the magnetic moments have the same periodicity. Antiferromagnets give rise to additional reflections on a supercell of the nuclear cell. The magnetic peaks can be indexed with hkl values and the magnetic unit cell, which may be of the same size or bigger than the crystallographic unit cell, can be determined. For example, if the antiferromagnetic ordering results in a doubling of the unit cell in all three directions one of the additional peaks will be (hkl) = (½,½,½). The magnetic peaks are normally observed at long d-spacings because of the fall off in the magnetic scattering length with θ. A magnetic model should be created that is in agreement with the symmetry and the saturated magnetic moment for each atom in the magnetic structure can then be calculated by refinement of this model.

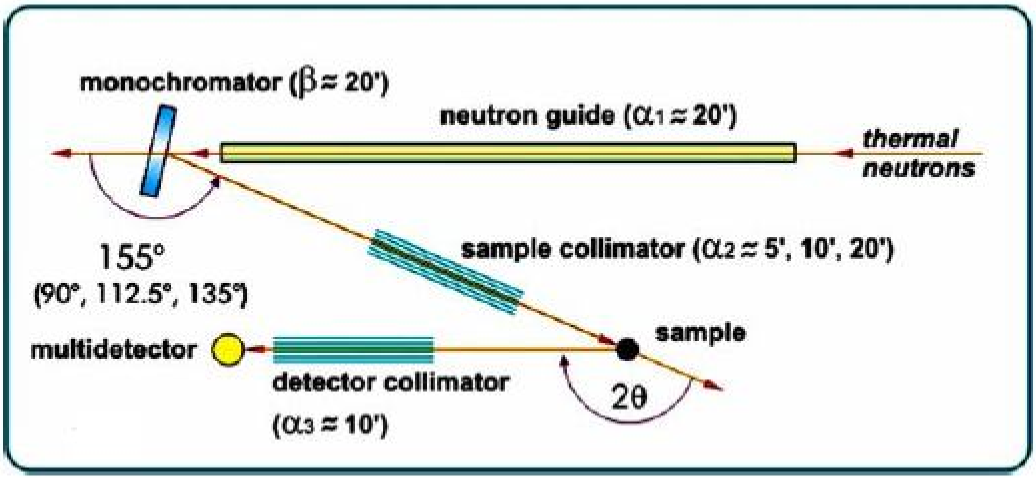

Figure 3.4: Principle of the structure powder diffractometer SPODI at the FRM-II [83].

Neutron diffraction data were collected at the research neutron reactor FRM-II (Garching near Munich, Germany) at the structure powder diffractometer SPODI [82]. Apart from routinely working with a high take-off angle (2θ) of 155° as shown in Fig. 3.4, the key use of a thermal neutron guide for the SPODI diffractometer makes it achieve a better resolution and a higher intensity. The use of sample collimator also influences and improves its resolution over a wide 2θ range

3.2.4.2 Magnetic symmetry

As mentioned in case of antiferromagnetic structure, the magnetic unit cell may be doubled in one or more directions compared to the chemical unit cell. This can also be seen as an extension of the symmetry through the inclusion of anti-translation leading to an expansion from the 14 standard Bravais lattices in ordinary crystallography to 36 magnetic Bravais lattices [84]. From these, 1421 space groups can be developed by addition of a new antisymmetry operation, designated R, which reverses the direction of the magnetic moment. Including the 230 standard crystallographic space groups, this gives a total of 1651 so called

'Shubnikov groups' applicable to materials with ferromagnetic and antiferromagnetic structures [85].

3.2.5 Mössbauer spectroscopy

Mössbauer spectroscopy relies on the recoil free resonant emission and absorption of γ radiation. The effect was discovered by Rudolf Mössbauer in 1957.

^{57}Co decays with a half life time of 270 days into an excited state of ^{57}Fe. The excited ^{57}Fe state with nuclear spin $I_e = 3/2$ will decay with a half life time of $\tau_{1/2} = 98$ ns to ground state with spin $I_g = 1/2$, creating a γ-ray with an energy of 14.4 KeV. This γ-ray may then be resonantly absorbed by another nucleus. If the nuclei are isolated conservation of momentum will impart a recoil energy to the emitting nucleus reducing the energy of the γ-rays. So the energy of the γ-rays will not be sufficient to excite another iron nucleus. However, if the emitted and absorbing nuclei are in crystal lattices the entire lattice may absorb the recoil, making the recoil energy small. The probability of this occurring is proportional to the f-factor given by $f = e^{-(\frac{E_\gamma^2}{h^2c^2} < u^2 >)}$, where E_γ is the γ- ray energy, c is the velocity of light and $<u^2>$ is the mean square vibrational amplitude of atoms in crystal, which increases as the temperature increases. The requirements for a large f –factor is a low E_γ and small thermal vibration of the nuclei, ^{57}Fe in solid materials satisfies these conditions.

In a conventional Mössbauer experiment a radioactive source containing the Mössbauer isotope in an excited state, for example radioactive ^{57}Co in Rh matrix for ^{57}Fe is moving relative to an absorber consisting of the material to be investigated containing ^{57}Fe nuclei in the ground state.

If a source of emitting nuclei is moved at a velocity v compared to an absorber, the emitted γ-ray energy will suffer a Doppler shift of $\Delta E = v/c$, where v is the source velocity. For example if v = 1mm/s, $\Delta E = 10^{-8}$ eV, which is comparable to energy shifts and splitting of nuclear states caused by hyperfine interaction ($\sim 10^{-7}$ eV). The Mössbauer spectrum thus obtained consists of a plot of the intensity of γ- radiation transmitted through the absorber (or relative absorption) as a function of the source velocity. In ^{57}Fe Mössbauer spectroscopy a source velocity in the interval ±10 mm/s is enough to compensate for the shifts due to the hyperfine interaction.

3.2.5.1 Hyperfine interactions

The Mössbauer spectrum, which is described by the number, position, shape and relative intensity of the absorption lines is governed by the nature of the different hyperfine interactions. These interactions perturb the nuclear energy levels and give rise to the hyperfine parameters: the isomer shift, the quadrupole splitting and the magnetic hyperfine field.

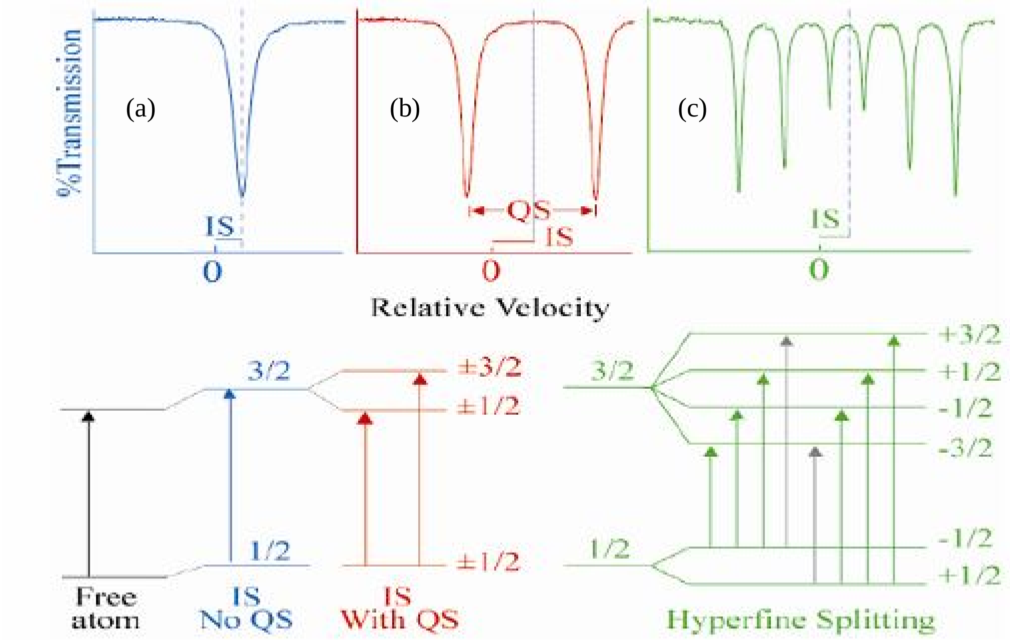

Figure 3.6: Different local environments around atomic nuclei result in energy difference. The simplest case produces a velocity shift of the peak in the transmission spectrum (a), called an isomer shift and denoted by IS. The notation 1/2 and 3/2 refer to the nuclear spin, or angular momentum quantum numbers I. When the quadrupole moment at the nucleus interacts with the electric field gradient at the nucleus, it causes the ^{57}Fe Mössbauer spectrum to show a doublet. The phenomenon is called quadrupole splitting and is denoted by QS (b). If there is a magnetic field present at the nucleus, then hyperfine or Zeeman splitting takes place in the nuclear energy levels, producing a sextet in the Mössbauer spectrum (c). The arrows in gray represent transitions that are disallowed by the selection rule $|\Delta m_I| \leq 1$ [86].

3.2.5.2 The isomer shift

The isomer shift arises due to the non-zero volume of the nucleus and the electron charge density due to s-electrons within it leading to an electric monopole (coulomb) interaction which alters the nuclear energy levels. The volume of the nucleus in its ground and excited states are different and the s electron densities are affected by the chemical environment. This shift is known as isomer shift or center shift. It is recorded in mm/s, and is denoted by IS, CS, or δ (Fig. 3.6a). Any difference in the s-electron environment between emitter and absorber thus produces a shift in the resonance energy of the transition. This shift cannot be measured directly and so a suitable reference is necessary, such as a specific source or an absorber. In all of the results presented in this thesis isomer shifts are quoted relative to α-Fe at room temperature.

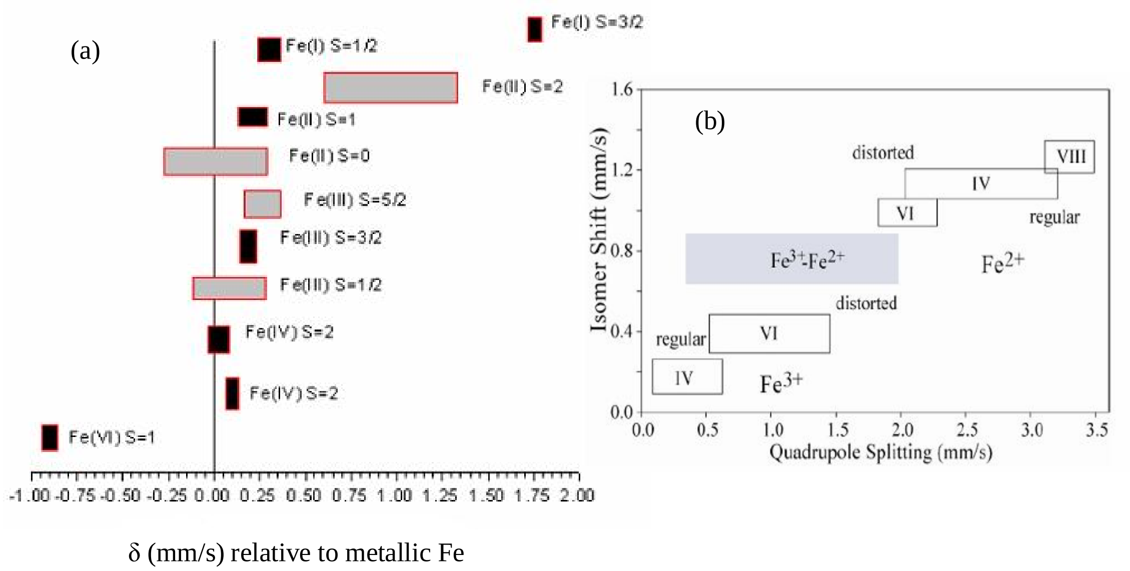

Figure 3.7: Distribution of isomer shift and quadruple splitting ranges with respect to spin and oxidation state [86].

The isomer shift is good for probing the valence state of the Mössbauer atom. As the wave functions of the s-electrons penetrate into outer shells changes in these shells will directly alter the s-electron charge density at the nucleus. For example, Fe^{2+} and Fe^{3+} have electron configurations of $(3d)^6$ and $(3d)^5$ respectively. The ferrous ions have less s-electron density at the nucleus due to the greater screening of the d-electrons. This produces a positive isomer shift greater in ferrous iron than in ferric (Fig. 3.7a). Although isomer shift itself is not temperature dependent, the non-zero mean squared velocity of the nuclei results in a change of isomer shift with temperature. This phenomenon is known as a second order Doppler shift, and is typically denoted by δ_{SOD}. Isomer shift then becomes

$$\delta(T) = \delta_1 + \delta_{SOD}(T)$$

The second order Doppler shift (SODS) is a temperature-dependent effect on the center shift of a Mössbauer spectrum. Above 0 K atoms in a lattice oscillate about their mean position. The frequency of this oscillation is of the order of 10^{12} Hz meaning that the average displacement during the lifetime of a Mössbauer event is zero. However, second order Doppler shift depends on $<\upsilon^2>$ leading to the mean square displacement being non-zero. This energy shift is given by

$$\frac{\delta E_\gamma}{E_\gamma} = -\frac{\langle \upsilon^2 \rangle}{2c^2}$$

3.2.5.3 Electric quadrupole hyperfine interactions

When the quantum spin number, I, is greater than 1 in the nucleus (Fig, 3.6b), there is no longer nuclear spherical symmetry. For a non-spherical nucleus, electric quadrupole hyperfine interactions could alter their energy levels if a local electric field gradient (EFG) ∇E exists,

$$\nabla E_{ij} = -\frac{\partial^2 V}{\partial x_i \partial x_j} = -V_{ij},$$

$$\{x_i, x_j\} = \{x, y, z\} \text{(3.1)}$$

where V is the electrostatic potential. There are two contributions to the EFG

i) lattice contributions from charges on distant ions and

ii) valence contributions due to incompletely filled electron shells. If a suitable coordinate system is chosen the EFG can be represented by three principal axes, V_{xx}, V_{yy} and V_{zz}.

If an asymmetry parameter is defined using these axes as

$$\eta = (V_{xx} - V_{yy})/V_{zz}, \qquad (3.2)$$

where $|V_{zz}| > |V_{xx}| \geq |V_{yy}|$ so that $0 \leq \eta \leq 1.0$.

This interaction partially removes the (2I + 1)-fold degeneracy of the nuclear energy states, causing the I = 3/2 nuclear energy level to split. The phenomenon is called quadrupole splitting and is denoted by QS, Δ, or ΔEQ. The result is two peaks (a doublet) instead of one in the Mössbauer spectrum. Quadrupole splitting is the distance between the two peaks, which corresponds to the energy difference between the split states. Quadrupole splitting, like isomer shift, is sensitive to the coordination number and oxidation state of the atom because it, too, results from changes in the local electronic environment. Fig. 3.7b shows the variation of quadrupole splitting and isomer shift with coordination number and oxidation state.

3.2.5.4 Magnetic hyperfine field interactions

There is a magnetic moment associated with the ^{57}Fe nucleus that is caused by an interaction between the nucleus and its electrons. This magnetic moment can interact with external magnetic fields that originate from the structure of the iron-bearing material. The result is a complete loss of degeneracy in the energy levels of the ^{57}Fe nucleus, causing 6 peaks to appear in the spectrum instead of one or two (Fig. 3.6c). This is called magnetic hyperfine interaction or Zeeman interaction. In most cases, selection rules for the nuclear energy level transitions exist, ($|\Delta m_I| \leq 1$), forbidding the transitions from I = 1/2 to I = -3/2 and I = -1/2 to I = 3/2, such as in Fe foil. The hyperfine splitting is determined by the hyperfine magnetic fields which, in turn, are determined by the chemical environment of the iron atom.

3.2.5.5 Combined magnetic and quadrupole interaction

When dealing with quadrupole or magnetic splitting separately with chemical isomer shifts the recorded spectrum has uniform shifts of resonance lines with no change in their relative separation. Since the quadrupolar and magnetic interactions are angle dependent, so when they are both present the interpretation of the spectrum can be complex. The situation can be simplified a great deal if two assumptions are made

1- The electric field gradient is axially symmetric with its principal axis, V_{zz}, at angle θ to the magnetic axis.

2- The strength of the quadrupole interaction is smaller than the magnetic interaction.

The situation to the Hamiltonian can be then solved by treating the quadrupole interactions as a perturbation. So that the resultant spectrum is given in Fig. 3.8.

For most ^{57}Fe spectra the result is a shift in the relative position of lines 1, 6 with lines 2, 3, 4, 5. For a positive quadrupole splitting lines 1, 6 are shifted positively relative to lines 2, 3, 4, 5 and *vice versa*. The line separations are equal when there is no quadrupole effect or when $\cos\theta = 1/\sqrt{3}$.

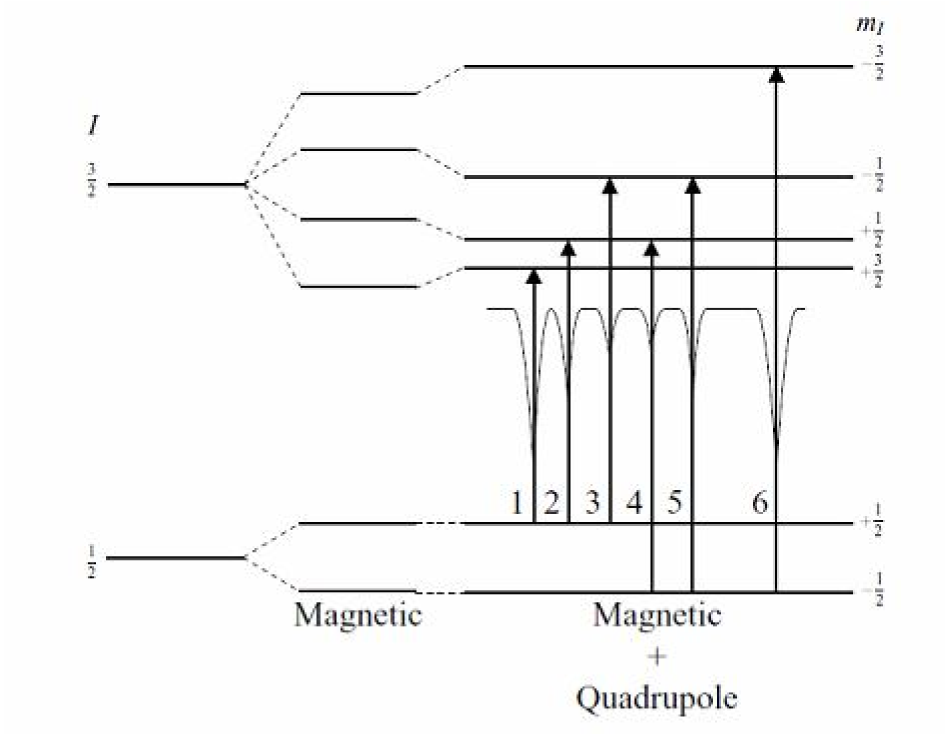

Figure 3.8: The effect of a first order quadrupole perturbation on a magnetic hyperfine spectrum for 3/2 → ½ transition. Lines 2, 3, 4, 5 are shifted relative to lines 1, 6.

It was recently shown that in the case of powdered absorbers exhibiting mixed hyperfine interactions, e.g. magnetic dipole and electric quadrupole ones, the method of invariants is particularly useful [87] because it serves as a method of decomposition of spectra into the subspectra, thus avoiding the so called ambiguity problem [88]. In the case of ^{57}Fe Mössbauer spectroscopy there are four excited sublevels of I = 3/2 nuclear state and therefore there are only four independent hyperfine parameters available in the experiment with texture free absorbers. To avoid ambiguity during the fitting procedure one can describe each subspectrum by a set of invariants.

3.2.5.6 The method of invariants for dominating magnetic interaction

The line positions in the Mössbauer spectra of texture free absorbers can be given explicitly by invariants S_0, S_1, S_2, constructed from the electric field gradient (EFG) tensor **V** and the hyperfine magnetic field (HMF) pseudovector **B**:

$$\begin{aligned} S_0 &= a\sqrt{\mathrm{Tr}\boldsymbol{V}^2}\,, \\ S_1 &= a\,\boldsymbol{m}^T \cdot \boldsymbol{V} \cdot \boldsymbol{m}\,, \\ S_2 &= a\,\sqrt{\boldsymbol{m}^T \cdot \boldsymbol{V}^2 \cdot \boldsymbol{m}}, \end{aligned} \tag{3.3}$$

where $$a = eQc \,/\, E_\gamma \tag{3.4}$$

is the proportionality constant between the EFG components (in [V/m^2], SI units). The invariants are expressed conveniently for applications in [mm/s]. Q is the nuclear quadrupole moment, e is the elementary charge, c is the speed of light, E_γ is the energy between the ground and the excited state, **m** = **B**/B. The positions of absorption lines and their intensities in a Mössbauer spectrum can be given explicitly by coefficients of the secular equation for the excited nuclear states

$$u^4 + pu^2 + qu + r = 0, \tag{3.5}$$

where

$$\begin{aligned} p &= -\frac{1}{12}\left(30u_B^2 + S_0^2\right), \\ q &= -S_1 u_B^2, \\ r &= \frac{1}{576}\left(\left(18u_B^2 + S_0^2\right)^2 - 144u_B^2 S_2^2\right) \end{aligned} \tag{3.6}$$

$u_B = g_{3/2}\mu_N Bc/E_\gamma$ is the characteristic velocity and $g_{3/2}$ is the nuclear g-factor of the excited nuclear spin 3/2 state. The absorption line positions $u_{\alpha\beta}$ (expressed conveniently in the velocity units) in the Mössbauer spectrum are:

$$u_{\alpha\beta} = u_\alpha - \beta\,\frac{g_{1/2}\mu_N Bc}{2E_\gamma} \tag{3.7}$$

where $g_{1/2}$ denotes the nuclear g-factor of the ground state. The index $\beta = \pm 1$ corresponds to two ground states and u_α are four roots of (3.5). Relative line intensities for a texture free sample (the trace of the intensity tensor) have an explicit form [87]:

$$\mathrm{Tr}\,\boldsymbol{I}_{\alpha\beta} = \frac{3}{8} + \frac{3\beta u_B}{16}\cdot\frac{40u_\alpha^2 + 16u_\alpha S_1 - S_0^2 + 4S_2^2 - 18u_B^2}{24u_\alpha^3 - u_\alpha\left(30u_B^2 + S_0^2\right) - 6S_1 u_B^2} \tag{3.8}$$

All physically possible numerical values of invariants (3.3) obey two rules [88]:

$$S_1^2 \le S_2^2, \qquad 4S_2^2 \le S_1^2 + 2S_0^2 \tag{3.9}$$

The method of invariants [88] is particularly useful when magnetic and quadrupole interactions are of the same order. When the magnetic interaction is much stronger than the quadrupole one, a certain ambiguity appears. The line intensities and positions are given with a satisfactory precision by the expansion of (3.7) and (3.8) to the first order in a small parameter $eQV_{zz}/g_{3/2}\mu_N B$. The relative line intensities in the spectrum of a texture free absorber are 3:2:1:1:2:3. The line positions are shifted with respect to the line positions in the pure Zeeman sextet and the shift is given by a single parameter proportional to V_{zz}. In such a case the spectrum contains not enough information to extract all the invariants S_0, S_1, S_2. Therefore, one should work out a proper data treatment in case of a small quadrupole interaction using invariants, and avoid ambiguity. To solve this problem one may ask about the exact shape of the spectrum (the line intensities and positions given by the full Hamiltonian equations 5.2 and 6.8 of [87]), which is most similar to the shape given by the first order expansion in the small parameter $eQV_{zz}/g_{3/2}\mu_N B$. This requirement can be precisely formulated by the condition that the eigenvalues of the excited nuclear state must be equally separated, i.e. must have the form: $u_1 = -3x+y$, $u_2 = -x-y$, $u_3= x-y$, $u_2 = -3x-y$, where x and y are some values for which $x^2>>y^2$. Thus, the coefficients of the polynomial in equation (3.5) should be equal to those in the $(u-u_1)(u-u_2)(u-u_3)(u-u_4)$, which is equivalent to:

$$\begin{aligned} 10x^2 + 2y^2 &= \frac{1}{12}\left(30u_B^2 + S_0^2\right), \\ 16x^2 y &= S_1 u_B^2, \\ 9x^4 - 10x^2y^2 + y^4 &= \frac{1}{576}\left(\left(18u_B^2 + S_0^2\right)^2 - 144u_B^2 S_2^2\right) \end{aligned} \qquad (3.10)$$

From the set of three eqs (3.10), two constants x and y can be eliminated, resulting in a lengthy relation between S_0, S_1 and S_2 for the given u_B, which is given by sixth order polynomial in u_B. Since in our problem the parameter u_B is much larger than any of S_0, S_1, S_2, one can show that the exact solution of (3.10) may be approximated by:

$$2S_0^2 + 17S_1^2 - 20S_2^2 = 0 \qquad (3.11)$$

This result shows the final relation between S_0, S_1 and S_2 for small quadrupole interactions. Thus, when simultaneous fitting of several Mössbauer spectra is carried out, and the spectra correspond to the case of small quadrupole interactions with respect to the magnetic one, the relation (3.11) reduces the number of the free parameters.

In summary, one can say that an efficient method of exact treatment (3.7), (3.8) with additional constraint (3.11) is proposed to be used in the case of small quadrupole interactions.

3.2.6 Synchrotron X-ray powder diffraction

The low temperature, high-resolution experiments were carried out at the synchrotron facility HASYLAB/DESY (Hamburg, Germany) with the powder diffractometer at beamline B2 [89]. The powder sample consisted of a completely filled and sealed quartz capillary (0.3 mm). It was mounted with a capillary spinner in Debye-Scherrer geometry inside a He closed-cycle cryostat [90] equipped with a silicon diode as the temperature sensor. A wavelength of 0.53904 (6) Å was selected from the direct white synchrotron beam using a Si(111) double flat-crystal monochromator and determined from eight reflection positions of a LaB_6 reference sample (NIST SRM 660a). The beam size of 0.4 x 3 mm at the sample position was cut by slits. All diffraction patterns were collected using an on-site readable position-sensitive image-plate detector (2θ range 5˚–70˚). Several patterns were collected during heating from 200 K up to 300 K

Chapter 4

Effect of cation distribution on dielectric and magnetic properties of $GaFeO_3$

4 Introduction

In this chapter, we describe the syntheses of $GaFeO_3$ (GFO) by solid state reaction (SR) and sol gel (SG) methods and the examination of the materials by X-ray and neutron powder diffraction, Mössbauer spectroscopy, dielectric measurement and dc magnetic susceptibility in order to throw light on the effect of low temperature annealing method on the structural, magnetic and dielectric properties of GFO

4.1 Powder characterization

Fig. 3.1 depicts the TG–DTA curves of as-prepared GFO dried gel precursors. The first weight loss process takes place between room temperature and 195 °C, which corresponds to the loss of adsorbed water. The second weight loss occurs at 195–550 °C associated with a weak exothermal peak, which can be ascribed to the combustion of organic citrate acid ligands and the decomposition of nitrates. Thereafter, no mass loss was observed in TG curves with further increase of temperature and no remarkable endothermic or exothermic peaks appear in DTA curves, which indicate that the decomposition and combustion of all organic materials in the precursors were over below 550 °C. X-ray diffraction pattern of powder annealed at 600°C prepared by sol gel method is shown in Fig. 4.1.

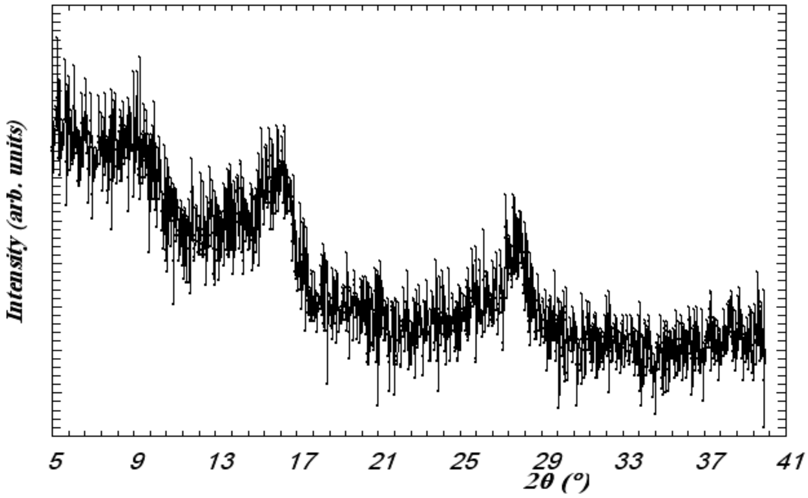

Figure 4.1: XRD of GFO prepared by sol gel method and annealed at 600 °C.

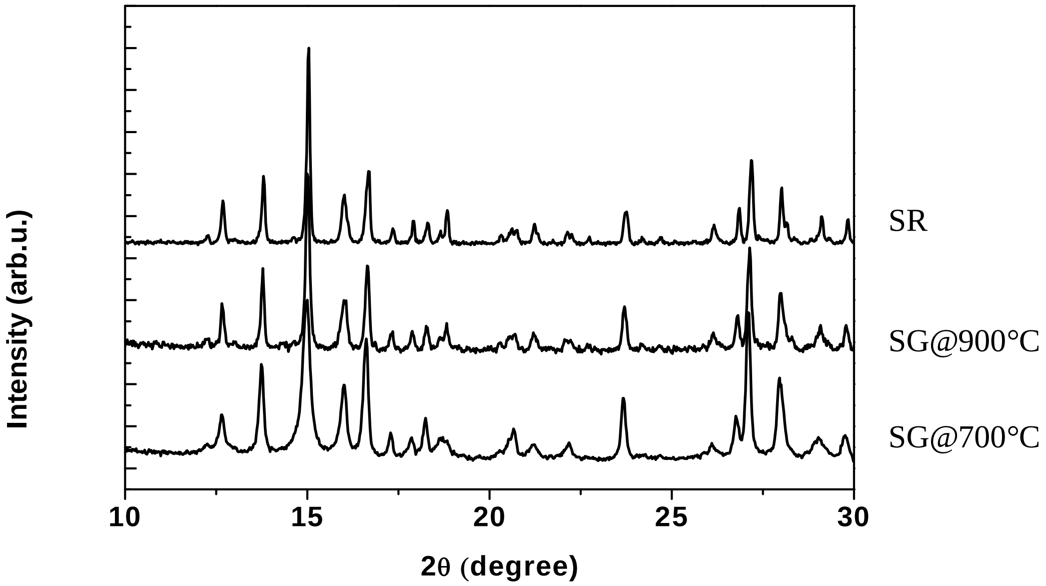

Figure 4.2: XRD patterns of GFO powders prepared by solid state reaction (SR) and sol gel (SG, annealed at 900°C and 700°C) methods.

The pattern shows several broad peaks corresponding to the main reflections of orthorhombic GFO. The crystalline phase is obtained when the sample is heated at 700°C. Fig. 4.2 shows the comparison between the XRD patterns for GFO samples at room temperature prepared by solid state reaction (SR) and sol gel (SG, annealed at 900°C and 700°C) methods. The XRD peaks of GFO (SG) were broadened compared with GFO (SR). The broadening of the XRD lines corresponds to the decrease of particle size.

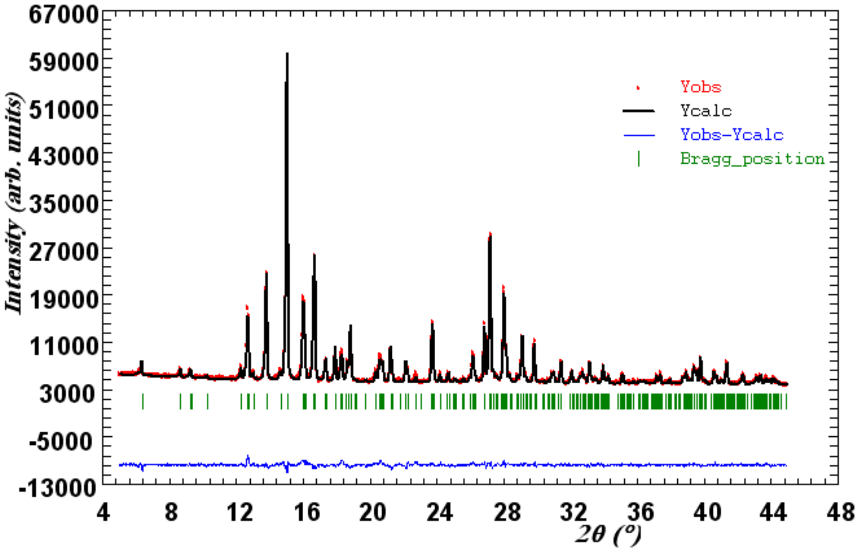

Figure 4.3: Rietveld refinement profile for the SG@900°C sample performed using FullProf.

Samples crystallize in the orthorhombic system with space group (P c 2_1 n). No diffraction peaks of other phases were found as shown in Fig. 4.3. TEM micrograph of a batch of GFO annealed at 600°C is shown in Fig. 4.4d. The average particle size is of the order of 8 nm. Inset of Fig. 4.4d shows an electron diffraction pattern of the GFO nanoparticles in a selected area. The diffraction pattern obtained by TEM shows the characteristic ring reflexions of a nanometric polycrystalline material while the distances between the planes correspond in a very close approximation with the distances obtained by XRD. Also, Fig. 4.4 shows the SEM images after sintering of the products of sol gel and solid state reaction syntheses. It can be observed that the samples prepared by the sol gel method gave a more homogenous grain size distribution (Figs. 4.4b and c), whereas large and different grain sizes are observed in the sample obtained through the solid state route (Fig. 4.4a). The average crystallite size, d, of the sintered samples were estimated using Scherrer's formula,

$$d = \frac{k\lambda}{B\cos\theta}$$

where k = 0.9 is the particle shape factor, considering a spherical shape of the nanoparticles, λ = 0.709703 Å is the wavelength of Mo K_α radiation, here B = $(B_M^2 - B_S^2)^{1/2}$, where B_M is the full width at half maximum (FWHM) of the (221) peak and B_S is standard instrumental broadening, and θ is the diffraction angle of the peak. The average particle size values in case of SR, SG (900°C) and SG (700°C) samples are 205, 75 and 50 nm, respectively. The lattice parameters obtained from Rietveld refinement are listed in Table 4.1. The lattice constants a, b, c and V increase with decreasing annealing temperature.

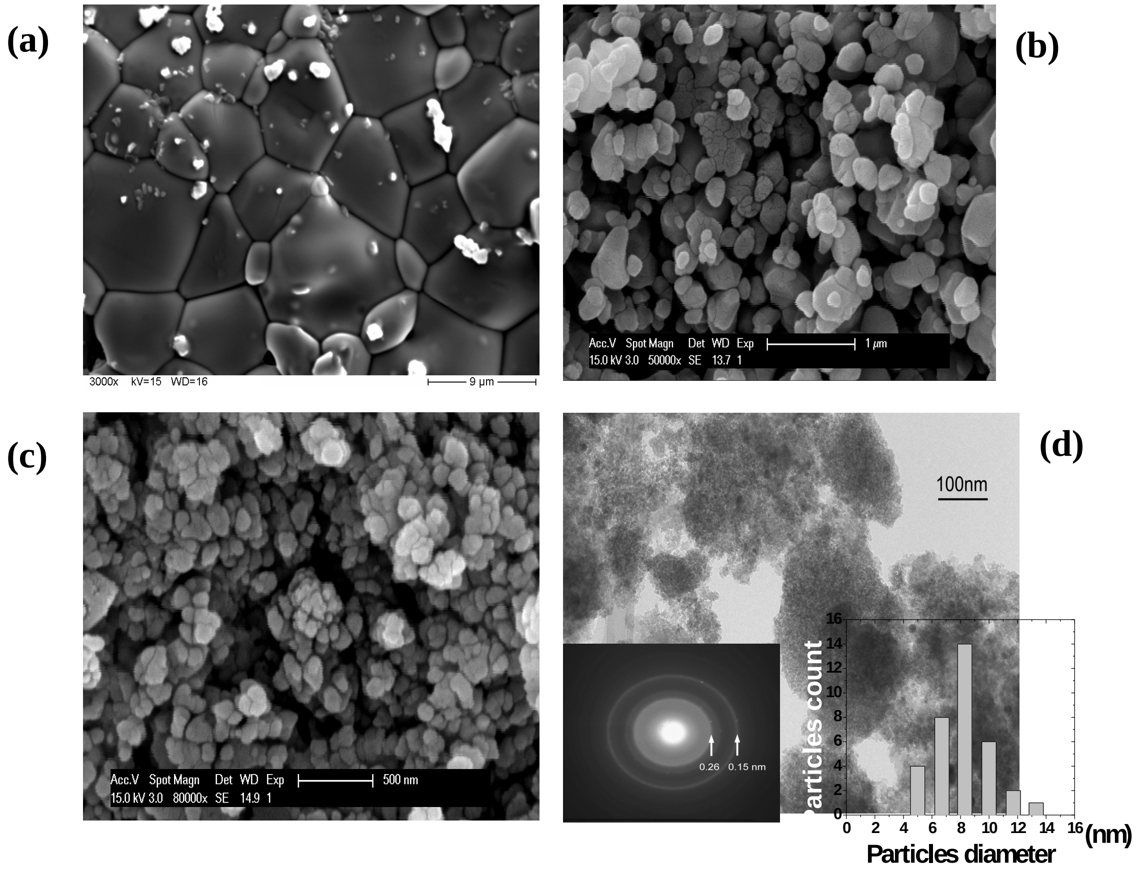

Figure 4.4: SEM photographs of GFO prepared by solid state reaction (a), sol gel method and annealed at (b) 900°C, (c) 700°C and (d) TEM photograph for sample annealed at 600°C. The insets show diffraction pattern and particle size distributions.

The reduction in particle size relaxes the lattice leading to a cell volume expansion; a similar behavior has been reported for other oxide systems such as Al_2O_3 [91].

Table 4.1: Lattice parameters determined by Rietveld refinement and magnetic properties for GFO powder prepared by solid state reaction (SR) and sol gel (SG) methods.

Sample	SR	SG @900°C	SG @700°C
a(Å)	8.7451(4)	8.7619(1)	8.7648(1)
b(Å)	9.3915(1)	9.4120(2)	9.4150(2)
c(Å)	5.0819(7)	5.0868(7)	5.0808(9)
V(Å^3)	417.38(2)	419.50(1)	419.92(1)
M_s (emu/Fe)	0.77	0.89	1.32
H_c (Oe)	6435	4035	6771
T_c (K)	225	300	310

4.2 Magnetization

The temperature dependence of the FC and ZFC magnetization is shown in Fig. 4.5 for all samples. The usual ferromagnetic (ferrimagnetic) to paramagnetic transition appears at different temperature depending on the preparation method. The corresponding Curie temperatures, T_c, are 225 K, 300 K and 310 K for SR, SG (900°C) and SG (700°C) samples, respectively.

The cation distribution deviation in nano size samples from that expected of the bulk counterpart can lead to magnetization enhancement/reduction. Size reduction can lead to a reduction in the magnetic transition temperature due to finite size effect if the size is smaller than the correlation length, $<d> \leq \zeta$. In addition, lattice effects can also reduce T_c: whatever be the case, in general the size reduction decreases T_c [92]. In our case the transition temperature value of the sol gel sample is found to be greater than that of the sample prepared by solid state reaction (bulk) which is just the opposite. Chinnasamy et al. [92] found a similar effect for the $NiFe_2O_4$ spinel system prepared by ball milling. First an increase in T_C value was observed with a decrease in particle size but finally it decreased. These authors argued that the increase in the value of T_C for the initial stages of milling is due to the predominance of a change in cation distribution over the finite size effect on magnetic transition temperature. So we will examine later the cation distribution by Mössbauer spectroscopy to understand the reason for the increase of the transition temperature in our case.

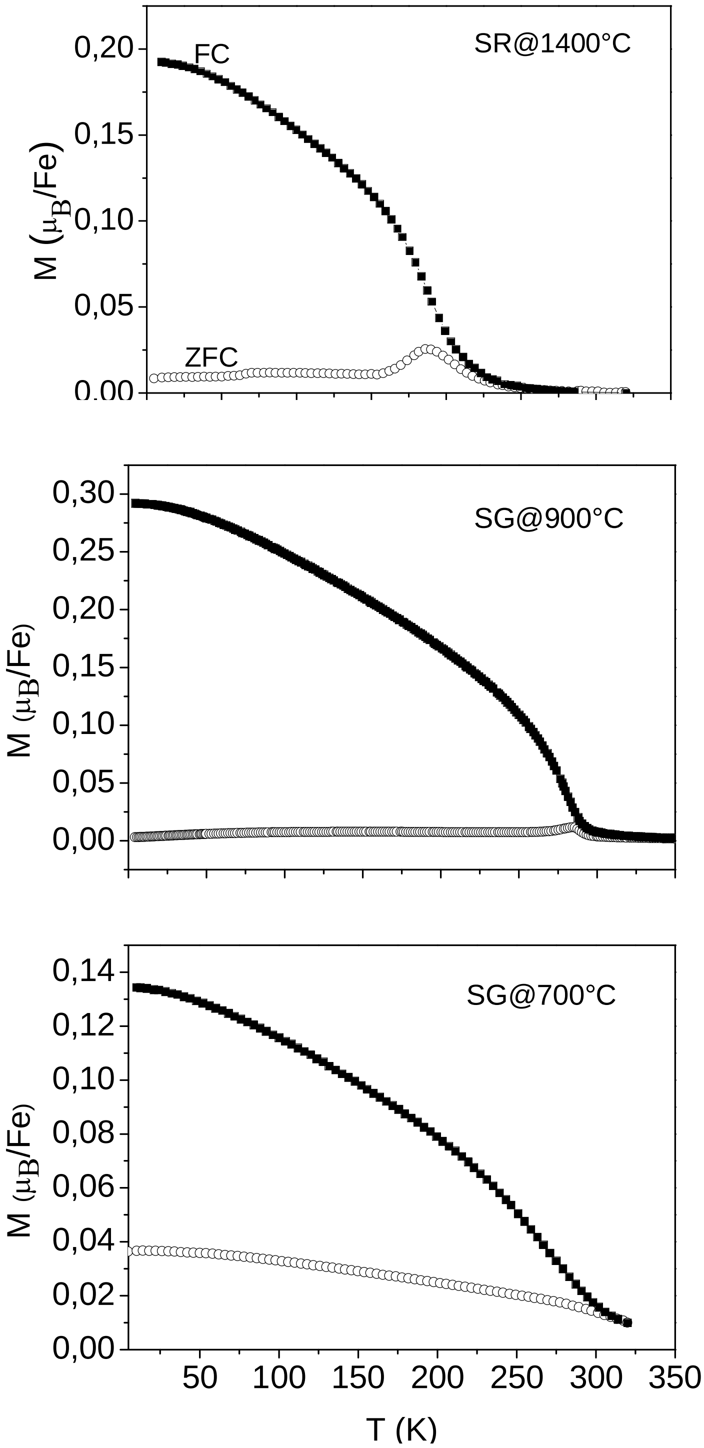

Figure 4.5: Field cooled (FC) and zero field cooled (ZFC) magnetization curves of polycrystalline GFO (SR and SG) samples, measured under applied magnetic field 100 Oe.

Isothermal magnetization as a function of the applied magnetic field at T = 10 K, for all samples, is depicted in Fig. 4.6. The magnetization does not saturate even at the highest applied magnetic field. Parameters such as saturation magnetization (M_s; was derived by linear extrapolation of 1/H to zero), and coercivity (H_c) were determined from the hysteresis graphs. The saturation magnetization increases from 0.77 μ_B/Fe (SR) to 1.32 μ_B/Fe (SG@700°C). While the coercivity decreases from 6435 Oe (SR) to 4035 Oe (SG@900°C) then increases again to 6771 Oe (SG@700°C). We understand the increase of the coercivity with decreasing size until a certain limit as being due to the enhanced role of the surface and its strong anisotropy, as opposed to the weaker bulk anisotropy [93]. The saturation magnetization, M_s, for the GFO (SG) is found to be larger than (SR), which can be attributed to surface spin canting.

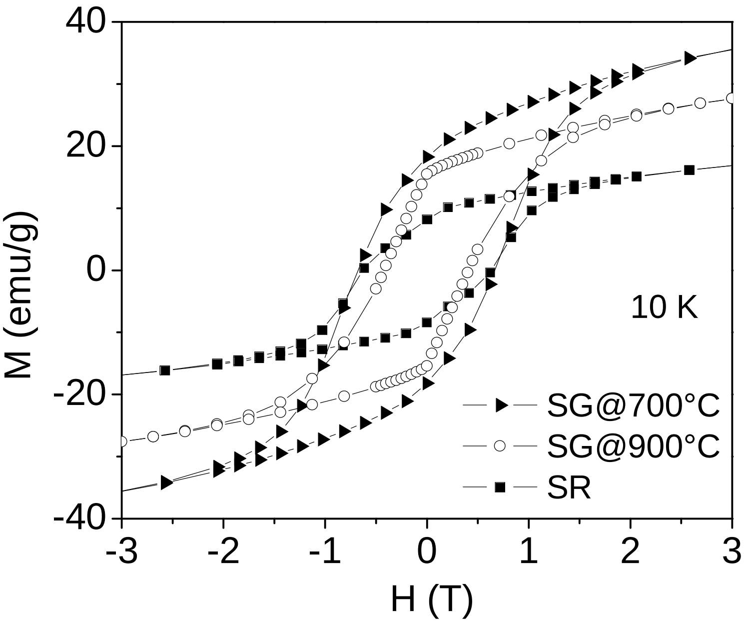

Figure 4.6: Hysteresis loops measured at 10 K for GFO prepared by solid state (SR) and sol-gel (SG@900°C and SG@700°C) methods.

4.3 Dielectric measurements

Fig. 7.7 shows the results of the dielectic constant (ε') and dielectric loss (tan δ) for GFO samples prepared by SR, SG@900°C and SG@700°C. At lower temperature ε' and tan δ are found almost constant only after certain temperature ε' and tan δ increase with temperature. At low frequencies such as 10 kHz, the dielectric constant is higher than that at 100 kHz. This behavior is due to the fact that at low frequency the dipols are able to follow the applied field whereas at high frequency the orientation and space charge polarization does not contribute. Sun et al. [74], claimed the existence of an anomaly of the permittivity near the magnetic transition point T_c for their SR sample, as indication for magentoelectric coupling in GFO. Our results do not show any anomaly at or near T_c for all samples.

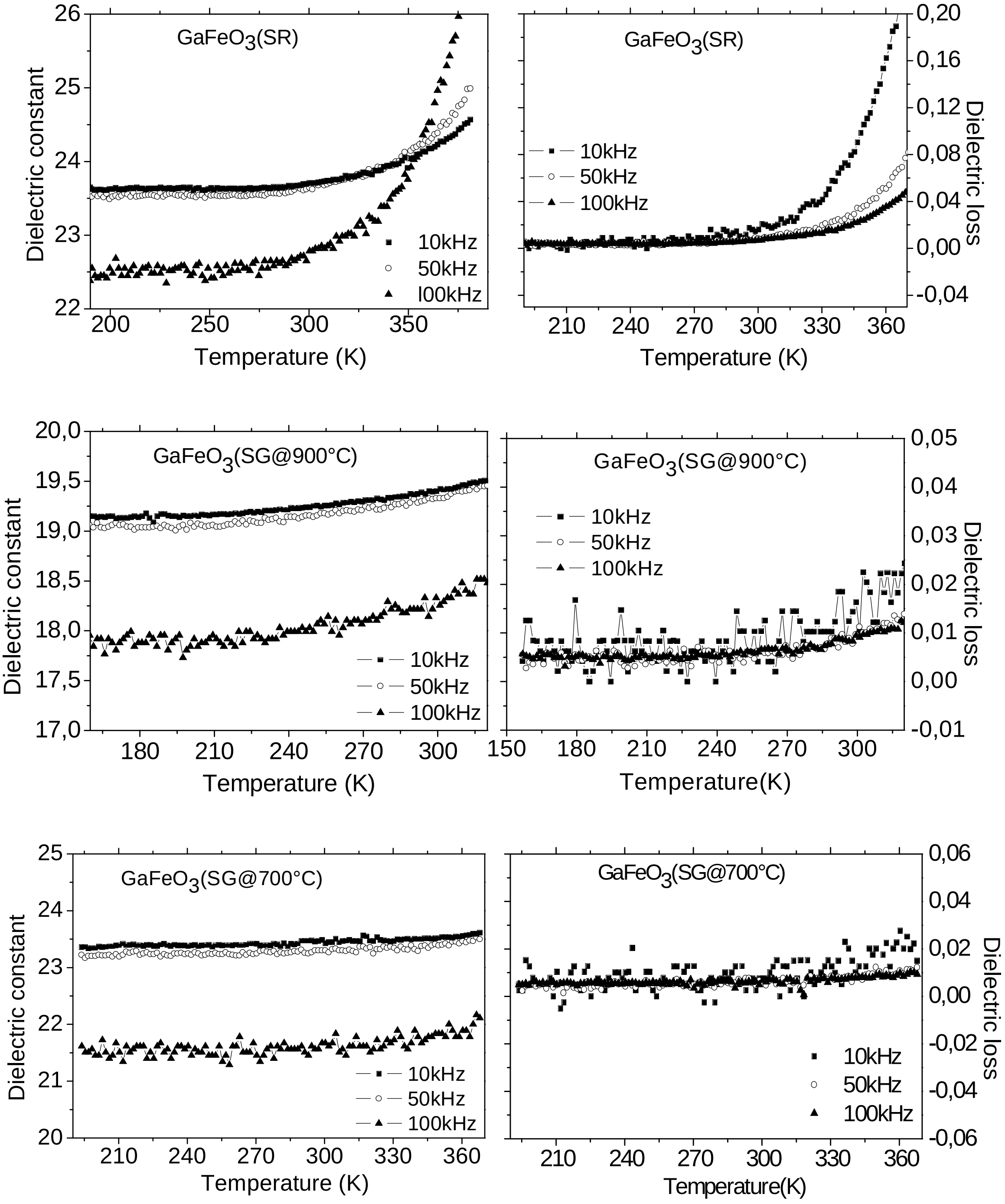

Figure 4.7: Permittivity (ε) and dielectric loss (tan δ) as a function of temperature at 1, 10, 50 and 100 kHz for GFO prepared by solid state reaction (SR) and sol gel (SG@700°C and SG@900°C) methods.

4.4 Neutron diffraction and Mössbauer spectroscopy

In order to explain the increase in T_c as the method of preparation changes, two samples will be used in this comparison: one sample prepared by solid state reaction (SR) and the other prepared by sol gel method and annealed at 900°C (SG).

4.4.1 Crystal structure

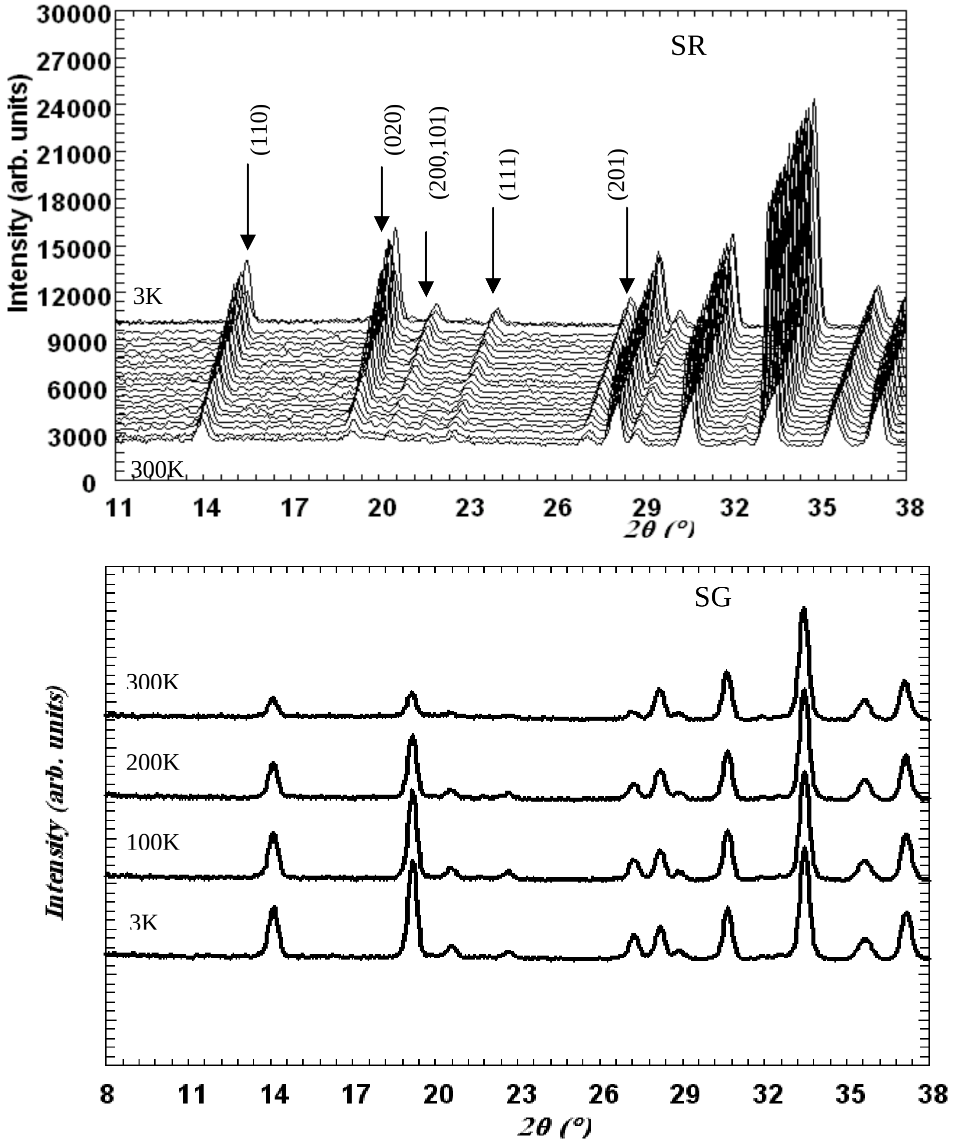

Figure 4.8: NPD collected at various temperatures to investigate magnetic scattering for GFO (SR and SG) samples in the temperature ranges of 3-300 K.

The refinement of the atomic structure was started with the P c 2_1 n structure of GFO as given in [17]. From the neutron diffraction data, symmetry does not change in the temperature range between 3 and 300 K (Fig. 4.8).

4.4.2 Temperature variation of the structural parameters

The temperature variation of the lattice parameters and the unit cell volume as deduced from the refinement of the NPD patterns (Fig. 4.14) are represented in Fig. 4.10. All lattice parameters and volume exhibit a regular thermal expansion, indicating no abnormal structural changes with decreasing temperature. A slight increase in the cell volume with decreasing annealing temperature is stated. As found for the isostructural phases $AlFeO_3$ and ε-Fe_2O_3, which were previously reported [94, 95], the cation coordination polyhedra are two distorted and one less distorted octahedron and one tetrahedron, as represented in Fig. 4.9.

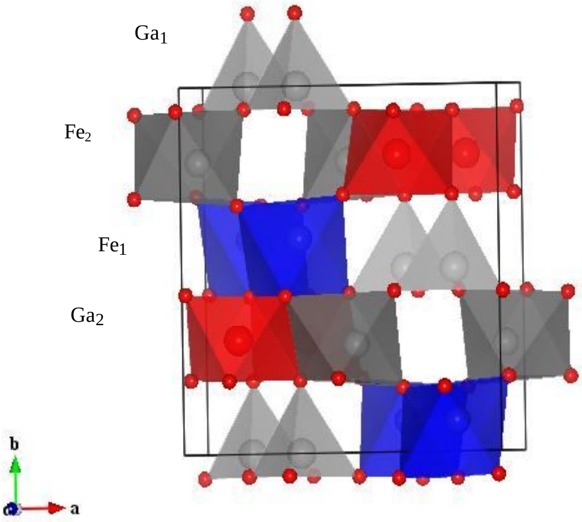

Figure 4.9: Crystal structure of GFO.

The most characteristic interatomic distances are presented in Table 4.2 at 3 and 300 K. The coordination octahedra for both Fe_1 and Fe_2 sites are highly distorted Fe–O bonds but the coordination tetrahedron around Ga_1 is quite regular. The coordination polyhedron of Ga_2 is significantly smaller in comparison with those of Fe_1 and Fe_2 sites. The Fe-O and Ga-O bond lengths are shown in Fig. 4.11 and 4.12 as function of temperature for SR samples. All bond lengths are found to be constant within the experimental error, and do not show any anomaly at or near T_c for this sample.

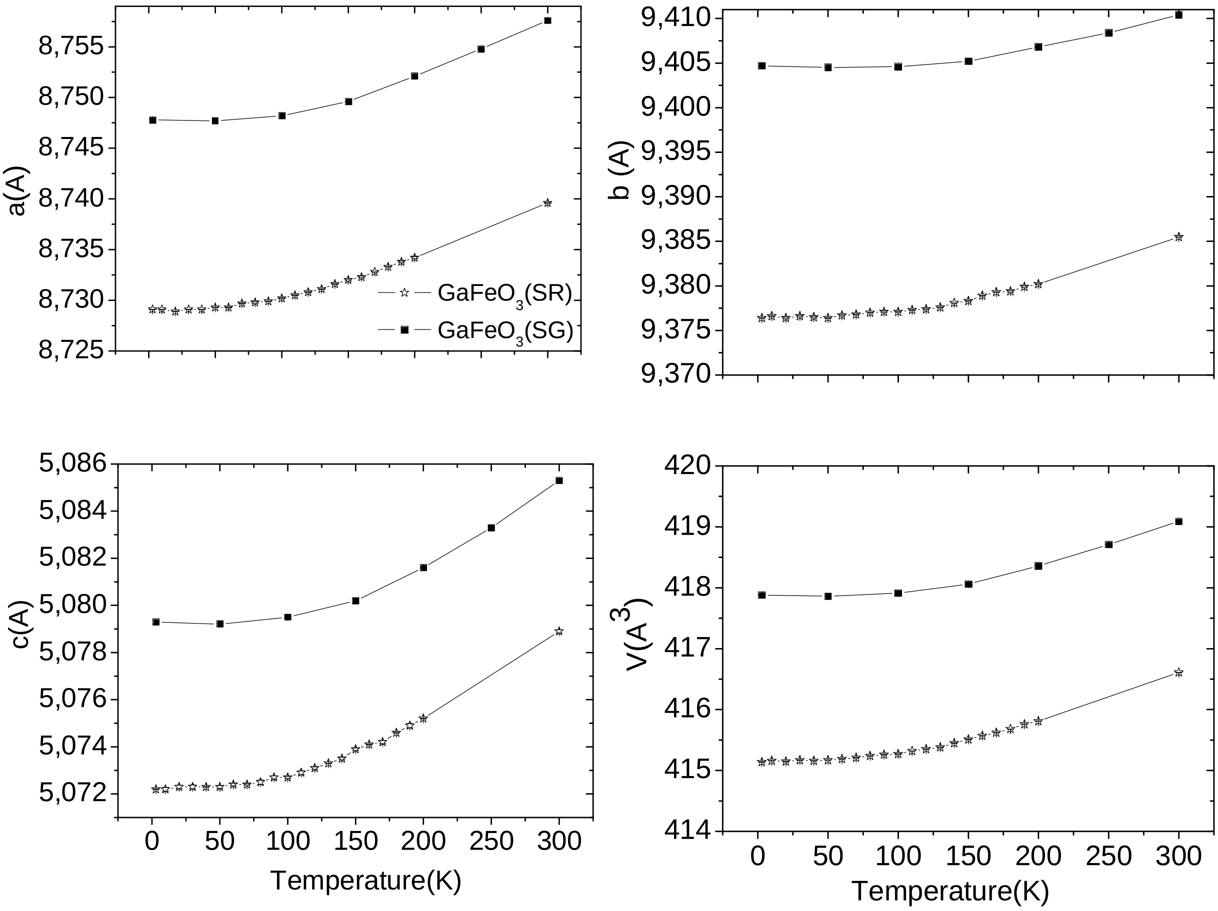

Figure 4.10: The cell parameters and volume with respect to temperature for GFO (SR and SG) as derived from the NPD refinement.

Also, the shift of Fe atoms from the centre of the octahedra (using IVTON program [96]) does not change with temperature, Fig. 4.13a. On the other hand, superexchange interaction between neighboring Fe^{3+} ions in the compounds should be affected by the Fe-O-Fe bond angles [17]. The departure of the Fe-O-Fe angle from 180° modulates the strength of the Fe-O-Fe interaction and affects the magnetic transition temperature. The superexchange interaction in the $GaFeO_3$ system is defined by the strongest bond angles Fe_1-O_1-Fe_2, Ga_1-O_4-Ga_2, Ga_2-O_1-Fe_1 and Ga_1-O_6-Fe_2 [17]. The calculated bond angle from the structural parameters listed in Table 4.2, which in general change slightly as the method of preparation change. The bond angles are almost independent of temperature as shown in Fig. 4.13b for the SR sample. The average value of the largest bond angle Fe_1–O–Fe_2 at all temperatures is 167.4° which is larger than the one obtained for a single crystal; 166° [17].

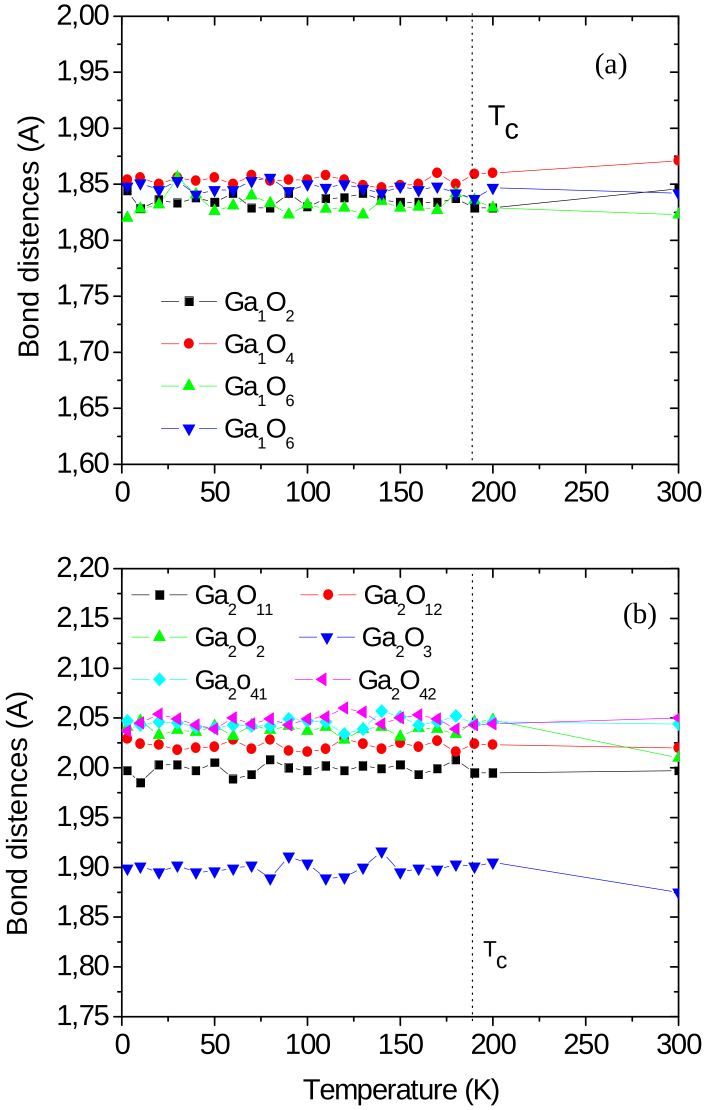

Figure 4.11: Temperature dependence of bond distances around Ga_1 and Ga_2 of GFO (SR) as function of temperature.

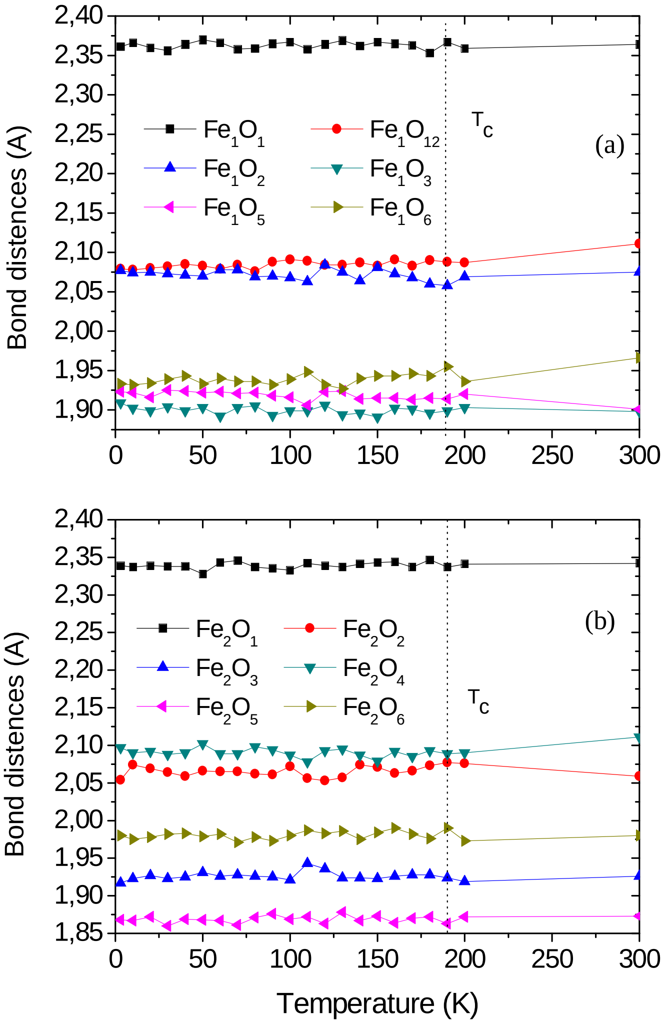

Figure 4.12: Temperature dependence of bond distances around Fe$_1$ and Fe$_2$ of GFO (SR) as a function of temperature.

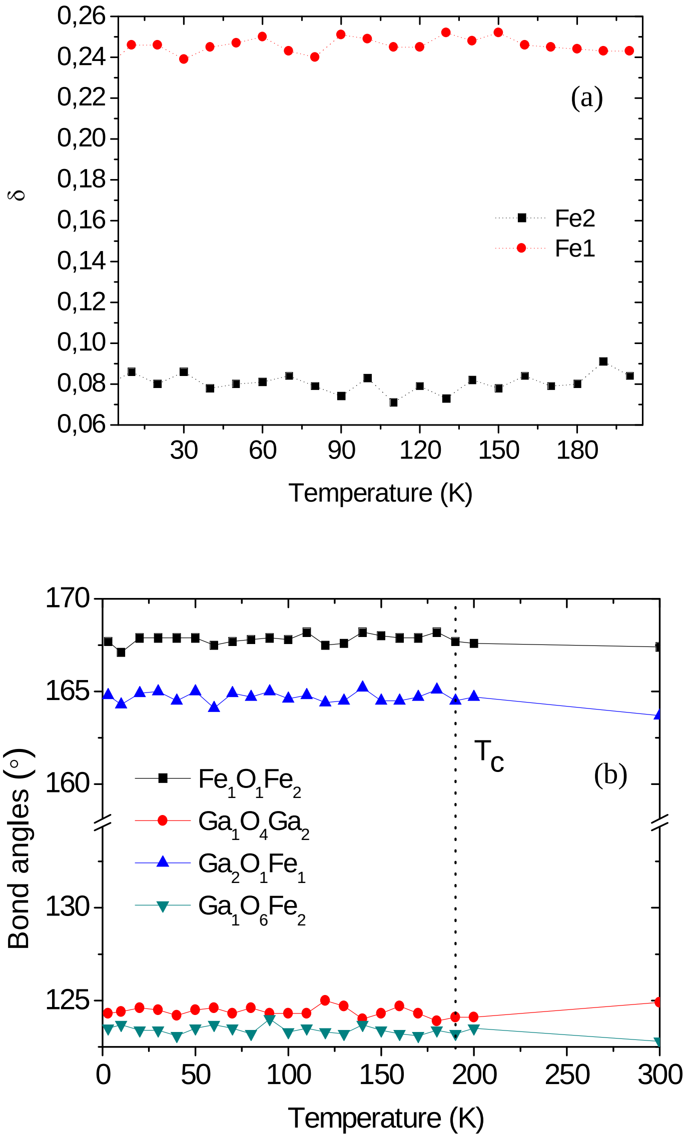

Figure 4.13: Temperature dependence of (a) Fe_1 and Fe_2 displacement from the center of the octahedron and (b) bond angle M-O-M, M=Fe or Ga of GFO (SR) as a function of temperature.

Table 4.2: Polyhedral bond (Ga, Fe-O) distances and angles for GFO (SR) and GFO (SG) samples as obtained from Rietveld refinements of neutron powder diffraction data at different temperature in Å. Numbers in parentheses are estimated statistical errors referring to the last significant digit.

	GFO(SR)		GFO(SG)	
	3K	300K	3K	300K
Bond length (Å)				
Ga_1-O_2	1.845(2)	1.841(1)	1.817(1)	1.832(3)
Ga_1-O_4	1.852(3)	1.877(2)	1.876(1)	1.874(2)
Ga_1-O_6	1.823(1)	1.821(5)	1.833(3)	1.837(1)
Ga_1-O_6	1.854(5)	1.846(2)	1.860(1)	1.842(2)
Ga_2-O_1	1.991(1)	2.010(1)	1.993(1)	2.001(6)
Ga_2-O_1	2.020(2)	2.022(3)	2.010(1)	2.010(2)
Ga_2-O_2	2.044(3)	2.013(2)	2.022(2)	2.022(1)
Ga_2-O_3	1.891(2)	1.871(1)	1.891(3)	1.901(3)
Ga_2-O_4	2.054(5)	2.055(4)	2.052(1)	2.053(1)
Ga_2-O_4	2.042(1)	2.053(2)	2.064(4)	2.054(2)
Fe_1-O_1	2.364(3)	2.362(2)	2.343(3)	2.351(1)
Fe_1-O_1	2.081(2)	2.114(4)	2.103(3)	2.108(7)
Fe_1-O_2	2.077(1)	2.082(2)	2.092(2)	2.018(2)
Fe_1-O_3	1.911(1)	1.900(1)	1.907(4)	1.910(1)
Fe_1-O_5	1.925(4)	1.901(1)	1.915(1)	1.912(1)
Fe_1-O_5	1.932(1)	1.975(3)	1.995(2)	1.995(6)
Fe_2-O_1	2.341(5)	2.342(4)	2.363(5)	2.362(5)
Fe_2-O_2	2.057(2)	2.054(5)	2.110(1)	2.112(1)
Fe_2-O_3	1.916(5)	1.935(1)	1.946(6)	1.942(1)
Fe_2-O_4	2.090 (3)	2.117(1)	2.050(1)	2.062(2)
Fe_2-O_5	1.870(2)	1.871(1)	1.821(1)	1.821(7)
Fe_2-O_6	1.983(1)	1.982(2)	1.974(4)	1.973(5)
Bond angle (°)				
Fe_1-O_1-Fe_2		167.4(4)		168.8(2)
Ga_1-O_4-Ga_2		124.9(4)		123.9(4)
Ga_2-O_1-Fe_1		163.7(4)		165.5(3)
Ga_1-O_6-Fe_2		122.8(5)		124.8 (4)

4.4.3 Determination of site occupancies

The interpretation of the magnetic structure and other properties require prior determination of cation occupancies. Since Fe and Ga atomic numbers are close to each other their X-ray scattering factors are similar and therefore a precise determination of the site occupancies is hindered. Neutron diffraction offers a better chance for correct determination of occupancies.

4.4.3.1 Neutron powder diffraction

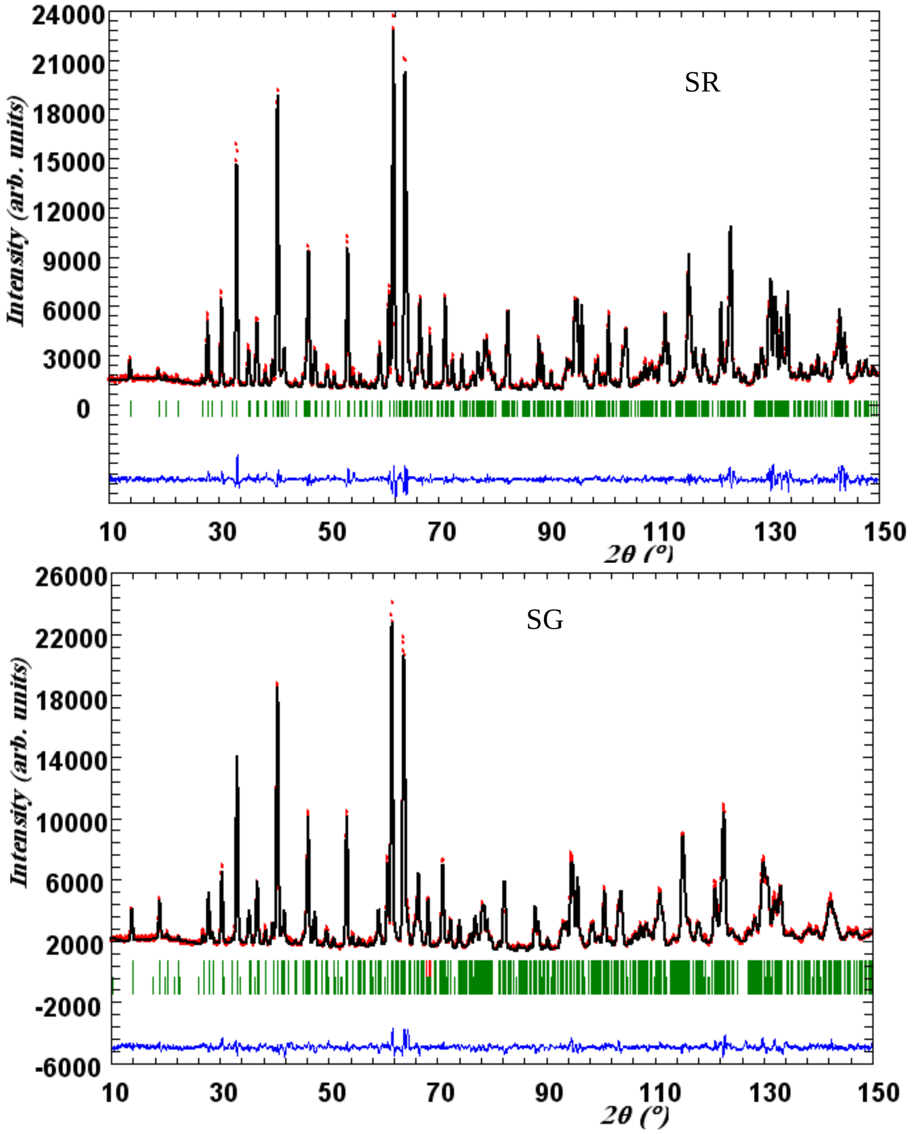

Figure 4.14: The profile fitting resulting from Rietveld refinement for GFO NPD patterns at 300 K; (a) SR and (b) SG samples. Tick bars stand for (from top to bottom) nuclear and magnetic contributions. At the bottom in each figure, the difference plot, $I_{obs}-I_{calc}$, is shown.

In order to determine the site occupancies, Fe atoms were introduced at Fe_1 and Fe_2 positions and Ga atoms were introduced at Ga_1 and Ga_2 positions, and the occupancy factors were refined, constrained to full occupancy, notably improving the quality of the fit. Then, the possibility of partial occupancy of Ga_1 and Ga_2 positions by some Fe cations and *vice versa* was also checked and this also led to a drop of the discrepancy factors. The good agreement between experiment and calculated NPD patterns is illustrated in Fig. 4.14. Table 4.3 presents the crystallographic parameters at 300 K, occupancies of Ga/Fe cations and the corresponding discrepancy factors for both samples obtained from the refinement. The occupancies of Fe ions in different cation sites show reduction of Fe occupancy in Ga_1 and Fe_1 sites and increase of Fe occupancy in Ga_2 and Fe_2 sites as the annealing temperature decrease.

Table 4.3: Atomic parameters, lattice parameters, sites occupancies and reliability factors for GFO prepared by solid state reaction and sol gel methods; obtained by Rietveld analyses of NPD patterns at 300 K using Fullprof [81].

Atom		Wyckoff	GFO (SR)	GFO (SG)
Ga_1	x	4a	0.1514(6)	0.1542(1)
	z		0.1780(8)	0.1782(5)
	Biso(Å^2)		0.78(3)	0.28(8)
	Occ.(Ga/Fe)		0.8/0.2	0.96/0.04
Ga_2	x		0.1591(4)	0.1611(9)
	y		0.3105(2)	0.3102(5)
	z		0.8075(4)	0.8073(4)
	Biso(Å^2)		0.40(4)	0.24(8)
	Occ.(Ga/Fe)		0.45/0.55	0.25/0.75
Fe_1	x	4a	0.1509(5)	0.1521(9)
	y		0.5871(3)	0.5849(1)
	z		0.1858(1)	0.1847(4)
	Biso(Å^2)		0.34(1)	0.25(7)
	Occ.(Ga/Fe)		0.30/0.70	0.49/ 0.51
Fe_2	x		0.0320(9)	0.0330(9)
	y		0.7978(8)	0.7947(9)
	z		0.6780(5)	0.6808(1)
	Biso(Å^2)		0.43(5)	0.26(3)
	Occ.(Ga/Fe)		0.45/0.55	0.28/ 0.72
O_1	x	4a	0.3221(3)	0.3238(5)
	y		0.4284(4)	0.4282(8)

	z		0.9763(6)	0.9784(6)
O_2	x	4a	0.4865(6)	0.4881(5)
	y		0.4333(9)	0.4352(8)
	z		0.5131(2)	0.5052(8)
O_3	x	4a	0.9989(8)	0.9995(6)
	y		0.2059(1)	0.2028(5)
	z		0.6564(9)	0.6561(8)
O_4	x	4a	0.1608(4)	0.1571(2)
	y		0.1986(2)	0.1992(6)
	z		0.1525(5)	0.1555(5)
O_5	x	4a	0.1673(7)	0.1658(1)
	y		0.6738(9)	0.6761(8)
	z		0.8487(2)	0.8499(1)
O_6	x	4a	0.1708(1)	0.1674(9)
	y		0.9405(4)	0.9390(7)
	z		0.5181(1)	0.5199(2)
	Biso(Å^2)		0.49(1)	0.41(5)
a (Å)			8.7427(7)	8.7577(3)
b (Å)			9.3875(5)	9.4104(6)
c (Å)			5.0803(7)	5.0853(5)
Vol.(Å^3)			416.96(2)	419.10(5)
Reliability factors				
R_P (%)			9.10	9.42
R_{wp} (%)			10.5	9.93
R_B (%)			4.59	4.31

The use of neutron diffraction is still difficult because one needs to determine the positions of 10 non-equivalent atomic sites and four occupancies of the cation sites. Because of the necessity of fitting, it is reasonable to add information from an independent experiment. The Mössbauer spectroscopy offers such information, although the interpretation of the Mössbauer spectra of GFO is not easy. The components of Mössbauer spectra are not clearly resolved either at high or at low temperatures [15, 21 ,70, 73, 71, 97]. Thus, one does not know which of the absorption lines belong to which component (doublets at high or sextets at low temperatures). The Mössbauer spectra measured at low temperatures and at high external magnetic fields show splitting of the components [21] and three components can be resolved [100, 73]. Recently Mössbauer measurements at room temperature on a single crystal were reported, and a sequence of absorption lines was assigned to the three doublets [73]. Another problem is the assignment of the identified components to the crystal sites. This is a particularly difficult task because one often considers that Ga_1 and Ga_2 sites are occupied mainly by Ga [15, 17]. However, our neutron scattering measurements suggest that Ga_2 site is occupied predominantly by Fe. Also in [100] one of the Ga_2 sites has the largest Fe occupancy. Moreover, as noticed in [73] the results of the point charge calculations for different sites do not reproduce the observed quadrupole splitting. Thus, the results of the point charge calculations are not helpful for the site assignments.

4.4.3.2 Mössbauer measurements

The Mössbauer spectra were recorded in transmission geometry with a standard constant acceleration spectrometer. The source was ^{57}Co in a Cr matrix. Powdered absorber with surface density of GFO about 20 - 22 mg/cm^2 which corresponds to the effective thickness [101] t_a =3.1-3.4 were used. The spectra measured at the lowest temperatures and at highest temperatures were selected for simultaneous fitting. Transmission integral was used [101]. The width of the source, Γ_{source}, determined in calibration experiment was kept constant.

The spectra of sample prepared by solid state reaction (Fig. 4.15a) are consistent with already reported works [15, 21, 70, 71, 72, 97, 98]. Room temperature spectra are composed of two overlapped and symmetrically located doublets. There is a small absorption line located at 0.3 mm/s indicating the presence of iron in the paramagnetic state even at T = 14 K, reported also in [71] for T = 87 K. It is clear from Fig. 4.5 that in the spectra below the magnetic transition point strong temperature dependence of the line widths is observed. This behavior is typical for Ga-Fe and Al-Fe oxides [15, 71, 97].

The spectra of the sample prepared by SG method (Fig. 4.15b) exhibit larger magnetic inhomogeneities at moderate temperatures and clearly higher transition temperature than that of SR samples.

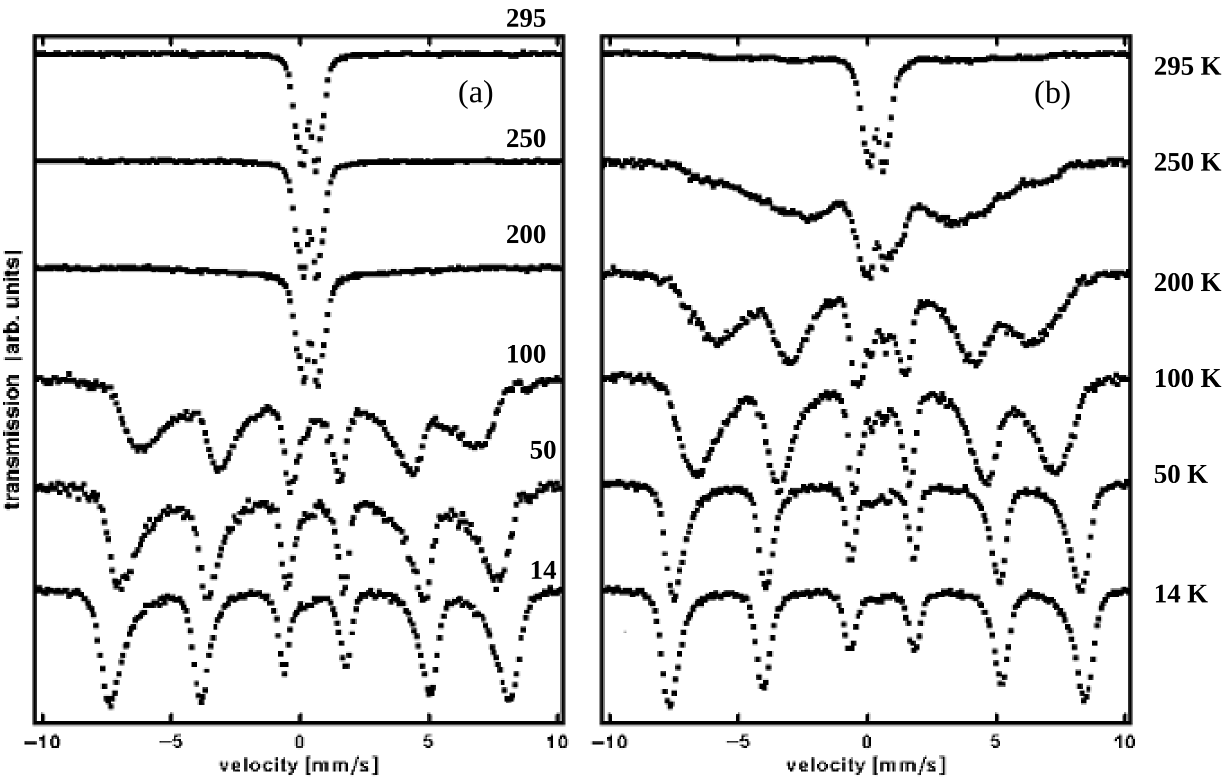

Figure 4.15: Mössbauer spectra of the GFO compounds at various temperatures; (a) spectra of the sample prepared by solid state reaction, (b) spectra of the sample prepared by sol-gel method.

Three main subspectra plus impurity phase component with common relative areas corrected by temperature dependence of recoilless f-factor in Debye approximation were used. The impurity phase component is seen in the T =14 K spectrum (Fig. 4.16 b, d) at velocity about 0.5 mm/s. Centre shift of the components at different temperatures were constrained by second order Doppler shift within the Debye approximation. The Debye temperature for all components was the same and calculated as free parameter. The isomer shift of each component was another free parameter. At high temperatures separation of the lines in the doublets are proportional to the S_0 invariant, that is proportional to the quadrupole splitting. At low temperatures, the line positions are determined by the values of hyperfine field and S_1 invariant. The invariants were constrained by ineq. (3.9) and equation (3.11). Temperature dependence of EFG was neglected.

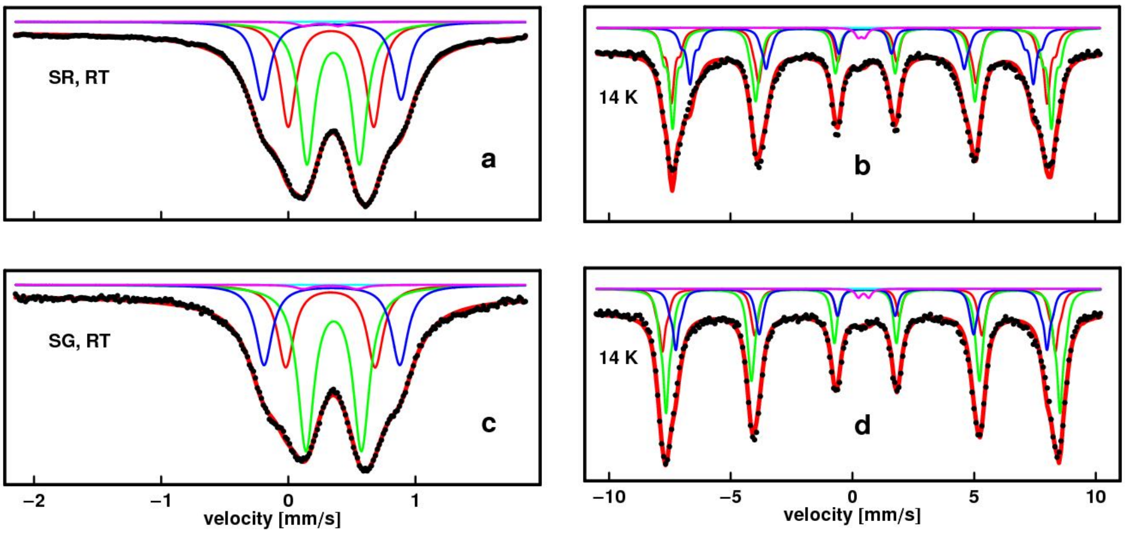

Figure 4.16: Results of simultaneous fits of 3 components and impurity phase for (a), (b) SR and (c), (d) SG sample

In the initial fits the shape of both, magnetic and paramagnetic, components were assumed to be Lorentzian. It follows from Fig. 4.16 that the absorption lines measured at high temperature are rather narrow while at low temperatures substantial broadening is observed, indicating presence of certain distribution of hyperfine magnetic field. Thus Gaussian distribution of hyperfine magnetic field was assumed to account for the broadening. The common width of the Gaussian distribution of HMF was a free parameter. All spectra shown in Fig. 4.16 a, b were fitted simultaneously and the different components are shown by lines of different colours. Although simultaneous fits to the spectra measured at different temperatures reduces ambiguity substantially, we were able to find fits of similar quality in which doublets at high temperature spectra were located as in Fig. 14.6a, RT. However, in these cases the sequence of absorption lines forming doublets was different from that reported in [73]. Parameters of the components are listed in Table 4.4.

Table 4.4: Parameters obtained by simultaneous fit of high and low temperature Mössbauer spectra of the SR sample. Upper (lower) part of the table corresponds to symmetric (asymmetric) arrangement of absorption lines of the main components. $S_0/6^{1/2}$ is equal to separation of the lines in the doublet when *HMF B* is zero. Δ is standard deviation of the Gaussian distribution of the *HMF*. Γ_{LT} and Γ_{HT} are FWHMs of Lorentzian lines of the nuclear cross section for gamma ray absorption. Data for isomer shift (*IS*) in columns 5, 6 are constrained by second order Doppler shift in Debye approximation with Debye temperature T_D. Isomer shift is given relative to alpha-Fe at room temperature.

SR, 4 comp., common parameters: Δ = 1.05T, T_D = 389 K, Γ_{LT} = 0.26 mm/s, Γ_{HT}=0.135 mm/s, Γ_{source}=0.13 mm/s							
row no.		Are	$S_0/6^{1/2}$ [mm/s]	B [T]	S_1 [mm/s]	IS [mm/s]	
	col. no.	1	2	3	4	5	6
	T[K]			14	14	14	RT
1	red	0.34	0.65	49.2	-0.41	0.47	0.34
2	green	0.38	0.39	47.1	-0.44	0.48	0.35
3	blue	0.18	1.02	43.9	-0.29	0.46	0.34
4	l. blue	0.08	1.19	40.1	-0.12	0.48	0.35
5	magenta	0.01	0.28	0.0	0.0	0.37	0.25

SR, 3comp, common parameters: Δ = 1.57 T, T_D = 399 K, Γ_{LT} =0.292 mm/s, Γ_{HT} =0.146 mm/s, Γ_{source} =0.13mm/s							
row no.		Are	$S_0/6^{1/2}$ [mm/s]	B [T]	S_1 [mm/s]	IS [mm/s]	
	col. no.	1	2	3	4	5	6
	T[K]			14	14	14	RT
1	red	0.32	0.67	47.8	-0.66	0.46	0.34
2	green	0.43	0.41	48.3	-0.26	0.48	0.35
3	blue	0.24	1.09	43.4	-0.27	0.47	0.34
4	magenta	0.01	0.29	0. 0	0.0	0.38	0.26

Since the results of neutron data analysis indicates the possibility of location of iron at Ga_1 sites, we also performed simultaneous fits with four components plus impurity phase component. The results of the fit are shown in Fig. 4.17 and in Table 4.4. A similar procedure was applied to the SG samples. However, 3 component (+impurity phase) fits resulted in unrealistic occupancy of the site exhibiting small quadrupole splitting. Thus, the probabilities were constrained to physically acceptable values, ($\Sigma p_i=1$, $p_i<1/2$). These constraints need not to be used in the case of four component fits. Results for SG sample are shown Table 4.5.

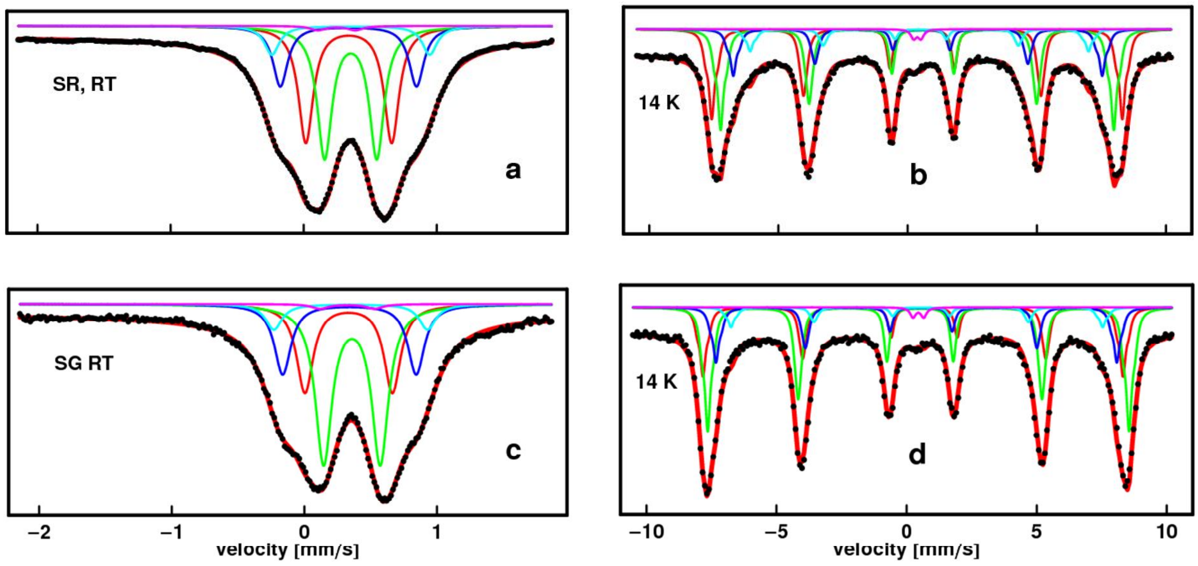

Figure 4.17: Results of simultaneous fits of 4 components and impurity phase for (a), (b) SR and (c), (d) SG sample.

Table 4.5: Parameters obtained by simultaneous fit of high and low temperature Mössbauer spectra of the SG sample. Further description as in Table 4.4.

	SG, 4 comp., common parameters: Δ = 0.98T, T_D = 382 K, Γ_{LT} = 0.26 mm/s, Γ_{HT} = 0.15 mm/s, Γ_{source} = 0.13mm/s						
row no.		Are	$S_0/6^{1/2}$ [mm/s]	B [T]	S_1 [mm/s]	IS [mm/s]	
	col. no.	1	2	3	4	5	6
	T [K]			14	14	14	RT
1	red	0.25	0.66	49.9	-0.87	0.46	0.33
2	green	0.45	0.43	50.1	-0.13	0.49	0.36
3	blue	0.20	1.01	47.5	-0.37	0.47	0.34
4	l. blue	0.07	1.16	43.9	-0.34	0.48	0.35
5	magenta	0.01	0.41	0.0	0.0	0.45	0.32

	SG, 3 comp, common parameters: Δ =1.06 T, T_D = 382 K, Γ_{LT} =0.28 mm/s, Γ_{HT} =0.16 mm/s, Γ_{source} =0.13 mm/s						
row no.		Are	$S_0/6^{1/2}$ [mm/s]	B [T]	S_1 [mm/s]	IS [mm/s]	
	col. no.	1	2	3	4	5	6
	T [K]			14	14	14	RT
1	red	0.25	0.70	50.0	-0.78	0.46	0.33
2	green	0.49	0.44	50.1	-0.20	0.49	0.36
3	blue	0.24	1.07	47.0	-0.42	0.47	0.34
4	magenta	0.01	0.42	0.0	0.0	0.46	0.33

Assignment of crystallographic sites to spectra components

The procedure of simultaneous fitting used in this thesis is applied to obtain the hyperfine parameters and the respective probabilities that would fit to the low and the high temperature spectra. Probabilities, proportional to the Are, given in col. 1 of Tables 4.4 and 4.5, allow estimation of the i-th site occupancy, equal to $2Are_i / \sum_{k=1}^{4} Are_k$. However, from this information site assignment is not straightforward. To our best knowledge hyperfine structure calculations for GFO are not available. Having determined the distribution of Fe, see column 1 in Tables 4.4 and 4.5, one can check how different assignments of the occupancies in Ga_1, Ga_2, Fe_1 and Fe_2 sites fit to the neutron experiment. Since there are four non-equivalent sites and in the simplest case a three component fit is used, one can assume, in agreement with the published data [17, 73] that Ga_1 site is fully occupied by Ga. The three components (abbreviated in Tables 4.4, 4.5 as red, green, blue) must concern the Ga_2, Fe_1 and Fe_2 sites. Every possible combination of assignment (see rows 1, 2, 3, 4 in Table 4.6) results in a different reliability factor R_{mag}, of the refinement of neutron data. The factors R_{mag} are listed in the lower part of Table 4.6. The best refinements for samples SR and SG are obtained when the green component is assigned to Ga_2, the blue one to Fe_1 and the red one to Fe_2, see column 1 of Table 4.4. However, one can note that it is easier to make such assignment in the case of the SG sample than for SR one. Nevertheless, the fact that for both samples the lowest values of R_{mag} are obtained for the same combinations makes the choice of minimal R_{mag} the most sensible one, other possible site occupancy assignments are listed in Appendix A.

Table 4.6: Results of refinement obtained by the Rietveld analysis of neutron diffraction performed at T = 3 K. Six columns correspond to permutations of Ga_1/Ga_2/Fe_1/Fe_2 sites e.g. colors in the column 1,2,...6 indicates assignment of the Mössbauer components to the crystal site. Reliability factor R_{mag} (%) of the refinement are shown in rows and the best refinements are bolded.

A	crystal site site	assignment of the Mössbauer components					
		1	2	3	4	5	6
1	Ga_1	**lb**	lb	lb	lb	lb	lb
2	Ga_2	**g**	r	b	b	r	g
3	Fe_1	**b**	b	r	g	g	r
4	Fe_2	**r**	g	g	r	b	b
	no of comp./sample	R_{mag} (%)					
5	3 comp. /SR	**6.59**	7.20	7.68	6.89	9.87	7.41
6	4 comp. /SR	**5.69**	7.44	8.14	9.14	10.2	10.5
7	3 comp./SG	**9.77**	13.8	13.4	12.4	12.8	10.3
8	4 comp. SG	**6.42**	11.0	13.4	6.68	7.2	9.01

Fe atoms may also be located at Ga_1 sites, therefore four components are expected to be present in the Mössbauer spectra. The results of fits (Fig. 4.17) show indeed non zero Ga_1 occupation by Fe. However, because the four and the three component fits are of similar quality, the difference of fitted values were used to estimate uncertainties of the site occupancies. For the SR sample we have Fe/Ga occupancies: Ga_1 9/91, Ga_2 83/17, Fe_1 42/58, Fe_2 66/34 (the uncertainty of Fe occupancy is 9, 5, 6, and 3 per cent, respectively), and for the SG sample Ga_1 8/92, Ga_2 96/4, Fe_1 45/55, Fe_2 52/48 (the uncertainty of Fe occupancy is 9, 2, 4, and 2 per cent, respectively).

4.4.4 Magnetic structure

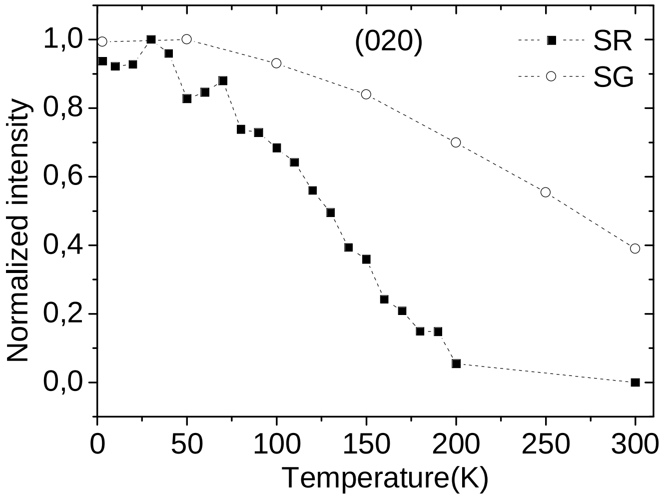

Figure 4.18: Temperature dependencies of normalized intensity of the strongest magnetic peak (020) in the neutron diffraction patterns for GFO prepared by solid state and sol gel methods.

The thermal evolution of the NPD diagrams is shown in Fig. 4.8 for GFO (SR) and (SG) samples. As the temperature decreases, the intensities of a number of peaks (110), (020), (200/101), (111) and (201) at Bragg positions 13.92, 18.99, 20.27, 22.41 and 27.02 enhance substantially as a result of significant magnetic contributions. The (020) reflection is the strongest of all observed magnetic Bragg peaks at low temperature and this is consistent with the observation of Arima et al. [17] in single crystal GFO. The thermal evolution of the integrated intensity for (020) Bragg reflections are shown in Fig. 4.18. In the thermal evolution of the intensity, no changes are observed that could suggest a variation in the magnetic arrangement. The identical positions of magnetic and nuclear peaks indicate an equivalent magnetic and chemical unit cell.

Table 4.7: Atomic parameters, lattice parameters, magnetic moment components (m_x, m_y, m_z) reliability factors for GFO prepared by solid state reaction (SR) and sol gel (SG) methods obtained by the Rietveld analyses of NPD patterns at 3 K.

Atom		GFO (SR)			GFO (SG)	
	x	y	z	x	y	z
Ga_1	0.1524(7)	0	0.1787(8)	0.1570(3)	0	0.1748(8)
Ga_2	0.1608(8)	0.3086(5)	0.8088(3)	0.1602(6)	0.3117(4)	0.8065(1)
Fe_1	0.1522(1)	0.5844(9)	0.1888(8)	0.1500(3)	0.5860(1)	0.1877(2)
Fe_2	0.0326(2)	0.7940(8)	0.6784(4)	0.0320(5)	0.7967(4)	0.6787(6)
O_1	0.3231(3)	0.4262(5)	0.9739(1)	0.3209(5)	0.4298(5)	0.9774(1)
O_2	0.4893(6)	0.4317(7)	0.5161(1)	0.4896(2)	0.4353(2)	0.5052(8)
O_3	0.9991(6)	0.2025(7)	0.6529(4)	1.0002(6)	0.2064(7)	0.6568(2)
O_4	0.1599(5)	0.1965(6)	0.1552(5)	0.1583(1)	0.2012(6)	0.1497(7)
O_5	0.1675(1)	0.6723(9)	0.8486(1)	0.1661(5)	0.6801(6)	0.8461(4)
O_6	0.1693(8)	0.9406(2)	0.5174(5)	0.1658(1)	0.9373(3)	0.5218(9)
	a [Å]	b [Å]	c [Å]	a [Å]	b [Å]	c [Å]
	8.7324(5)	9.3797(6)	5.0742(5)	8.7482(7)	9.4050(9)	5.0795(8)
	m_x (μ_B)	m_y (μ_B)	m_z (μ_B)	m_x (μ_B)	m_y (μ_B)	m_z (μ_B)
	0.52(9)	1.18(2)	3.00(3)	0.52(7)	0.02(8)	4.37(5)
			Reliability factors			
R_P		6.87			9.61	
R_{wp}		6.87			10.5	
R_B		2.44			4.19	
R_{mag}		4.79			8.71	

Therefore the three-dimensional long range ordered magnetic structure can be described by a propagation vector $\mathbf{K} = \mathbf{0}$, in good agreement with the neutron diffraction data given by Arima et al. from single crystals [17]. The possible magnetic structures compatible with the orthorhombic crystallographic structure, $P\ c\ 2_1\ n$ space group, and associated with the propagation vector, $\mathbf{K} = \mathbf{0}$ at low temperature, were determined by representational analysis, following the formalism of Bertaut [99] as implemented in the program BasiReps [81], more details in Appendix B. The representation Γ is constructed with the Fourier components m^k corresponding to the Fe atoms of the Wyckoff position 4a. The decomposition of the representation Γ in terms of the irreducible representations Γ_k is for the 4a site,

$$\mathbf{\Gamma}(4a) = 3\mathbf{\Gamma_1} + 3\mathbf{\Gamma_2} + 3\mathbf{\Gamma_3} + 3\mathbf{\Gamma_4}.$$

The different basis vectors, which are associated with each irreducible representation were calculated with the program BasiReps [81] using the projection operator technique. Table B.5, Appendix B, gives the four possible magnetic structures, consistent with the $P\ c\ 2_1\ n$ symmetry and the resulting magnetic space groups, as determined from the ‘‘magnetic space group tables’’ [102]. According to the refinements of the 3 K data, Fig. 4.19, the magnetic structure is given by the irreducible representation Γ_1 with basis functions: [A_x, C_y, G_z], while all other models clearly failed to fit the experimental data. The symbols A (+--+), C(++--) and G(+-+-) correspond to Bertaut’s notation [154]. Using the + and – sequence of Γ_1, the refinements yield a magnetic structure with Fe^{3+} magnetic moments ordered mainly along the c-axis with a small component along a and b. A view of the magnetic structure is displayed in Fig. 4.20. It can be described as a collinear magnetic structure. Within the a-c plane the magnetic moment vector is not perfectly aligned along the crystallographic c-axis but tilted away from it. Fig. 4.21 shows the thermal variation of the ordered magnetic moment of Fe.

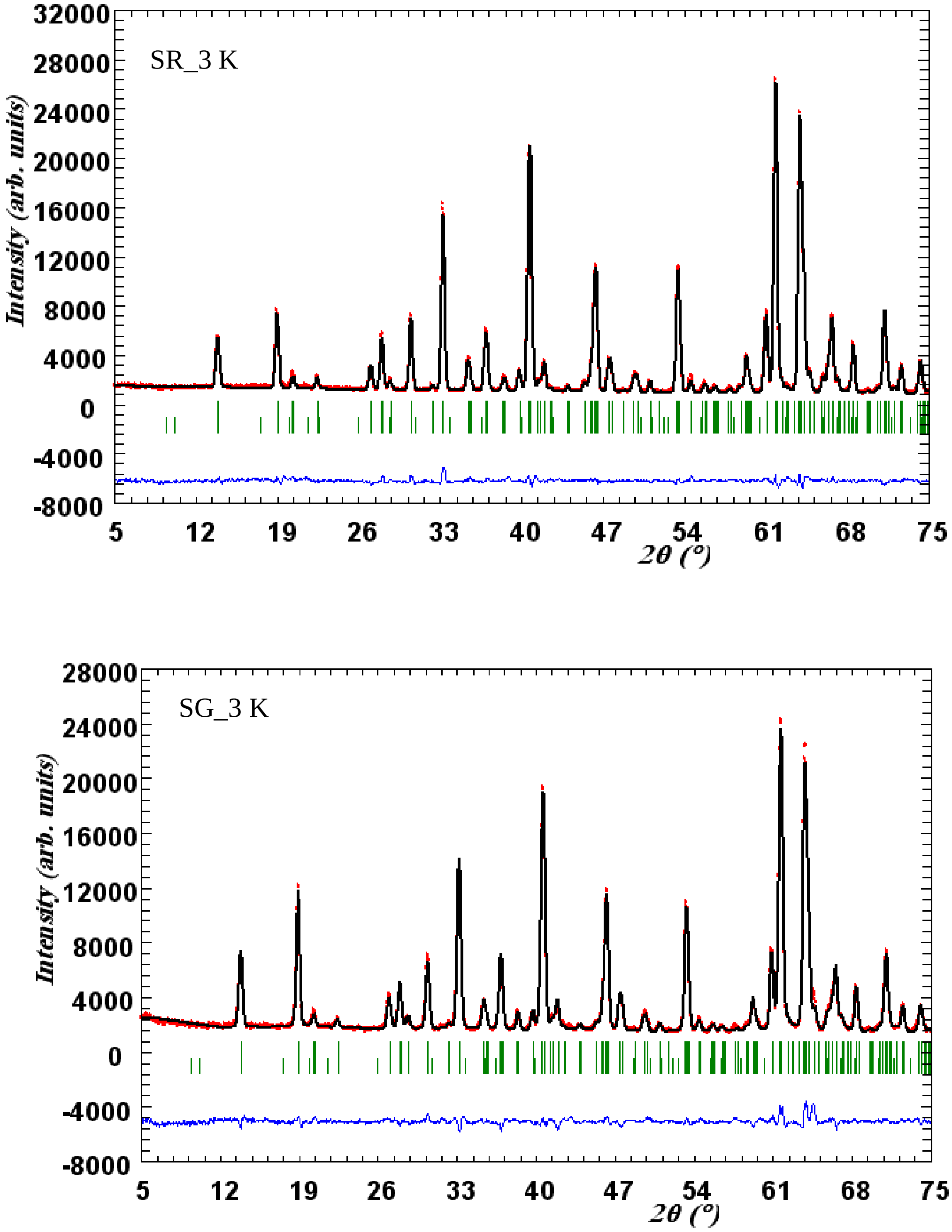

Figure 4.19: The profile fitting resulting from the Rietveld refinement for GFO neutron powder diffraction patterns at T = 3K; occupancy was taken from the Mössbauer experiment for (a) SR and (b) SG samples. Upper bars indicate nuclear while lower ones magnetic contribution. At the bottom, the residuals I_{obs}–I_{calc}, are shown.

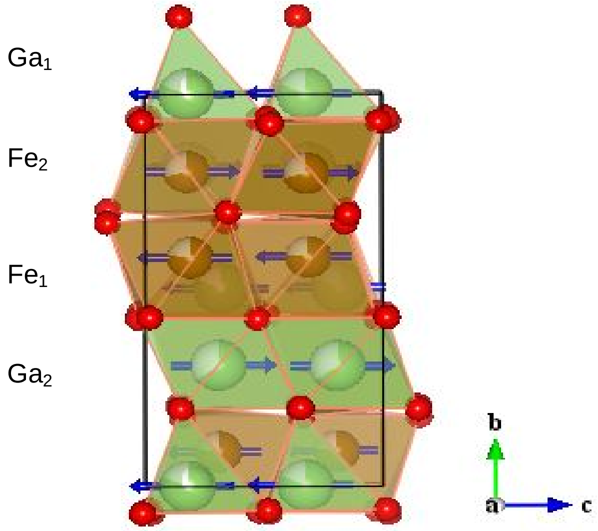

Figure 4.20: A view of the magnetic structure of GFO, arrows indicate Fe moments.

The total magnetic moment in GFO at 3 K amounts to 3.2 and 4.4 μ_B in case of SR and SG samples, respectively, which is distinctly lower than the theoretical spin only value of high spin Fe^{3+} of 5.92 μ_B . This reduction from the theoretical value may result from the chemical disorder on the cation sites, magnetic linkages between Fe^{3+} ions being randomly disrupted by non-magnetic Ga^{3+} ions. A similar situation happens in case of isostructural $AlFeO_3$ where the mean Fe^{3+} magnetic moment at T = 30 K is 3.4 μ_B, a value lower than expected [94].

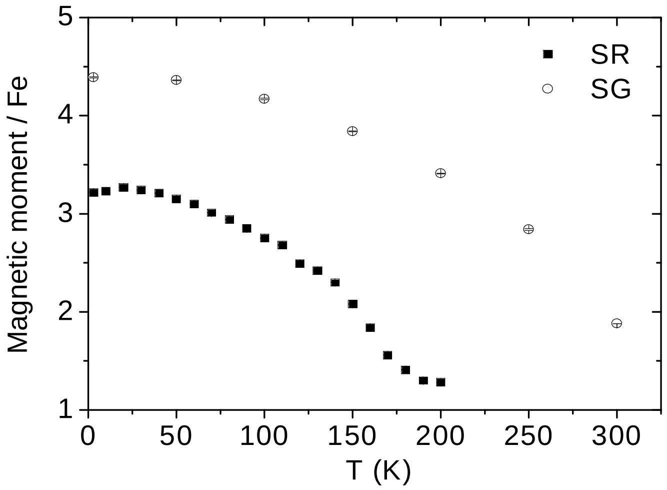

Figure 4.21: Temperature dependence of the ordered magnetic Fe moment magnitude calculated from neutron powder diffraction refinement for GFO (solid state reaction (SR) and sol gel (SG) samples).

The increase in magnetic moment value in case of SG sample as compared to the SR sample is consistent with the magnetization measurement. However, this value is in reasonable agreement with the magnetic moments of Fe found previously in magnetically ordered Fe-based perovskites [103].

4.5 Discussion

The chapter presents the results of the systematic analysis of the Mössbauer and the neutron diffraction experiments. The large number of free parameters, resulting from the nature of the system, presence of four non-equivalent cation sites in particular, was reduced by constraints resulting from the Mössbauer experiment. Simultaneous fits of the Mössbauer spectra resulted in the determination of components consistent with the recent results [73] of the experiment performed on the single crystal. In the complicated case of GFO the determination of the structure does not allow a unique identification of the components, e.g. their assignments to the crystallographic sites. Therefore, refinements of the neutron diffraction data were carried out for all possible site assignments, which resulted in clear indication of the most likely distribution of Fe among the crystallographic sites. This assignment is consistent with the one presented in [73]: the intense component with the small quadrupole splitting corresponds to Ga_2 while the intense component with the large quadrupole splitting corresponds to Fe_1 site. Although the consistency has been achieved, the obtained results indicate that Ga_2 site is occupied predominantly by Fe and not by Ga. Band structure calculations [66] indicate that the energy resulting from the Fe interchange with the Ga_2 site can be as small as 1 meV per formula unit while interchange with Ga_1 site requires energy almost two orders of magnitude larger. This explains why Ga_2-Fe disorder is high, yet does not explain why the Fe concentration in Ga_2 site is so high. Although the occupancies (see Table 4.4 and 4.5) indicate better ordering in the SG sample, it is hard to draw a conclusion that the site occupancies are mainly responsible for the differences in magnetic properties. We may speculate that the sensitivity of the macroscopic properties to the sample preparation may result in a short range ordering of the cations which cause specific local distortions of the oxygen polyhedra around the cations. Although the site occupancies are hard to control, it is rather well documented that samples prepared with a larger disorder, e.g. quenched or synthetized at higher temperatures, possess a lower transition temperature than the more ordered samples, that have been e.g. prepared at lower temperatures or annealed [15, 17]. Our result of slightly better ordering in the SG sample is consistent with this general trend. We observe also that HMFs in the SG sample are larger and hyperfine fields of different magnetic components (compare column 3 of Table 4.5 and Table 4.6) are closer to each other than HMFs in the SR sample. As discussed in [97] these differences are due to supertransferred hyperfine field resulting from Fe-O-Fe interaction depending on the bond angle. It is worth noting that in the disordered compound the estimation of the supertransferred field based on the bond angles determined from the diffraction experiment may be misleading because local bond angles can differ from those ones that were derived from the average positions of the atoms. A small amount of paramagnetic phase is observed in both studied samples, SR and SG, even at the lowest measured temperatures, e.g. 14 K, similarly to [71]. This may arise e.g. from the presence of Fe^{3+} in β-Ga_2O_3

Chapter 5

Structural, magnetic and electric properties of Mn and Cr doped $GaFeO_3$

5 Introduction

Manganese is a particularly interesting element for substitution, because it easily changes its oxidation state, furthermore, the ionic radii of Fe^{3+} and Mn^{3+} are practically identical $<r_i> = 0.645$Å [104]. The number of d electrons and effective magnetic moments, however, are different for Fe^{3+} and Mn^{3+}. There are five 3d electrons and an effective magnetic moment of $\mu_{eff} = 5.9\ \mu_B$ for Fe^{3+} and four 3d electrons and effective magnetic moment of $\mu_{eff} = 4.9\ \mu_B$ for Mn^{3+}. Thus even though Fe^{3+} and Mn^{3+} have equivalent ionic radii the magnetic interaction is affected by the substitution. In the $BiFe_{1-x}Mn_xO_3$ system, a substitution of Fe by Mn does not alter the space group but enhances multiferroic properties. In $BiFeO_3$, the ferroelectric (FE) Curie temperature ($T_E = 1123$ K) [105] and antiferromagnetic ordering temperature ($T_N = 650$ K) [106] are well above room temperature. For practical applications, it is highly desirable to find multiferroics with both T_E and T_N close to room temperature. Recently, Kan et al. [107] try to understand why $(In_{1-x}M_x)MO_3$ ($M = Mn_{0.5}Fe_{0.5}$) has a significantly lower T_N (about 270 K for $x \approx 0.176$) [108] than does $BiFeO_3$ (650 K) and they expect that $(Tl_{1-x}M_x)MO_3$ ($M = Mn_{0.5}Fe_{0.5}$) and $(Ga_{1-x}M_x)MO_3$ ($M = Mn_{0.5}Fe_{0.5}$) compounds have T_E lower than that of $(In_{1-x}M_x)MO_3$. Also, GFO contains only trivalent metals in the structure like rare earth orthoferrites, making them attractive systems for investigations of isovalent substitutions.

In particular, the replacement of Fe^{3+} by Cr^{3+} and its effect on structural, magnetic and other properties have been reported [109 - 111] for rare earth orthoferrites. For example, in the lanthanum orthoferrites, partial replacement of Fe by Cr leads to a reduction in the Néel temperature from 750 K in $LaFeO_3$ to 280 K in $LaCrO_3$. Moreover, Cr doping is one of the most adopted strategies to tailor the dielectric and piezoelectric properties of ferroelectrics for practical applications. It is well known that Cr is effective in decreasing the aging effect and the dielectric loss; thus, the effect of doping of Cr^{3+} is that of a stabilizer of the piezoelectric and dielectric properties [112, 113]. In Cr doped $BiFeO_3$ [114], the dielectric constant and the magnetization increase considerably with the Cr doping level. Also, the density of ceramics can be increased using a small amount of Cr_2O_3. However, a large content of Cr_2O_3 will inhibit grain growth because of the accumulation of Cr^{3+} at the grain boundary, which results in the decrease in grain size [115, 116].

5.1 $GaFe_{1-x}Mn_xO_3$ solid solution

5.1.1 Structural studies and phase formation

X-ray measurements revealed that the maximum Mn doped amounts for the samples prepared by solid state reaction is 10%, while annealing of the samples which were prepared by the sol gel method in air give admixture of Ga_2MnO_4 and other phases but in oxygen flow the Mn substitution range increase up to x = 0.2 (annealed at 1000°C), x = 0.25 (annealed at 900°C) and x = 0.4 (annealed at 800°C and 700°C, Fig. 5.1). With higher Mn content other phases are present; the identified phases are shown in Table 5.1. For samples prepared by solid state reaction, at an annealing temperature below 1300°C other phases formed as shown in detail in Table 5.1. The monophasic structure of these series could be indexed on the basis of GFO with space group P c 2_1 n, Fig. 5.2 shows the Rietveld refinement of $GaFe_{1-x}Mn_xO_3$ (SR, x = 0.1 and SG annealed at 700°C, x = 0.4). The substitution of iron by manganese leads to a decrease in the lattice parameters a and b, while c increases. This evolution, which results in a global unit cell volume decrease, is shown in Fig. 5.3 for samples prepared by the sol gel method and annealed at 700°C.

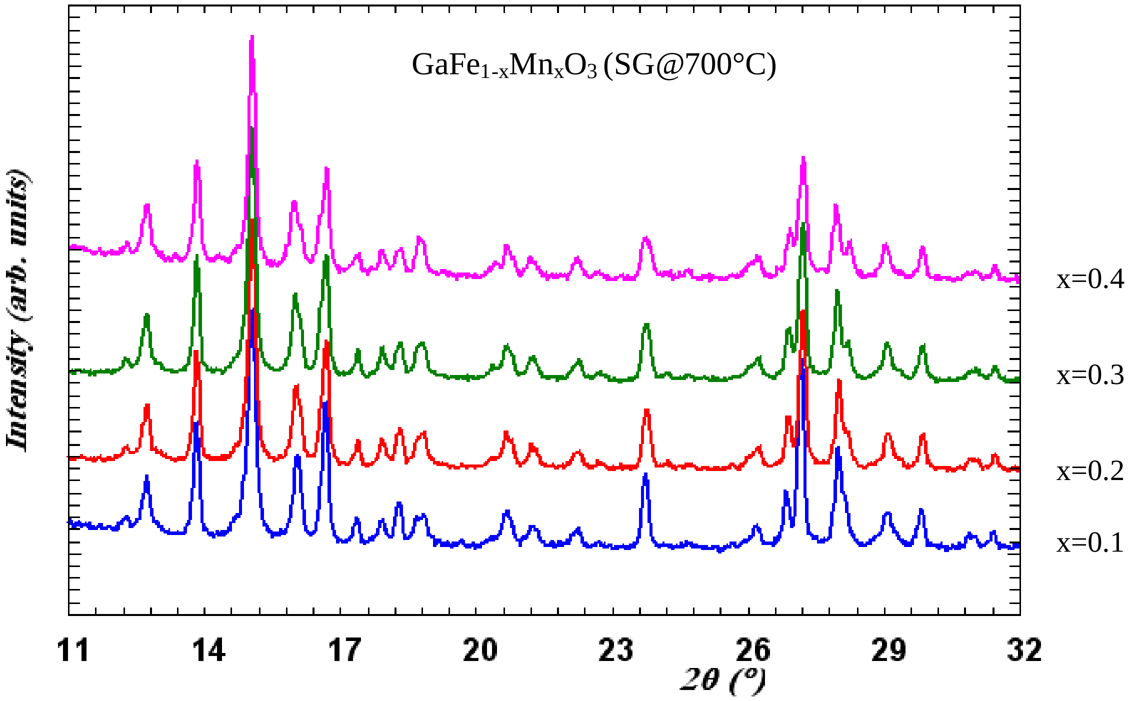

Figure 5.1: X-ray diffraction patterns of $GaFe_{1-x}Mn_xO_3$ prepared by sol gel method annealed at 700°C.

Table 5.1: Phase analysis for $GaFe_{1-x}Mn_xO_3$ samples prepared by solid state and sol gel methods; O:orthorhombic GFO (sp.gr.,$Pc2_1n$), G1: monoclinic Ga_2O_3 (sp.gr. C 1 2/m 1), F: rhombohedral Fe_2O_3 [Hematite] (sp.gr. R -3 c), M: cubic Mn_2O_3 [Bixbyite C] (sp.gr. I a 3), C:cubic Ga_2MnO_4 (sp.gr.F d -3 m),M1: tetragonal MnO_2 [Pyrolusite](sp.gr. P 42/m n m), M2: tetragonal Mn_3O_4 [Hausmannite] (sp.gr. I 41/a m d), M3: cubic Mn_2O_3 [Bixbyite C] (sp.gr. I 2_1 3), C:cubic Ga_2MnO_4 (sp.gr.F d -3 m), G2: rhombohedral Ga_2O_3 (sp.gr. R -3 c); S.G.= space group.

Solid state reaction method (SR)

Temperature	900 °C	1100 °C	1200 °C	1300 °C	1400 °C
x=0.00	G1,F	O,G1,F	O,G1	O	O
x=0.05	--	--	--	O	O
x=0.10	G1,F,M	O,G1	O,G1	O	O
x=0.15	--	--	--	O,C	O,C
x=0.20	G1,F,M	O,G1	O,G1	O,C	--
x=0.40	G1,F,M	O,C,G1	O,C,G1	O,C,G1	O,C,G1
x=0.60	G1,F,M	O,C,G1,M1	C,G1	C,G1	--
x=0.80	G1,M	C,G1,M2	C,G1	C,G1	--
x=1.00	G1,M	C,G1,M2	C,G1	C,G1	--

Sol gel method (SG)

Temperature	700 °C	800 °C	900 °C	1000°C
x=0.00	O	O	O	O
x=0.10	O	O	O	O
x=0.20	O	O	O	O
x=0.30	O	O	O,M	O,M
x=0.40	O	O	O,M	O,M
x=0.50	O,M	O,M	O,M	O,M
x=0.60	O,M	O,M,G1	O,M,G1	O,M,G1
x=0.80	G1,M	G1,M	G1,M	G1,M1,M3,C
x=1.00	C,M	G1,M	G1,M,M2,C	G1,G2,M1,M2,C

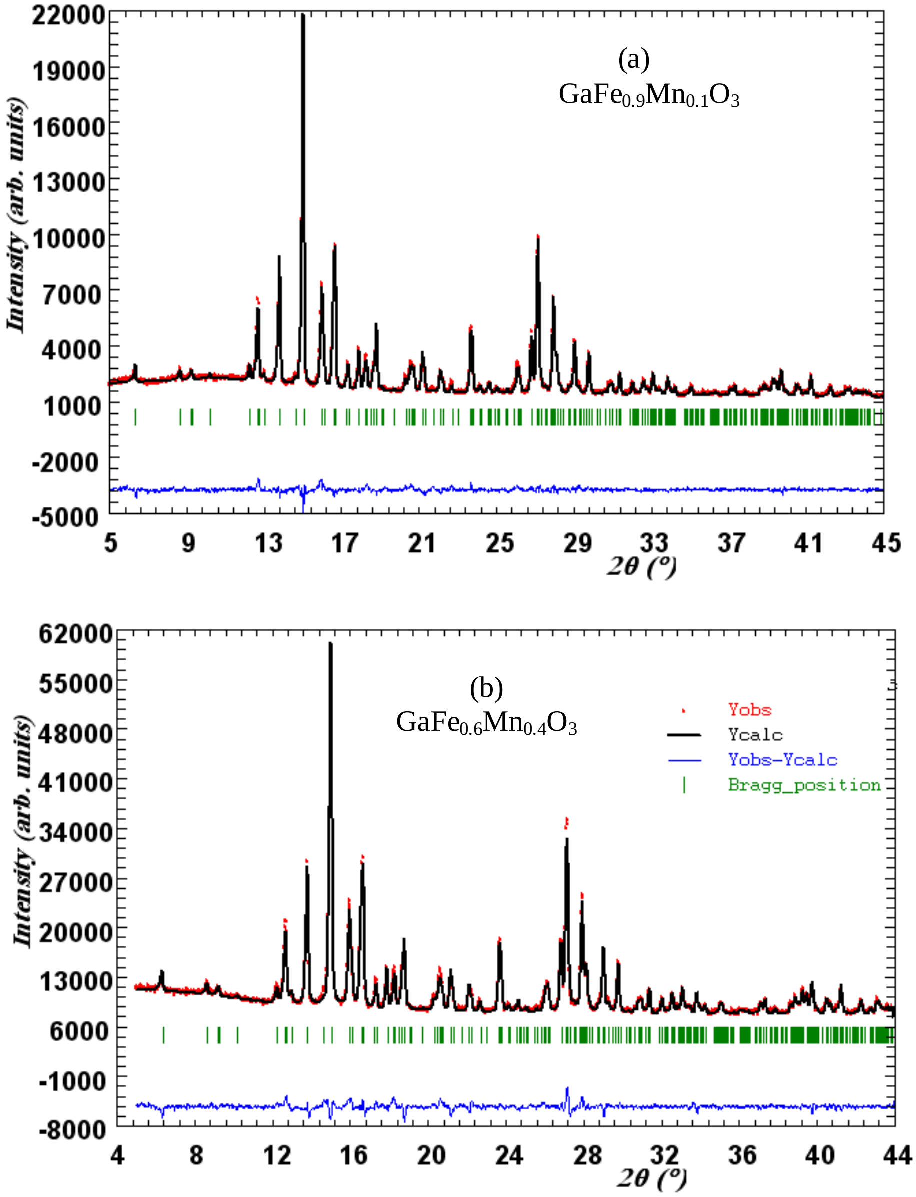

Figure 5.2: Observed (red curve) and calculated (black curve) XRD patterns of $GaFe_{0.9}Mn_{0.1}O_3$ prepared by solid state reaction at 1300°C (a) and $GaFe_{0.6}Mn_{0.4}O_3$ prepared by sol gel method at 700°C (b). The vertical bars at the bottom indicate the expected Bragg reflection positions, and the lowest curve is the difference between the observed and the calculated XRD patterns.

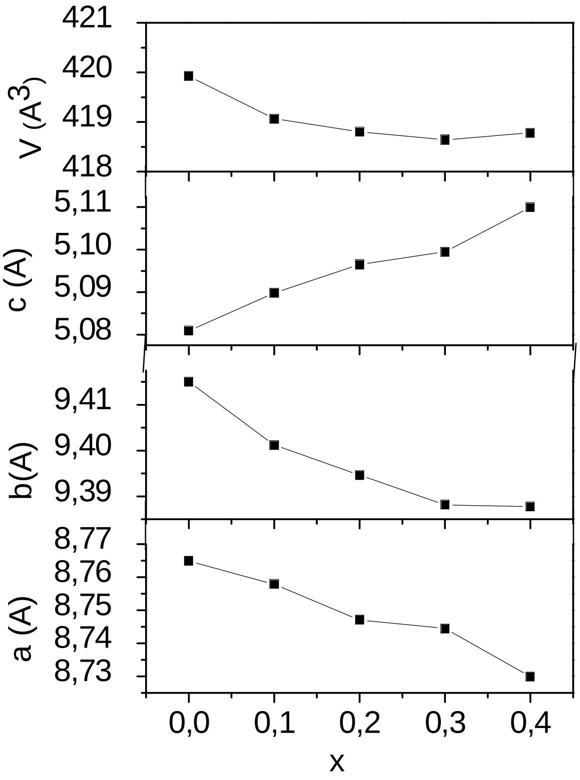

Figure 5.3: Lattice parameters and cell volume of $GaFe_{1-x}Mn_xO_3$ samples prepared by sol gel method and annealed at 700°C.

The change in the lattice constants indicates that the substitution of Mn induced a distortion in the crystal lattice as in the case of the $PrFe_{1-x}Mn_xO_3$ system [117]. The unit cell volume of the solid solution $GaFe_{1-x}Mn_xO_3$ ($0 \leq x \leq 0.4$) decreases from about V = 420 to V = 418.8 nm^3, when x is changed from 0 to 0.4 at 700°C. The refined lattice parameters together with the unit cell volume of pure solid solutions prepared by the two methods are given in Table 5.2. The decrease of the unit cell volume caused by the substitution of manganese for iron may mainly be attributed to the difference between the ionic radii of iron and manganese as in the $LaFe_{1-x}Mn_xO_3$ system [118], where the ionic radius of the trivalent iron ion for six coordination is 0.785 Å in the high spin state Fe^{III} ($t_{2g}^3 e_g^2$) and 0.69 Å in the low spin state Fe^{III} ($t_{2g}^5 e_g^0$), respectively [104].

Table 5.2: Summary of phase analysis for $GaFe_{1-x}Mn_xO_3$ samples prepared by solid state and sol-gel methods.

x	Conditions	Lattice parameters			
		a(Å)	b(Å)	c(Å)	V(Å^3)
Solid state reaction method (SR)					
0.05	SR@1300°C	8.7364(4)	9.3819(3)	5.0810(1)	416.46(2)
0.1	SR@1300°C	8.7365(6)	9.3819(4)	5.0841(6)	416.72(7)
Sol gel method (SG)					
0	SG@1000°C	8.7557(6)	9.4028(3)	5.0862(9)	418.75(2)
	SG@800 °C	8.7645(7)	9.4113(6)	5.0868(1)	419.59(4)
0.1	SG@1000°C	8.7441(8)	9.3909(2)	5.0859(6)	417.63(9)
	SG@900 °C	8.7449(2)	9.3925(7)	5.0853(4)	417.69(7)
	SG@800 °C	8.7509(7)	9.3907(3)	5.0882(5)	418.14(3)
	SG@700 °C	8.7578(4)	9.4012(3)	5.0897(8)	419.06(6)
0.2	SG@1000°C	8.7355(5)	9.3811(6)	5.0896(2)	417.09(2)
	SG@900 °C	8.7469(6)	9.3992(3)	5.0959(3)	418.96(1)
	SG@800 °C	8.7365(5)	9.3801(7)	5.0880(4)	416.96(8)
	SG@700 °C	8.7470(8)	9.3946(2)	5.0964(8)	418.80(6)
0.25	SG@900 °C	8.7429(6)	9.3936(2)	5.0988(3)	418.75(8)
0.3	SG@800 °C	8.7351(6)	9.3790(6)	5.0950(3)	417.42(5)
	SG@700 °C	8.7444(1)	9.3881(1)	5.0995(1)	418.64(2)
0.4	SG@800 °C	8.7236(1)	9.3769(5)	5.1032(3)	417.44(9)
	SG@700 °C	8.7299(2)	9.3877(5)	5.1099(6)	418.78(4)

For the six-coordinated manganese ion, the ionic radius of the trivalent manganese ion in the high spin state $Mn^{III}(t_{2g}^3 e_g^1)$ and in the low spin state $Mn^{III}(t_{2g}^4 e_g^0)$ is 0.785 and 0.72 Å, respectively. If the high spin state Fe^{3+} ion in GFO, is replaced by the high spin state Mn^{3+} ion, no change in the lattice parameters of the compound occurs because of identical ionic radii of the high spin states of Fe^{3+} ion and of the Mn^{3+} ion (0.785 Å). Therefore, we may assume also that manganese ions or most of the manganese ions in $GaFe_{1-x}Mn_xO_3$ are in the low spin state. Fig. 5.4a shows that the average bond distance split further for a manganese content greater than 0.2 and reaches its maximum value at x = 0.3. More remarkable is the evaluation of the bond distance variance for the four cation sites (Fig. 5.4b). The variance on a set of n bond distances d is defined as

$$\sigma^2 = \frac{\sum (d - \langle d \rangle)^2}{n} \qquad (5.1)$$

In unsubstituted $GaFeO_3$, Ga_1, Ga_2 and Fe_2 sites are less distorted than the Fe_1 site. This trend is continuous with more Fe sites distortion as Mn ion substitution increase and becomes very large with Mn amounts of 30 % for Fe_1 site. Also, the bond angles change with Mn content as shown in Fig. 5.7. The change in the bond lengths and angles seems to indicate that a distortion is introduced into the crystal lattice of $GaFeO_3$ by the substitution with Mn. Moreover, it is well known that Mn^{3+} with four d-electrons is a Jahn-Teller (J-T) ion and has an orbital doublet ground state on the octahedral site. The degeneracy of the doublet is lifted by a deformation of the lattice. The J-T effect of Mn may contribute to the deformation of the crystal lattice in addition to the size effect mentioned above.

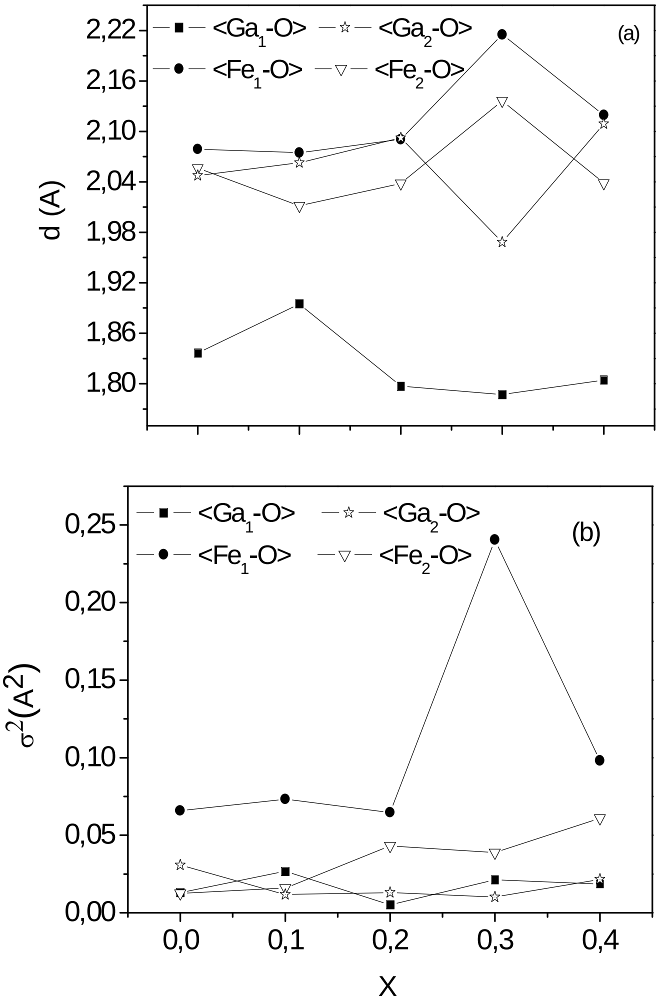

Figure 5.4: Evaluation of average (a) bond length and (b) bond length variance with manganese content (x) in $GaFe_{1-x}Mn_xO_3$ (SG@700°C).

5.1.2 Magnetic properties of $GaFe_{1-x}Mn_xO_3$

The substitution of manganese for iron in GFO (solid state reaction and sol gel samples annealed at 900°C and 700°C), revealed a significant change in the magnetic transition temperature. Temperature dependent magnetization data for sol gel samples annealed at 700°C shown in Fig. 5.5a indicate a clear PM (paramagnetic) – FIM (ferrimagnetic) transition at low temperature in an applied field of 100 Oe. For all samples annealed at different temperature, the transition and magnetization values decrease with Mn substitution and the magnetization behavior is similar. The corresponding Curie temperatures, T_c, are listed in Fig. 5.6b. The lowest magnetization transition temperature T_c= 149 K is obtained for a concentration of x = 0.4. Similar results were reported for the $RFe_{1-x}Mn_xO_3$ (R = Pr, Gd, Dy) systems [117], where T_c decreases as the Mn content increases.

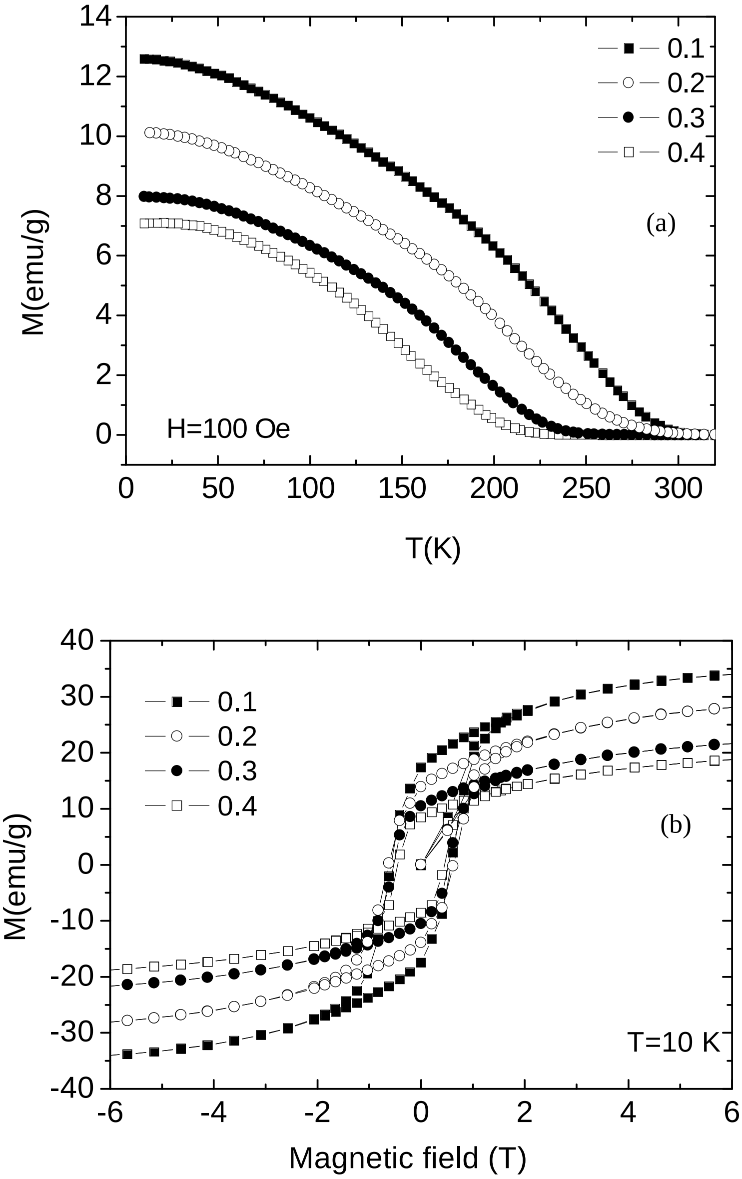

Figure 5.5: (a) Temperature dependence of DC magnetizations (b) hysteresis curve for $GaFe_{1-x}Mn_xO_3$ prepared by sol gel method and annealed at 700°C.

In order to understand the decrease in magnetic transition temperature in the $GaFe_{1-x}Mn_xO_3$ system, the various magnetic interactions in these oxides have to be taken into account.

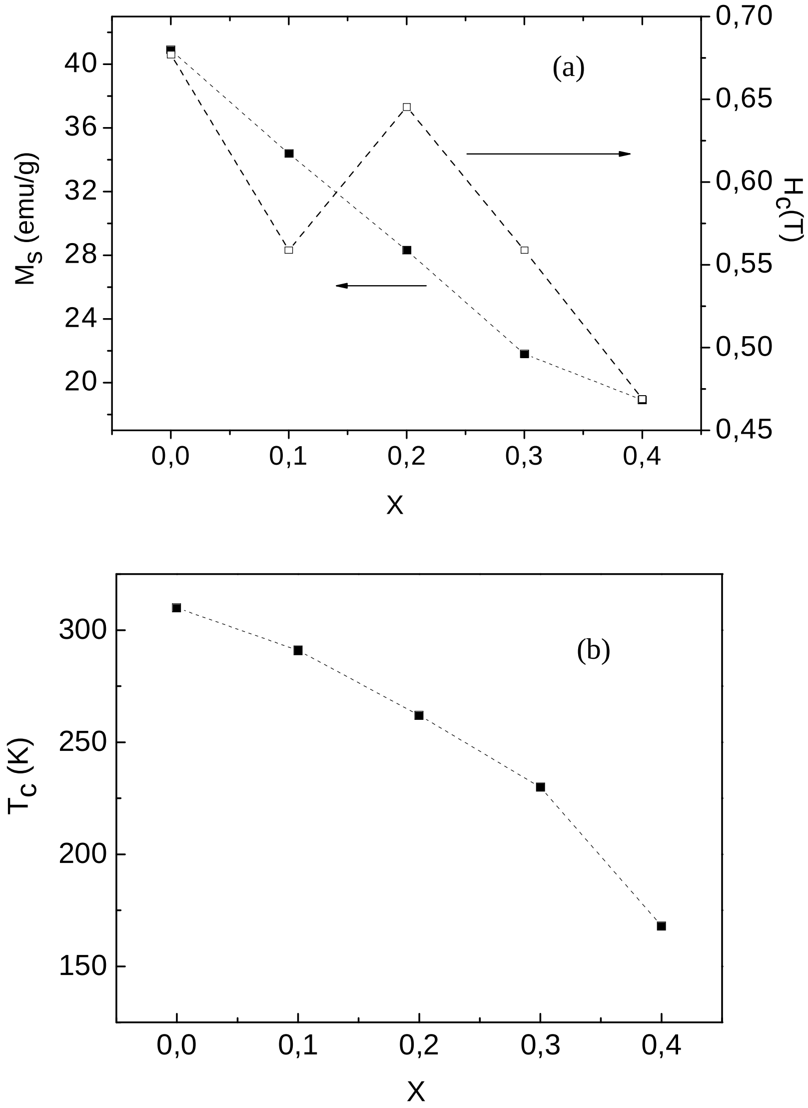

Figure 5.6: Compositional dependence of the (a) saturation magnetization (M_s) and the coercivity (H_c) and (b) transition temperature (T_c) for $GaFe_{1-x}Mn_xO_3$ prepared by sol gel method and annealed at 700°C.

The possible interactions are Fe^{3+}-O^{2-}-Fe^{3+}, Mn^{3+}-O^{2-}-Mn^{3+} and Fe^{3+}-O^{2-}-Mn^{3+} superexchanges. Of these, the Fe^{3+}-O^{2-}-Fe^{3+} interaction is strongly antiferromagnetic [119], also Mn^{3+}-O^{2-}-Mn^{3+} interaction is antiferromagnetic [120]. On the other hand, the Fe^{3+}-O^{2-}-Mn^{3+} interaction could be both ferromagnetic or antiferromagnetic. The additional Fe^{3+}-O^{2-}-Mn^{3+} interaction in the solid solutions is thought to be antiferromagnetic and weaker than that of Fe^{3+}-O^{2-}-Fe^{3+}. Hence as the Mn amount increases, the Curie temperatures, T_c, decrease. This may be due to a reduction in the Fe-Fe linkages and angles between them in the system under study.

Magnetization curves M(H) at 10 K under an external field (H) varying up to 60 kOe are shown for various Mn content for SG (annealed at 700°C) samples in Fig. 5.5b which show unsaturated values of magnetization, even at higher applied field (up to 6 kOe). Fig. 5.6a reveals the saturation magnetization (M_s) and coercivity (H_c). The coercive field and saturation magnetization values for x = 0.1 are 5710 Oe and 34.4 emu/g, whereas for x = 0.4, they are 4581 Oe and 18.9 emu/g, respectively.

Table 5.3: Parameters obtained from the hysteresis loops: saturation magnetization (M_s) and coercive field (H_c) for $GaFe_{1-x}Mn_xO_3$ samples prepared by solid state reaction at 1300°C (SR), sol gel at 900°C (SG@900°C) and sol gel at 700°C (SG@700°C) samples at 10 K together with the magnetic transition temperature T_c for all pure substituted samples.

$GaFe_{1-x}Mn_xO_3$	x	0.05	0.1	0.2	0.25	0.3	0.4
SR	T_c (K)	205	176				
	M_s(emu/g)		12.2				
	Coercivity(Oe)		1527				
SG@900°C	T_c (K)		267		226		
	M_s(emu/g)		26.4		21		
	Coercivity(Oe)		5894		6045		
SG@700°C	T_c (K)		291	262		230	201
	M_s(emu/g)		34.4	28.3		21.8	18.9
	Coercivity(Oe)		5710	6234		5279	4581

In chapter 4, we argue the enhancement in magnetization for SR and SG sample prepared at 900°C using neutron powder diffraction due to cation redistribution over four different cation sites. The parent GFO compound has a ferrimagnetic structure of the G-type, with Fe^{3+} along the c-axis where the antiparallel Fe^{3+} spins interact via the intervening oxygen ions. When Fe^{3+} ions in GFO are replaced by Mn^{3+} ions, the magnetization appears to be affected by the contribution of Mn^{3+}. Furthermore it was found by the refinement of X-ray diffraction data that the bond angle of the Fe^{3+}-O^{2-}-Fe^{3+} (or Mn^{3+}) is nearly 169° at x = 0 and increases slightly with the Mn content. Therefore, the antiferromagnetic coupling among Fe ions (or Mn ions) is enhanced by the Mn substitution; this may cause the observed decrease in magnetization, Table 5.3.

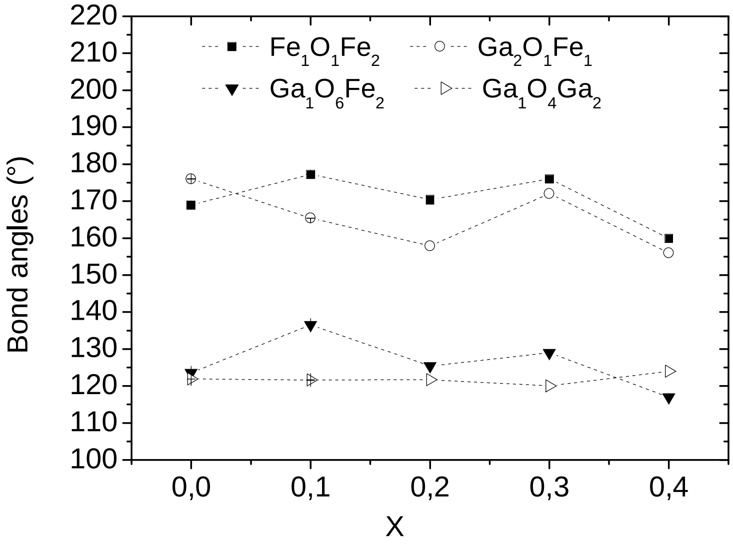

Figure 5.7: Evaluation of average bond angles with manganese content (x) in $GaFe_{1-x}Mn_xO_3$ series.

The observed variation in the coercivity of the $GaFe_{1-x}Mn_xO_3$ system is similar to that reported in the Mn substituted $CoFe_2O_4$ [121], where the coercivity of all samples almost decreases with increasing Mn content. However, for the composition with $x = 0.1$, an unexpected decrease in coercivity is observed. This is probably due to some peculiar changes in the cation distribution in the octahedral and tetrahedral sites near this composition [122].

5.1.3 Dielectric properties of $GaFe_{1-x}Mn_xO_3$ single phases

The temperature dependence of the dielectric constant at several selected measurement frequencies (10 to 100 KHz) of GFO samples prepared by solid state reaction and sol gel (annealed at 900°C) methods were reported in chapter 4. In these samples, the dielectric constant and dielectric loss do not show any anomaly at the transition temperature.

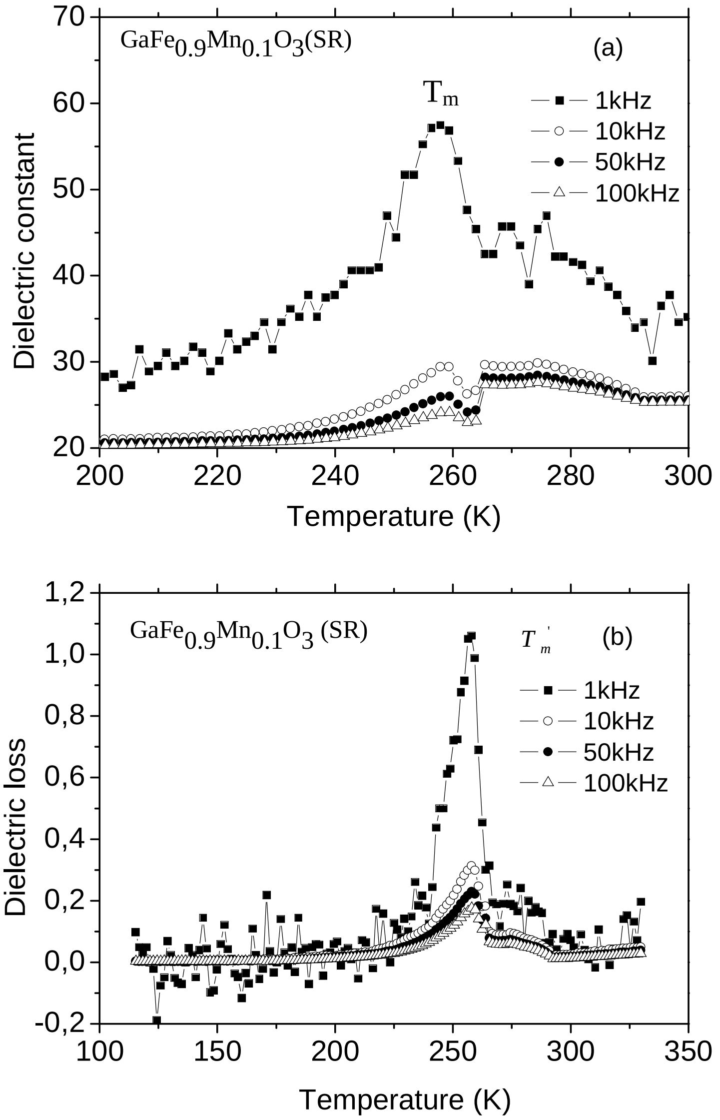

Figure 5.8: Temperature dependence of (a) dielectric constant and (b) dielectric loss for $GaFe_{0.9}Mn_{0.1}O_3$ (SR) at different frequencies.

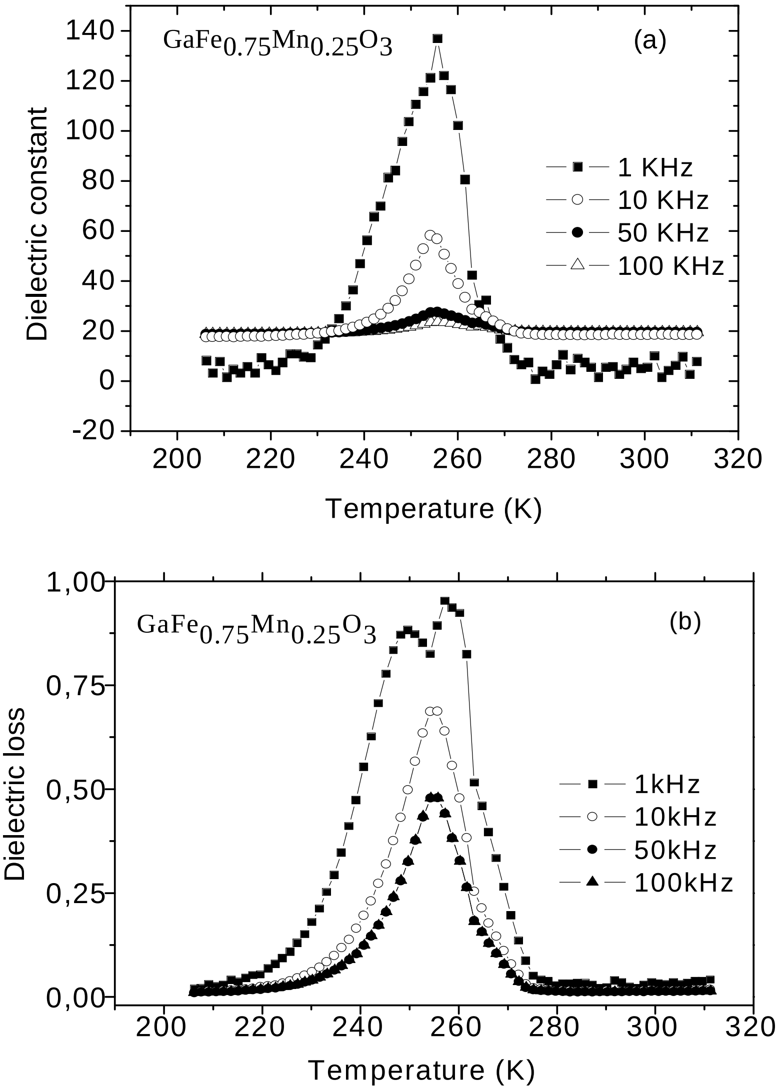

Figure 5.9: Temperature dependence of (a) dielectric constant and (b) dielectric loss for $GaFe_{0.75}Mn_{0.25}O_3$ (SG@900°C) at different frequencies.

Fig. 5.8 and 5.9 show a comparison of the temperature dependence of ε' and tanδ at different frequencies for $GaFe_{0.90}Mn_{0.1}O_3$ (SR) and $GaFe_{0.75}Mn_{0.25}O_3$ (SG@900°C). All samples have a dielectric anomaly at ~ 250 K; as frequency is increased, the dielectric constant is observed to decrease in all samples, since there is no remarkable shift of peaks being absorbed over the investigated frequency range, which is usually observed in $BaTiO_3$ ferroelectric [123]. Fig. 5.10 shows the frequency dependence of T_m and $T_m^{'}$ from both samples; T_m and $T_m^{'}$ are the temperatures at maximum dielectric constant and dielectric loss, respectively. The temperature T_m and $T_m^{'}$ are almost independent of frequency.

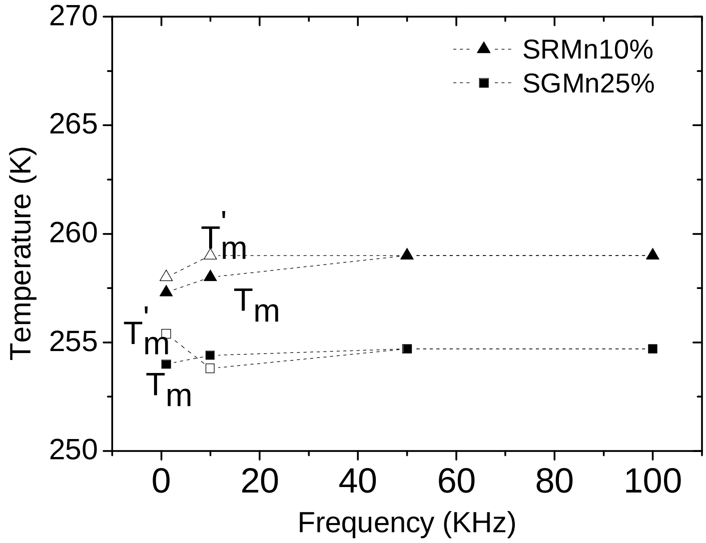

Figure 5.10: Frequency dependence of T_m and $T_m^{'}$

This behavior indicates that these samples do not behave like a ferroelectric relaxor. The phase transition occurring in ferroelectric materials could be predicted from a plot of 1/ε' vs. T. Figs. 5.11a and 5.12a show the plots of thermal variation of 1/ε' for $GaFe_{0.9}Mn_{0.1}O_3$ (SR) and $GaFe_{0.75}Mn_{0.25}O_3$ (SG@900°C) samples, respectively. A linear region is observed above 274 and 264 K for $GaFe_{0.9}Mn_{0.1}O_3$ (SR) and $GaFe_{0.75}Mn_{0.25}O_3$ (SG@900°C) samples, respectively, at 100 kHz indicating that the dielectric constant obeys the Curie–Weiss law.

$$\varepsilon' = \frac{C}{T - T_0} \quad (T>T_o) \qquad (5.2)$$

where C is the Curie–Weiss constant and T_o is the Curie–Weiss temperature.

The deviation from the Curie–Weiss law can be defined by ΔT_m as follows:

$$\Delta T_m = T_{cw} - T_m \qquad (5.3)$$

where T_{cw} denotes the temperature from which the dielectric constant starts to deviate from the Curie–Weiss law, and T_m represents the temperature at which the dielectric constant reaches the maximum. This difference is defined as the degree of thermal diffuseness. The Curie–Weiss temperature T_o is obtained by extrapolating a linear part above T_{CW} to the temperature axis.

The following equation describes the modified Curie–Weiss law [124], which takes into account the diffuseness of dielectric peaks at the fixed frequency.

$$\frac{1}{\varepsilon'}-\frac{1}{\varepsilon'_m}=\frac{(T-T_m)^\gamma}{C} \qquad (5.4)$$

where T_m represents the temperature at which the dielectric constant reaches the maximum (ε'_m) and γ reflects the degree of diffuseness. The value of γ varies between 1 and 2, indicating the normal ferroelectric transition and the ideal relaxor ferroelectric behavior, respectively. Fig. 5.11b and 5.12b show the plots of $\log(1/\varepsilon'-1/\varepsilon'_m)$ versus $\log(T-T_m)$ for different samples at 100 KHz. The mechanism of diffuse phase transition in ferroelectric materials is known to be generally associated with compositional inhomogeneities or other structural defects. The diffuseness in the dielectric property in the vicinity of the phase transition temperature of the present samples may originate from the irregular distribution of charged defects/impurities. The calculated value of γ was found to be 1.1 and 1.3 in $GaFe_{0.90}Mn_{0.10}O_3$ (SR) and $GaFe_{0.75}Mn_{0.25}O_3$ (SG@900°C), respectively, which confirms the diffuse phase transition in the compounds.

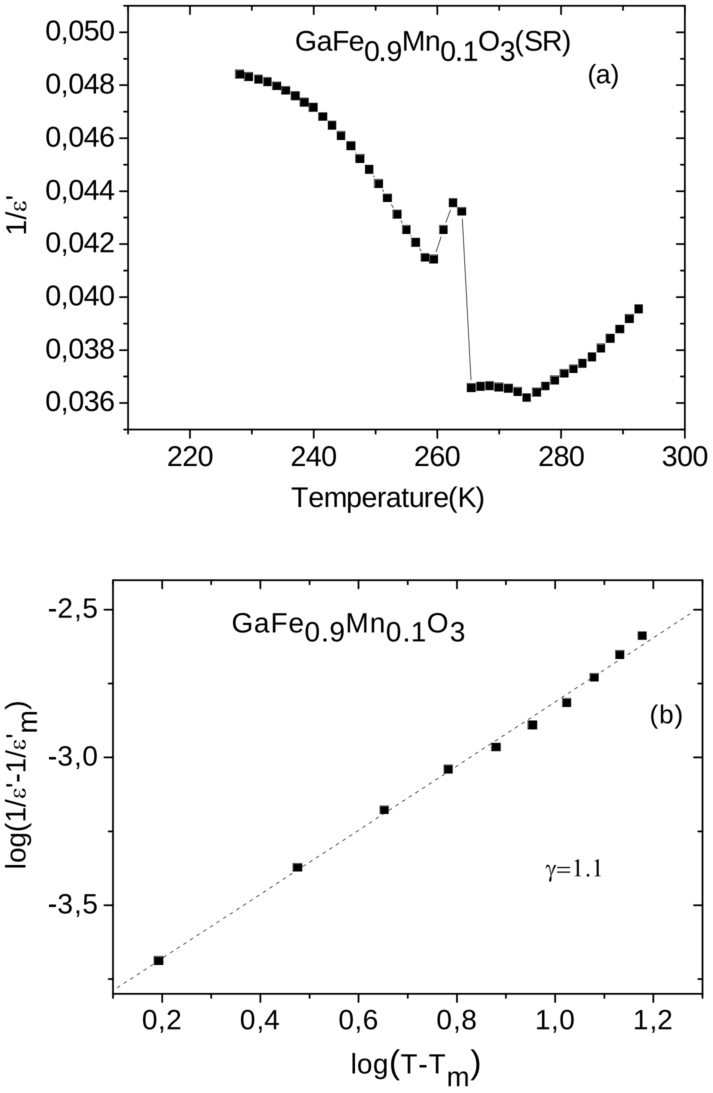

Figure 5.11: Plots of (a) 1/ ε' vs temperature and (b) log (1/ ε'−1/ε'$_m$) vs log (T−T$_m$) for $GaFe_{0.9}Mn_{0.1}O_3$ (SR) at 100 KHz.

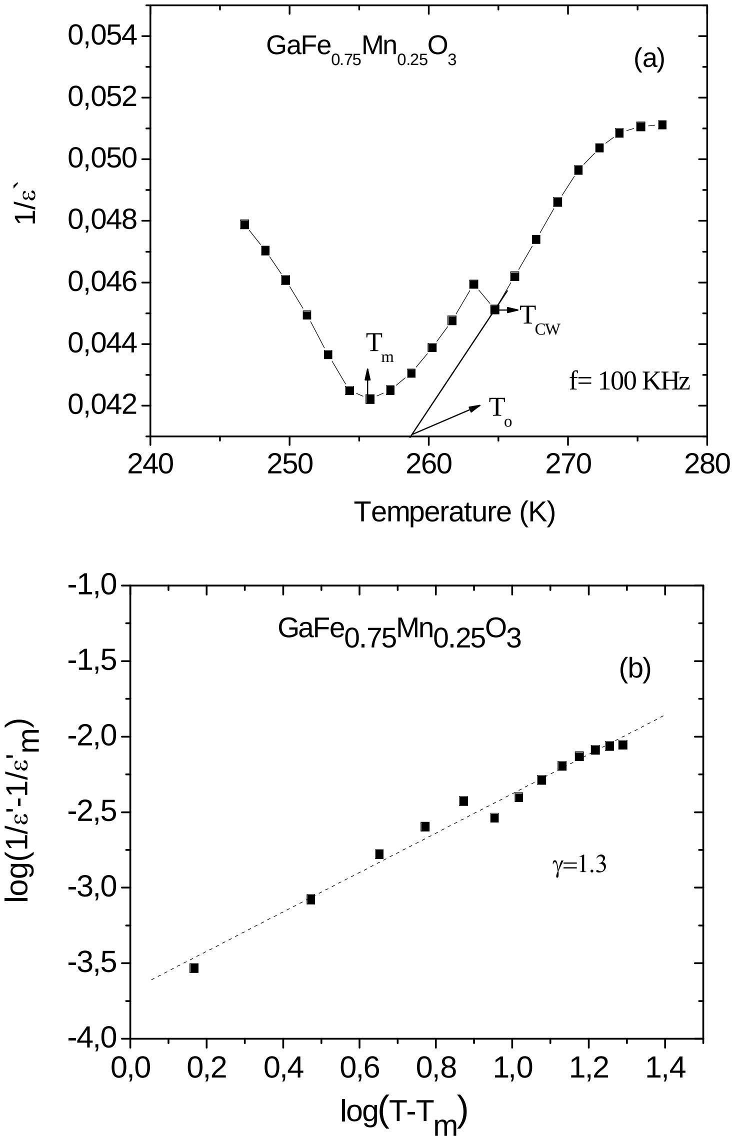

Figure 5.12: Plots of (a) 1/ ε' vs temperature and (b) log (1/ ε'−1/ε'$_m$) vs log (T−T$_m$) for GaFe$_{1-x}$Mn$_x$O$_3$ (SG@900°C) at 100 KHz.

In order to test for ferroelectric behavior the polarization vs. applied electric field was measured for $GaFe_{0.9}Mn_{0.1}O_3$ pellet. The hysteresis loops are shown in Fig. 5.13. The shapes of the curves are not consistent with ferroelectric behavior but rather indicative of conduction.

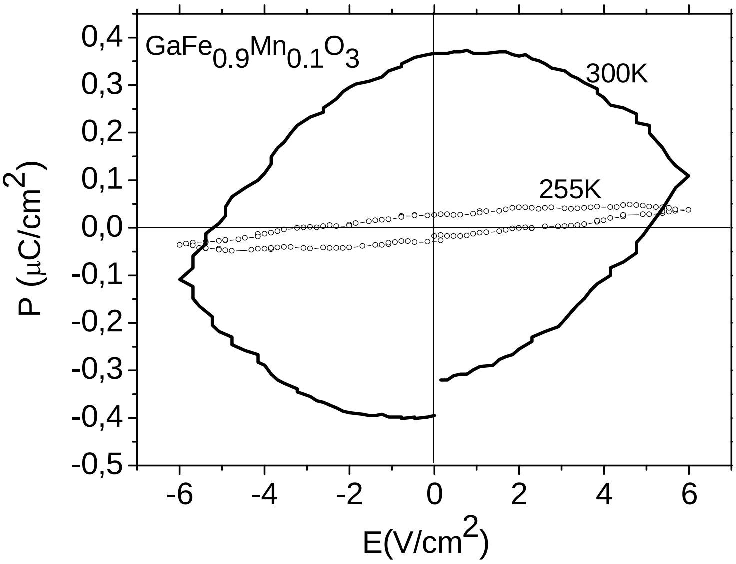

Figure 5.13: Hysteresis loop of $GaFe_{0.9}Mn_{0.1}O_3$ (SR) measured at 255 and 300 K.

5.1.4 Variable temperature neutron diffraction

No structure transitions or additional magnetic peaks were observed on cooling $GaFe_{1-x}Mn_xO_3$ samples to 3 K (Fig. 5.14) and all of the diffraction patterns were therefore indexed on the orthorhombic P c 2_1 n structure model as the unsubstituted sample. The cell parameters and atomic coordinations were all refined. Also the occupation of Mn, Fe and Ga were refined. Fe atoms were introduced at Fe_1 and Fe_2 positions and Ga atoms were introduced at Ga_1 and Ga_2 positions, and the complementary occupancy factors were refined, constrained to full occupancy, notably improving the quality of the fit. Then the possibility of partial occupancy of Ga_1 and Ga_2 positions by some Fe cations and *vice versa* was also checked and this also led to a drop of the discrepancy factors. Finally, the sharing of Mn in four different cation sites was tested, which leads to an improvement in refinement. Fig. 5.16a shows the Rietveld refinement for NPD for $GaFe_{0.75}Mn_{0.25}O_3$ at 300 K. The lattice parameters and Ga/Fe/Mn occupation of the cations obtained in the refinement for substituted samples are shown in Table 5.4.

Table 5.4: Fe/Mn partial occupancies at Ga_1, Ga_2, Fe_1 and Fe_2 sites, lattice parameters with standard deviation, reliability factors as deduced by Rietveld analysis of NPD for $GaFe_{1-x}Mn_xO_3$ (SR and SG@900°C) at room temperature.

	SR		SG@900°C	
Occupancies	$GaFe_{0.95}Mn_{0.05}O_3$	$GaFe_{0.9}Mn_{0.1}O_3$	$GaFe_{0.9}Mn_{0.1}O_3$	$GaFe_{0.75}Mn_{0.25}O_3$
Ga_1/Fe/Mn	0.87/0.12/0.01	0.87/0.09/0.04	0.963/0.037/0	0.877/0.087/0.036
Ga_2/Fe/Mn	0.51/0.47/0.02	0.51/0.44/0.05	0.54/0.37 /0.09	0.484/0.286/0.23
Fe_1/Ga/Mn	0.69/0.27/0.04	0.66/0.27/0.07	0.61/0.34/0.05	0.527/0.392/0.08
Fe_2/Ga/Mn	0.60/0.37/0.03	0.61/0.37/0.02	0.789/0.154/0.06	0.600/0.247/0.15
	Lattice parameter			
a (A)	8.7363(8)	8.7364(7)	8.7517(1)	8.7363(9)
b (A)	9.3818(7)	9.3818(1)	9.4024(4)	9.3883(5)
c (A)	5.0810(1)	5.0841(7)	5.0897(4)	5.0953(4)
V (A^3)	416.45(7)	416.71(8)	418.81(8)	417.92(4)
	Reliability factors			
R p(%)	9.53	4.42	3.37	3.67
Rwp(%)	9.96	4.33	4.20	4.62
R_B(%)	5.72	4.4	3.93	4.8

Atomic parameters from Rietveld fit to powder diffraction data can be found in Appendix C. The refinement of occupancies shows the presence of Fe and Ga in all four crystallographic sites. Furthermore the distribution changes with Mn content. This decrease in the Fe amount by Mn substitution reduces the exchange strength between iron neighbours and a decrease in T_c results. The unit cell lengths a, b and c and the volume all decrease slightly with temperature decreasing and there is no discontinuity in variation (Fig. 5.15).

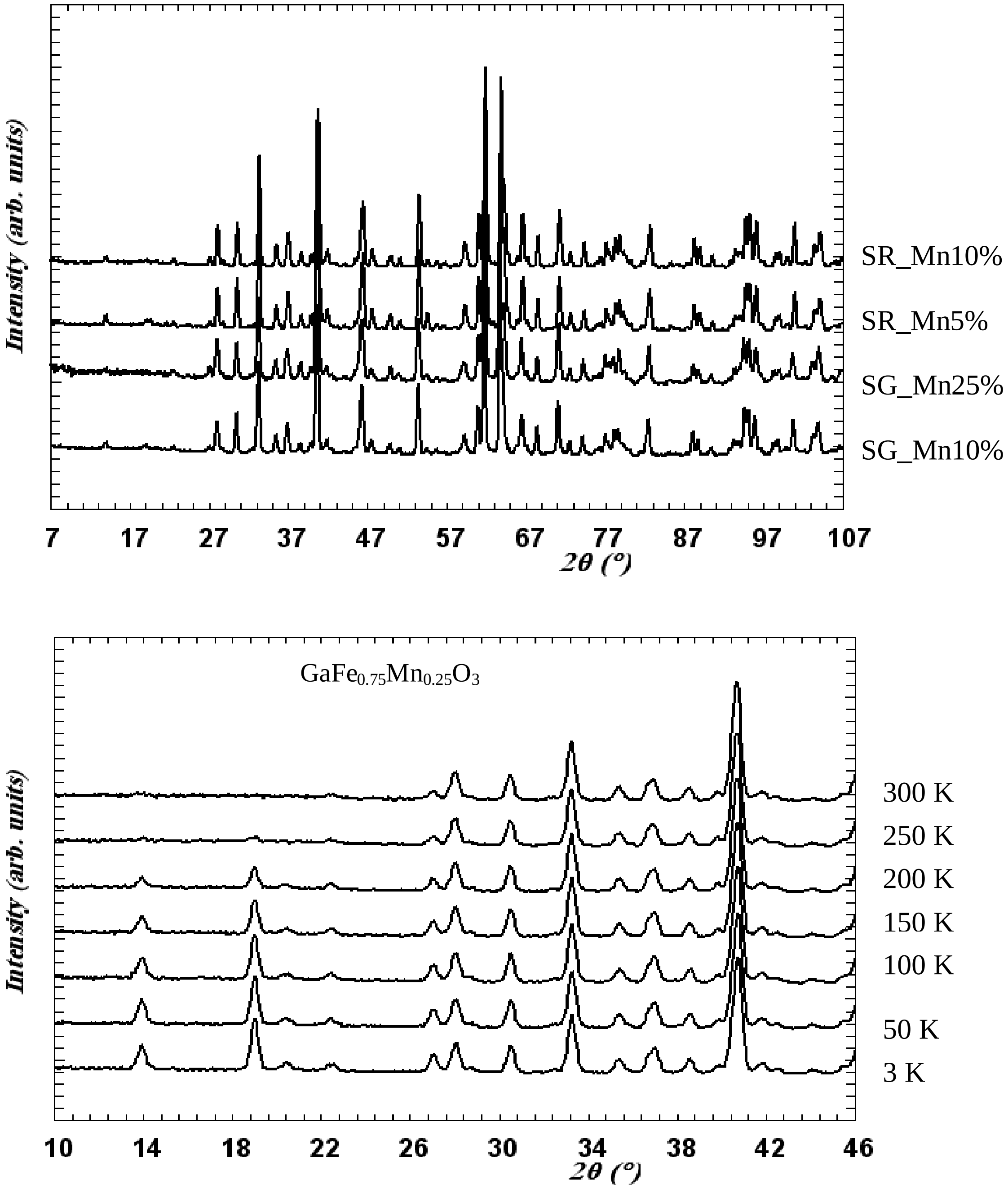

Figure 5.14: NPD (a) for $GaFe_{1-x}Mn_xO_3$ (SR, x = 0.05, 0.1 and SG@900°C, x = 0.1, 0.25) at 300 K and (b) collected at various temperatures to investigate the magnetic structure for $GaFe_{0.75}Mn_{0.25}O_3$

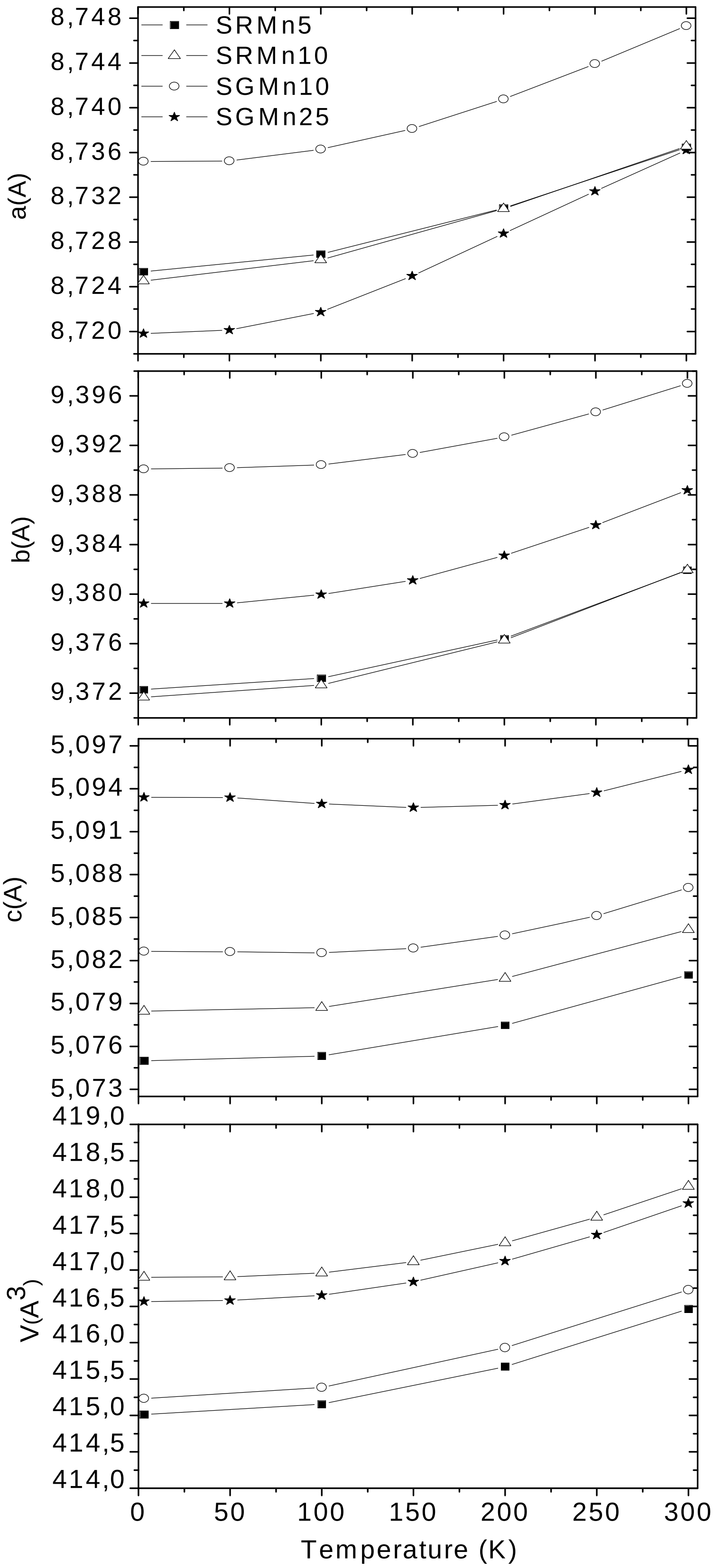

Figure 5.15: Temperature dependence of cell parameters for GaFe$_{1-x}$Mn$_x$O$_3$ (SR, x = 0.05, 0.1 and SG@900°C, x = 0.1, 0.25).

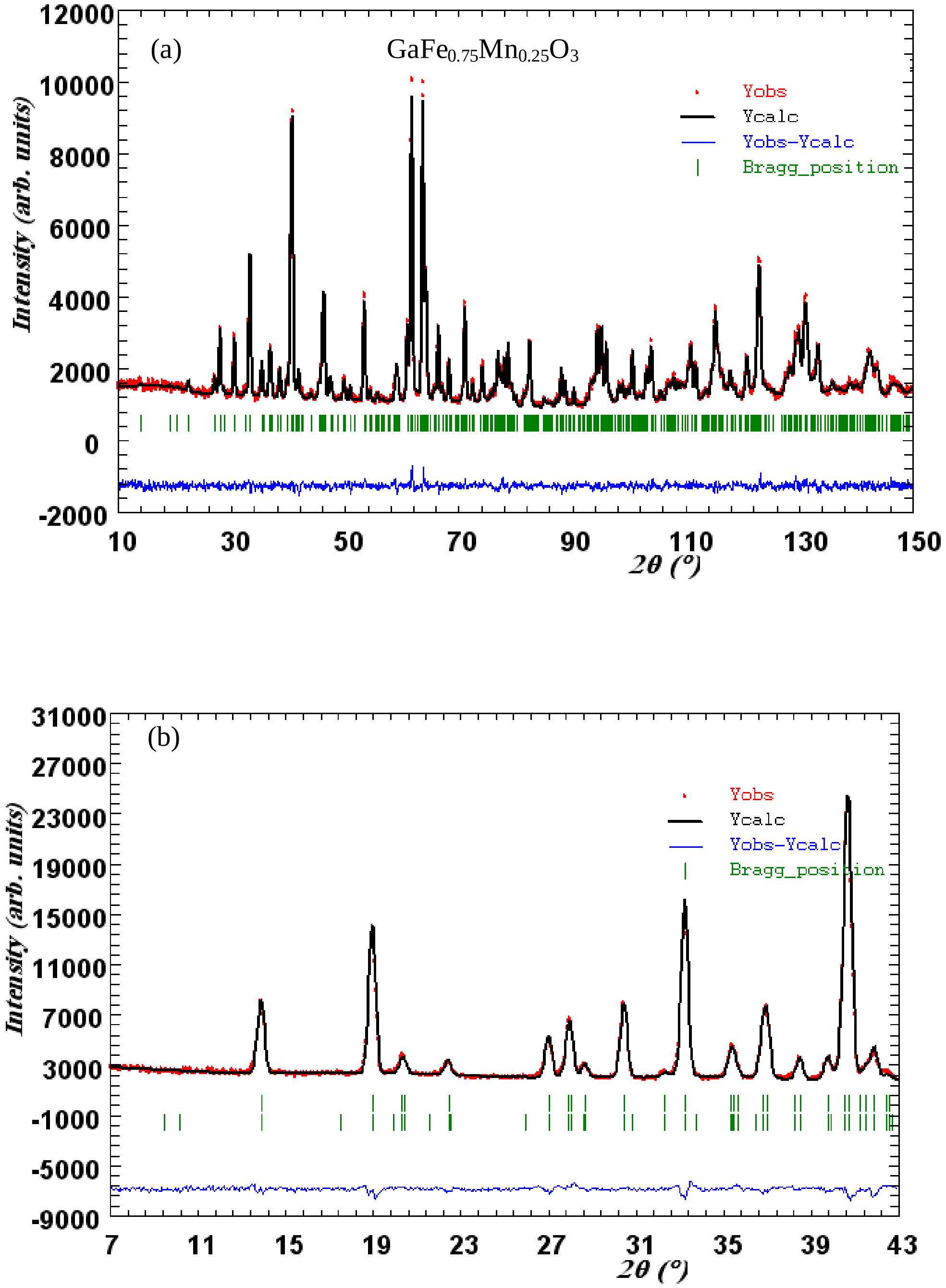

Figure 5.16: Agreement between observed and calculated intensities for $GaFe_{0.75}Mn_{0.25}O_3$ (SG@900°C) at (a) 300 K and (b) 3 K. The difference curves are shown at the bottom. The upper line of reflection marks correspond to the crystal structure, the lower lines indicate the diffraction angles of the magnetic Bragg peaks.

Fig. 5.16b shows the low angle region of the fit at 3 K, where the magnetic structure was treated as unsubstituted GFO, chapter 4. The derived magnetic moments of Fe^{3+}/

Mn^{3+}obtained from the Rietveld refinements for Mn doped samples at 3 K are 2.9, 2.7, 4.2, 3.6 μ_B for SRMn5%, SRMn10%, SGMn10% and SGMn25%, respectively.

5.1.5 High resolution X-ray diffraction

Fig. 5.18 and 5.19 show the variation of the lattice parameters and the unit cell volume of SRMn10% and SGMn25% with temperature over the range (200 K – 300 K) obtained from synchrotron powder diffraction analysis. The Rietveld fit for the two samples are shown in Fig. 5.17. An obvious anomaly is detected in all the parameters variation below 250 K. This effect was not detected in NPD probably because the temperature scans have been done with rather large temperature steps (50 K). Neither splitting of reflections due to symmetry changes nor broadening were observed in the powder diffraction patterns in the temperature range from 300 K down to 200 K; the patterns were successfully indexed according to the space group $P\ c\ 2_1\ n$. A similar feature was detected in orthorhombic $TmMnO_3$ [125]; ferroelectricity induced from magnetic order is related to competing magnetic interactions, whose competition at low temperature is reduced through small lattice distortions that result in switchable electric polarization and also in $A_3BFe_3D_2O_{14}$ with A=Ba, Sr, Ca, B=Ta, Nb, Sb and D=Ge, Si compound [126]; an anomaly has been observed at 35 K which might indicate the presence of a structural phase transition coupled to the onset of magnetic order. Also, an anomaly in the lattice parameters and the unit cell volume are observed in the Co_2SiO_4 system [127, 128], which can be attributed to magnetostriction. In our case this anomaly in lattice parameter may be the reason for dielectric property which has been observed in Mn doped samples.

Further NPD diffraction with high resolution and small step scan experiments is mandatory in order to determine the nature of this phase transition.

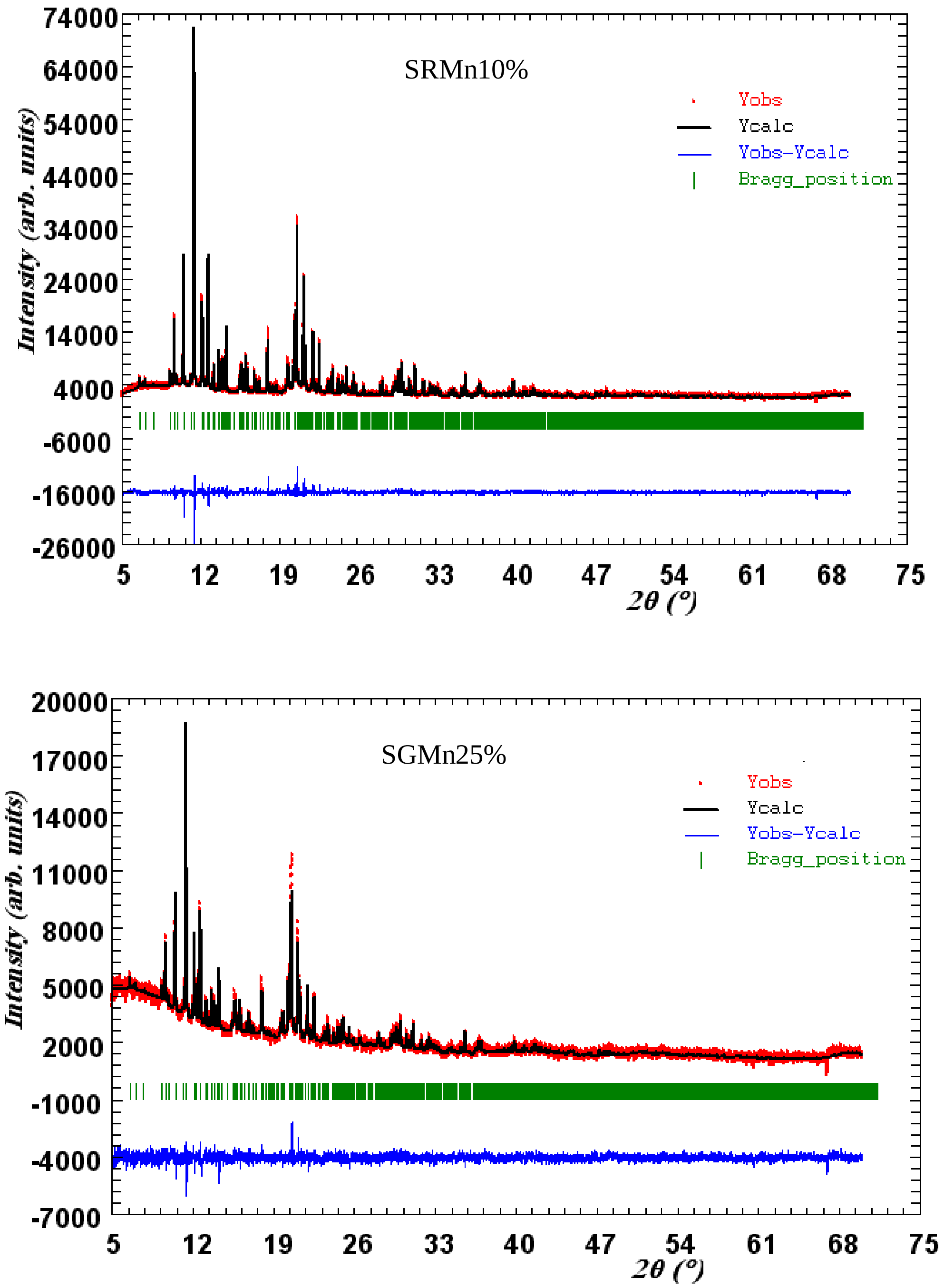

Figure 5.17: High-resolution synchrotron powder diffraction data refinement for SRMn10% and SGMn25% at 240 K. Solid circles indicate the experimental data and the calculated data are the continuous line overlapping them. The lowest curve shows the difference between experimental and calculated patterns. The vertical bars indicate the Bragg reflection positions.

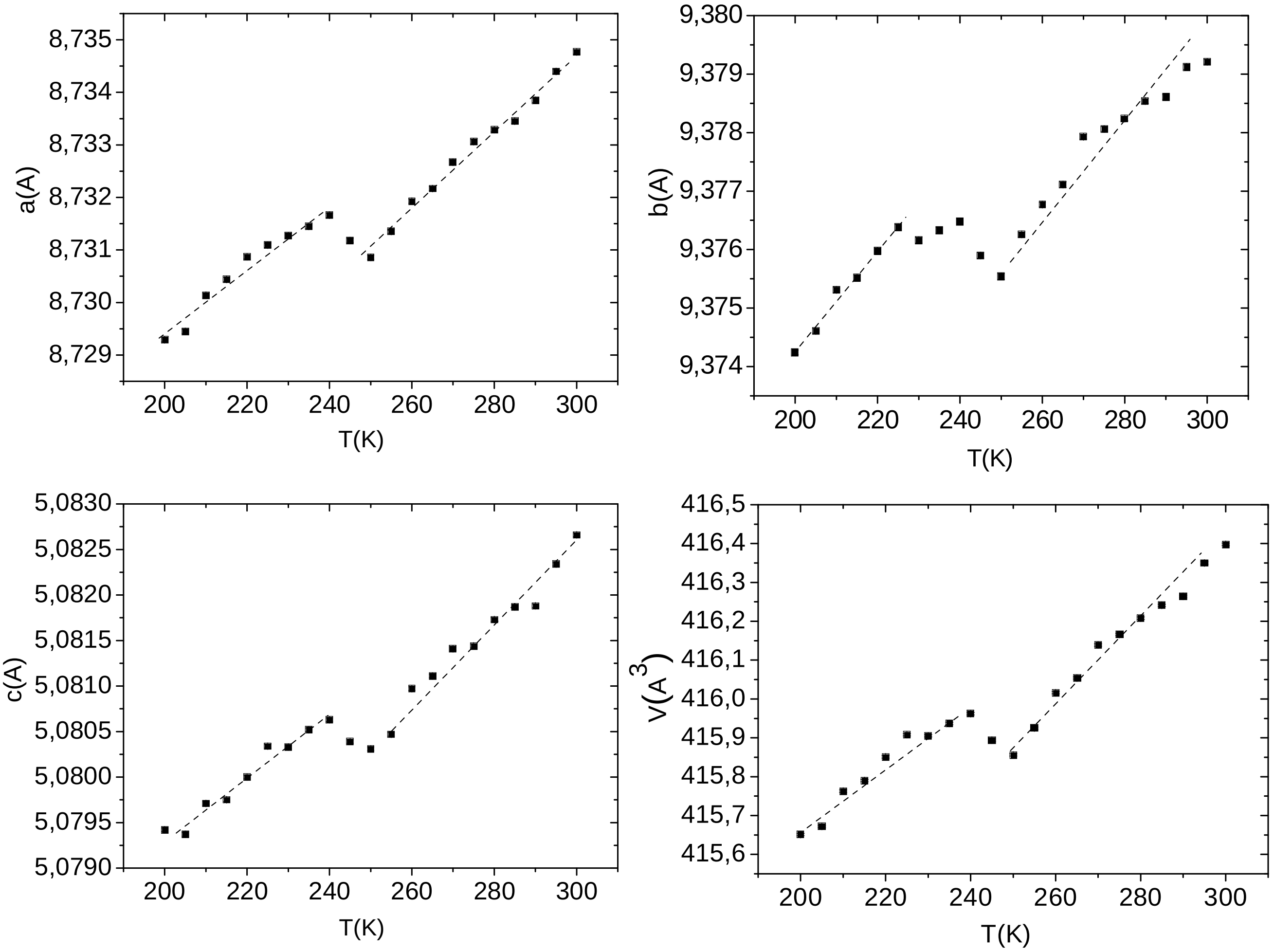

Figure 5.18: Temperature dependence of the lattice parameters and the cell volume of SRMn10% sample.

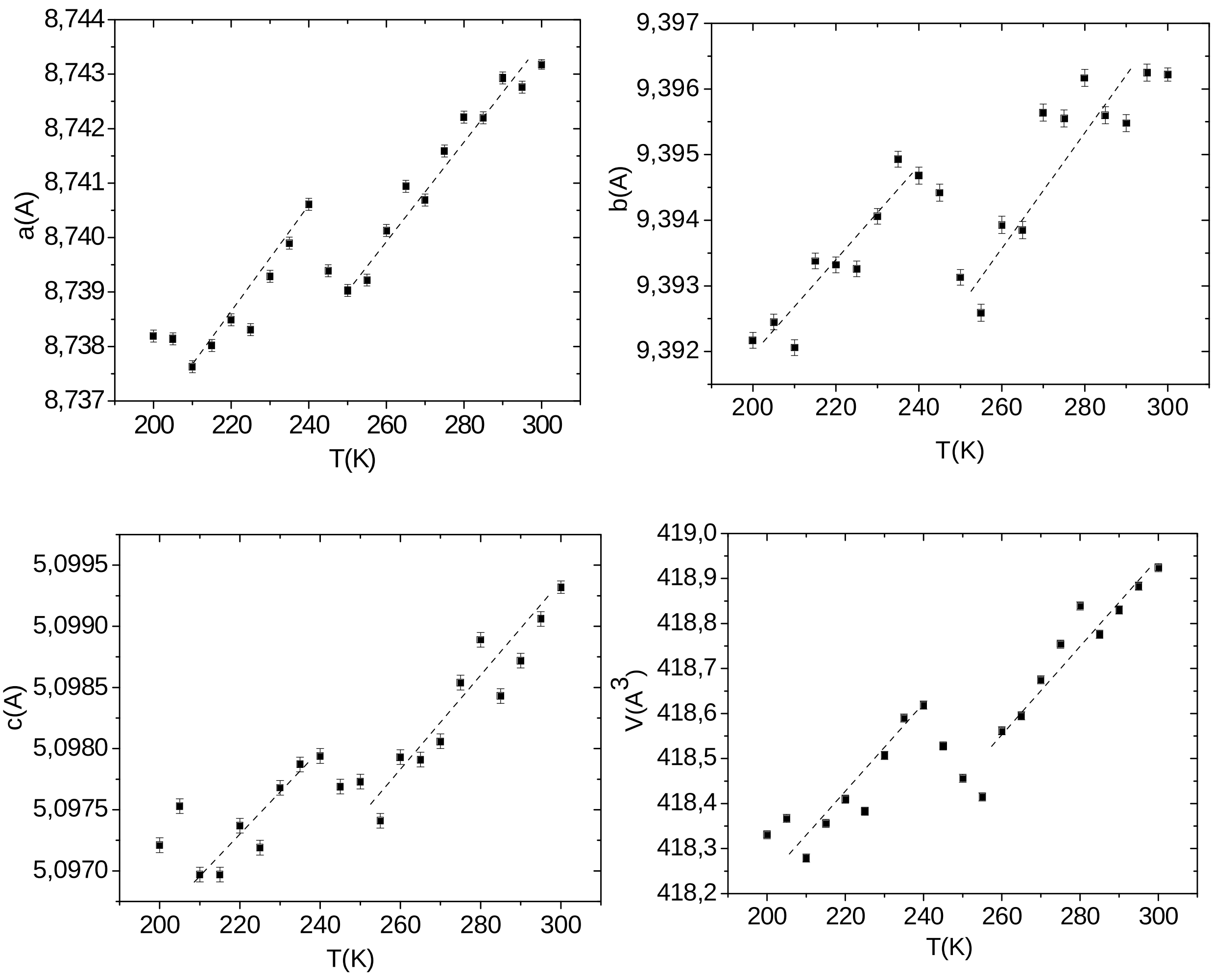

Figure 5.19: Temperature dependence of the lattice parameters and the cell volume of SGMn25% sample.

In order to test if other transition metals substitution Fe in GFO behave similarly, other elements were tested such as Co, Ni and Cr but the only one which gives a single phase after substitution is Cr. This will be investigated in more details in the next section.

5.2 Cr doped $GaFe_{1-x}Cr_xO_3$ system

5.2.1 Structure and microstructure

Rietveld analysis results reveal that all $GaFe_{1-x}Cr_xO_3$ (x= 0.05, 0.1 and 0.15) samples have orthorhombic structure (P c 2_1 n) as shown in Fig. 5.20 for the $GaFe_{0.85}Cr_{0.15}O_3$ sample. A small decrease in the volume of all cell parameters has been observed on doping Cr as shown in Table 5.5. This decrease in unit cell volume with increasing Cr substitution is expected since the ionic radius of Cr^{3+} is slightly smaller than that of Fe^{3+}. The SEM micrograph of the sintered pellet is shown in Fig. 5.21. The micrograph revealed a uniform distribution of the grains of varying shape with well defined boundaries and average grain size in the range of ~1-3 μm.

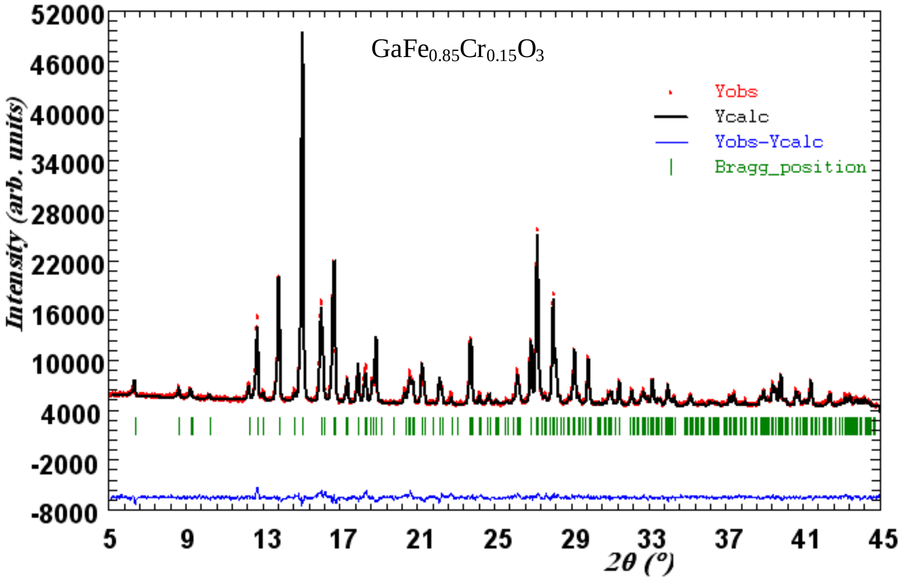

Figure 5.20: Rietveld analysis results of XRD pattern at RT for the $GaFe_{0.85}Cr_{0.15}O_3$ sample. Solid circles indicate the experimental data and the calculated data are the continuous line overlapping them. The lowest curve shows the difference between experimental and calculated patterns. The vertical bars indicate the Bragg reflection positions.

Table 5.5: Details of structure refinements with standard deviation and magnetic properties $GaFe_{1-x}Cr_xO_3$.

x	0.05	0.1	0.15
a (Å)	8.7348(9)	8.7532(4)	8.7308(7)
b(Å)	9.3799(1)	9.3776(5)	9.3756(4)
c(Å)	5.0771(2)	5.0769(9)	5.0765(5)
V($Å^3$)	415.98(1)	415.78(3)	415.55(3)
	Reliability factors		
R_p	10.3	9.90	10.1
R_{wp}	9.34	8.30	8.73
R_B	4.84	4.56	5.06
X^2	3.61	3.45	4.19
	Magnetic properties		
H_c(Oe)	4325	3142	1938
M_s(emu/g)	11.43	5.67	3.43
M_r(emu/g)	26.53	15.83	15.22

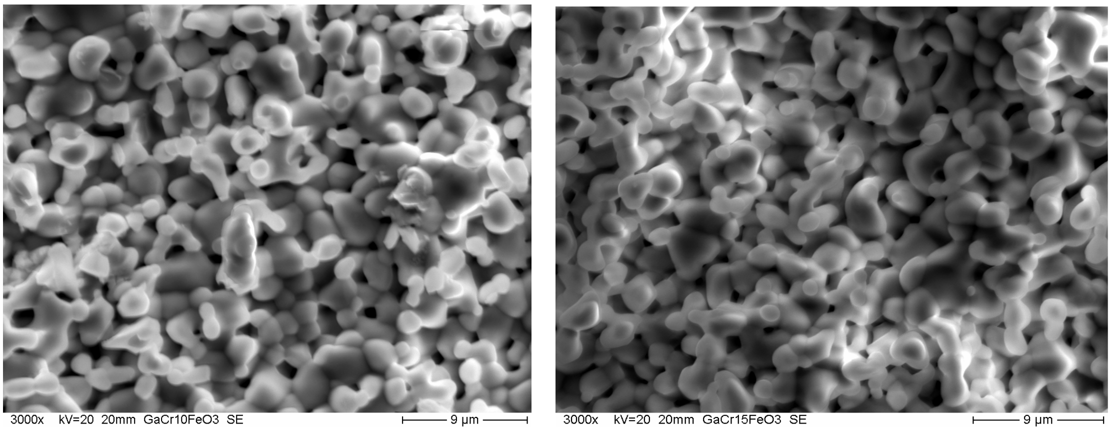

Figure 5.21: The SEM surface images of $GaFe_{1-x}Cr_xO_3$ samples: (a) $x = 0.1$, (b) $x = 0.15$.

5.2.2 Magnetic properties

The magnetic properties of $GaFe_{1-x}Cr_xO_3$ (x = 0.05, 0.1 and 0.15) samples are shown in Fig. 5.22a. The temperature dependence of the magnetization (zero field cooling; ZFC and field cooling, FC), measured over the temperature range from 5 to 300 K under 100 Oe field, indicates that the magnetization is decreased by Cr doping. The magnetization of $GaFe_{0.85}Cr_{0.15}O_3$, which is 3.7 emu/g, is found to be less than that of the undoped sample (6.3 emu/g) at 5 K.

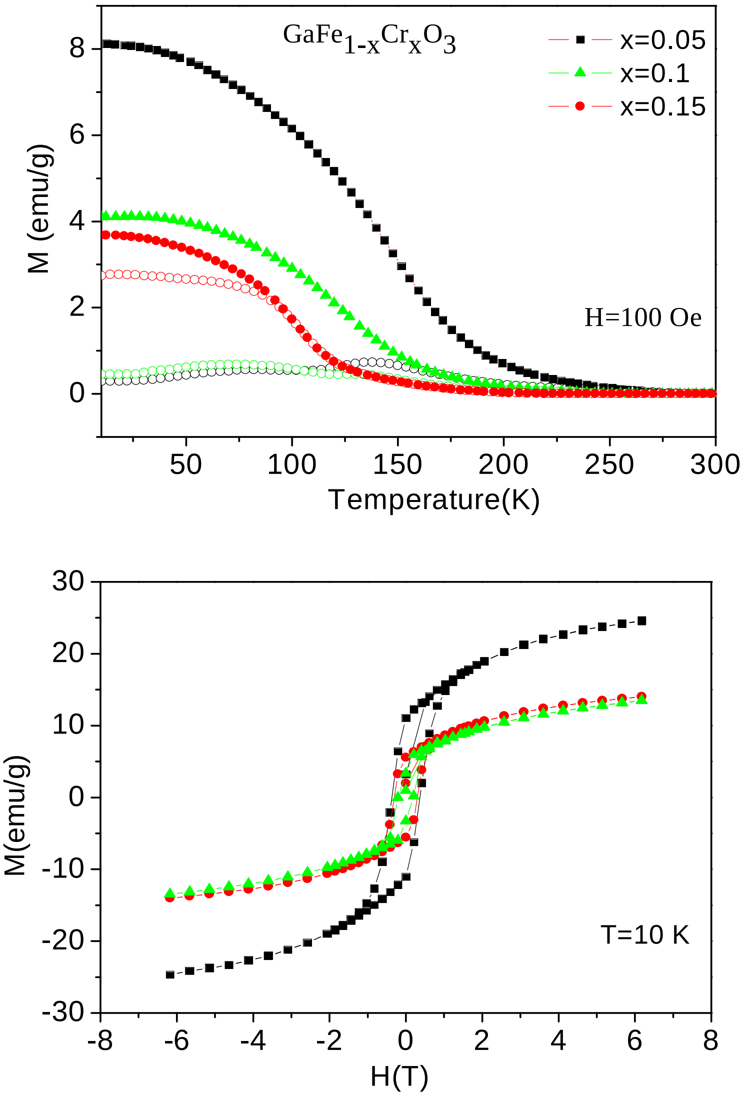

Figure 5.22: (a) Temperature dependence of magnetization for ZFC (open) and FC (solid) modes measured at 100 Oe (b) Magnetic hysteresis loop M(H) measured at 10K for the $GaFe_{1-x}Cr_xO_3$ samples.

The magnetic transition temperatures (T_c) are around 198, 175 and 126 K for Cr = 5, 10 and 15 %. The Curie temperature T_c decreases with increasing Cr content in $GaFe_{1-x}Cr_xO_3$. A similar behavior has been observed in the $CoCr_xFe_{2-x}O_4$ system [129]. The lowering of T_c may be related to the weak $Cr^{3+}(3\mu_B)$-O-$Cr^{3+}(3\mu_B)$ [130] and $Fe^{3+}(3\mu_B)$-O-$Cr^{3+}(3\mu_B)$ interaction [131] as compared to Fe^{3+}–O–Fe^{3+}. Fig. 5.22b presents the magnetization as a function of field. All samples exhibit hysteresis behavior in the M-H curve, indicative of ferrimagnetism. The saturation magnetization (M_s), remnant magnetization (M_r), and coercivity (H_c) of the samples obtained from the hysteresis curves are presented in Table 5.5. It is seen that M_s, M_r and H_c exhibit decreasing trends with increasing x. If the spin of the substituting Cr^{3+}ion align with the Fe^{3+} ion, the spin magnetic moment (SMM) of $Cr^{3+}(d^3)$ ion is 3 μ_B, thus, the net SMM is expected to be reduced by 2 μ_B per formula unit [132].

5.2.3 Dielectric properties

The frequency dependence of the dielectric constant, ε′, and the dielectric loss, tanδ, at 353 K for Cr =10 and 15 % are shown in Fig. 5.23. ε′ clearly shows a Debye- like relaxation from a high value at low frequency to a small saturated value at higher frequency for both samples.

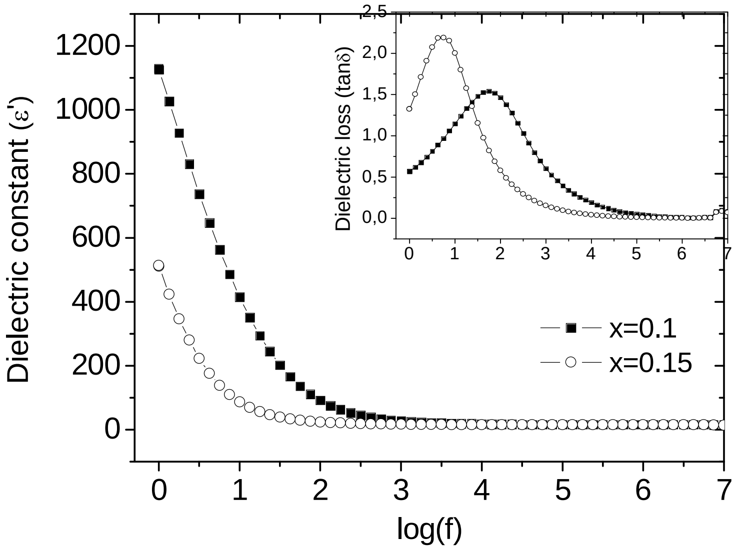

Figure 5.23: Frequency dependence of ε' and tan δ (inset) of $GaFe_{1-x}Cr_xO_3$; x = 0 .1 and 0.15 at 353 K.

The decrease of the dielectric constant and the higher dielectric loss as a function of Cr-content may be related with the grain size. In general the dielectric constant and the dielectric polarization are proportional to the grain size [133]. In our case, however, a different behavior was observed similar to Cr doped $Ba_{0.6}Sr_{0.4}TiO_3$ thin films [134]. A possible explanation may be a change in concentration of oxygen vacancies and defect related dipoles due to variable oxidation state of both Fe and Cr. In general, the dielectric constant of any material is due to dipolar, electronic, ionic, and interfacial polarizations [135, 136]. The dipolar and interfacial polarizations contribute significantly to the dielectric constant at low frequencies. Both these polarizations are strongly temperature dependent. In the high frequency region ε′ is almost the same for all samples as the contribution to the dielectric constant arises from electronic and ionic polarizations at high frequencies which are frequency independent. The frequency dependence of the dielectric loss spectrum (tanδ) shown in inset of Fig. 5.23 implies that the hopping of charge carriers plays an important role in their transport process because a loss peak is an essential feature of the charge carrier hopping transport [137]. The monotonous increase in the loss factor at low frequency is probably due to the contribution of the d.c. conductivity [138].

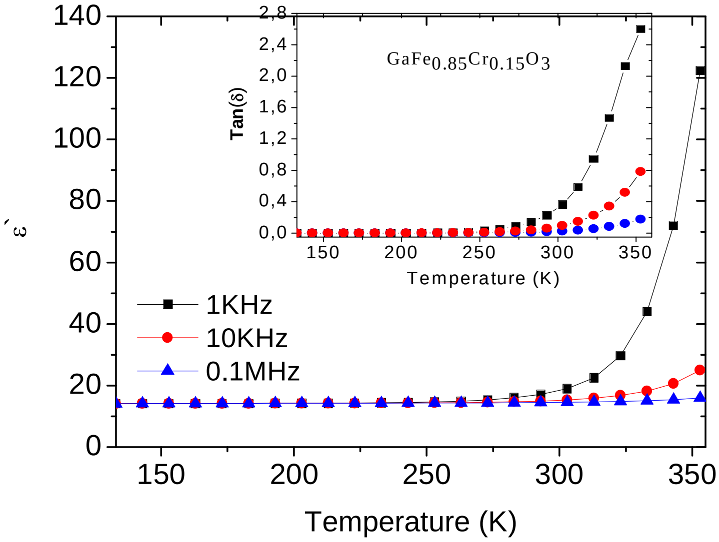

Figure 5.24: Variation of dielectric constant (ε') and tangent (tan δ, inset) with temperature in $GaFe_{0.85}Cr_{0.15}O_3$ at selected frequencies.

The dielectric constant and the dielectric loss at 100 Hz-10 MHz for the sample of Cr = 15% versus temperature (T) are shown in Fig. 5.24.

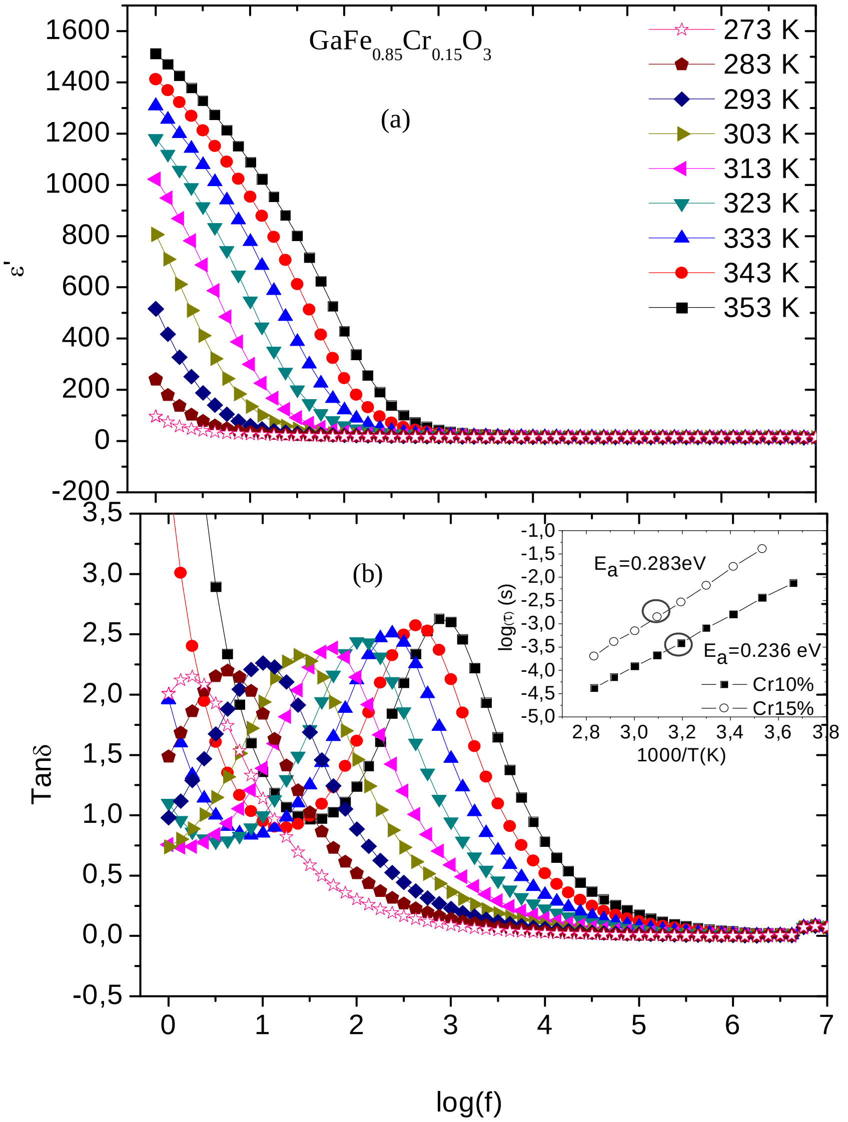

Figure 5.25: Frequency dependence of (a) ε' and (b) tan δ of GaFe$_{0.85}$Cr$_{0.15}$O$_3$ at different temperature, and the inset is ln τ vs. 1000/*T*.

The dielectric constant is high at 1 KHz and decreases very sharply with increasing frequency at temperatures above 350 K. Such a drastic decrease in the value of the dielectric constant at higher frequencies can be explained in terms of the interfacial space charge polarization. The space charge polarization increases with increasing temperature due to the increase in dc conductivity, moreover, it decreases with increasing frequency due to the decrease in ac conductivity [139]. The frequency (f) dependence of the ε′ and tanδ of $GaFe_{0.85}Cr_{0.15}O_3$ as a function of temperature are shown in Fig. 5.25a and b. The peak in tanδ shifts to a lower frequency on lowering the temperature.

The values of the most probable relaxation time τ_m were obtained from the peak frequencies ω_m ($\omega_m\tau_m = 1$) of tanδ. The variation of τ_m vs $10^3/T$ shown in Fig. 5.25 suggest that the relaxation time follows the Arrhenius law

$$\tau = \tau_o \exp(E_a/K_BT) \qquad (5.5)$$

where E_a is the activation energy for the dielectric relaxation, K_B is the Boltzmann constant and T is the absolute temperature. The activation energy for the dielectric relaxation obtained from the slope of the fitted line is 0.24 and 0.28 eV for Cr = 10 and 15%, respectively.

It has to be mentioned that the samples have been synthesized at high temperature ≥ 1200 ºC; a slight amount of oxygen loss can occur and may be expressed by the Kroger-Vink notation [140]:

$$O_o^x = V_o^{\cdot\cdot} + 1/2O_2 \text{ (gas) } + 2e^{\prime},$$

where O_o^x is the loss of lattice oxygen, $V_o^{\cdot\cdot}$ is the presence of oxygen-ion vacancy and e′ is the electron released or captured. The released electron may be captured by Fe^{3+} to generate Fe^{2+} for charge compensation such as in $LaFe_{0.9}Ni_{0.1}O_3$ [141]. The $V_o^{\cdot\cdot}$ and Fe^{2+}, contribute not only to the conductivity but also to the dielectric response. So, the activation energy values obtained above are almost equal to the activation energy of electron hopping between an Fe^{2+} and an Fe^{3+} ion in the oxide [142]. Again the strong increase in the dielectric characteristics with increasing temperature may be due to thermally induced oxygen ion vacancies and enhancement of hopping conduction as we will see later [143].

Polycrystalline samples may be analyzed by considering the impedance Z(ω) spectra as an electric modulus M(ω) spectra in order to emphasize the grain and grain boundary contributions to the electric properties [144]. From the physical point of view, the electric modulus corresponds to the relaxation of the electric field in the materials when the electric displacement remains constant [145]. Fig. 5.26 shows the logarithmic frequency dependence of real and imaginary parts of electric modulus for $GaFe_{0.9}Cr_{0.1}O_3$ as a function of temperature. In terms of the dielectric constant ε(ω), the electric modulus is given by

$$M(\omega) = M'(\omega) + jM''(\omega) = 1/\varepsilon \qquad (5.6a)$$

$$M'(\omega) = \varepsilon'(\omega) /[\varepsilon'(\omega)^2+ \varepsilon''(\omega)^2] \tag{5.6b}$$

$$M''(\omega)= \varepsilon''(\omega)/[\varepsilon'(\omega)^2+ \varepsilon''(\omega)^2] \tag{5.6c}$$

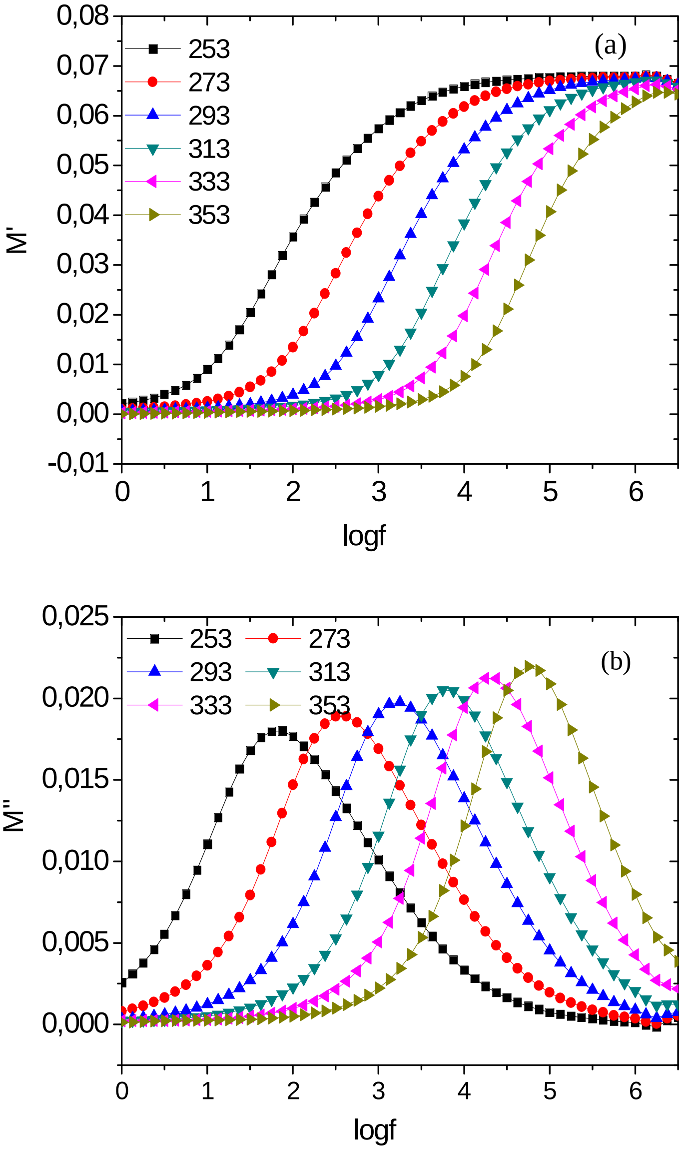

Figure 5.26: Frequency dependence of (a) real and (b) imaginary part of the electrical modulus for $GaFe_{1.9}Cr_{0.1}O_3$ at several temperature values.

M'(ω) shows a dispersion tending towards M_∞ (the asymptotic value of M'(ω) at higher frequencies (Fig. 5.26a) , while M"(ω) exhibits a relaxation peak (Fig. 5.26b) centered at the dispersion region of M'(ω). The relaxation peak for M"(ω) shifts towards lower frequencies during cooling the sample as shown in Fig. 5.26b. Consequently, it means that the relaxation rate for this process decreases with decreasing temperature. The frequency region below the peak maximum (M_m'') determines the range in which charge carriers are mobile on long distances. At frequency above peak maximum the carriers are confined to potential wells, being mobile on short distances.

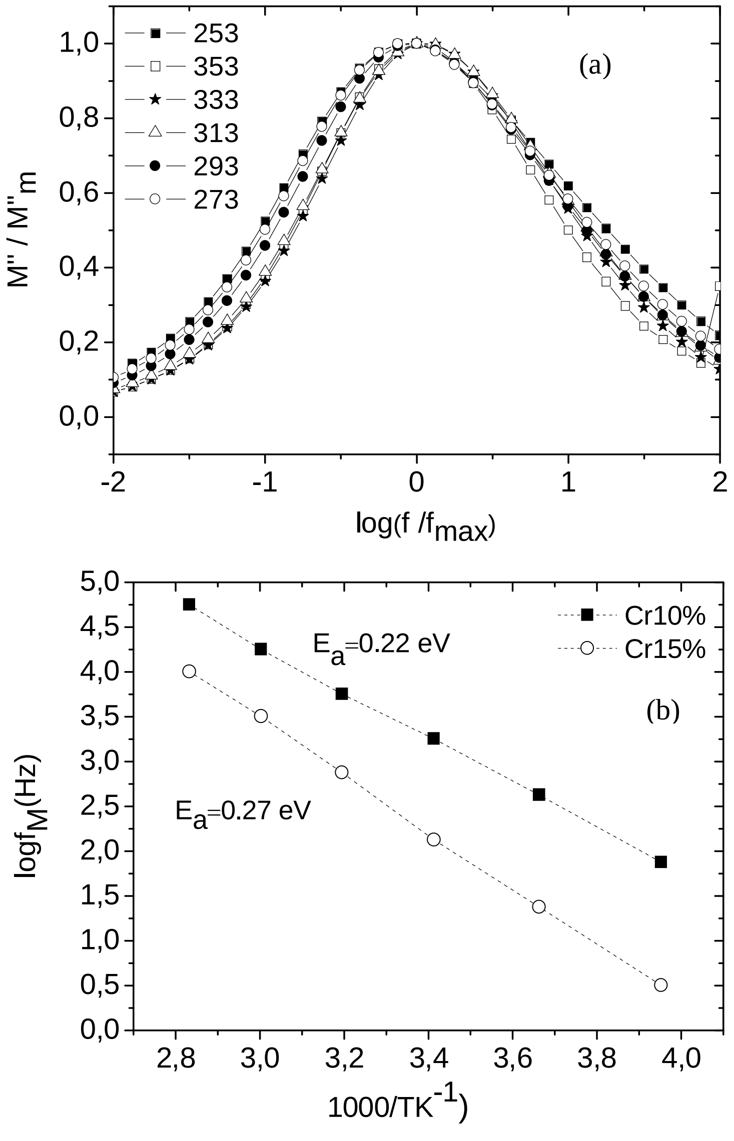

Figure 5.27: (a) Normalized modulus (M/M_m) as a function of frequency at different temperatures, (b) Arrhenius plot of the peak frequencies f_m for $GaFe_{1-x}Cr_xO_3$, x = 0.1 and 0.15.

Fig. 5.27a shows the scaling behavior of the imaginary part of electric modulus (M''(ω)) for $GaFe_{0.9}Cr_{0.1}O_3$, where we have scaled each M'' by M_m'' and each frequency by f_m. The overlap of the curves for all the temperatures into a single master curve indicates that they describe the same mechanism at various temperatures. The temperature dependence of the characteristic relaxation time as shown in Fig. 5.27b satisfies the Arrhenius law. From the least square fitting, the activation energies are calculated, and are found to be 0.22 and 0.27 eV for Cr = 10 and 15%, respectively. It is clear that the activation energy of the compounds (calculated from loss and modulus spectrum) is nearly the same. It suggests that the relaxation process may be attributed to the same type of charge carriers.

Complex impedance for $GaFe_{1-x}Cr_xO_3$ samples at 353 K are shown in Fig. 5.28. The real and imaginary components of the impedance decrease with an increase of Cr amount. Impedance spectra have been analyzed by an equivalent circuit, as displayed in the inset of Fig. 5.28.

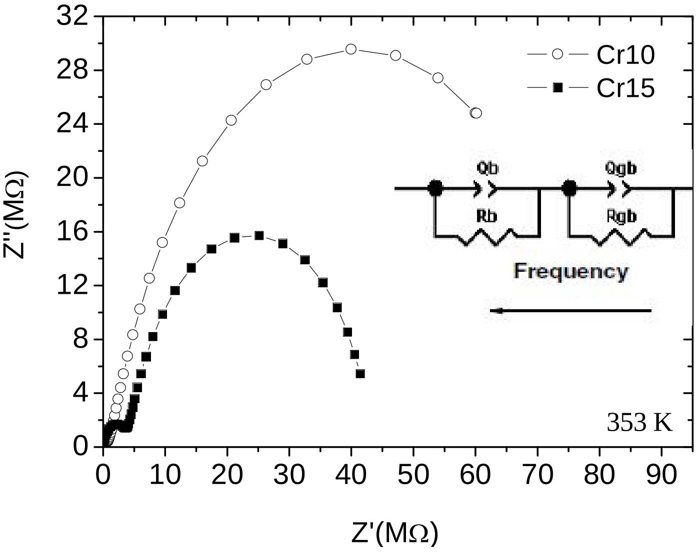

Figure 5.28: Nyquist plots of $GaFe_{1-x}Cr_xO_3$ samples at 353 K, inset represents the proposed circuit model. Solid curves represent the fitting of RC equivalent circuit.

The impedance plots indicate a depressed semicircle, whose center lies on a straight line below the real axis, suggesting departure from ideal Debye-type behavior. Hence, in the equivalent circuit, the constant phase elements (Q) capacitance $Q(\omega) = B(i\omega)^{n-1}$ are assumed to describe the depressed semicircle [144]. The parameter B is constant for a given set of experimental data. The exponent n varies between 0 and 1 (n = 1 for an ideal capacitor and n = 0 for ideal resistor). Grain (R_g) and grain boundary (R_{gb}) resistances have been calculated from the impedance spectrum. The best fitting of RC equivalent circuit at 353 K using the software" ZsimpWin" are R_g = 0.7 x10^6 and 3,51 x10^6 Ω, R_{gb} = 88,81 x10^6 and 40.89 x10^6 Ω , C_g = 8.186 x10^{-12} and 6.506 x10^{-12} F, C_{gb} = 0.995 7 x10^{-9} and 0.477 9 x10^{-9} F for Cr=10 and 15 %, respectively. Thus, the impedance spectroscopy analysis clearly demonstrates that the grain boundaries are more resistive than the grain in $GaFe_{1-x}Cr_xO_3$ system.

In order to further elucidate the transport mechanism in this system, the electric conductivity at different temperatures is studied. Electric conductivity can be calculated from the dielectric data as

$$\sigma (\omega) = \omega\varepsilon_0\varepsilon' \tan\delta, \qquad (5.7)$$

where ω is the angular frequency and ε_0 is the vacuum permittivity. Fig.5.29a shows frequency dependence of a.c. conductivity ($\sigma_{a.c.}$) at various temperatures for $GaFe_{1.85}Cr_{0.15}O_3$. It can be seen that at low frequencies and above room temperature plateaus of $\sigma_{a.c.}$(frequency independent values of conductivity) exist which corresponds to d.c. conductivity. The observed frequency dependent conductivity can be described by the equation [135]

$$\sigma(\omega) = \sigma_{d.c}+A\omega^n , \qquad (5.8)$$

where n is the frequency exponent in the range of $0 < n < 1$ and for an ideal Debye-type behavior it is equal to 1. A and n are thermally activated quantities, hence electrical conduction is a thermally activated process. According to Jonscher [146], the origin of the frequency dependence of conductivity lies in the relaxation phenomena arising due to mobile charge carriers. When mobile charge carriers hop onto a new site from its original position, it remains in a state of displacement between two potential energy minima, which includes contributions from other mobile defects. After a sufficiently long time, the defect could relax until the two minima in lattice potential energy coincide with the lattice site.

Extrapolating these curves towards low frequency gives the dc conductivity ($\sigma_{d.c.}$). The resulting $\sigma_{d.c.}$ is plotted as a function of reciprocal temperature in Fig. 5.29b and it well obeys the Arrhenius law,

$$\sigma = \sigma_0 \exp (E_{cond}/K_BT),$$

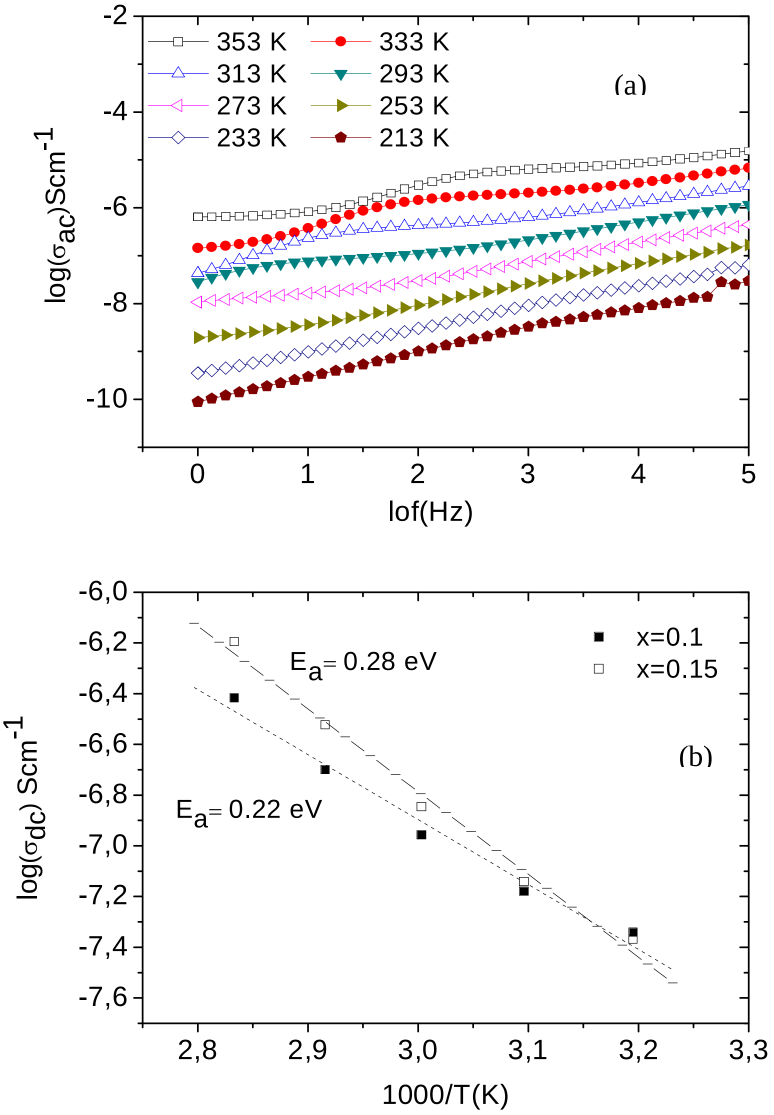

Figure 5.29: (a) Frequency dependent electric conductivity at various temperature for $GaFe_{0.85}Cr_{0.15}O_3$, (b) Arrhenius plot of dc conductivity for $GaFe_{1-x}Cr_xO_3$, x = 0.1 and 0.15 samples, dash lines represent linear fit.

where σ_0 is the pre-exponential term, E_{cond} is the conduction activation energy, and K_B is the Boltzmann constant. From the fitting E_{cond} are 0.22 and 0.28 eV, for Cr = 10 and 15%, respectively. This thermal activation energy of the intragrain conductivity is very close to that obtained from the dielectric relaxation, which suggests that the conductivity may play a very important role in these materials.

Chapter 6

Summary

The effect of annealing temperature and substitution on structure, magnetic and electric properties of multiferroic magnetoelectric $GaFeO_3$ were investigated.

$GaFeO_3$ was prepared by solid state reaction (SR) and sol gel (SG) methods. All samples have orthorhombic structure ($P\ c\ 2_1\ n$). The lattice parameters and volume increase as the annealing temperature decrease. This was explained by the reduction in particle size which relaxes the lattice and leads to a cell volume expansion. The magnetic transition temperature (T_c) increases from 225 K to 310 K as the particle size decreases from 205 nm to 50 nm. This increase in T_c may be due to the change in cation distribution. The hysteresis loops do not saturate even at the highest applied magnetic fields. The saturation magnetization increases from 0.77 μ_B/ Fe (SR) to 1.32 μ_B/ Fe (SG@700°C), which is attributed to the surface spin canting while the coercivity decreases from 6435 Oe (SR) to 4035 Oe (SG@900°C) then increases again to 6771 Oe (SG@700°C). The increase in the coercivity with decreasing particle size until a certain limit is due to the enhanced role of the surface and its anisotropy as opposed to the weaker bulk anisotropy. Dielectric measurements do not show any anomaly at or near T_c for samples prepared by SR and SG methods as claimed by other authors [74, 77, 80], as indication for magnetodielectric coupling in the $GaFeO_3$ compound. A neutron powder diffraction (NPD) study for $GaFeO_3$ (SR and SG@900°C) samples shows that the lattice parameters and volume exhibit a regular thermal expansion which indicated no abnormal structural change with decreasing temperature.

NPD does not show any anomaly in bond lengths, angles and the shift of Fe atoms from the centre of their octahedron at the magnetic transition temperature. The superexchange antiferromagnetic interaction between Fe^{3+} neighbors in $GaFeO_3$ slightly changes while iron ions fractions over the four sites Ga_1, Ga_2, Fe_1 and Fe_2 are greatly influenced by the annealing temperature. The average value of the largest bond angle Fe_1-O-Fe_2 is 167.4° and 168.8° for SR and SG@900°C samples, respectively, which is slightly higher than that one obtained from single crystals prepared by float zone method (Fz); 166° [17]. T_c in our case (SR and SG@900°C) ~ 225 and 300 K, respectively, and in case of single crystals prepared by (Fz) and flux grown method ~ 205 and 280 K [147], respectively.The bond angles analysis alone can not explain the reason for change in T_c as the method of preparation change. The interpretaion of the magnetic behavior require prior determination of cation occupancies. NPD refinement at 300 K shows that the occupancies of Fe ions in different cation sites show reduction of Fe occupancy in Ga_1 and Fe_1 sites and increase of Fe occupancy in Ga_2 and Fe_2 sites as the annealing temperature decreases, Table 6.1. The use of NPD with $GaFeO_3$ polycrystalline material is still difficult because one needs to determine the positions of 10 non equivalent atomic sites and four occupancies of the cation sites. The Mössbauer spectroscopy is used as a complementry method to explain results obtained from NPD, although the interpretation of the Mössbauer spectra of $GaFeO_3$ is not straight forward. The Mössbauer spectra measured at paramagnetic and magnetically ordered state were simultaneously fitted using the method of invariants. The hyperfine structure of the $GaFeO_3$ samples prepared by two different methods was determined. Another problem is the assignment of the identified components to the crystal sites which can be solved by using NPD data refinement. This assignment is consistent with the one which is presented in [73]. During the Mössbauer analysis two assumptions were proposed, Fe occupies 3 sites as performed at room temperature on the single crystals (Fz) [73]) or 4 sites assuming Fe ions sharing Ga_1 site. Because the four and also the three component fits are of similar quality, the differences of fitted values from NPD were used to estimate uncertainties of the site occupancies, the comparison between occupancies obtained from different methods and techniques are summarized in Table 6.1. It is clear that Fe occupied most of Ga_2 site and as the annealing temperature decreases the Ga_2 site are more occupied by Fe atoms.

Table 6.1: Fe partial occupancies at the Ga_1, Ga_2, Fe_1 and Fe_2 sites as deduced by a Rietveld analysis of neutron powder diffraction (NPD) and combined Mössbauer and NPD for $GaFeO_3$ (SR and SG@900 °C) samples at room temperature. The parameters for the flux-grown and float zone crystals reported in [17, 147] are also listed for comparison.

Method of preparation, annealing temperature, characteristic tool.		Ga_1	Ga_2	Fe_1	Fe_2
SR, 1300 °C, NPD.		0.2	0.55	0.7	0.55
SG@900 °C, 900 °C, NPD.		0.04	0.75	0.51	0.72
SR, NPD& Mössbauer.	3-components		0.86	0.48	0.64
	4-components	0.16	0.76	0.36	0.68
SG@900 °C, NPD& Mössbauer.	3-components		0.98	0.48	0.50
	4-components	0.14	0.9	0.4	0.5
Float zone, 1600 °C, time of flight neutron powder diffraction [17].		0.18	0.35	0.77	0.7
Flux, 1100 °C , Polarized neutron [147].		0.08	0.62	0.73	0.87

Band structure calculations [66] indicate that the energy resulting from the Fe interchange with the Ga_2 site can be as small as 1 meV per formula unit while interchange with Ga_1 site requires energy almost two orders of magnitude larger. This explains why Ga_2-Fe disorder is high, yet does not explain why the Fe concentration in Ga_2 site is so high. It is rather well documented that samples prepared with a larger disorder, e.g. quenched or synthesized at higher temperatures, possess a lower transition temperature than the more ordered samples, that have been e.g., prepared at lower temperatures or annealed [15, 17]. Our results of slightly better ordering in the SG sample is consistent with this trend. The magnetic structure was found to be ferrimagnetic with the propagation vector **K** = **0** in good agreement with the NPD data studied previously by other authors on single crystals [17, 147]. The refinement of 3 K data shows that the magnetic structure is given by the irreducible representation Γ_1 with basis functions: [A_x, C_y, G_z]. The Fe^{3+} magnetic moment ordered mainly along c- axis with small components along a and b axes which is in agreement with the result obtained for $GaFeO_3$ (single crystals) [17, 147]. The total magnetic moment at 3 K is increased in case of SG sample (4.4 μ_B) as compared to SR sample (3.2 μ_B) in agreement with the magnetization measurement and comparable with the value obtained from single crystal (flux method, 4.8 μ_B [147]).

Polycrystalline samples of Mn-doped $GaFeO_3$ were prepared by conventional solid state synthesis and sol gel method techniques. The maximum Mn doped amount for the samples prepared by SR is 10 %. The Mn substitution amount increases up to 20 % (annealed at 1000 ºC), 25 % (annealed at 900 ºC) and 40% (annealed at 800 ºC and 700ºC) for the samples prepared by SG under flow of oxygen. Upon manganese doping the cell parameters a and b decrease, while c increases, causing a unit cell volume decrease. Also the decrease in the unit cell volume caused by the substitution of Mn for Fe may be attributed to the presence of Mn ions as most of Mn ions in $GaFe_{1-x}Mn_xO_3$ are in the low spin state. The polyhedra around Ga_1, Ga_2, Fe_1 and Fe_2 become more distorted as Mn ions substitution increases. Also, the bond lengths and angles change with Mn content which indicate that a distortion is introduced into the crystal lattice of $GaFeO_3$ by Mn substitution. This may be due to the presence of Jahn Teller effect Mn^{3+} ion in the crystal. Magnetic measurements show that all single phase samples with $GaFeO_3$ structure in the $GaFe_{1-x}Mn_xO_3$ system are ferrimagnetic below room temperature. The decrease in transition temperature, coercivity and saturation magnetization with Mn content leads to suggest an antiferromagnetic coupling between Mn and Fe spins, reducing the average ordered magnetic moment. The Mn substituted system induced an anomaly in the dielectric constant around 250 K but ferroelectric measurements show a ferroelectric hysteresis behavior for lossy dielectric; due to conduction of the samples. High resolution X-ray diffraction (synchrotron) reveals an anomaly in lattice parameters at around 250 K but no crystal structure phase transition is noticed. The reason at the moment is not clear and needs further neutron studies. Neutron diffraction refinement shows that the Fe distribution at different sites is influenced by the amount of Mn substitution. The ferrimagnetic structure does not change with Mn doped $GaFeO_3$. The iron magnetic moment progressively decreases as Mn content increase. The observed magnetic moments of Fe^{3+}/

Mn^{3+}obtained from the Rietveld refinements for Mn doped samples at 3 K are 2.9, 2.7, 4.2, 3.6 μ_B for SRMn5%, SRMn10%, SGMn10% and SGMn25%, respectively.

In order to investigate the effect of doping on the dielectric properties of $GaFeO_3$ and test the dielectric behavior with other substituted transition material $GaFeO_3$ doped Cr system has been prepared by solid state reaction method. Phase purity investigations showed that the solubility limit of Cr in the host $GaFeO_3$ crystal lattice was around 15%. The surface morphology of the compounds is studied through SEM, which gives the average grain size as the order of ~1-3 µm. The magnetic properties decrease due to the weakening of the Fe^{3+}–O–Fe^{3+} superexchange interaction strength when the Cr^{3+} ions replaces some of the Fe ions. Dielectric measurements do not show any anomaly like in the Mn doped system. The frequency dependence of the dielectric constant and loss for Cr doped samples show a Debye-like relaxation from a high value at low frequency to a small saturated value at higher frequency. The frequency dependent maxima in the imaginary electric modulus at various temperatures are found to obey Arrhenius law with activation energies of ~ 0.22 and 0.27 eV, for $GaFe_{1-x}Cr_xO_3$, x = 0.1 and 0.15, respectively, which has been interpreted by hopping of electrons between ions of the same element but in different oxidation states. The scaling behavior of the imaginary part of electric modulus (M") suggests that the relaxation describes the same mechanism at various temperatures. Impedance spectroscopy along with the equivalent circuit model was used to determine the resistance and capacitance associated with the grain and grain boundary, which shows that the grain boundaries are more resistive than the grain in the $GaFe_{1-x}Cr_xO_3$ system.

We can summarize that the sol gel method is the best method for preparation of $GaFeO_3$ powders; the magnetic transition temperature is above room temperature. By combining the advantage of low temperature annealing and doping $GaFeO_3$ with a proper amount of Mn, a magnetoelectric multiferroic compound at 250 K can be obtained.

Rare-earth perovskite-type orthogallates $LnGaO_3$ (Ln = La–Gd) show a wide range of unique physical properties. Well known applications for substrate materials are for high temperature superconductive (HTSC), colossalmagnetoresistive (CMR) and GaN films [148–151]. Also, rare-earth orthoferrite shows vastly different transition temperatures: ~ 8 K for $YbFeO_3$ and ~ 90 K for $ErFeO_3$ and $TmFeO_3$, while Néel temperatures in these magnetodielectrics were roughly the same: T_N ~ 630 K [152]. $DyFeO_3$ shows a large ferroelectric polarization combined with a strong magnetoelectric coupling [153]. Furthermore, the ferroelectric polarization in $DyFeO_3$ is induced by the peculiar magnetic structure, obtained on applying an external magnetic field.

The large magnetodielectric effect exhibited by $Ga_{0.5}Al_{0.5}FeO_3$ [80] and dielectric anomaly in $GaFe_{1-x}Mn_xO_3$ demonstrate the importance of substitution of A or B sites cations. Displacements of the cations and the disorder associated with their occupancies markedly affect the dielectric and magnetodielectric properties in a significant manner as predicted by Kan et al. [107]. More over the substitution of Ga or Fe site by rare-earth may improve $GaFeO_3$ properties.

Appendix A

Mössbauer and neutron powder diffraction combination for Fe occupancies determination among different sites

Table A.1. Results of refinement obtained by Rietveld analysis of neutron diffraction performed at T = 3 K. Site occupancies are taken from Table 1, col. 8 and Table 2, col. 7. Sequence of colors in the column 2,3,...7 indicates assignment of Mössbauer components to the sites listed in column 1.

B	crystal site	assignment of the Mössbauer components					
		1	2	3	4	5	6
1	Ga_1	b	b	b	b	b	b
2	Ga_2	lb	lb	r	r	g	g
3	Fe_1	r	g	lb	g	r	lb
4	Fe_2	g	r	g	lb	lb	r
	No. of comp. /sample	R_{mag} (%)					
5	3 comp. /SR	22.6	16.3	10.9	16.3	22.6	11.7
6	4 comp. /SR	15.6	47.2	7.35	14.9	15.3	5.34
7	3 comp. /SG	37.3	21.1	22.7	24.3	23.4	12.9
8	4 comp. /SG	22.7	14.4	15.5	8.90	13.8	9.14

C	crystal site	assignment of the Mössbauer components					
		1	2	3	4	5	6
1	Ga_1	r	r	r	r	r	r
2	Ga_2	lb	lb	b	b	g	g
3	Fe_1	b	g	g	lb	b	lb
4	Fe_2	g	b	lb	g	lb	b
	No. of comp. /sample	R_{mag} (%)					
5	3 comp. /SR	27.1	17.0	17.0	22.1	27.1	15.0
6	4 comp. /SR	15.0	15.1	13.8	12.4	16.8	12.5

7	3 comp. /SG	37.2	21.4	24.3	13.1	23.4	14.5
8	4 comp. /SG	24.5	14.9	10.5	20.3	14.9	12.6

D	crystal site	assignment of the Mössbauer components					
		1	2	3	4	5	6
1	Ga_1	g	g	g	g	g	g
2	Ga_2	lb	lb	r	r	b	b
3	Fe_1	b	r	lb	b	r	lb
4	Fe_2	r	b	b	lb	lb	r
	No. of comp. /sample	R_{mag} (%)					
5	3 comp. /SR	73.0	16.3	11.9	16.3	73.0	11.3
6	4 comp. /SR	37.1	14.7	12.3	16.2	13.9	8.66
7	3 comp. /SG	27.0	23.8	13.4	21.3	21.3	16.5
8	4 comp. /SG	14.5	15.5	9.71	11.5	11.2	7.25

Appendix B

Representation theory and prediction of magnetic structures

In non-primitive cells we must determine the relation between the different magnetic moments in the cell. This relation can be very difficult to derive and is often found by comparison with known magnetic structures, or by trial and error. Group theory arguments allow us to calculate symmetry allowed relations between the moments and to greatly simplify this process.

Determining the magnetic structure means:

1. Determining the relation between magnetic and chemical unit cell i.e. propagation vector (In the ferrimagnetic case, **K** = **0**, so that the magnetic unit cell is the same as the chemical unit cell.).
2. Determining the magnetic moment direction.
3. Determining the symmetry relationship between different magnetic moments in the unit cell.

B.1. Matrix presentation of symmetry element and atomic position

The space group P c 2_1 n contains 4 symmetry operations {E, 2_{1y}, n_{xy}, c_{yz}}. The symmetry operators correspond to the identity element, a two fold screw axis along the y axis, n-glide perpendicular to the c axis, and a glide plane perpendicular to x with transition along c, all elements can be represented by a matrix as follows:

$$E = \begin{pmatrix} 1 & 0 & 0 \\ 0 & 1 & 0 \\ 0 & 0 & 1 \end{pmatrix},\ 2_y = \begin{pmatrix} \bar{1} & 0 & 0 \\ 0 & 1 & 0 \\ 0 & 0 & \bar{1} \end{pmatrix},\ n_{xy} = \begin{pmatrix} \bar{1} & 0 & 0 \\ 0 & \bar{1} & 0 \\ 0 & 0 & 1 \end{pmatrix} \text{ and } c_{yz} = \begin{pmatrix} 1 & 0 & 0 \\ 0 & \bar{1} & 0 \\ 0 & 0 & \bar{1} \end{pmatrix}$$

The atomic positions for $GaFeO_3$ can be separated into rotational and transitional components as represented in Table B.1.

Table B.1: Fe atoms coordinate in general position 4a with rotational matrix part for space group P c 2_1 n.

	x, y, z- components	Rotation matrix R
1	$(x, 0, z)$	$\begin{pmatrix} 1 & 0 & 0 \\ 0 & 0 & 0 \\ 0 & 0 & 1 \end{pmatrix}$
2	$(\bar{x}, \frac{1}{2}, \bar{z})$	$\begin{pmatrix} \bar{1} & 0 & 0 \\ 0 & 0 & 0 \\ 0 & 0 & \bar{1} \end{pmatrix}$
3	$(x + \frac{1}{2}, \frac{1}{2}, \bar{z} + \frac{1}{2})$	$\begin{pmatrix} 1 & 0 & 0 \\ 0 & 0 & 0 \\ 0 & 0 & \bar{1} \end{pmatrix}$
4	$(\bar{x} + \frac{1}{2}, y, z + \frac{1}{2})$	$\begin{pmatrix} \bar{1} & 0 & 0 \\ 0 & 0 & 0 \\ 0 & 0 & 1 \end{pmatrix}$

B.2. Effect of symmetry elements on atomic positions and the permutation representation, Γ_{perm}

A crystal is invariant under all of the symmetry operations of its space group. However, equivalent atoms can be interchanged under the different symmetry operations. For example, operation 2_y interchanges atom 1 (X_1) and 2 (X_2) in the 4a site in the Fe (4a) site whereas operation E keeps them invariant.

$$2_y X_1 = \begin{pmatrix} \bar{1} & 0 & 0 \\ 0 & 1 & 0 \\ 0 & 0 & \bar{1} \end{pmatrix} \begin{pmatrix} 1 & 0 & 0 \\ 0 & 0 & 0 \\ 0 & 0 & 1 \end{pmatrix} = \begin{pmatrix} \bar{1} & 0 & 0 \\ 0 & 0 & 0 \\ 0 & 0 & \bar{1} \end{pmatrix} = X_2$$

$$EX_1 = \begin{pmatrix} 1 & 0 & 0 \\ 0 & 1 & 0 \\ 0 & 0 & 1 \end{pmatrix} \begin{pmatrix} 1 & 0 & 0 \\ 0 & 0 & 0 \\ 0 & 0 & 1 \end{pmatrix} = \begin{pmatrix} 1 & 0 & 0 \\ 0 & 0 & 0 \\ 0 & 0 & 1 \end{pmatrix} = X_1$$

The manner in which all symmetry operations of a group permute the labels of equivalent atoms can be represented by a large matrix, called the permutation representation, Γ_{perm}. The character of the permutation representation for a symmetry operation, χ_{perm}, is simply the number of position labels that are unchanged under its action as listed in the Table B.2.

Table B.2: Transformation of the positions for the magnetic sites 4a

	1	2	3	4
E	1	2	3	4
2_y	2	1	4	3
n_{xy}	4	3	2	1
c_{yz}	3	4	1	2

From the table, the only non zero trace of Γ_{perm} are E

$$\chi_{\text{perm}}(E) = 4 \text{ and}$$

$$\chi_{\text{perm}}(2_y) = \chi_{\text{perm}}(n_{xy}) = \chi_{\text{perm}}(c_{yz}) = 0.$$

B.3. Effect of symmetry elements on magnetic moments and the magnetic representation, Γ_{mag}

A magnetic moment is described by an axial vector which, for convenience, will be represented in the axis system of the point or space group that we are using. We will always refer to moment components defined with respect to the crystallographic axes, not Cartesian projections. If the moment vector of an atom is $\vec{S} = (S_x, S_y, S_z)$, then the action of a rotational symmetry element is simply

$$\vec{S}' = R\vec{S} * \det(R)$$

Where the determinant, det(R), is required to describe the current loop symmetry of an axial vector (which is not reversed by the inversion operation). The axial vector representation, Γ_{axial}, describes how the components of a moment vector are changed by the different symmetry operations. The character of a given symmetry element is χ_{axial}. Numerically, it is simply the trace (the sum of the leading diagonal elements) of the rotation matrix of the symmetry operation multiplied by the determinant of the rotation matrix. For example, for n_{xy} symmetry element,

$\chi_{axial}(n_{xy}) = (-1 - 1 + 1) \times 1 = -1$

Table B.3: Transformation of the components S_x, S_y and S_z of a magnetic moment $\vec{S}$.

	E	2_y	n_{xy}	c_{yz}
S_x	S_x	$-S_x$	$-S_x$	S_x
S_y	S_y	S_y	$-S_y$	$-S_y$
S_z	S_z	$-S_z$	S_z	$-S_z$
χ_{axial}	3	-1	-1	-1

B.4. The magnetic representation:

The magnetic representation, Γ_{mag}, describes both the result of the symmetry operations on the atomic positions and on the axial vectors that describe the atomic moments. As these effects are independent, the magnetic representation is given by their direct product:

$$\Gamma_{mag} = \Gamma_{axial} \times \Gamma_{perm}$$

The characters of these representations are related according to:

$$\chi_{mag} = \chi_{axial} \times \chi_{perm} \qquad \text{(B.1)}$$

B.5. Irreducible representations of the space groups

Irreducible representations are matrices that map onto the algebra of the space group symmetry operations. They are of particular significance because they are the smallest unique blocks out of which all other representations can be made. In other words, any representation can be written in terms of the different irreducible representations of the group so that the representation can be decomposed into irreducible representations. The dimensionality of an irreducible representation is the dimensionality of the matrix representatives of the representation. The irreducible representations of the space group G_k=P c 2_1 n for **K** = **0** can be obtained from Kovalev's book [102] and are listed in Table B.4.

TableB.4: Characters of space group P c 2_1 n with Symmetry elements in International Tables (IT) and Kovalev's (KV) notations.

Element g_n	g_1	g_2	g_3	g_4
IT notation	E	2_y	n_{xy}	c_{yz}
KV notation	h_1	h_4	h_{26}	h_{27}
Γ_1	1	1	1	1
Γ_2	1	1	-1	-1
Γ_3	1	-1	1	-1
Γ_4	1	-1	-1	1

B.6. Decomposition of the magnetic representation into irreducible representations

Γ_{mag} describes how the atomic moments change under all the different symmetry operations of a space group. It is reducible and can be written in terms of the irreducible representations of the space group. Therefore, Γ_{mag} can be decomposed into the irreducible representations of the space group. In this case, the magnetic representation for an atomic site can be decomposed into contributions from the irreducible representations as

$$\Gamma_{mag} = \sum_{v} n_v \Gamma_v$$

where n_v is the number of times the irreducible representation n_v appears in the magnetic representation Γ_{mag}. n_v is given by:

$$n_v = \frac{1}{n(G_k)} \sum_{g \in G_k} x\Gamma_{mag}(g) x^* \Gamma_v(g)$$

Here $\chi\Gamma_{mag}(g)$ is the character of the magnetic representation calculated from equation B.1 and $\chi^*\Gamma_v(g)$ is the complex conjugate of the character of the irreducible representation with index ν for element g .

In our case,

For ν = 1 (the Γ_1 representation),

n_1=1/4[(12*1)+(0*1)+(0*1)+(0*1)]=3

For ν = 2 (the Γ_2 representation),

n_2=1/4[(12 x 1)+(0 x 1)+(0 x-1)+(0 x -1)]=3

For ν = 3 (the Γ_3 representation),

n_3=1/4[(12 x 1)+(0 x -1)+(0 x 1)+(0 x -1)]=3

For ν = 4 (the Γ_4 representation),

n_3=1/4[(12 x 1)+(0 x -1)+(0 x -1)+(0 x 1)]=3

the decomposition of Γ_{mag} into irreducible representations of G_k:

$$\Gamma_{mag} = 3\Gamma_1 + 3\Gamma_2 + 3\Gamma_3 + 3\Gamma_4 \qquad \text{(B.2)}$$

$x\Gamma_1$ implies that the Γ_1 contains x number of basis vectors.

B.7. Deduction of the magnetic modes

The basic vectors of all irreducible matrix representations are obtained by the projection operator technique. Using the respective transformation properties of the 4a positions and spin components from Tables B.3 and B.4, also for the simplicity we will use Wollan-Köhler-Bertaut notation [154]:

$G=S_1-S_2+S_3-S_4$ (G-mode),
$A=S_1-S_2-S_3+S_4$ (A-mode),
$C=S_1+S_2-S_3-S_4$ (C-mode),
$F=S_1+S_2+S_3+S_4$ (F-mode).

$$\Psi_1^{\Gamma_1} = \frac{1}{4}[1.\begin{pmatrix} S_{1x} \\ S_{1y} \\ S_{1z} \end{pmatrix} + 1.\begin{pmatrix} -S_{2x} \\ S_{2y} \\ -S_{2z} \end{pmatrix} + 1.\begin{pmatrix} -S_{3x} \\ -S_{3y} \\ S_{3z} \end{pmatrix} + 1.\begin{pmatrix} S_{4x} \\ -S_{4y} \\ -S_{4z} \end{pmatrix}] = \frac{1}{4}\begin{pmatrix} A_x \\ C_y \\ G_z \end{pmatrix},$$

$$\Psi_1^{\Gamma 2} = \frac{1}{4}[1.\begin{pmatrix} S_{1x} \\ S_{1y} \\ S_{1z} \end{pmatrix} + 1.\begin{pmatrix} -S_{2x} \\ S_{2y} \\ -S_{2z} \end{pmatrix} - 1.\begin{pmatrix} -S_{3x} \\ -S_{3y} \\ S_{3z} \end{pmatrix} - 1.\begin{pmatrix} S_{4x} \\ -S_{4y} \\ -S_{4z} \end{pmatrix}] = \frac{1}{4}\begin{pmatrix} G_x \\ F_y \\ A_z \end{pmatrix},$$

$$\Psi_1^{\Gamma 3} = \frac{1}{4}[1.\begin{pmatrix} S_{1x} \\ S_{1y} \\ S_{1z} \end{pmatrix} - 1.\begin{pmatrix} -S_{2x} \\ S_{2y} \\ -S_{2z} \end{pmatrix} + 1.\begin{pmatrix} -S_{3x} \\ -S_{3y} \\ S_{3z} \end{pmatrix} - 1.\begin{pmatrix} S_{4x} \\ -S_{4y} \\ -S_{4z} \end{pmatrix}] = \frac{1}{4}\begin{pmatrix} C_x \\ A_y \\ F_z \end{pmatrix},$$

$$\Psi_1^{\Gamma 4}=\frac{1}{4}[1.\begin{pmatrix}S_{1x}\\S_{1y}\\S_{1z}\end{pmatrix}-1.\begin{pmatrix}-S_{2x}\\S_{2y}\\-S_{2z}\end{pmatrix}-1.\begin{pmatrix}-S_{3x}\\-S_{3y}\\S_{3z}\end{pmatrix}+1.\begin{pmatrix}S_{4x}\\-S_{4y}\\-S_{4z}\end{pmatrix}]=\frac{1}{4}\begin{pmatrix}F_x\\G_y\\C_z\end{pmatrix}.$$

From symmetry space group calculated magnetic modes are given in Table B.5.

Table B. 5: Basic vectors of the irreducible matrix representations of G_k

Character	x	y	z
Γ_1(1, 1, 1, 1)	A_x	C_x	G_z
Γ_2(1, 1, -1, -1)	G_x	F_y	A_z
Γ_3(1, -1, 1, -1)	C_x	A_y	F_z
Γ_4(1, -1, -1, 1)	F_x	G_y	Cz

Appendix C

Tables of structural parameters

Table C.1: Structure parameters of $GaFe_{0.95}Mn_{0.05}O_3$ prepared by solid state reaction; obtained by Rietveld analyses of NPD patterns.

	SR	x = 0.05			
	Temperature	3 K	100 K	200 K	300 K
Lattice Parameters	a(Å)	8.7252(3)	8.7268(4)	8.7310(3)	8.7363(8)
	b(Å)	9.3721(8)	9.3731(2)	9.3764(5)	9.3818(7)
	c(Å)	5.0749(8)	5.0753(3)	5.0775(1)	5.0810(1)
	volume($Å^3$)	415.00(3)	415.15(1)	415.67(5)	416.45(7)
Coordinates	Ga_1 x	0.1512(1)	0.1507(5)	0.1507(2)	0.1505(4)
	y	0.00000	0.00000	0.00000	0.00000
	z	0.1755(2)	0.1760(3)	0.1761(9)	0.1766(2)
	Ga_2 x	0.1613(8)	0.1609(3)	0.1612(7)	0.1610(2)
	y	0.3104(5)	0.3101(1)	0.3102(2)	0.3099(2)
	z	0.8064(3)	0.8065(7)	0.8072(8)	0.8063(6)
	Fe_1 x	0.1525(1)	0.1521(6)	0.1524(7)	0.1517(5)
	y	0.5856(7)	0.5853(3)	0.5854(2)	0.5855(4)
	z	0.1854(8)	0.1852(3)	0.1853(5)	0.1837(1)
	Fe_2 x	0.0316(3)	0.0313(7)	0.0318(4)	0.0316(2)
	y	0.7945(1)	0.7940(7)	0.7944(8)	0.7943(2)
	z	0.6795(5)	0.6796(3)	0.6790(9)	0.6796(7)
	O_1 x	0.3241(8)	0.3240(6)	0.3245(3)	0.3243(6)
	y	0.4274(8)	0.4271(4)	0.4272(3)	0.4275(4)
	z	0.9694(3)	0.9693(4)	0.9696(1)	0.9695(1)
	O_2 x	0.4898(6)	0.4895(4)	0.4894(2)	0.4891(6)

	y	0.4341(6)	0.4338(1)	0.4341(9)	0.4333(9)
	z	0.5120(6)	0.5120(4)	0.5124(7)	0.5121(6)
O_3	x	1.0010(6)	1.0011(5)	1.0011(6)	1.0007(3)
	y	0.2013(7)	0.2011(2)	0.2007(8)	0.2013(2)
	z	0.6554(1)	0.6548(4)	0.6550(8)	0.6552(6)
O_4	x	0.1581(1)	0.1586(9)	0.1585(3)	0.1584(6)
	y	0.1978(1)	0.1979(6)	0.1982(4)	0.1982(2)
	z	0.1536(6)	0.1530(2)	0.1526(1)	0.1530(1)
O_5	x	0.1670(1)	0.1667(4)	0.1667(8)	0.1666(1)
	y	0.6722(6)	0.6724(3)	0.6720(4)	0.6723(7)
	z	0.8482(2)	0.8486(7)	0.8489(1)	0.8489(4)
O_6	x	0.1669(4)	0.1674(6)	0.1681(4)	0.1682(9)
	y	0.9406(7)	0.9407(1)	0.9413(4)	0.9415(2)
	z	0.5193(4)	0.5196(2)	0.5195(6)	0.5198(2)
R_{wp}		6.02	5.97	9.98	9.96
R_p		4.48	4.44	9.45	9.53
R_{exp}		4.34	4.35	7.38	7.70
R_B		4.65	4.81	5.49	5.72

Table C.2: Structure parameters of $GaFe_{0.9}Mn_{0.1}O_3$ prepared by solid state reaction; obtained by Rietveld analyses of NPD patterns.

	SR	x = 0.1			
	Temperature	3 K	100 K	200 K	300 K
Lattice	a(Å)	8.7244(1)	8.7263(2)	8.7309(1)	8.7364(7)
Parameters	b(Å)	9.3715(1)	9.3725(1)	9.3761(6)	9.3818(1)
	c(Å)	5.0784(15	5.0787(1)	5.0807(5)	5.0841(7)
	volume(Å^3)	415.21(9)	415.37(5)	415.92(2)	416.71(8)
Coordinates	Ga_1 x	0.1528(1)	0.1530(1)	0.1532(6)	0.1532(7)
	y	0.00000	0.00000	0.00000	0.00000
	z	0.1755(7)	0.1760(1)	0.1757(7)	0.1761(4)
	Ga_2 x	0.1601(5)	0.1601(7)	0.1601(8)	0.1604(1)
	y	0.3105(8)	0.3102(4)	0.3100(8)	0.3098(1)
	z	0.8107(5)	0.8115(1)	0.8116(2)	0.8110(3)
	Fe_1 x	0.1493(8)	0.1490(3)	0.1485(1)	0.1486(5)
	y	0.5877(1)	0.5876(1)	0.5874(18	0.5873(8)
	z	0.1887(4)	0.1891(3)	0.1892(1)	0.1881(2)
	Fe_2 x	0.0315(4)	0.0315(1)	0.0316(6)	0.0320(8)

	y	0.7955(3)	0.7958(8)	0.7955(4)	0.7955(1)
	z	0.6770(4)	0.6769(6)	0.6770(1)	0.6768(6)
O_1	x	0.3234(6)	0.3233(8)	0.3235(9)	0.3241(8)
	y	0.4263(6)	0.4261(1)	0.4260(1)	0.4264(1)
	z	0.9730(9)	0.9743(6)	0.9744(9)	0.9749(2)
O_2	x	0.4899(1)	0.4899(7)	0.4899(5)	0.4894(7)
	y	0.4344(8)	0.4346(8)	0.4346(8)	0.4339(4)
	z	0.5173(6)	0.5178(5)	0.5185(2)	0.5183(5)
O_3	x	1.0027(2)	1.0026(9)	1.0025(8)	1.0025(1)
	y	0.2041(1)	0.2045(4)	0.2044(3)	0.2044(7)
	z	0.6570(1)	0.6576(3)	0.6568(9)	0.6566(8)
O_4	x	0.1584(2)	0.1591(4)	0.1588(3)	0.1589(8)
	y	0.1983(4)	0.1982(9)	0.1985(1)	0.1981(1)
	z	0.1539(6)	0.1537(8)	0.1536(5)	0.1546(8)
O_5	x	0.1658(3)	0.1665(7)	0.1667(5)	0.1667(3)
	y	0.6734(2)	0.6736(8)	0.6735(4)	0.6733(4)
	z	0.8492(3)	0.8498(5)	0.8487(5)	0.8502(7)
O_6	x	0.1668(2)	0.1669(1)	0.1677(1)	0.1678(7)
	y	0.9408(4)	0.9411(1)	0.9414(4)	0.9414(1)
	z	0.5203(6)	0.5206(1)	0.5196(3)	0.5200(6)
R_{wp}		4.82	4.68	4.52	4.33
R_p		4.32	3.92	4.34	4.42
R_{exp}		4.03	4.31	3.89	3.62
R_B		3.56	3.71	4.5	4.40

Table C.3: Structure parameters of $GaFe_{0.9}Mn_{0.1}O_3$ prepared by sol gel method; obtained by Rietveld analyses of NPD patterns.

	SG	x = 0.1			
	Temperature	3 K	100 K	200 K	300 K
Lattice Parameters	a(Å)	8.7410(9)	8.7415(2)	8.7444(1)	8.7517(1)
	b(Å)	9.3963(3)	9.3962(1)	9.3976(3)	9.4024(4)
	c(Å)	5.0860(2)	5.0856(2)	5.0863(6)	5.0897(4)
	volume(Å^3)	417.73(6)	417.71(8)	417.98(1)	418.81(8)
Coordinates	Ga_1 x	0.1512(8)	0.1533(6)	0.1533(5)	0.1526(9)
	y	0.00000	0.00000	0.00000	0.00000
	z	0.1777(5)	0.1748(3)	0.1762(3)	0.1780(5)

Ga_2	x	0.1596(8)	0.1601(8)	0.1594(1)	0.1591(9)
	y	0.3071(3)	0.3090(1)	0.3080(2)	0.3073(6)
	z	0.8117(9)	0.8092(4)	0.8122(8)	0.8128(2)
Fe_1	x	0.1518(4)	0.1503(9)	0.1504(7)	0.1511(1)
	y	0.5845(8)	0.5856(6)	0.5848(8)	0.5844(2)
	z	0.1910(6)	0.1899(1)	0.1908(4)	0.1903(7)
Fe_2	x	0.0310(1)	0.0314(5)	0.0316(7)	0.0315(6)
	y	0.7974(8)	0.7985(8)	0.7974(8)	0.7967(3)
	z	0.6749(2)	0.6756(3)	0.6762(6)	0.6754(1)
O_1	x	0.3230(1)	0.3229(5)	0.3227(8)	0.3226(8)
	y	0.4283(1)	0.4293(5)	0.4286(4)	0.4281(5)
	z	0.9782(4)	0.9797(8)	0.9801(1)	0.9793(8)
O_2	x	0.4872(3)	0.4874(5)	0.4879(8)	0.4879(4)
	y	0.4339(5)	0.4358(4)	0.4358(8)	0.4348(6)
	z	0.5122(4)	0.5112(7)	0.5136(1)	0.5140(3)
O_3	x	1.0003(3)	0.9972(2)	0.9976(2)	0.9983(2)
	y	0.2017(3)	0.2022(7)	0.2025(9)	0.2020(9)
	z	0.6568(5)	0.6545(9)	0.6538(8)	0.6543(1)
O_4	x	0.1609(9)	0.1591(3)	0.1594(1)	0.1597(3)
	y	0.1990(2)	0.1985(4)	0.1984(1)	0.1992(1)
	z	0.1607(3)	0.1590(2)	0.1605(1)	0.1625(8)
O_5	x	0.1688(7)	0.1701(6)	0.1711(6)	0.1705(2)
	y	0.6744(6)	0.6743(1)	0.6739(6)	0.6744(5)
	z	0.8497 (7)	0.8459(5)	0.8468(5)	0.8501(8)
O_6	x	0.1674(9)	0.1665(8)	0.1670(1)	0.1681(9)
	y	0.9392(9)	0.9392(1)	0.9393(2)	0.9394(2)
	z	0.5156(4)	0.5163(5)	0.5165(9)	0.5173(1)
R_{wp}		4.82	8.24	4.68	4.20
R_p		3.67	7.40	3.72	3.37
R_{exp}		1.7	1.68	1.67	1.69
R_B		3.34	4.00	3.94	3.93

Table C.4: Structure parameters of $GaFe_{0.75}Mn_{0.25}O_3$ prepared by sol gel method; obtained by Rietveld analyses of NPD patterns.

	SG	x = 0.25			
	Temperature	3 K	100 K	200 K	300 K
Lattice	a(Å)	8.7233(1)	8.7259(9)	8.7289(2)	8.7363(9)
Parameters	b(Å)	9.3831(8)	9.3801(6)	9.3832(1)	9.3883(9)
	c(Å)	5.0955(5)	5.0930(2)	5.0928(2)	5.0953(5)
	volume(Å^3)	417.08(7)	417.09(9)	417.12(8)	417.92(4)
Coordinates	Ga_1 x	0.1547(3)	0.1531(3)	0.1541(9)	0.1551(8)
	y	0.00000	0.00000	0.00000	0.00000
	z	0.1777(8)	0.1766(2)	0.1745(5)	0.1741(8)
	Ga_2 x	0.1595(4)	0.1589(9)	0.1588(1)	0.1605(5)
	y	0.3111(2)	0.3092(6)	0.3094(4)	0.3081(3)
	z	0.8140(6)	0.8139(6)	0.8147(8)	0.8185(9)
	Fe_1 x	0.1501(6)	0.1495(2)	0.1498(1)	0.1490(8)
	y	0.5887(1)	0.5889(1)	0.5889(2)	0.5878(7)
	z	0.1895(6)	0.1892(1)	0.1887(5)	0.1887(2)
	Fe_2 x	0.0302(7)	0.0292(9)	0.0299(2)	0.0303(3)
	y	0.8006(5)	0.8006(4)	0.7993(3)	0.7982(8)
	z	0.6718(8)	0.6723(7)	0.6734(9)	0.6758(7)
	O_1 x	0.3205(1)	0.3206(1)	0.3202(6)	0.3215(2)
	y	0.4321(5)	0.4312(8)	0.4297(6)	0.4298(7)
	z	0.9755(2)	0.9632(8)	0.9654(9)	0.9689(6)
	O_2 x	0.4904(9)	0.4855(4)	0.4859(9)	0.4863(4)
	y	0.4370(7)	0.4360(8)	0.4361(4)	0.4356(9)
	z	0.5138(8)	0.5139(8)	0.5149(1)	0.5161(8)
	O_3 x	0.9959(1)	1.0026(4)	1.0020(6)	0.9999(1)
	y	0.2055(7)	0.2065(6)	0.2064(5)	0.2057(9)
	z	0.6569(3)	0.6615(5)	0.6605(3)	0.6542(4)
	O_4 x	0.1584(4)	0.1629(3)	0.1627(1)	0.1613(2)
	y	0.2000(1)	0.2009(1)	0.2008(9)	0.2001(6)
	z	0.1618(3)	0.1518(9)	0.1518(4)	0.1580(3)
	O_5 x	0.1715(1)	0.1665(1)	0.1673(7)	0.1691(1)
	y	0.6778(2)	0.6782(4)	0.6793(4)	0.6788(2)
	z	0.8466(3)	0.8414(7)	0.8426(1)	0.8400(2)
	O_6 x	0.1647(1)	0.1709(1)	0.1719(7)	0.1721(1)
	y	0.9419(6)	0.9436(8)	0.9430(7)	0.9434(1)
	z	0.5166(1)	0.5095(3)	0.5095(1)	0.5112(3)

R_{wp}	3.86	4.78	4.48	4.62
R_p	2.99	3.81	3.52	3.67
R_{exp-}	1.85	2.34	1.87	2.43
R_B	3.9	4.5	4.53	4.80

Bibliography

[1] X. Mao, W. Wang, X. Chen and Y. Lu. Multiferroic properties of layer structured $Bi_5Fe_{0.5}Co_{0.5}Ti_3O_{15}$ ceramics. *Appl. Phys. Lett.* **95** 082901 (2009).

[2] M. Fiebig. Revival of the magnetoelectric effect. *J. Phys. D: Appl. Phys.* **38** R123 (2005).

[3] S. Ju, T. Cai, G. Guo, and Z. Li. Electrically controllable spin filtering and switching in multiferroic tunneling junctions. *Phys. Rev. B* **75** 064419 (2007).

[4] M. Kumar and K. L. Yadav. Rapid liquid phase sintered Mn doped $BiFeO_3$ ceramics with enhanced polarization and weak magnetization. *Appl. Phys. Lett.* **91** 242901 (2007).

[5] H. Schmid. On a magnetoelectric classifications of materials. *Int. J. Magn.* **4** 337 (1973).

[6] Y. F. Popov, A. M. Kadomtseva, S. S. Kratov, D. V. Belov, G. P. Vorb’ov, P. N. Makhov and A. K. Zvezdin. Features of the magnetoelectric properties of $BiFeO_3$ in high magnetic fields. *J. Low Temp. Phys.* **27** 478(2001).

[7] T. Kimura, S. Kawamoto, I. Yamada, M. Azuma, M. Takano and Y. Tokura. Magnetocapacitance effect in multiferroic $BiMnO_3$. *Phys. Rev. B* **67** 180401 (2003).

[8] T. Katsufuji, S. Mori, M. Masaki, Y. Moritomo, N. Yamamoto and H.Takagi. Dielectric and magnetic anomalies and spin frustration in hexagonal $RMnO_3$ (R = Y, Yb and Lu). *Phys. Rev. B* **64** 104419 (2001).

[9] N. A. Hill. Why are there so few magnetic ferroelectrics?. *J. Phys. Chem. B* **104** 6694 (2000).

[10] D. I. Khomskii. Multiferroics: different ways to combine magnetism and ferroelectricity. *J. Magn. Magn. Mater.* **306** 1 (2006).

[11] Z. J. Huang, Y. Cao, Y. Y. Sun, Y. Y. Xue, and C.W. Chu. Coupling between the ferroelectric and antiferromagnetic orders in $YMnO_3$. *Phys. Rev. B* **56** 2623 (1997).

[12] J. Y. Kim, T.Y. Koo and J. H. Park. Orbital and bonding anisotropy in a half-filled $GaFeO_3$ magnetoelectric ferrimagnet. *Phys. Rev. Lett.* **96** 047205 (2006).

[13] K. Sawada and N. Nagaosa. Optical magnetoelectric effect in multiferroic materials: evidence for a lorentz force acting on a ray of light. *Phys. Rev. Lett.* **95** 237402 (2005).

[14] J. H. Jung, M. Matsubara, T. Arima, J.P. He, Y. Kaneko and Y. Tokura. Optical magnetoelectric effect in the polar $GaFeO_3$ ferrimagnet. *Phys. Rev. Lett.* **93** 037403 (2004).

[15] K. U. Kang, S. B. Kim, S. Y. An, S. Cheong and C. S. Kim. Magnetic properties of $GaFeO_3$ prepared by slow cooling and quenched heat treatment method. *J. Magn. Magn. Mater.* **304** e769 (2006).

[16] W. Kim, JH .We, SJ. Kim and CS. Kim. Effects of cation distribution for $AFeO_3$ (A = Ga,Al). *J. App. Phys.* **101** 09M515 (2007).

[17] T. Arima, D. Higashiyama, Y .Kaneko, J. P. He, T. Goto, S. Miyasaka, T. Kimura, K. Oikawa, T. Kamiyama, R. Kuumai and Y. Tokura. Structural and magnetoelectric properties of $Ga_{2-x}Fe_xO_3$ single crystals grown by a floating-zone method. *Phys. Rev. B* **70** 064426 (2004).

[18] J. P. Remeika. $GaFeO_3$: A ferromagnetic-piezoelectric compound. *J. Appl. Phys.* **31** 263S (1960).

[19] E. A. Wood. The unit cell and space group of gallium iron oxide, a piezoelectric ferromagnetic crystal. *Acta Cryst.* **13** 682 (1960).

[20] C. H. Nowlin and R. V. Jones. Magnetism of piezoelectric $Ga_{2-x}Fe_xO_3$. *J. Appl. Phys.* **34** 1262 (1963).

[21] R. B. Frankel, N. A. Blum, S. Foner, A. J. Freeman and M. Schieber. Ferrimagnetic structure of magnetoelectrric $Ga_{2-x}Fe_xO_3$. *Phys. Rev. Lett.* **15** 958 (1965).

[22] G. T. Rado. Observation and possible mechanisms of magnetoelectric effects in a ferromagnet. *Phys. Rev. Lett.* **13** 335 (1964).

[23] J. B. Goodenough. Direct cation-cation interactions in several oxides. *Phys. Rev.* **117** 1442 (1960).

[24] P. W. Anderson. Antiferromagnetism, theory of superexchange interaction. *Phys. Rev.* **79** 350 (1950).

[25] E. O. Wollan and W .C. Koehler. Neutron diffraction study of the magnetic properties of the series of perovskite-type compounds [(1-x)La, xCa]MnO_3. *Phys. Rev.* **100** 545 (1955).

[26] W. C. Koehler, E. O. Wollan and M. K. Wilkinson. Neutron diffraction study of the magnetic properties of rare-earth-iron perovskites. *Phys. Rev.* **1** 58 (1960).

[27] M. A. Gilleo. Crystallographic studies of perovskite-like compounds. III. La(M_x, Mn_{1-x})O_3 with M = Co, Fe and Cr. *Acta Crys.* **10** 161 (1957).
[28] L. Nèel, *Ann. Phys.* **3** 137 (1948).

[29] S. Blundell. Magnetism in condensed matter (Oxford University press: Oxford, 2001).

[30] L. D. Landau and E. M. Lifshitz. Quantum Physics (Pergamon press, New York, 1965).

[31] R. Coelho. Physics of dielectrics for engineer (Elsevier scientific pub. Co., 1979).

[32] P. Debye. Polar Molecules (Dover, New York, 1929).

[33] G. A. Samara. The relaxational properties of compositionally disordered ABO_3 perovskites. *J. Phys.: Condens. Matter* **15** R367 (2003).

[34] L. E. Cross. *Ferroelectrics*, **76** 241 (1987).

[35] D. Vandeven, J. Galy, M. Pouchard and P. Hagenmuller. Evolution structurale en fonction de la temperature de quelques bronzes oxygenes de tungstene pauvres en element d'insertion. *Mat. Res. Bull* **2** 809 (1967).

[36] Kwan Chi Kao. Dielectric phenomena in solids (California: Elsevier, 2004).

[37] J. F. Scott. Ferroelectrics go bananas. *J. Phys.: Condens. Matter* **20** 021001 (2008).

[38] W. Eerenstein, N. D. Mathur and J. F. Scott. Multiferroic and magnetoelectric materials. *Nature* **442** 759 (2006).

[39] B. B. van Aken, J. P. Rivera, H. Schmid and M. Fiebig. Observation of ferrotoroidic domains. *Nature* **449** 702 (2007).

[40] H. Schmid. *Ferroelectricity* **162** 317 (1994).

[41] D. Khomskii. Classifying multiferroics: mechanisms and effects. Physics **2**, 20 (2009).

[42] N. A. Spaldin, M. Fiebig and M. Mostovoy. The toroidal moment in condensed-matter physics and its relation to the magnetoelectric effect. *J.Phys.: Condens. Matter* **20**, 434203, (2008).

[43] W. F. Brown, Jr., R. M. Hornreich and S. Shtrikman, Upper bound on the magnetoelectric susceptibility. *Phys. Rev.* **168** 574 (1968).

[44] L .D. Landau, E. M. Lifshitz and L. P. Pitaevskii. Electrodynamics of continuous media. Elsevier, Heidelberg, 2nd edition, 1984. pp.130-135, 172-177, This book was first published in 1957 (in Russian) by Landau and Lifshitz, translated to english in 1960 (Pergamon press).

[45] R. R. Birss. Symmetry and magnetism. vol. 3. (North-Holland publ. Co., Amsterdam, pp.128-129, 133-136, 1964).

[46] T. Kimura, T. Goto, H. Shintani, K. Ishizaka, T. Arima and Y. Tokura. Magnetic control of ferroelectric polarization. *Nature* **426** 55 (2003).

[47] N. Hur, S. Park, P. A. Sharma, J. S. Ahn, S. Guha and S-W. Cheong. Electric polarization reversal and memory in a multiferroic material induced by magnetic fields. *Nature* **429** 392 (2004).

[48] S. W. Cheong and M. Mostovoy. Multiferroics: a magnetic twist for ferroelectricity. Nat. Mater. **6** 13 (2007).

[49] K. F. Wang, J. M. Liu, and Z. F. Ren. Multiferroicity: the coupling between magnetic and polarization order. *Adv. Physics* **58** 321 (2009).

[50] R. Seshadri and N. A. Hill. Visualizing the role of Bi 6s “lone pairs” in the off center distortion in ferromagnetic $BiMnO_3$. *Chem. Mater.* **13** 2892 (2001).

[51] T. Kimura, S. Kawamoto, I. Yamada, M. Azuma, M. Takano, and Y. Tokura .Magnetocapacitance effect in multiferroic $BiMnO_3$. *Phys. Rev.B* **67** 180401(R) (2003).

[52] J. Y. Son and Y. H.Shin. Multiferroic $BiMnO_3$ thin films with double $SrTiO_3$ buffer layers. *Appl. Phys. Lett.* **93** 062902 (2008).

[53] J. Wang, J. B. Neaton, H. Zheng, V. Nagarajan, S. B. Ogale, B. Liu, D. Viehland, V. Vaithyanathan, D. G. Schlom, U. V. Waghmare, N. A. Spaldin, K. M. Rabe, M. Wuttig and R. Ramesh. Epitaxial $BiFeO_3$ multiferroic thin film heterostructures. *Science* **299** 1719 (2003).

[54] D. Lebeugle, D. Colson, A. Forget, and M.Viret. Very large spontaneous electric polarization in $BiFeO_3$ single crystals at room temperature and its evolution under cycling fields. *Appl. Phys. Lett.* **91** 022907 (2007).

[55] I. V. Solovyev and Z. V. Pchelkina. Orbital ordering and magnetic interactions in $BiMnO_3$. *New J. Phys.* **10** 073021 (2008).

[56] G. Catalan and J. F. Scott. Physics and applications of bismuth ferrite. *Adv. Mater.* **21** 2463 (2009).

[57] I. Sosnowska, T. Peterlin-Neumaier, and E. Steichele. Spiral magnetic ordering in bismuth ferrite. *J. Phys. C: Solid State Phys.* **15** 4835 (1982).

[58] H. L. Yakel, W. C. Koehler, E. F. Bertaut, and E. F. Forrat. On the crystal structure of the manganese (III) trioxides of the heavy lanthanides and yttrium. *Acta Crystallogr., Sect. A: Found. Crystallogr.* **16** 957 (1963).

[59] B. B. Van Aken, T. T. M. Palstra, A. Filippetti, and N. A. Spaldin. The origin of ferroelectricity in magnetoelectric $YMnO_3$. *Nat. Mater.* **3** 164 (2004).

[60] W. C. Koehler, H. L. Yakel, E. O. Wollan, and J. W. Cable. A note on the magnetic structures of rare earth manganese oxides. *Phys. Lett.* **9** 93 (1964).

[61] B. B. Van Aken, T. T. M. Palstra, A. Filippetti, and N. A. Spaldin. The origin of ferroelectricity in magnetoelectric $YMnO_3$. *Nature Mater.* **3** 164 (2004).

[62] A. D. Christianson, M. D. Lumsden, M. Angst, Z. Yamani, W. Tian, R. Jin, E. A. Payzant, S. E. Nagler, B. C. Sales, and D. Mandrus. Three dimensional magnetic correlations in multiferroic $LuFe_2O_4$. *Phys. Rev. Lett.* **100** 107601 (2008).

[63] N. Ikeda, H. Ohsumi, K. Ohwada, K. Ishii, T. Inami, K. Kakurai, Y. Murakami, K. Yoshii, S. Mori, Y. Horibe, and H. Kito. Ferroelectricity from iron valence ordering in the charge-frustrated system $LuFe_2O_4$. *Nature* **436** 1136 (2005).

[64] S. C. Abrahams, J. M. Reddy, and J. L. Bernstein. Crystal structure of piezoelectric Ferromagnetic Gallium Iron Oxide. *Journal of chemical physics* **42** 3957 (1965).

[65] W. Kim, J. Hoon We, S. J. Kim, and C. S. Kim. Effects of cation distribution for $AFeO_3$ (A = Ga, Al) . *J. App. Phys.* **101** 09M515 (2007).

[66] M. J. Han, T. Ozaki and J. Yu. Magnetic ordering and exchange interactions in multiferroic $GaFeO_3$. *Phys. Rev. B* **75** 060404R (2007)

[67] H. Schmid and A. J. Freeman. Magnetoelectric interaction phenomena in crystals, (Gordon and Breach, New York , 1975).

[68] J. Igarashi and T. Nagao. Analysis of optical magnetoelectric effect in $GaFeO_3$. *Phys .Rev. B* **80** 054418 (2009).

[69] Yu. F. Popov, A. M. Kadomtseva, G. P. Vorob'ev, V. A. Timofeeva, D. M. Ustinin, A. K. Zvezdin and M. M. Tegeranchi. Magnetoelectric effect and toroidal ordering in $Ga_{2-x}Fe_xO_3$. *J. Exp. Theor. Phys.* **87** 146 (1998).

[70] J. M. Trooster. Mössbauer measurements on $Ga_{2-x}Fe_xO_3$. *Phys. Lett.* **16** 21 (1965).

[71] J. M. Trooster and A. Dynanus. Mössbauer effect in $Ga_{2-x}Fe_xO_3$ and related compounds. *Phys. status solidi* **24** 487 (1967).

[72] E. F. Bertaut, G. Bassi, G. Buisson, J. Chappert, A. Delapalme, R. Pauthenet, H. P. Rebouillat and R. Aléonard. *J. Phys. (Paris)* **27** 433 (1966).

[73] S. Nakamura, S. Morimoto, T. Saito and Y. Tsunoda. Mössbauer study on the polar ferrimagnet $GaFeO_3$. *Journal of Physics: Conference Series* **200** 012140 (2010).

[74] Z. H. Sun, B. L. Cheng, S. Dai, L. Z. Cao, Y. L. Zhou, K. J. Jin, Z. H. Chen and G. Z. Yang. Dielectric property studies of multiferroic $GaFeO_3$. *J.Phys. D: Appl. Phys.* **39** 2481 (2006).

[75] Y. Aikawa, T. Katsufuji, T. Arima, and K. Kato. Effect of Mn trimerization on the magnetic and dielectric properties of hexagonal $YMnO_3$. *Phys. Rev. B* **71** 184418 (2005).

[76] T. Kimura, Y. Sekio, H. Nakamura, T. Siegrist, and A. P. Ramirez. Cupric oxide as an induced-multiferroic with high T_C. *Nature Mater.* **7** 291 (2008).

[77] V. B. Naik and R. Mahendiran, Electrical, magnetic, magnetodielectric and magnetoabsorption studies in multiferroic $GaFeO_3$. *J. Appl. Phys.* **106** 123910 (2009).

[78] B. Lorenz, Y. Q. Wang, Y. Y. Sun, and C. W. Chu, Large magnetodielectric effects in orthorhombic $HoMnO_3$ and $YMnO_3$. *Phys. Rev. B* **70** 212412 (2004).

[79] M. Dawber, K. M. Rabe and J. F. Scott, Physics of thin-film ferroelectric oxides. *Rev. Mod. Phys.* **77** 1083 (2005).

[80] A. Shireen, R. Saho, P. Mandal, A. Sundaresan and C. N. R. Rao. Multiferroic and magnetodielectric properties of the $Al_{1-x}Ga_xFeO_3$ family of oxides. *J. Mater. Chem.* **21** 57 (2011).

[81] J. Rodríguez-Carvajal. *Phys. B (Amsterdam, Neth.)* **192** 55 (1993).

[82] M. Hoelzel, A. Senyshyn, R. Gilles, H. Boysen, and H. Fuess. The structure powder diffractometer Spodi at the FRM II. *Neutron News* **18** 23 (2007).

[83] http://www.frm2.tum.de/en/index.html.

[84] G. E. Bacon. Neutron diffraction. (Clarendon Press: Oxford, 1975).

[85] A.V. Shubnikov and N. V. Belov. Colored symmetry. (Oxford Pergamon Press: New York, 1964).

[86] N. B. Greenwood and T. C. Gibb. Mössbauer spectroscopy. London: (Chapman and Hall, 1971).

[87] K. Szymański. Explicit expression for the Intensity tensor for 3/2-1/2 transitions and solution of the ambiguity problem in the Mössbauer spectroscopy. *J. Phys.: Condens. Matter* **12** 7495 (2000).

[88] D. Satuła, K. Szymanski, L. Dobrzynski, V.H. Tran and R. Troc. Mössbauer data analysis based on invariants and application to UFe_5Sn. *Phys. Rev. B* **78** 014411 (2008).

[89] M. Knapp, C. Baehtz, H. Ehrenberg, and H. Fuess, *J. Synchrotron Radiat.* **11** 328 (2004).

[90] J. Ihringer and A. Küster. Cryostat for synchrotron powder diffraction with sample rotation and controlled gas atmosphere in the sample chamber. *J. Appl. Crystallogr.* **26** 135 (1993).

[91] P. Ayyub, V. R. Palkar, S. Chattopadhyay, and M. Multani. Effect of crystal size reduction on lattice symmetry and cooperative properties**.** *Phys. Rev. B* **51** 6135 (1995).

[92] C. N. Chinnasamy, A. Narayanasamy, N. Ponpandian, R. Justin Joseyphus, B. Jeyadevan, K. Tohjib and K. Chattopadhyay. Grain size effect on the Nèel temperature and magnetic properties of nanocrystalline $NiFe_2O_4$ spinel. *J. Magn. Magn. Mater.* **238** 281 (2002).

[93] K. Maaz, A. Mumtaz, S. K. Hasanain and A. Ceylan. Synthesis and magnetic properties of cobalt ferrite ($CoFe_2O_4$) nanoparticles prepared by wet chemical route. *J. Magn. Magn. Mater.* **308** 289 (2007).

[94] F. Bouree, J. L. Baudour, E. Elbadraoui, J. Musso, C. Laurent and A. Rousset. Crystal and magnetic structure of piezoelectric, ferrimagnetic and magnetoelectric aluminium iron oxide $FeAlO_3$ from neutron powder diffraction. *Acta Crystallogr. B* **52** 217 (1996).

[95] M. Gich, C. Frontera, A. Roig, E. Taboada, and E. Molins. High- and low-temperature crystal and magnetic structures of ε-Fe_2O_3 and their correlation to its magnetic properties. *Chem. Mater.* **18** 3889 (2006).

[96] T. Balic Zunic and I. Vickovic. IVTON - a program for the calculation of geometrical aspects of crystal structures and some crystal chemical applications. *J. Appl. Cryst.* **29** 305 (1996).

[97] M. Pissas, D. Stamopoulos, Y. Sanakis and A. Simopoulos, Magnetic properties of the magnetoelectric $Al_{2-x}Fe_xO_3$ (x = 0.8, 0.9 and 1). *J. Phys.: Condens. Matter* **20** 415222 (2008).

[98] K. J. D. Mackenzie and I. W. M. Brown. The Mössbauer spectrum and structure of iron (Ill) aluminium oxide, $FeAlO_3$. *Mater. Sci. Lett.* **3** 159 (1984).

[99] E. F. Bertaut In: G. Rado, H. Suhl. Magnetism Vol. III. (Academic Press, New York 1963).

[100] K. Sharma, V. R. Reddy, D. Kothari, A. Gupta, A. Banerjee, and V. G. Sathe, Low temperature Raman and high field ^{57}Fe Mössbauer study of polycrystalline $GaFeO_3$. *J. Phys. : Condens. Matter* **22** 146005(2010).

[101] S. Margulies and J. R. Ehrman. Transmission and line broadening of resonance radiation incident on a resonance absorber. *Nucl. Instrum. Methods* **12** 131 (1961).

[102] O.V. Kovalev. Representations of the crystallographic space groups: irreducible representations, induced representations and corepresentations, Nauka, Moscow, 1986 (Gordon and Breach, Yverdon, Switzerland, 1993).

[103] S. A. Ivanov, P. Nordblad, R. Tellgren, T. Ericsson, R. Rundlof. Structural, magnetic and Mössbauer spectroscopic investigations of the magnetoelectric relaxor $Pb(Fe_{0.6}W_{0.2}Nb_{0.2})O_3$. *Solid State Sci.* **9** 440 (2007).

[104] R. D. Shannon, Revised effective ionic radii and systematic studies of interatomic distances in halides and chalcogenides. *Acta Crystallogr. A* **32** 751 (1976).

[105] J. R. Teague, R. Gerson, W. James. Dielectric hysteresis in single crystal $BiFeO_3$. *Solid State Commun.* **8** 1073 (1970).

[106] S. V. Kiselev, A. N. Kshnyakina, R. P. Ozerov and G. S. Zhdanov. *Sov. Phys. Solid St.* **5** 2425 (1964).

[107] E. Kan, H. Xiang, C. Lee, F. Wu, J. Yang and M-H Whangbo. Ferroelectricity in perovskites with s^0 A-Site cations: toward near room-temperature multiferroics. *Angew. Chem. Int. Ed.* **49** 1603(2010).

[108] A. A. Belik, T. Furubayashi, Y. Matsushita, M. Tanaka, S. Hishita, and E. T. Muromachi. Indium based perovskites: a new class of near-room-temperature multiferroics. *Angew. Chem.* **121** 6233 (2009).

[109] H. Taguchi. Relationship between crystal structure and electrical properties of $Nd(Cr_{1-x}Fe_x)O_3$. *J. Solid State Chem.* **131** 108 (1997).

[110] A. Belayachi, E. Loudghiri, M. El Yamani, M. Nouges, J. L. Dormann, M. Taibi, Ann. Chim. Unusual magnetic behavior in $LaFe_{1-x}Cr_xO_3$ comportement magnétique inhabituel du système $LaFe_{1-x}Cr_xO_3$. *Sci. Mater.* **23** 297 (1998).

[111] Maxim V. Kuznetsov, Quentin A. Pankhurst, Ivan P. Parkin and Yury G. Morozov. Self-propagating high-temperature synthesis of chromium substituted lanthanum orthoferrites $LaFe_{1-x}Cr_xO_3(0 \leq x \leq 1)$. *J. Mater. Chem.* **11** 854 (2001).

[112] J. H. Li and Q. C. Sun. Effects of Cr_2O_3 Doping on the electrical properties and the temperature stabilities of PZT binary piezoelectric ceramics. *Rare Metals* **27** 362 (2008).

[113] Z. P. Yang, R. Zhang, L. L. Yang and Y. F. Chang. Effects of Cr_2O_3 doping on the electrical properties and the temperature stabilities of PNW–PMN–PZT ceramics. *Mater. Res. Bull.* **42** 2156 (2007).

[114] Y. Du, Z. X. Cheng, S. X. Dou, M. Shahbazi, X. L. Wang. Enhancement of magnetization and dielectric properties of chromium-doped $BiFeO_3$ with tunable morphologies. *Thin Solid Films* **518** e5 (2010).

[115] M. Takahashi. Space charge effect in lead zirconate titanate ceramics caused by the addition of impurities. *Jpn. J. Appl. Phys.* **9** 1236 (1970).

[116] Y. D. Hou, P. X. Lu, M. K. Zhu, X. M. Song, J. L. Tang, B. Wang, H. Yan. Effect of Cr_2O_3 addition on the structure and electrical properties of $Pb((Zn_{1/3}Nb_{2/3})_{0.2}(Zr_{0.5}Ti_{0.5})_{0.80})O_3$ ceramics. *Mater. Sci. Eng. B* **116** 104 (2005).

[117] Y. Nagata, S. Yashiro, T. Mitsuhashi, A. Koriyama, Y. Kawashima, H. Samata. Magnetic properties of $RFe_{1-x}Mn_xO_3$ (R=Pr, Gd, Dy). *J. Magn. Magn. Mater.* **237** 250 (2001).

[118] Y. Q. Jia, S. T. Liu, Y. Wu, M. Z. Jin, X. W. Liu and M. L. Liu. Crystal structures and Mössbauer spectra of $LaFe_{1-x}Mn_xO_3$ and $LaFe_{1-x}Co_xO_3$ (x = 0 to 0.9). *Physic status solidi (a)* **143** 15 (2006).

[119] J. Kanamori. Superexchange interaction and symmetry properties of electron orbitals. *J. Phys. Chem. Solids* **10** 87 (1959).

[120] G. H. Jonker. Magnetic compound with perovskite structure IV, conducting and non conducting compounds. *Physica* **22** 707 (1956).

[121] B. Zhou, Y. W. Zhang, C. S. Liao and C. H. Yan. Magnetism and phase transition for $CoFe_{2-x}Mn_xO_4$ nanocrystalline thin films and powders. *J. Magn. Magn. Mater.* **247** 70 (2002).

[122] R. C. Kambale, P. A. Shaikh, C. H. Bhosale, K.Y. Rajpure and Y. D. Kolekar. The effect of Mn substitution on the magnetic and dielectric properties of cobalt ferrite synthesized by an autocombustion route. *Smart Mater Struct.* **18** 115028 (2009).

[123] L. Cui, Y-D. Hou, S. Wang, C. Wang and M-K. Zhu. Relaxor behavior of $(Ba,Bi)(Ti,Al)O_3$ ferroelectric ceramic. *J. Appl. Phys.* **107** 054105 (2010).

[124] K. Uchino, S. Nomura. *Ferroelectr. Lett.* **44** (1982)55.

[125] V. Y. Pomjakushin, M. Kenzelmann, A. Dönni, A. B. Harris, T. Nakajima, S. Mitsuda, M. Tachibana, L. Keller, J. Mesot, H. Kitazawa and E. Takayama-Muromachi. Evidence for large electric polarization from collinear magnetism in $TmMnO_3$. *New Journal of Physics* **11** 04301 (2009).

[126] K. Marty, P. Bordet, V. Simonet, M. Loire, R. Ballou, C. Darie, J. Kljun, P. Bonville, O. Isnard, P. Lejay, B. Zawilski, and C. Simon. Magnetic and dielectric properties in the langasite-type compounds: $A_3BFe_3D_2O_{14}$ (A = Ba, Sr, Ca; B = Ta, Nb, Sb; D = Ge, Si). *Phys. Rev. B* **81**, 054416 (2010).

[127] A. P. Sazonov. Peculiarities of crystal and magnetic structures of synthetic Co-Olivine, Co_2SiO_4. (dissertation, der Rheinisch-Westfälischen Technischen Hochschule Aachen, 2009).

[128] W. Lottermoser and H. Fuess. Magnetic structure of the orthosilicates Mn_2SiO_4 and Co_2SiO_4. *Physic status solidi (a)***109** 589 (1988).

[129] K. P. Chae, Y. B. Lee, J. G. Lee and S. H. Lee. Crystallographic and magnetic properties of $CoCr_xFe_{2-x}O_4$ ferrite powders. *J. Magn. Magn. Mater.* **220** 59 (2000).

[130] H. C. Fang, Z. Yang, C. K. Ong, Y. Li and C. S. Wang. Preparation and magnetic properties of (Zn–Sn) substituted barium hexaferrite nanoparticles for magnetic recording. *J. Magn. Magn. Mater.* **187** 12 (1998).

[131] S .W. Lee, S. Y. An, G. Y. Ahn and C. S. Kim. Atomic migration in $MgFe_{2-x}Cr_xO_4$. *J. Appl. Phys.* **87** 6238 (2000).

[132] K. J. Kim, H. J. Lee, J. H. Lee, S. Lee and C. S. Kim. Magnetotransport properties of inverse-spinel $Cr_xFe_{3-x}O_4$ thin films. *J. Appl. Phys.* **104** 083912 (2008).

[133] M. W. Cole, C. Hubbard, E. Ngo, M. Ervin and M. Wood. Structure property relationships in pure and acceptor-doped $Ba_{1-x}Sr_xTiO_3$ thin films for tunable microwave device applications. *J. Appl. Phys.* **92** 475 (2002).

[134] M-F. Hu, Y Zhuo, S-X. Wang and Y. Tian. Study on dielectric and tunable properties of Cr-doped $Ba_{0.6}Sr_{0.4}TiO_3$ thin films by rf sputtering. *J. Mater. Sci.* **43** 3162 (2008).

[135] A. K. Jonscher. Dielectric relaxation in solids. (Chelsea Dielectric Press, London, 1983).

[136] N. K. Singh, R. N. P. Choudhary and A. Panigrahi. Ferroelectric phase transition in $Ba_5LaTi_{3-x}Zr_xNb_7O_{30}$ [x=0, 1, 2, 3] ceramics. *Matter. Lett.* **57** 36 (2002).

[137] A. Dutta and T. P. Sinha. Dielectric relaxation and electronic structure of $Ca(Fe_{1/2}Sb_{1/2})O_3$. *Phys. Rev. B* **76** 155113 (2007).

[138] A. Dutta and T. P. Sinha. Impedance spectroscopy study of $BaMg_{1/3}Nb_{2/3}O_3$: Frequency and time domain analyses. *Physica B* **405** 1475 (2010).

[139] R. K. Dwivedi, D. Kumar and O. Parkash. Valence compensated perovskite oxide system $Ca_{1-x}La_xTi_{1-x}Cr_xO_3$ Part II Electrical transport behavior. *J. Mater. Sci.* **36** 3649 (2001).

[140] F. A. Kroger and H. Vink. Relations between the concentrations of imperfections in crystalline solids. *J. Solid State Phys.* **3** 307 (1956).

[141] M. Idress, M. Nadeem and M. M. Hassan. Investigation of conduction and relaxation phenomena in $LaFe_{0.9}Ni_{0.1}O_3$ by impedance spectroscopy. *J. Phys. D: Appl. Phys.* **43** 155401 (2010).

[142] M. Tanaka, K. Siratori and N. Kimizuka. Mössbauer study of RFe_2O_4. *J. Phys. Soc. Jpn.* **53** 760 (1984).

[143] V. A. Khomchenko, D. A. Kiselev, J. M. Vieira, Li Jian , A. L. Kholkin, and A. M. L. Lopes, Y. G. Porelov, J. P. Araujo and M. Maglione. Effect of diamagnetic Ca, Sr, Pb, and Ba substitution on the crystal structure and multiferroic properties of the $BiFeO_3$ perovskite. *J . Appl. Phys.* **103** 024105 (2008).

[144] J. R. Macdonald, E. Barsoukov, Impedance spectroscopy: theory, experiment, and application. (2nd ed.,Wiley/Intersience, New Jersey, 2005).

[145] A. Molak, M. Paluch, S. Pawlus, J. Klimontko, Z. Ujma and I. Gruszka. Electric modulus approach to the analysis of electric relaxation in highly conducting $(Na_{0.75}Bi_{0.25})(Mn_{0.25}Nb_{0.75})O_3$ ceramics. *J. Phys. D: Appl. Phys.* **38** 1450 (2005).

[146] A. K. Jonscher. The 'universal' dielectric response. *Nature* **267** 673 (1977).

[147] A. Delapalme. Etude cristallographique du compose $Fe_xGa_{2-x}O_3$ par neutrons polarises. J. Phys. Chem. Solids **28** 1451 (1967).

[148] A. Mogro-Campero, L. G. Turner, E. L. Hall, M. I. Garbauskas and N. Lewis. Epitaxial growth and critical current density of thin films of $YBa_2Cu_3O_{7-x}$ on $LaAlO_3$ substrates. *Appl. Phys. Lett.* **54** 2719(1989).

[149] R. L. Sandstrom, E. A. Giess, W. J. Gallaher, A. Segmuller, E. I. Cooper, M. F. Chisholm, A. Gupta, S. Shinde and R. B. Laibowitz. Lanthanum gallate substrates for epitaxial high temperature superconducting thin films. *Appl. Phys. Lett.* **53** 1874(1988).

[150] V. V. Mamutin, A. A. Toropov, N. F. Kartenko, S. V. Ivanov, A. Wagner and B. Monemar. MBE GaN grown on (101) $NdGaO_3$ substrates. *Mater. Sci. Eng.* B **59** 56(1999).

[151] A Senyshyn, D. M. Trots, J. M. Engel , L. Vasylechko, H. Ehrenberg, T. Hansen, M. Berkowski and H. Fuess. Anomalous thermal expansion in rare-earth gallium perovskites: a comprehensive powder diffraction study. *J. Phys.: Condens. Matter* **21** 145405 (2009).

[152] L. T. Tsymbal, Ya. B. Bazaliy, V. N. Derkachenko, V. I. Kamenev, G. N. Kakazei, F. J. Palomares, and P. E. Wigen. Magnetic and structural properties of spin-reorientation transitions in Orthoferrites. *J. Appl. Phys.* **101**, 123919 (2007)

[153] Y. Tokunaga, S. Iguchi, T. Arima and Y. Tokura. Magnetic-Field-Induced Ferroelectric State in $DyFeO_3$. *Phys. Rev. Lett.* **101** 097205 (2008).

[154] E. F. Bertaut. Lattice theory of spin configuration. *J. Appl. Phys. Suppl.* **33** 1138 (1962).

Acknowledgements

The present thesis has been prepared under the direction of Prof. Dr.Ing. Dr. h. c. Hartmut Fuess in the Department of Structural Research at the Institute of Materials Science of the Technical University of Darmstadt. I would like to take this opportunity to thank him for providing me the possibility to carry out this thesis in his group and all the support I received during this time.

I would like to thank Prof. Dr. rer. nat. Lambert Alff for accepting to be the second referee of this work.

My further thanks go to:

Prof. Krzysztof Szymanski and Prof. Ludwik Dobrzynski (University of Bialystok, Faculty of Physics and the Soltan Institute of Nuclear Studies, Poland) for Mössbauer spectroscopy and for fruitful discussions.

Dr. A. Senyshyn and M. Hinterstein for helping in neutron and synchrotron powder diffraction measurements.

Also, I would like thank all colleagues from the Institute for Materials Science, TU Darmstadt.

I wish to acknowledge with gratitude and appreciation the Egyptian Cultural Bureau and Study Mission in Berlin, Germany for being supportive and helpful. Finally I would like to extend my sincere appreciation and gratitude to the Egyptian Government for the financial support.

I would like to avail this opportunity to express my heartiest gratitude to my wife for her encouragement, support during my study and our residence in Germany.

Erklärung

Ich erkläre hiermit an Eides Statt, dass ich meine Dissertation selbständig und nur mit den angegebenen Hilfsmitteln angefertigt habe.

Ich habe bisher noch keinen Promotionversuch unternommen.

Mohamed Bakr Mahmoud Mohamed

Darmstadt, 2011

Curriculum Vitae

Personal Information

Name: Mohamed Bakr Mahmoud Mohamed

Birthday: 30.01.1977
Birthplace: Cairo
Nationality: Egyptian

Education:

1999	Bachelor degree of Physics at Ain Shams University, Cairo, Egypt.
2005	Master degree of Physics at Ain Shams University, Cairo, Egypt.
2004	Diploma in condensed matter Physics (ICTP),Trieste, Italy.
2011	Ph.D. degree at Technical University of Darmstadt, Darmstadt, Germany

Publications

M. Bakr Mohamed, A. Senyshyn, H. Ehrenberg and H. Fuess. Structural, magnetic, dielectric properties of multiferroic $GaFeO_3$ prepared by solid state reaction and sol-gel methods, Journal of Alloys and Compounds **492** (1-2) L20 (2010).

M. Bakr Mohamed, H. Wang and H. Fuess. Dielectric relaxation and magnetic properties of Cr doped $GaFeO_3$. J. Phys. D: Appl. Phys. **43** 455409 (2010).

K. Szymański, L. Dobrzyński, M. Bakr, D. Satuła, W. Olszewski, G. Parzych and H. Fuess. Fe cation occupancies in $GaFeO_3$ prepared by sol-gel and solid state reaction. Phase Transitions. **83** 824 (2010).

M. Bakr Mohamed and H. Fuess. Effect of Mn doping on structural and magnetic properties of $GaFeO_3$, JMMM, 2011, in press.